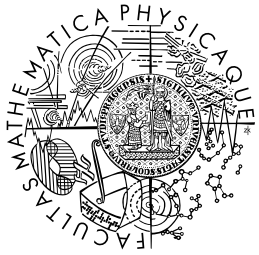

FACULTY
OF MATHEMATICS
AND PHYSICS
Charles University

DOCTORAL THESIS

Lukáš Chlad

Study of transverse flow of kaons in Au + Au collisions at $1.23A\,\mathrm{GeV}$

Nuclear Physics Institute CAS, p.r.i.

Supervisor of the doctoral thesis:	RNDr. Andrej Kugler, CSc.
Study programme:	Particle and Nuclear Physics
Study branch:	Physics

Prague 2021

I declare that I carried out this doctoral thesis independently, and only with the cited sources, literature and other professional sources.

I understand that my work relates to the rights and obligations under the Act No. 121/2000 Sb., the Copyright Act, as amended, in particular the fact that the Charles University has the right to conclude a license agreement on the use of this work as a school work pursuant to Section 60 subsection 1 of the Copyright Act.

In ..... date ..... signature of the author

I would like to first thank my family, which has grown significantly during my doctoral studies and which has supported me during this long period. I am very grateful to Dr. Kugler who has been my supervisor since the bachelor thesis and helped me a lot during these many years. Moreover, I would like to thank my colleagues at NPI: Pavel Tlustý, Ondřej Svoboda, Vladimír Wagner, Petr Chudoba, Pablo Ramos-Rodrigues and Alexander Prozorov. Last but not least, I owe a lot to colleagues from the HADES Collaboration, as without them this work would never see sunlight. The list would be too long not to forget anyone, but at least some of them really deserve to be named: Malgorzata Gumberidze, Jerzy Pietraszko, Adrian Rost, Behruz Kardan, Georgy Kornakov, and Tetyana Galatyuk.

Title: Study of transverse flow of kaons in Au + Au collisions at 1.23A GeV

Author: Lukáš Chlad

Institute: Nuclear Physics Institute CAS, p.r.i.

Supervisor: RNDr. Andrej Kugler, CSc., Nuclear Physics Institute CAS, p.r.i.

Abstract: The production and propagation of strange hadrons at the threshold energy are important probes of the in-medium hadron's properties and stiffness of the equation of state of nuclear matter. In this thesis, the transverse kaon flow at Au + Au collisions with kinetic beam energy 1.23A GeV measured with the HADES spectrometer is discussed. The motivation for such an analysis and the theoretical introduction are described first, followed by the characterization of the the individual parts of HADES spectrometer. The procedure to identify detected particles from the measured signals is introduced. Finally, the flow analysis and its results are presented. The differential directed and elliptic flow of kaons in measured gold on gold collisions is compared with published data and with kinetic transport model predictions.

Keywords: relativistic heavy-ion collisions, transverse flow, kaon flow

Contents

Introduction

The goal of this thesis is to present the results of an analysis focused on kaon flow measured in Au + Au collisions with kinetic beam energy $1.23A$ GeV by HADES spectrometer.

To achieve this goal, I shall introduce to the reader the problematic of heavy-ion collisions and what is our motivation for such kind of experiments. This introduction will be given in chapter 1 together with a presentation of the basics of Quantum Chromo Dynamics. If one wants to learn something from the experiments, the appropriate description of the phenomena by theory is necessary. In the case of heavy-ion collisions, we might need Statistical Hadronization Models, Kinetic Transport Models, or Relativistic Hydrodynamic Models. A short introduction to all of them will also be part of the first chapter. An overview of current experimental knowledge of kaon flow in heavy-ion collisions at similar energy will be presented as well.

In the following chapter 2, I will briefly describe all subsystems of the HADES spectrometer. Understanding the tools that we are using for the measurement is essential when problems occur and we need to overcome them in the future. That is also why the HADES spectrometer is constantly upgraded, and many members of the HADES collaboration are not only purely focused on the physics analysis of recorder data but also come into contact with the actual hardware. In the last section of the second chapter, I will illustrate the problematic of TOF detector calibration.

Chapter 3 is dedicated to the so-called low-level data analysis and the principles of particle identification from data. Full details are not given, but fundamentals on how to reconstruct particle properties such as mass, charge, momentum, and velocity from registered hits in HADES detectors are described.

The explanation of my analysis starts in chapter 4, where the details of the identification of both charged kaons and short-lived neutral kaons are presented. In the case of charged kaons, the candidates are selected on the basis of the track quality parameters and specific energy loss within the volume of the MDC and TOF detectors. The number of background entries is estimated by fitting the mass spectra. The short-lived neutral kaon candidates are reconstructed using their decay into two charged pions. To suppress the combinatorial background, the neural network was trained on the simulations, and the optimized cuts of the decay topology variables were later applied to the experimental data. The background of pion pair invariant mass spectrum is described with the mixed-event technique.

The next chapter 5 is devoted to the flow analysis. A historical introduction into the field of transverse flow in heavy-ion collisions is presented with the intention to explain the method of flow applied flow analysis in this thesis. I think it is important to explain the theoretical development of the flow analysis, which accompanied the experimental effort in which the increase of collision energy brought several difficulties.

Finally, the chapter 6 starts with the evaluation of systematic uncertainty. This is followed by the presentation of the results on differential kaon flow that are later compared with model predictions.

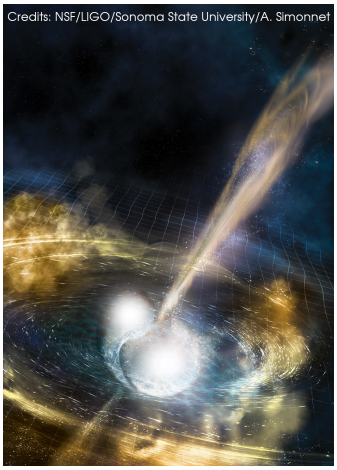

Chapter 1

Hot and dense baryonic matter

In the first chapter, I will present the basic theoretical concepts necessary for understanding of the topic of this thesis. The elementary particles and fundamental forces which together constitute the theory that is called Standard Model of elementary particles are introduced in section 1.1. After that, the focus of section 1.2 will be on the heavy-ion collisions that are used to study the basic properties of hadron interactions. The quantum field theory that describes such interactions is presented in 1.3. Subsequently, the theoretical models which predict the outcome of heavy-ion collisions, thus eventually educating us on the importance of different aspects which participate in this complex process, are characterized in 1.4. In the next two sections 1.5 and 1.6 I will introduce two of the goals of the physics program of heavy-ion collisions, namely, the description of the phase diagram of strongly interaction matter and its equation-of-state. Finally, the motivation for the analysis presented by this thesis is explained in section 1.7 together with a summary of previous experimental findings.

1.1 Standard model of elementary particles

Almost all of the weight of matter visible to our eyes is made up of particles called baryons. Among those, we classify well-known stable protons and slightly less stable neutrons. Together they make up an atomic nucleus and around them are electrons bound in atomic orbitals.

Baryons are not, in distinction to electrons, elementary particles. Their defining property is that they are a bound state of three constituent quarks. The quarks are, up to date knowledge, elementary particles which do not exist free but only in bound states. All particles which are made from quarks are called hadrons, and except for the already mentioned baryons, we have detected mesons which are made of one quark and one antiquark. The rules by which a combination of quarks and antiquarks can exist are described by the theory of quantum chromodynamics (QCD). The other allowed states predicted since the origin of Quark Model [1–3], are, for example, tetraquarks and pentaquarks, whose experimental confirmation is still not well established among the scientific community although recent results [4, 5] suggest that it might change.

The quarks have several quantum properties: charge $(+2/3\,e, -1/3\,e)$[1], spin

[1] e is the absolute value of charge of positron.

$(+1/2, -1/2)$, flavour (up, down, strange, charm, bottom, top) and color (red, green, blue). Very interesting is also the mass of quarks, where we distinguish two terms, current quark mass and constituent quark mass. The current quark mass is understood as a mass of imaginary free quark and the constituent mass is with additional gluon particle field surrounding quarks inside hadrons. In numerical terms, these two are very different (for the lightest u-quark current mass $\sim 1\,\mathrm{MeV}/c^2$ and constituent model-dependent mass $\sim 100\,\mathrm{MeV}/c^2$). This difference is however not caused by additional mass of gluons since they are massless but rather by their binding energy[2].

A very small fraction (around 0.05 %) of visible mass comes from the mass of electrons bound in atomic orbitals. The electron belongs to leptons, and all of them are elementary particles. The known leptons are electrons, muons, tauons, and their neutrinos. The mass of electrons, muons, and tauons is well known, but the mass of neutrinos is still under experimental investigation [6–8].

To complete the Standard Model of elementary particles, we need to introduce a few more particles which are responsible for the propagation of three important forces acting between particles (the last fourth force, the gravitational force, is negligible at the subatomic level, see table 1.1). These particles are called gauge (or vector) bosons: photons, W and Z bosons (all together participating in electroweak interaction) plus the mentioned gluons (strong interaction). There is one more boson which is not a vector but a scalar, the famous Higgs boson [9, 10], that interacts with all elementary particles, see figure 1.1.

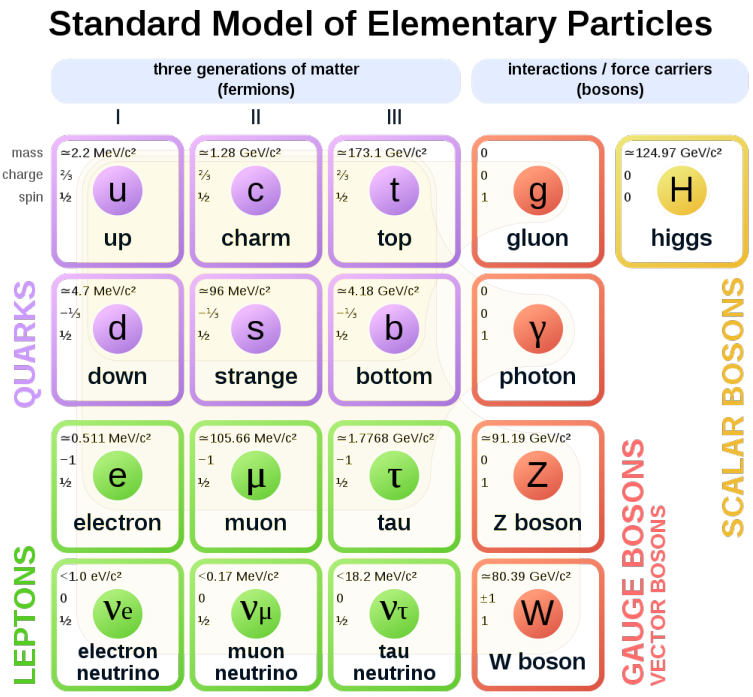

Figure 1.1: Overall table of elementary particles within the Standard Model of Particle Physics. Figure taken from [11].

[2]The connection of mass and energy is well known thanks to Einstein's relation $E = mc^2$.

fundamental force	coupling constant	relative strength
Strong force	$\alpha_s(Q^2) = \frac{12\pi}{(33-2n_f)\ln\left[\frac{Q^2}{\Lambda^2_{QCD}}\right]}$ $\alpha_{\mathrm{S}}(m_{Z^0}) = 0.1179$	1
Electromagnetic force	$\alpha_{em}(Q^2) = \frac{\alpha(0)}{1-\Pi(Q^2)}$ $\alpha(0) \approx \frac{1}{137}$	10^{-2}
Weak nuclear force[a]	$\frac{G_F}{(\hbar c)^3} = 1.166 \times 10^{-5}\,\mathrm{GeV}^{-2}$ valid at scales $\sim 1\,\mathrm{GeV}$	10^{-6}
Gravitational force	$\frac{G_N}{\hbar c} = 6.709 \times 10^{-39}\,(\mathrm{GeV}/c^2)^{-2}$ tested on scales $\sim 1\,\mathrm{m}$	10^{-38}

[a] It is known that at energies $\sim 100\,\mathrm{GeV}$ weak and electromagnetic forces are unified into electro-weak force. Next unification, so called grand unification, of strong and electro-weak forces is predicted to happen at energies $\sim 10^{15}\,\mathrm{GeV}$. Final unification with gravitational force is subject of the theory of everything and with present knowledge it is unclear at what scales it might happen.

Table 1.1: Comparison of strength of four fundamental forces. Values from [12].

1.2 Heavy-ion collisions

To understand the processes that occurred just a few microseconds after the Big bang [13] (see figure 1.2), or that may occur during the recently observed neutron star merge with gravitational waves [14], experiments in laboratories are necessary. The only way to replicate similar conditions is to collide heavy ions (HIC). With the aim of probing the phase-space diagram of nuclear matter and studying the nuclear equation of state, it is needed to study the whole spectrum of HIC using different ions and scan as many interaction energies as possible.

We can identify three stages of HIC: first-chance nucleon-nucleon (NN) collisions, high density (fireball formation and its adiabatic expansion), and freeze-out stage (chemical and kinetic freeze-out), see figure 1.3. Using the SIS18 accelerator, it is possible to achieve up to three times the density of the nuclear ground state ($\rho \approx 3\rho_0$ where $\rho_0 \approx 0.16\,\mathrm{N/fm}^3$) and temperatures up to $100\,\mathrm{MeV}$[3] [16]. The matter at such extreme conditions creates the so-called fireball which has a very short lifetime $\sim 10^{-22}\,\mathrm{s}$ after which the matter is expanding and cools down. The next important moment happens when the energy of a possible collision is low enough that no inelastic processes are possible and except the decay of resonances, the created particles will not change their nature, this moment is called chemical freeze-out. However, the particles still undergo elastic interactions until the kinetic freeze-out, which is the last milestone of the HIC after which the particles travel unchanged to the detector again except for a possible decay.

An essential measure of HIC is the impact parameter b, which is defined as the distance between the centers of colliding nuclei. With decreasing values of impact parameters, we are speaking about increasing centrality of the collision. When the two nuclei overlap almost completely, we are speaking about a central colli-

[3] We are using energy units due to the conversion $E = kT$, the room temperature $300\,\mathrm{K} = 25.852\,\mathrm{meV}$.

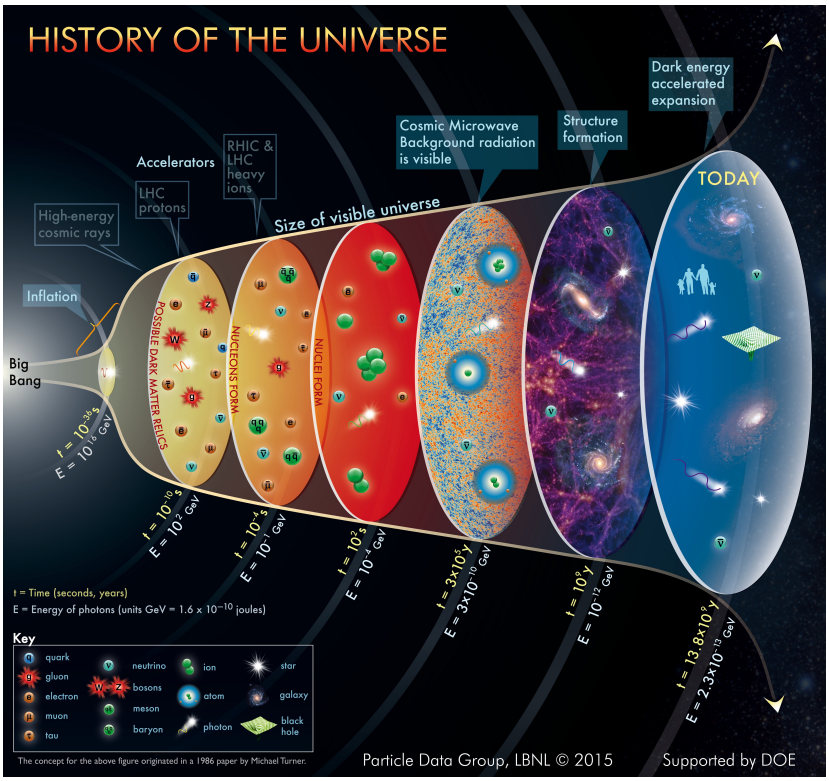

Figure 1.2: History of the Universe. Figure taken from [15].

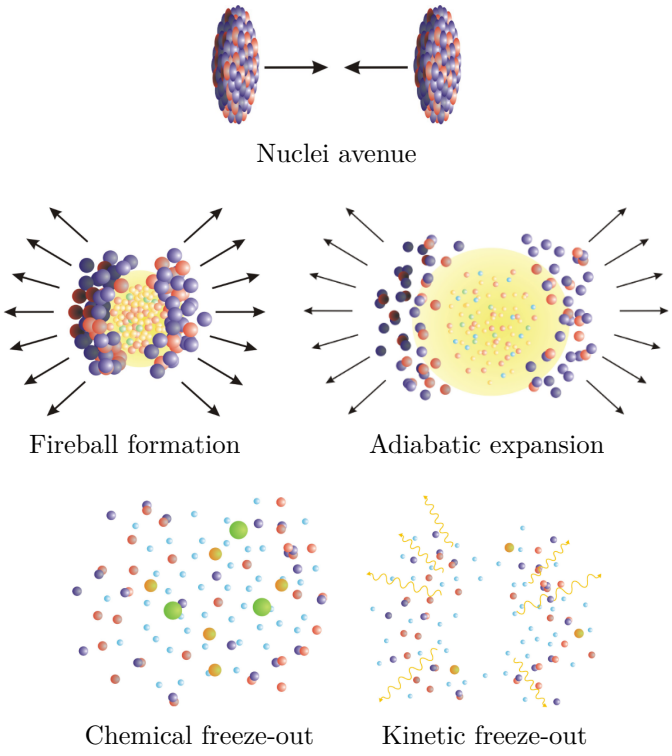

Figure 1.3: Stages of relativistic heavy-ion collision. Figures taken from [17].

sion, and when this overlap is only partial, we are speaking about the peripheral collision. Unfortunately, it is not possible with current technology to influence the centrality or to measure directly the impact parameter, hence it must be estimated based on the number of emitted particles (multiplicity). Often used theoretical description which is then compared with experimentally measured multiplicity is the Glauber model using Monte Carlo simulations [18]. We also distinguish between the nucleons which go through the reaction zone, which are called participants, and those who only pass around the so-called spectators.

1.2.1 Particle production

The important variable for particle production is the square root of the Mandelstam variable $s = (P_1 + P_2)^2$ [19], where P_1 and P_2 are four vectors of colliding particles. In the case of a fixed target experiment, the center-of-mass energy of the collision can be calculated

$$\sqrt{s} = \sqrt{2E_{\mathrm{kin,beam}} m_{\mathrm{target}} c^2 + (m_{\mathrm{beam}} + m_{\mathrm{target}})^2 c^4}, \tag{1.1}$$

where $E_{\mathrm{kin,beam}}$ and m_{beam} are the kinetic energy and the mass of beam particles and m_{target} is the mass of target particles. In the case of HIC with the same nuclei used as projectile and target, we can define $\sqrt{s_{\mathrm{NN}}} = \sqrt{s}/A$ the center-of-mass energy of NN collisions for easier comparison with elementary interactions (in case of Au+Au collisions with kinetic energy $1.23A$ GeV we obtain $\sqrt{s_{\mathrm{NN}}}\Big|_{\mathrm{Au+Au}} = 2.42\,\mathrm{GeV}$). The production of N_{particle} particles is conditioned with the so-called threshold energy

$$\sqrt{s_{\mathrm{thr}}} = \sum_{i=1}^{N_{\mathrm{particle}}} m_i c^2 \tag{1.2}$$

where m_i is the rest mass of each outgoing particle.

Using the equation (1.2), we can calculate the minimal energy of the elementary NN collision needed to produce strange particles, which is of interest in this thesis. Since the NN collision is subject to the strong interaction that preserves the additive quantum number strangeness,[4] the production of only one strange hadron is not possible (except for hidden strangeness, e.g. ϕ-meson which contains $|s\bar{s}\rangle$ pair). Using the nominal values of the masses of strange hadrons [12] and the sum rules of the strong interaction (strangeness conservation $N(s) - N(\bar{s}) = 0$ and baryon number conservation $N(B)_{\mathrm{in}} = N(B)_{\mathrm{out}}$) one can get the threshold energy values for production channels, see table 1.2. From this table we observe that all production channels from free NN collisions are above the available center-of-mass energy in studied Au + Au collisions, therefore, one would expect that the production of strangeness hadrons in this case is not possible. However, in the case of HIC, there are several mechanisms that can provide the additional energy or lower the threshold energy, thus the so-called subthreshold production is observed:

Fermi momentum Nucleons inside nuclei are influenced by the Pauli exclusion principle for fermions, and therefore nucleons are forced to populate higher energy states and gain additional momenta up to $p_{\mathrm{F}} \approx 250\,\mathrm{MeV}/c$.

[4] Hadrons containing anti-quark $\bar{s}$ have $S = +1$ and hadrons with quark s have $S = -1$.

Production channel	$\sqrt{s_{\mathrm{thr}}}$[GeV]	$\sqrt{s_{\mathrm{NN}}}\big\vert_{\mathrm{Au+Au}} - \sqrt{s}_{\mathrm{thr}}$[GeV]
$\mathrm{NN} \rightarrow \mathrm{N\Lambda K^+}$	2.55	-0.13
$\mathrm{NN} \rightarrow \mathrm{N\Lambda K^0}$	2.56	-0.14
$\mathrm{NN} \rightarrow \mathrm{N\Sigma K^+}$	2.62	-0.20
$\mathrm{NN} \rightarrow \mathrm{NNK^+K^-}$	2.86	-0.44
$\mathrm{NN} \rightarrow \mathrm{NN}\phi$	2.90	-0.48

Table 1.2: Possible production channels for hadrons containing strangeness with their threshold center-of-mass collision energy and the difference between this threshold and the available energy in measured Au + Au collisions.

Multistep processes During the dense stage of HIC, nucleons can be elastically scattered multiple times and gain enough momentum to produce strange hadrons. Within this option, we also include the possibility that an inelastic NN collision produces intermediate resonances like Δ or N^* which then again interact [20].

Strangeness exchange reaction A strange quark from one hadron can be exchanged with light (u or d quark) from another hadron, and via this mechanism the threshold for some processes might be lowered but still at least some NN interaction must produce a strange hadron in the first place. An example of such a process is the reaction $\pi^-(d\bar{u}) + \Lambda(uds) \rightarrow \mathrm{K}^-(s\bar{u}) + \mathrm{n}(udd)$ [21].

In medium modification Due to the potential between the strange hadron and the nucleon, the effective mass of the strange hadron might be smaller than the nominal vacuum mass [22]. Several theoretical models [23–27] predict strong attractive K^-N-potential compare to repulsive K^+N-potential resulting in decrease of effective energy threshold for channel $\mathrm{NN} \rightarrow \mathrm{NNK^+K^-}$.

Although all these mechanisms can participate in enabling subthreshold production of strange hadrons in HIC, the production rates are still very low compared to higher center-of-mass energies, see figure 1.4.

1.2.2 In medium hadron properties

At SIS18 energies of a few GeV per nucleon, where the dominating hadronic degrees of freedom are the baryons [44], the density of nuclear matter can reach up to three times the nuclear ground state density ($\rho \rightarrow 3\rho_0$) and the temperature can rise to 100 MeV. In such an environment the hadron properties (like pole mass, width of the spectral function, etc.) may change dramatically [45, 46] however before one can observe any differences an excellent knowledge of elementary NN and πN interactions are mandatory, see figure 1.5. The basic concepts of QCD will be given next to understand the possible links between theoretical models and hadron in medium modifications.

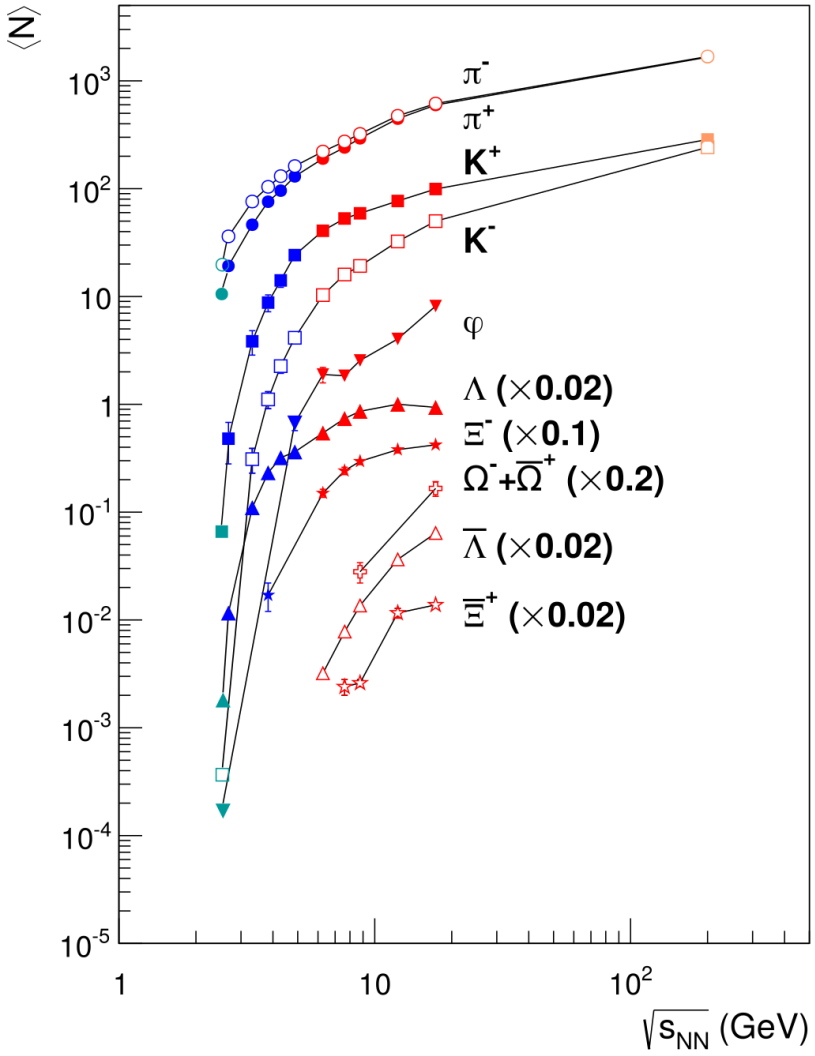

Figure 1.4: Excitation function of charged pions and strange hadrons. The data points indicate the measurements Pb+Pb and Au+Au from experiments at SIS18 (green), AGS (blue), SPS (red), and RHIC (orange). Data taken from: [28–43].

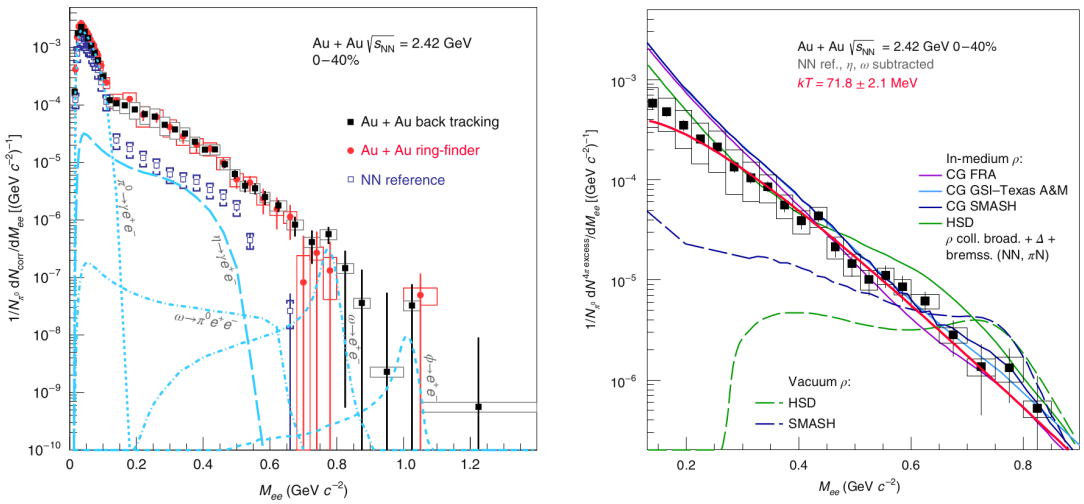

Figure 1.5: Left figure: Measured di-electron invariant mass spectra in Au + Au collisions at $\sqrt{s_{\mathrm{NN}}} = 2.42\,\mathrm{GeV}$ with HADES compared to reference NN spectra and known sources. Right figure: The excess yield of di-electrons compared to vacuum and in-medium ρ. Figures taken from [47].

1.3 Quantum Chromo Dynamics

QCD is a relativistic quantum field theory which describes the interactions between quarks and gluons (review in [12, 48]). The theory is a non-abelian gauge theory with the SU(3) symmetry group (the discovery of the possibility to renormalize this group of theories [49, 50] strongly supported QCD as a promising theory and gained the authors Nobel prize in 2004). Its name comes from Greek $\chi\rho\omega\mu\alpha$ which translates as color because the property of quarks and gluons, which is analogous to the electric charge in Quantum Electro-Dynamics (QED), is named color. We distinguish between three colors (red, green, and blue) and oppose to QED where only fermions have charge and the gauge boson (photon) is neutral, in QCD, both types of particles (fermionic quarks and gauge boson gluons) have a color. Thus, as was said, the symmetry group of QCD is SU(3), coming from three colors, and that it is non-abelian gauge theory because also gluons have a color. There are two peculiar properties of this theory: asymptotic freedom and confinement. The first one means that the bonds between two quarks or gluons become very weak, asymptotically going to zero, when these two particles are close to each other. The second property comes from the fact that despite the big experimental effort, single quarks have never been observed, which leads theorists to assume that quarks and gluons have to be confined to colorless objects (hadrons).

1.3.1 Chiral Symmetry

One of the most fundamental concepts of physical theory are symmetries which are connected through Noether's theorem on the conservation of quantities [51]. There are, however, two types of symmetries: local (acts independently at each space-time point) and global (is true for the whole space-time simultaneously). We already briefly touched the local symmetry group SU(3) due to which the

gauge bosons (gluons) must be adopted for the transformations of physical fields. One of the global symmetries of QCD[5] is chiral symmetry (from Greek $\chi\epsilon\iota\rho$ meaning hand) and it makes us distinguish between left and right-handed objects. The chirality of particles can be seen as massless limit of their helicity[6]. If a particle field is invariant under parity transformation, i.e., if it is the same no matter the sign of the spatial coordinates, then we say that it is chiral symmetric. We can divide the transformation of chiral symmetry into vector ($V = L + R$) and axial vector ($A = L - R$) parts.

As we have already mentioned in the footnote, the chiral symmetry [52] is only an approximate symmetry of QCD due to a small but nonzero current mass of quarks ($m_u \approx 2.5\,\mathrm{MeV}/c^2$, $m_d \approx 5\,\mathrm{MeV}/c^2$ and $m_s \approx 100\,\mathrm{MeV}/c^2$) which are generated through Higgs mechanism [53–55]. This phenomenon we call explicit breaking but with respect to chiral symmetry breaking scale $\Lambda_\chi \cong 4\pi f_\pi \approx 1\,\mathrm{GeV}$ (where $f_\pi \cong 93\,\mathrm{MeV}$ is pion weak decay constant) these masses can be considered as significantly smaller. Except for small explicit breaking, the spontaneous breaking of chiral symmetry exists, i.e., although the Lagrangian of QCD is symmetric, its vacuum ground state is not. Because of the spontaneous breaking, a non vanishing expectation value of quark condensate $\langle\bar{q}q\rangle$ occurs. If we would, for a moment, forget the explicit chiral symmetry breaking, the decisive argument for the spontaneous breaking would be the experimentally well-established mass difference between the states of the pseudoscalar and vector-meson octets. The spontaneous chiral symmetry breaking is also responsible for the biggest part of the hadron's mass (where the Higgs mechanism generates only small current masses of quarks and known hadron masses are a hundred times larger) through the mentioned formation of quark and gluon condensates. The restoration of chiral symmetry [56] is possible via two processes: thermal excitation (so-called melting) and/or compression of the chiral condensate (squeeze out). Both situations are achievable via heavy-ion collisions.

1.3.2 Application for HIC

The description of HIC is largely dependent on the energy scale [57]. In the case of large colliders (LHC and RHIC) where the transferred energy is large, the coupling constant of strong interaction α_s is decreasing, and this allows for a perturbative calculation of QCD. However, in the case of low-energy experiments (like fixed target experiments at SIS18), QCD becomes non-perturbative theory and the exact solutions are almost impossible. Luckily, at these low energies the hadronic processes are dominated by pions and the expansion of observables in terms of pion mass and momentum is possible, which is the principle of chiral perturbation theory (ChPT) [58]. Within these effective theories, which use the hadronic degrees of freedom (in contrast to quark and gluon degrees of freedom in QCD), a good characterization of interactions between pseudoscalar mesons and baryons can be deduced. A further reduction of the Lagrangian of ChPT to

[5]If theory has a global symmetry its Lagrangian $\mathcal{L}$ must be invariant with respect to this symmetry. In the case of QCD and chiral symmetry this statement holds only for the approximate case of massless quarks. This approximation will be argued below.

[6]The helicity is positive for particles when their spin vector is in the same direction as their momentum vector, then we talk about right-handed particles. Negative helicity is when the spin and momentum vector point in the opposite directions.

an effective Lagrangian where only some mesons and nucleons are used may be used to obtain a realistic picture of KN interactions. This way is very useful if one needs to avoid the coupled channel problem[7] which occurs when increasing numbers of particles are taken into account.

An important utilization of the above explained method with respect to the aim of this thesis is the production and propagation of strangeness in hot and dense nuclear matter. The first attempt to use a chiral Lagrangian for the description of kaon-nucleon interactions was made by Kaplan and Nelson [22, 59] and were followed by others [60–64]. Although it is possible to use a perturbative calculation on πN and KN interactions, $\bar{\mathrm{K}}$N is already too close to the threshold where resonances (like $\Lambda(1405)$) dominate. Therefore, the effective Lagrangian approach with mean field is preferable

$$\mathcal{L} = \bar{\mathrm{N}}(i\gamma^\mu\partial_\mu - m_\mathrm{N})\mathrm{N} + \partial^\mu\bar{\mathrm{K}}\partial_\mu\mathrm{K} - (m_\mathrm{K}^2 - \frac{\Sigma_\mathrm{KN}}{f_\pi^2}\bar{\mathrm{N}}\mathrm{N})\bar{\mathrm{K}}\mathrm{K} - \frac{3i}{8f_\pi^2}\bar{\mathrm{N}}\gamma^\mu\mathrm{N}\bar{\mathrm{K}}\overleftrightarrow{\partial_\mu}\mathrm{K}, \quad (1.3)$$

where $\mathrm{K} = (\mathrm{K}^+\ \mathrm{K}^0)$ and $\bar{\mathrm{K}} = (\mathrm{K}^-\ \bar{\mathrm{K}^0})$ are kaon field, $\mathrm{N} = (\mathrm{p}\ \mathrm{n})$ and $\bar{\mathrm{N}} = (\bar{\mathrm{p}}\ \bar{\mathrm{n}})$ are nucleon field, Σ_KN is kaon-nucleon sigma term [65]. The third term in the equation (1.3) comes from Kaplan and Nelson and is called the attractive scalar KN interaction term and the last term is Weinberg–Tomozawa [66, 67] and corresponds to the vector KN interaction which is found to be repulsive for kaons and attractive for antikaons. The sigma term can be expressed as the nucleon expectation value of Gell-Mann–Oakes–Renner equation ($m_\mathrm{K}^2 f_\mathrm{K}^2 \cong -1/2(m_u + m_s)\langle\bar{u}u + \bar{s}s\rangle$)

$$\Sigma_\mathrm{KN} = \frac{1}{2}(m_u + m_s)\langle\mathrm{N}\,|\bar{u}u + \bar{s}s|\,\mathrm{N}\rangle. \quad (1.4)$$

The in-medium kaon mass shift then can be evaluated as

$$m_\mathrm{K}^* \approx m_\mathrm{K}\left(1 - \frac{\Sigma_\mathrm{KN}}{m_\mathrm{K}^2 f_\mathrm{K}^2}\rho_S + \frac{3}{4}\frac{1}{m_\mathrm{K} f_\mathrm{K}^2}\rho_B\right), \quad (1.5)$$

where ρ_S and ρ_B are scalar and vector baryon density, respectively. The total strength of potentials can be compared to experiment V_KN from 20 to 30 MeV comes from K^+N scattering length and is in a good agreement, but for antikaons the predictions differ significantly due to the presence of $\Lambda(1405)$ resonance (the values of $V_{\bar{\mathrm{K}}\mathrm{N}}$ range from -50 to -200 MeV). As a result of the repulsive potential for kaons and the attractive potential for antikaons, the kaon condensation can occur in dense matter, e.g., in neutron stars. This would cause a softening of the equation of state and sequential reduction of the maximal neutron star mass to 1.5 solar masses (heavier stars would collapse into a black hole). Such a mass reduction contrasts with astronomical observations [68, 68] where neutron stars with 2 solar masses have been observed. Thus, new observables are needed to unravel this problem.

1.4 Theoretical Models

When one wants to figure out which fundamental mechanisms are important for such a complex dynamical process as heavy-ion collisions, the comparison

[7] For each species of particles, equation of motion is needed to solve separately, but due to interaction terms in Lagrangian these coupled equation create a complex problem.

of measurements with predictions of theoretical models is necessary. There are two major classes: static and dynamic models. The first is looking at a system in equilibrium and describing its properties, usually through statistical models based on stochastic probability distribution. This approach might be sometimes inappropriate because the experimental observables are consequences of several effects, whose role during the evolution of HIC might change. Hence, a theoretical dynamical description is needed. It is possible to consider the created system as a composition of fluid cells (hydrodynamical model with quasi-macroscopic ansatz) or particles (kinetic transport models with microscopical approach).

1.4.1 Statistical Hadronization Models

As was mentioned, these models [69–73] give a macroscopic static description of the system in thermal equilibrium. Nevertheless, they are able to predict particle yields reasonably well for a wide variety of collision systems and energies [74]. Another advantage is that for such predictions, they need only a very limited number of parameters. The underlying assumption is that all particles are emitted from a homogeneous source (fireball) in thermal equilibrium. In the grand canonical ensemble,[8] the models will provide a statistical description of the system of volume V and temperature T, where the particle type i number density $\rho_{i,\vec{q}}$ is proportional to the integral

$$\rho_{i,q} \propto \int_0^\infty p^2 \mathrm{d}p \exp\left(\frac{-E_i + \vec{\mu}\vec{q}_i}{kT}\right), \tag{1.6}$$

where E_i is the energy of particle type i, $\vec{\mu}$ are chemical potentials for quantum numbers $\vec{q}$ and k denotes the Boltzmann constant. The usual quantum numbers are the baryon number B, charge Q, and strangeness S. However, at SIS18 energy the strangeness production is subthreshold, making it rare and therefore explicit conservation of strangeness is implemented. A smaller volume V_C is imagined inside fireball where strangeness is exactly conserved with the canonical approach [75], the possibility of emitting open strange particles from elsewhere than this volume V_C is suppressed.

From the experimental physicist's point of view, the order is opposite. We measure different particle yields and fit these values to the model parameters (T,V,V_C,μ_B, and μ_Q) at the chemical freeze-out. An interesting result from different experiments at different centre-of-mass collision energies is that the obtained parameters tend to follow the universal freeze-out curve with $E/N \approx 1\,\mathrm{GeV}$ even in the case of low energies where the assumption of thermal equilibrium is probably not valid (the relaxation time corresponds to the life time of hot-dense phase), see figure 1.6.

1.4.2 Kinetic Transport models

In the framework of kinetic transport models, the heavy-ion collision is taken as a superposition of single NN collisions and the created particles are propagated

[8]The basic idea of ensemble theory is that using average over many ensembles would lead to the same result as average over time. The grand canonical ensemble can be imagined as an opened bottle at the bottom of the ocean, i.e. the volume and temperature are fixed and the total energy and number of particles can vary and are conserved on average.

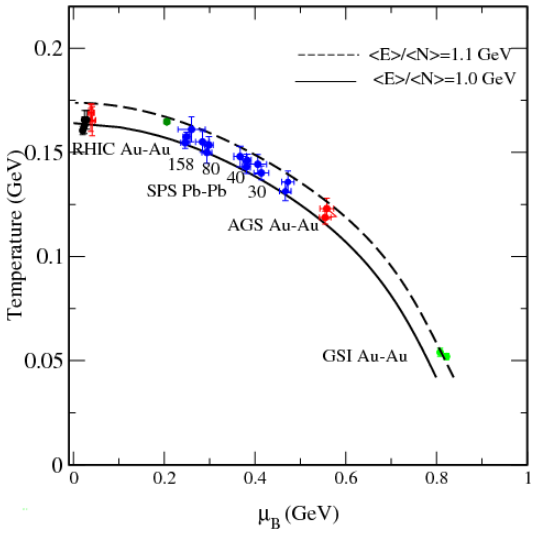

Figure 1.6: The chemical freeze-out parameters T and μ_B from different experiments at RHIC, SPS, AGS, SIS. The lines correspond to the freeze-out conditions $\frac{\langle E\rangle}{\langle N\rangle} = 1\,\text{GeV}$ and $1.1\,\text{GeV}$. Figure taken from [28, 76].

through space-time with the possibility of another interaction. Advantage of these models is their broad energy range usage thanks to the choice of particle types that would be the elementary degrees of freedom: for low energies, hadrons, for higher partons, or even strings.

These models are very sensitive to the input parameters like pole mass, life time in vacuum, and the cross-sections of many elementary processes. An ideal situation would be that all of these parameters would be measured in experiments; unfortunately, this is not true, e.g., some resonant particle production and parameterization are needed consequently. There are many parametrizations available [77–80], which can lead to rather large uncertainty of the unknown cross-sections. Moreover, the angular dependence is in most cases assumed to be isotropic, but in reality, this might not be the case. On the other hand, this effect is probably not as important for A+A collisions as it is for elementary and even for p+A collisions because of finite-state interactions.

The subthreshold production of particles is using multistep processes, where in the first step a resonance is excited, which is then propagated through the medium without affecting its bulk properties and later interacting again with its higher energy level, and therefore making the production of rare particles possible. It is clear that a good description of in-medium potential is essential because it can effectively lower the production threshold.

One set of transport models, called cascade models[9], treat particles as point-like, classical objects that propagate in space-time following the Boltzmann equation

$$\left(\frac{\partial}{\partial t} + \frac{\vec{p}}{m}\cdot\nabla_{\vec{x}} + \vec{F}\cdot\nabla_{\vec{p}}\right) f\left(\vec{x},\vec{p},t\right) = I_{\text{coll}} \tag{1.7}$$

where $f\left(\vec{x},\vec{p},t\right)$ is the particle distribution function, the first term on the left side is pure time dependence, the second is the diffusion term and the third describes the external forces. The right-hand side of the equation is the collision term, un-

[9] Origin of this denotation is in the imagination of HIC as a cascade of individual interactions.

der which we can include decay, scattering, or quantum effects like Pauli blocking. Due to the difficulty of obtaining an exact solution, a much simplified solution is used in practice resulting in different models (**V**lasov–**U**eling–**U**hlenbeck [81], **B**oltzmann–**U**eling–**U**hlenbeck [82], **R**elativistic **BUU** [83], **Gi**essen **BUU** [84], **A** **R**elativistic **T**ransport model [85], **H**adron **S**tring **D**ynamics [86], **P**arton **H**adron **S**tring **D**ynamics [87]). From the beginning of **I**ntranuclear **C**ascade **M**odel [88] the condition if two particles undergo collision was geometrical interpretation of the relevant cross section: if at any time step the distance of two particles d_{ij} is smaller than $\sqrt{\sigma/\pi}$ then these particles will collide. Recently, the stochastic approach [89, 90] was developed, which randomly selects two particles from a phase-space cell with a certain probability. Many-body interactions might be included in an external mean field, which demands quasi-particle approximation ansatz. Within this picture, the spectral function of a particle is substituted with an averaged weighted sum of many delta functions of position and momentum. One can deduce that with increasing number of delta functions (test particles) the quality of the description would get better at the price of significantly longer computational time (Monte-Carlo approach). The advantage of this approach is that the models are treating one-body problems. However, in the end one needs to solve the coupled equations for each particle species, e.g., hadrons in the case of low energies.

To simulate many-body systems like HIC, molecular dynamics can be adopted; the majority of models are based on **Q**uantum **M**olecular **D**ynamics [91]. In contrast to the above, the particles are represented by Gaussian density distribution in phase space following the uncertainty principle. The propagation is dealt with classically, however, the Gaussian smearing results in smoother behaviour of interactions, incorporate some quantum effects, and enable to dispense with effective mean field (pairwise potentials are dependent on coordinates $U(\rho(\{\vec{r}_1, \vec{r}_2, \ldots\})) \rightarrow U(r_{12})$). Thus, the calculation of HIC on event-by-event bases is possible. Among the most popular models are IQMD (**I**sospin **QMD**) [92], RQMD [93], and UrQMD [79] (**R**elativistic respective **U**ltra-**r**elativistic **QMD**).

Today, there are models that combine the advantages of the two approaches mentioned above, namely, JAM [94] and SMASH [95]. The time evolution of kinetic transport models is shown on figure 1.7.

1.4.3 Relativistic hydrodynamic models

The idea of using ideal hydrodynamics to characterize strongly interacting matter was first suggested by Landau [96], but only recently it showed its power to predict quantitatively experimental observables when the first results from RHIC [97–100] were available. The strength of hydro models is their simplicity and generality, however, the fundamental assumption of all such models is the local thermodynamic equilibrium, which turns out to be very strong especially for low collision energies. Because of the complexity of HIC, the multimodule modeling seems to be essential, i.e., one can include different fluctuations of the initial condition, equation of state, hadronization, and final state interactions before freeze-out. For this reason, hydrodynamic models look very promising, because of the possibility to easily include all of these different options. In addition, these models provide very accurate information about the quark-gluon plasma phase

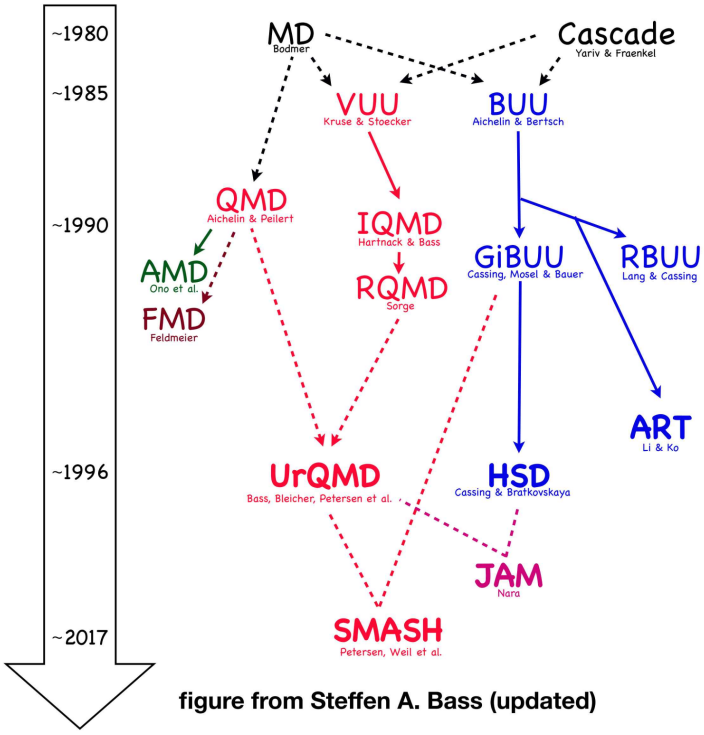

Figure 1.7: Time evolution of kinetic transport models. Credits to Steffen A. Bass.

when compared to high-energy heavy-ion experiments. The aim of this thesis is the analysis of low energy collisions where hydro models are not commonly used and therefore only a brief introduction will be mentioned here.

In the framework of an ideal (non-viscous) fluid, a set of five equations is used to describe the evolution of the system from a relativistic HIC

$$\partial_\mu T^{\mu\nu}_{\text{ideal}} = 0, \quad \partial_\mu J^\mu_B = 0. \tag{1.8}$$

These equations can be interpreted as conservation of energy and momentum ($T^{\mu\nu}_{\text{ideal}}$ is tensor of energy and momentum for ideal fluid) and baryon number (J^μ_B is net baryon current). Usually these variables are rewritten using six variables (ε energy density, $\mathcal{P}$ pressure, time-like flow four-vector u^μ and ρ_B baryon density):

$$T^{\mu\nu}_{\text{ideal}} = (\varepsilon + \mathcal{P})u^\mu u^\nu - \mathcal{P}g^{\mu\nu}, \quad J^\mu_B = \rho_B u^\mu \tag{1.9}$$

where $g^{\mu\nu} = \text{diag}(1, -1, -1, -1)$ is a metric tensor. Finally, we have to complete this set of equations with the equilibrium equation of state

$$\mathcal{P} = \mathcal{P}(\varepsilon, \rho_B). \tag{1.10}$$

This simplified picture of the ideal fluid is extended in first order by adding terms containing a shear viscosity η (Navier–Stokes formalism), and in second order dissipative terms of the entropy density current is added (Mueller–Israel–Stewart theory). For more details on relativistic hydrodynamic models, we recommend [101, 102].

1.5 Phase diagram of strongly interacting matter

The phase diagram contains information about the thermodynamical properties of matter. Just as we know about the three basic phases of water (liquid, solid, and vapor) and the transitions between them, we would like to investigate similar effects for strongly interacting matter. An example of how such a phase diagram might look is on figure 1.8, where the three axes are temperature, baryon chemical potential, and isospin chemical potential. Up to date, very little has been known about the phase diagram of strongly interacting matter on both the theory and experimental sides (a review of both can be found in [103]).

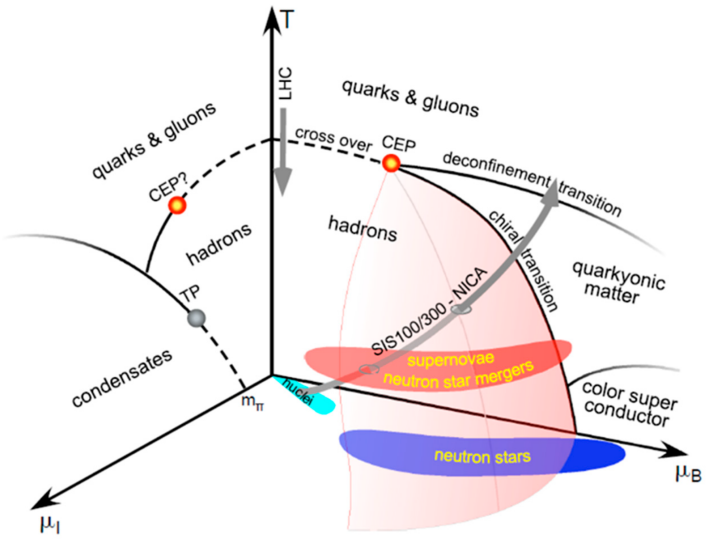

Figure 1.8: 3D schematic phase diagram of strongly interacting matter (the variables on axis: T temperature, μ_B baryon chemical potential, μ_I isospin-chemical potential). Depicted are the regions of known nuclei, neutron stars, and their mergers together with supernovae explosions. With lines, different phases of QCD matter are separated: hadrons, QGP and theoretical quarkyonic matter, color super conductor and (pion) condensates. The Critical-End-Point (CEP) and Triple-Point (TP) are also shown. Taken from [104].

The known nuclei are close to zero temperature (because of the scale of temperature axis which is given in MeV) and baryon chemical potential $\mu_B \approx 940\,\text{MeV}$ (chemical potentials define how the energy of a system would change if a particle with a given quantum number would be added to the system, therefore for nuclei the energy would increase approximately by the mass of nucleon), and on the other side of the phase diagram in $T - \mu_B$ plane are the conditions of the Early Universe after inflation with $T \approx 200\,\text{MeV}$ and zero baryon chemical potential. From the experiments at LHC, where conditions similar to the Early Universe can be created, together with Lattice QCD [105] calculations,[10] a crossover phase transition from hadron gas into quark-gluon plasma (QGP) for low baryon chemical potential and temperature around 154 MeV has been

[10]These calculations are based on solving the QCD equations on discrete space-time lattice using exact QCD Lagrangian.

predicted [106]. The crossover (smooth transition) can be imagined as hadron creation from quarks and gluons does not happen anymore because the rate of interaction between hadrons (mainly pions) is rapidly increasing as the system is heated up (gain energy). However, if one rises μ_B lattice calculations get into the numerical sign problem and cannot be used. The effective model must be used in such a case that predicts μ_B-driven first-order phase transition [107] for low temperatures, which implies the existence of a critical end point (CEP) [108, 109]. Exotic states of matter such as quarkyonic matter [110] or color super conductor [111] are also predicted.

There are several experiments probing the phase diagram using heavy-ion collisions ranging from high temperature at LHC, followed by experiments at RHIC where they systematically search for CEP using the Beam Energy Scan (with $\sqrt{s_{\mathrm{NN}}} = 7.7 - 200\,\mathrm{GeV}$), older AGS experiments at BNL and SPS at CERN, future FAIR [112] and NICA [113] experiments and among them, at the highest μ_B, are experiments at SIS18, e.g., HADES. In figure 1.9 one can see a collection of measurements made by the experiments mentioned above.

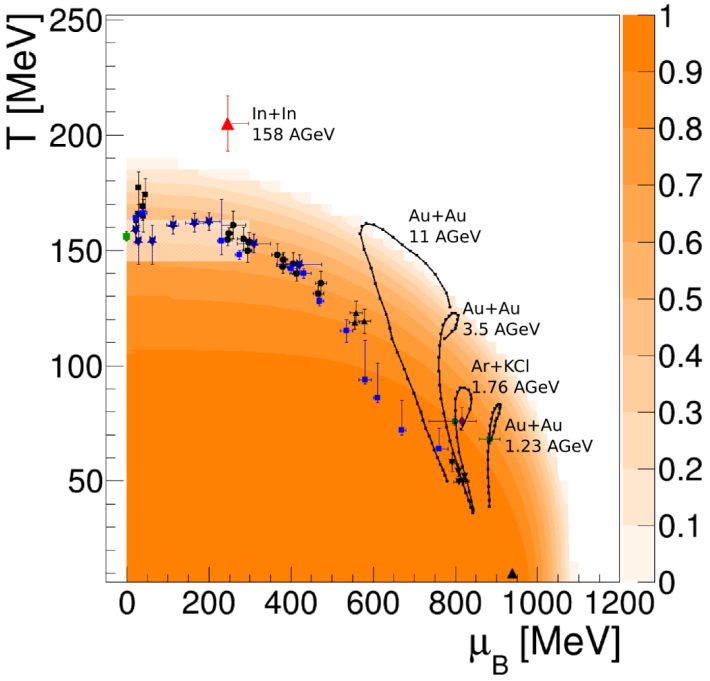

Figure 1.9: QCD phase diagram at temperature T and baryon chemical potential μ_B plane. With lines, a time evolution of HIC for given systems and energies is shown. The experimental points come from the fit of the statistical model to the particle yields. On z-axis is the quark condensate $\langle\bar{q}q\rangle_{T,\mu_B}/\langle\bar{q}q\rangle_{T=0,\mu_B=0}$. Taken from [114].

However, it is important to realise that during the heavy-ion collision the system is dynamically evolving, and therefore the representation of one point in the phase diagram might be a little misleading, the reality corresponds more to the arrow lines showing the time development of collision. These lines were obtained with a coarse-grain approach [16] which combine the advantages of hydrodynamic and transport models. In the first step of the transport model, in this case UrQMD, the ensemble calculations are averaged to obtain a smooth space-time

distribution. This is then divided into 4-dimensional cells within which the bulk properties (temperature, baryon density, and collective velocity) are calculated and later summed up to obtain these variables for the whole system. The comparison with statistical hadronization models can be seen from figure 1.9 as the last point of the arrow line versus the full green circles.

Finally, astrophysical observations are essential as well, e.g., measurements of the cosmic microwave background [115, 116], observations of compact objects like neutron stars, and very recently also their mergers [14] during which conditions similar to HIC occur [47].

1.6 Equation of state of nuclear matter

The connection between thermodynamic observables like pressure p, temperature T, density ρ, and number of particles N in equilibrium is prescribed by the equation of state of isospin symmetric nuclear matter (EOS):

$$\epsilon(\rho, T) = \epsilon_{\mathrm{th}}(\rho, T) + \epsilon_{\mathrm{C}}(\rho, T = 0) + \epsilon_0 \tag{1.11}$$

where ϵ denotes the total centre-of-mass energy per nucleon ($\epsilon = \frac{E}{A}$), ϵ_{th} and ϵ_{C} stand for the thermal respective compressional energy, and ϵ_0 is the binding energy in the ground state, see figure 1.10a. The last term might be deduced using Bethe–Weizsäcker formula [117, 118] $\epsilon_0 \approx -16\,\mathrm{MeV}$. The second term is strongly dependent on the incompressibility modulus κ which might be expressed as [119]

$$\kappa = -V\frac{\mathrm{d}p}{\mathrm{d}V} = 9\rho^2 \frac{\partial^2 \epsilon_{\mathrm{C}}(\rho, T = 0)}{\partial \rho^2}\bigg|_{\rho=\rho_0}. \tag{1.12}$$

One can differentiate between so-called soft ($\kappa \approx 200\,\mathrm{MeV}$) and hard/stiff ($\kappa \approx 380\,\mathrm{MeV}$ equations of state.

In the case of isospin asymmetric matter (neutron rich nuclei, neutron stars), we add to the equation (1.11) terms dependent on the asymmetry parameter $\delta = (\rho_{\mathrm{n}} - \rho_{\mathrm{p}})/\rho$ where ρ_i are neutrons, respective protons, densities:

$$\epsilon(\rho, T, \delta) = \epsilon(\rho, T) + \epsilon_{\mathrm{sym}}(\rho)\delta^2 + \mathcal{O}(\delta^4) + \dots. \tag{1.13}$$

The symmetry term can be described around the normal nuclear density ρ_0 using different parametrizations [120]

$$E_{\mathrm{sym}} = S_0 + \frac{L}{3}\left(\frac{\rho - \rho_0}{\rho_0}\right) + \frac{K_{\mathrm{sym}}}{18}\left(\frac{\rho - \rho_0}{\rho_0}\right)^2 \tag{1.14}$$

$$= E^{\mathrm{pot}}_{\mathrm{sym}} + E^{\mathrm{kin}}_{\mathrm{sym}} = C\left(\frac{\rho}{\rho_0}\right)^{\gamma} + \frac{1}{3}\varepsilon_{\mathrm{F}}\left(\frac{\rho}{\rho_0}\right)^{\frac{2}{3}}, \tag{1.15}$$

where the stiffness of the EOS influences the value of parameter $\gamma = 0.5$ for soft and $\gamma = 1.5$ for stiff EOS. The influence of symmetry energy on the binding energy of the nucleon is shown on figure 1.10b.

The EOS together with Tolman–Oppenheimer–Volkov equation [121, 122] directly predicts the upper limit of neutron star mass (using equation (1.13) with $\delta \approx 1$). This relation serves as one of the experimental tests of the stiffness of

the EOS. The other tests are usually connected to observables of HIC like meson production (pions revealed to be not so sensitive due to high cross-section, although kaons might be a good probe[11]) and collective flow. In the past, many results were supporting the soft EOS scenario [123–125], but recent observations of neutron stars with masses above $2M_\odot$ [68, 126] together with charged particle flow [127, 128] at SIS energy regime confront the picture of soft EOS and start again a discussion on the stiffness of EOS.

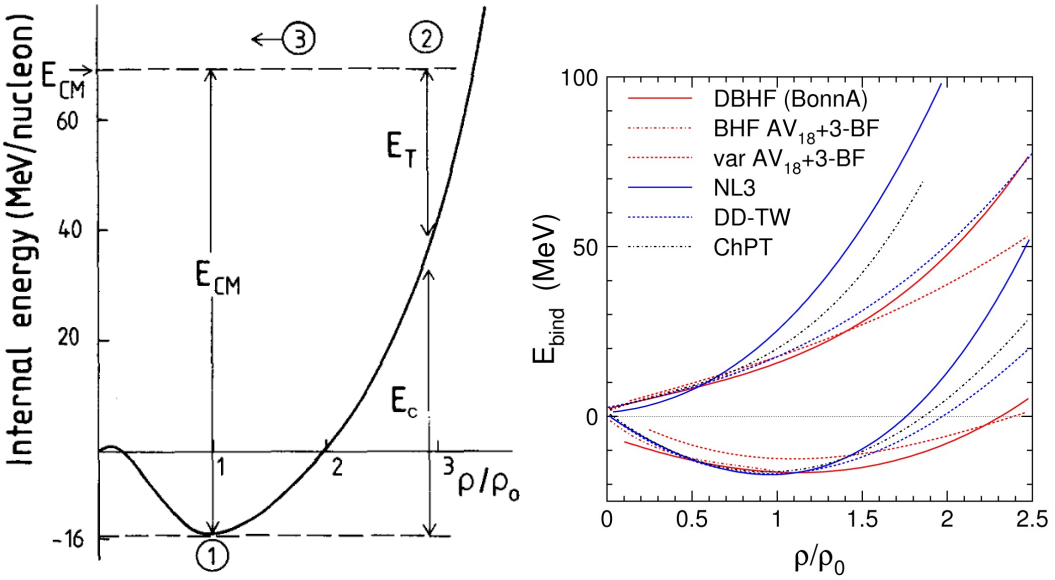

(a) (b)

Figure 1.10: (a) The sketch of the dependence of internal energy per nucleon on the relative density to normal nuclear density ρ_0. The reaction cycle for collision with center-of-mass energy $E_{\rm cm}$ is depicted via numbers: 1 - before interaction, 2 - maximum compression (the internal energy is shared between compression and thermal energy), and 3 - expansion (that leads to freeze-out). Taken from [129]. (b) Binding energy per nucleon for isospin-symmetric nuclear matter (lower bunch of curves) and neutron matter (upper bunch of curves) predicted by ab initio calculations (red), phenomenological density-dependent RMF functionals (blue), and chiral perturbation theory (black). Figure taken from [130].

1.7 Motivation for this thesis

On the basis of the arguments stated above, the kaon (collective) flow might be a very useful tool for studying several important aspects of heavy-ion collisions. Already in the mid-1990s (relativistic HIC experiments started in the early 1970s) the kaon flow was suggested as a possible good probe of HIC [131]. The total kaon-nucleon cross section is small ($\sigma_{\rm KN} \approx 10\,{\rm mb}$) compared to the pion-nucleon

[11] Thanks to the sensitivity of kaon yield at energies around threshold to the created density during collision. For softer EOS less energy to compress nuclear matter is necessary, which results in higher density. In the case of higher density the probability of kaon production through the multistep process is higher and therefore in experiments one observes higher yield of kaons.

cross section and therefore kaons are considered a good probe of the dense matter created at the early stage of HIC and of the kaon properties in compressed nuclear matter. It was shown in [132] that using the so-called azimuthal anisotropy parameters

$$R_1 = \frac{N(90°) + N(270°)}{N(0°) + N(180°)} \quad R_2 = \frac{N(90°)}{N(180°)} \tag{1.16}$$

where $N(\Delta\phi)$ denotes the number of kaons that escape the collision with azimuthal angle $\Delta\phi = \phi_{\mathrm{K}} - \phi_{\mathrm{RP}}$ with respect to the reaction plane. Using the relativistic transport model (RVUU) calculation with Au + Au collisions at $1A$ GeV and impact parameter $b = 3$ fm they obtained kaon azimuthal distributions for two rapidity regions and for three scenarios: without any potential, with only vector potential and with scalar and vector potential. From these they calculated the azimuthal anisotropy parameters and showed them as a function of a strength of the potentials, see figure 1.11. The conclusion they made was that for the mid-rapidity region the sensitivity of R_1 is very small, but for the target rapidity the sensitivity increases significantly and therefore the kaon flow might serve as a useful probe of the kaon nucleon potential in dense matter. The influence of repulsive kaon nucleon potential reduces the flow (even induces an antiflow), with respect to the flow of nucleons, and the attractive antikaon nucleon potential would lead to similar flow to that of nucleons, however, the large $\mathrm{K}^-\mathrm{p}$ cross section leads to strangeness exchange reactions resulting in an almost isotropic emission pattern [133].

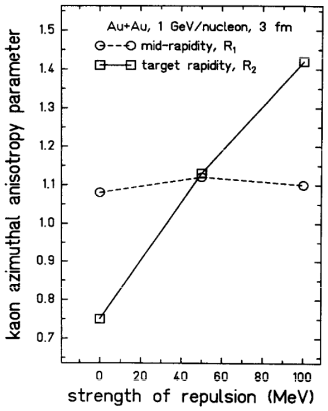

Figure 1.11: The azimuthal anisotropy parameters R_1 and R_2 as a function of the strength of KN repulsive potential. Taken from [132].

The first experimental results at both the SIS18 and AGS energies have shown almost zero flow, that is, the kaon average in-plane transverse momentum as a function of rapidity and its slope at mid-rapidity [134–136]. There were ideas on how to explain this vanishing kaon flow based on the isotropic production and canceling of the flow due to the production of kaons in the collision of hadrons with the opposite transverse flow. The theoretical calculations using transport models all predict that at the moment of creation, kaons have a positive initial transverse flow (inherited from nucleons), and this is later reduced because of the repulsive kaon potential in the nuclear medium. A quite surprising result was observed in the case of nucleon (proton) flow at incident energy, called the balance energy, where also vanishing flow was observed. However, it turned out

using the so-called differential flow analysis [137] (split the measured interval of transverse momentum into smaller and investigate the flow within these intervals) that there are two components: nucleons with high transverse momentum show positive flow and those with low p_T have negative flow.

Therefore, the differential approach for kaon flow is able to disentangle such effects and can bring more light to the problem of kaon properties in hot and dense matter. After the authors of [138] suggested, such an analysis was performed mainly in experiments with beam energies starting at several AGeV but seldom around the kaon production threshold energy (and never below). Due to the unprecedented statistics available in HADES gold beam time, such a measurement is possible for the first time.

1.7.1 Current experimental status of kaon flow at low energies

Due to the scare heavy-ion program at similarly low energies, the only relevant comparison is possible with experiments from GSI using SIS18 accelerator, namely, the experiments KaoS and FOPI. Very recently, STAR collaboration presented their results from fix-target experiment[12], and although the collision energy is still significantly higher than in presented analysis, in terms of system size (Au + Au) this is the closest measurement. Both GSI experiments are currently retired. They have measured many different systems (from light-ion to heavy-ion collisions) at several beam energies, which enabled them to obtain many important results on bulk properties. The published data on the kaon anisotropy of the azimuthal distribution w.r.t. reaction plane are usually integrated and differential analysis was solemnly performed and mainly for K^+. Flow of neutral kaons (K^0_S) is even more rare because of the need to reconstruct neutral kaons using their decay to charge pions.

In the deeply informative review [140], the influence of the in-medium KN potential and the rescattering on the final kaon flow parameters is discussed in detail. Thanks to the knowledge of the complete history of the virtual particles in the simulations, it is possible to distinguish between the final-state kaons which did not undergo any rescattering and which rescattered many times, see figure 1.12a. The repulsive KN potential pushes the created K^+ aside from the spectator matter, but the rescattering process has the opposite outcome. On the other hand, both of these effects add together in a nonlinear way when the azimuthal distribution of kaons with respect to the reaction plane at mid-rapidity region (where the directed flow is zero due to its antisymmetry for a symmetric collision system), see figure 1.12b. Moreover, using the time information from microscopic models, it is possible to study the dependence of the elliptic flow on the time of last contact with the system, displayed on figure 1.12c.

KaoS results

The Kaon Spectrometer [141] measured K^+ and K^- production as a function of the size of the collision system, the collision centrality, the collision centre-of-mass

[12] Using a golden foil insert inside the beampipe they achieved a lower the collision energy compared to two-beam collider mode from $\sqrt{s_{NN}} = 7.7\,\text{GeV}$ to $3.0\,\text{GeV}$ [139].

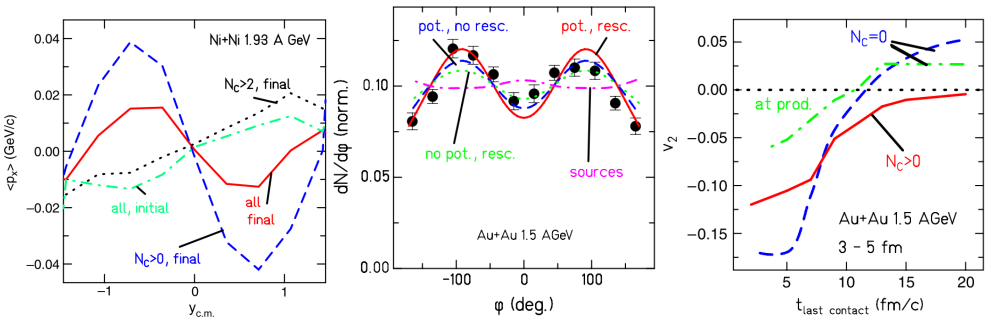

(a) (b) (c)

Figure 1.12: (a) Directed flow at creation and in the final state for different numbers of KN collisions (KN potential included). (b) The azimuthal distribution at mid-rapidity region for different scenarios (w/ or w/o potential and rescattering). (c) Elliptic flow as a function of the the time of last KN collision. All figures are for K^+. Figures taken from [140].

energy, the kaon energy, and its polar angle [142]. The azimuthal distribution was also studied, which is of interest for this thesis. The anisotropy in azimuthal distribution of π^+ and K^+ mesons with respect to reaction plane angle was measured in Au + Au reactions at $1.5A$ GeV and Ni + Ni reactions at $1.93A$ GeV where thanks to the higher kinetic beam energy also study of K^- meson flow was possible [143]. In both of these experiments, π^+ and K^+ show an enhancement in azimuthal region perpendicular to the reaction plane, additionally, this negative elliptic flow is observed to be smaller for Ni + Ni reactions compared to Au + Au reactions, which is expected due to the smaller system size. Within these results, the first in-plane elliptic flow of strange particles at SIS18 energy was published. Comparison with simulations using IQMD models with and without in-medium potentials was made. However, no strong conclusion on K^+N-potential was possible since most of the enhancement in the perpendicular direction to the reaction plane is explained by rescattering. All of these results are integrated in rapidity ($0.3 < \frac{y_{\mathrm{lab}}}{y_{\mathrm{proj}}} < 0.7$) and transverse momentum ($0.2\,\mathrm{GeV}/c < p_{\mathrm{T}} < 0.8\,\mathrm{GeV}/c$). The centrality of collisions is selected in case of Au + Au in terms of impact factor $5.9\,\mathrm{fm} < b < 10.2\,\mathrm{fm}$ and in case of Ni + Ni the range is $3.8\,\mathrm{fm} < b < 6.5\,\mathrm{fm}$.

FOPI results

Within the goals of the physics program of the 4π-detector system (FOPI) [144, 145] for measurements at SIS18 was the investigation of strangeness in HIC. The first results on the flow of strange hadrons [136] indicated negligible kaon flow (both K^+ and K^0_S) in Ni+Ni at $1.93A$ GeV however, at that time the presented directed flow was integrated over the transverse momenta with cut $\frac{p_{\mathrm{T}}}{m} > 0.5$. Later it was shown in [137] that the vanishing directed transverse flow of nucleons at the balance energies comes from the integration over the transverse momenta, and the new observable the differential flow was suggested to be compared with model predictions. A similar effect is also found for kaons. The differential kaon flow was measured in Ru + Ru at beam kinetic energy of $1.69A$ GeV and revisited data from Ni + Ni at $1.93A$ GeV [146]. The decreasing directed transverse flow

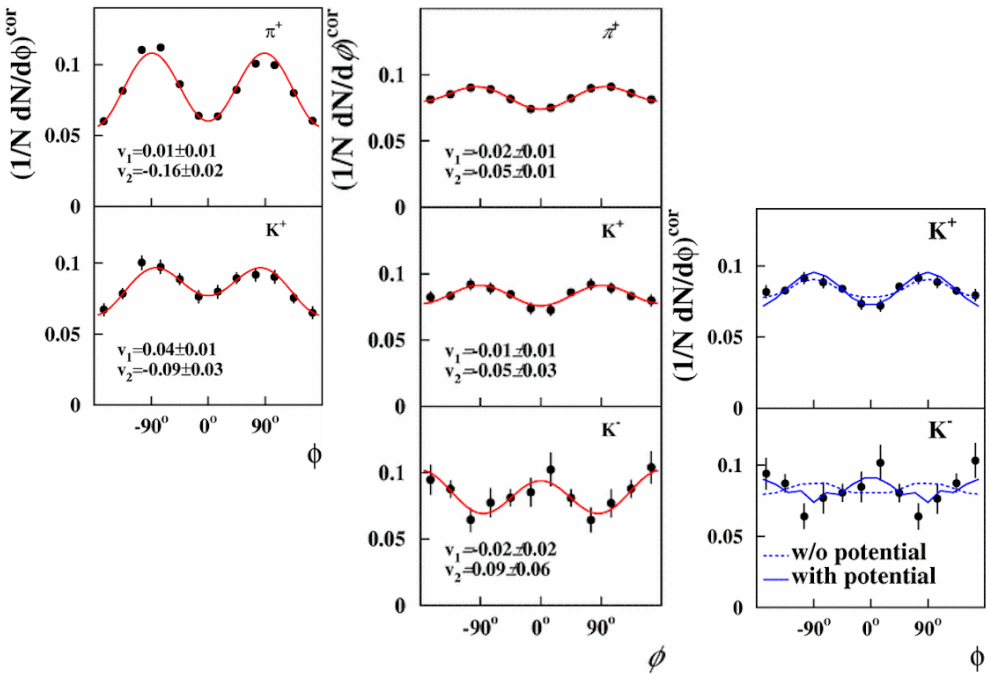

Figure 1.13: The azimuthal distributions of π^+ and charged kaons with respect to the reaction plane. On the left side are distributions from Au + Au collisions at 1.5A GeV, in the middle and on the right from Ni + Ni at 1.93A GeV. Two plots on the right side show results comparison with the IQMD model with and without KN and $\bar{\text{K}}$N potentials. Figures taken from [142].

with increasing transverse momenta was observed and compared to the RBUU model prediction. Without any in-medium K^+N potential, the model fails to describe the antiflow of kaons with low p_T, however, no strong conclusion was possible due to disagreement between model calculations and measured nucleon differential flow. The directed flow of neutral kaons was examined after the additional beam time in which collisions of Ni + Ni at 1.93A GeV were measured with the aim to enlarge the total statistics. Few tens of thousands of K^0_S were reconstructed [147] showing approximately zero directed flow in agreement with [136]. Unfortunately, no p_T differential analysis was performed. The latest result of the FOPI collaboration regarding kaon flow is in the publication [148]. The analysis presented there is again with the collision of Ni + Ni at 1.91A GeV, this time with an upgraded detector for time-of-flight measurement that provides better resolution and granularity. The resulting spectra of directed and elliptic flow as a function of normalized (scaled) rapidity $y_{(0)} = \frac{y_\text{lab}}{y_\text{proj,cm}} - 1$ are displayed on figure 1.14 together with p_T-differential directed flow of K^+ in central and peripheral collisions. Kaons with positive electric charge show a positive v_1 near target rapidity (so-called antiflow because of the different sign compared to protons) and negative v_2, meaning that they are squeezed out of the reaction plane. Due to the much lower statistic (approximately 2% of the K^+), the results for K^- are compatible with zero values of v_1 and v_2, respectively. The measured data are compared with two model predictions, HSD and IQMD. If the interaction strength between kaons and nucleons is not modified with potential, the expected outcomes of the models are negligible flow parameters v_1 and v_2. If the medium potentials are

turned on, the repulsive nature of the K^+N integration pushes the kaons away from protons, thus generating the already discussed antiflow pattern and negative elliptic flow. The measurements prefer the scenario with the in-medium potentials (slightly better agreement mainly for the p_T differential directed flow is with IQMD), however, the differences are not statistically significant.

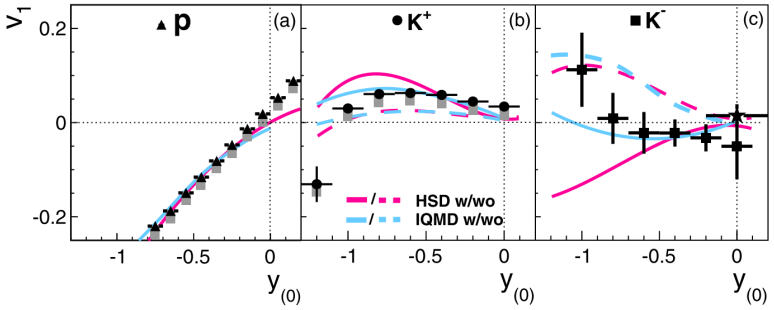

Directed flow of charged kaons and protons.

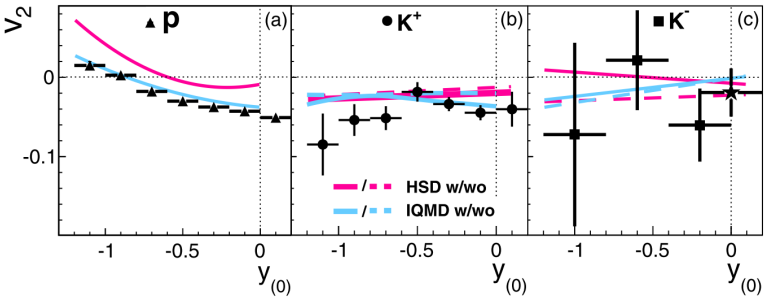

Elliptic flow of charged kaons and protons.

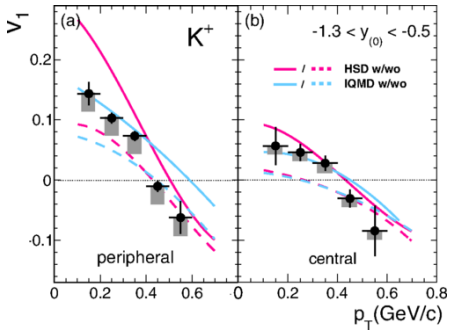

p_T differential directed flow of K^+.

Figure 1.14: Measurements of directed and elliptic flow from Ni + Ni collisions at 1.91A GeV beam kinetic energy for charged kaons and protons. Data are compared with simulation using HSD and IQMD models, both with and without inclusion of in-medium KN and $\bar{K}N$ potentials. Error bars (boxes) denote statistical (systematic) uncertainties. The star symbols for K^- mesons at mid-rapidity in (c) are from the high statistics data in the range $p < 1.0\,\mathrm{GeV}/c$ with $\frac{S}{B} > 5$. Figures taken from [148].

STAR results

The Solenoidal Tracker At RHIC (STAR) is a general purpose detector [149] designed to measure charged particles from high-energy heavy-ion (Au+Au) col-

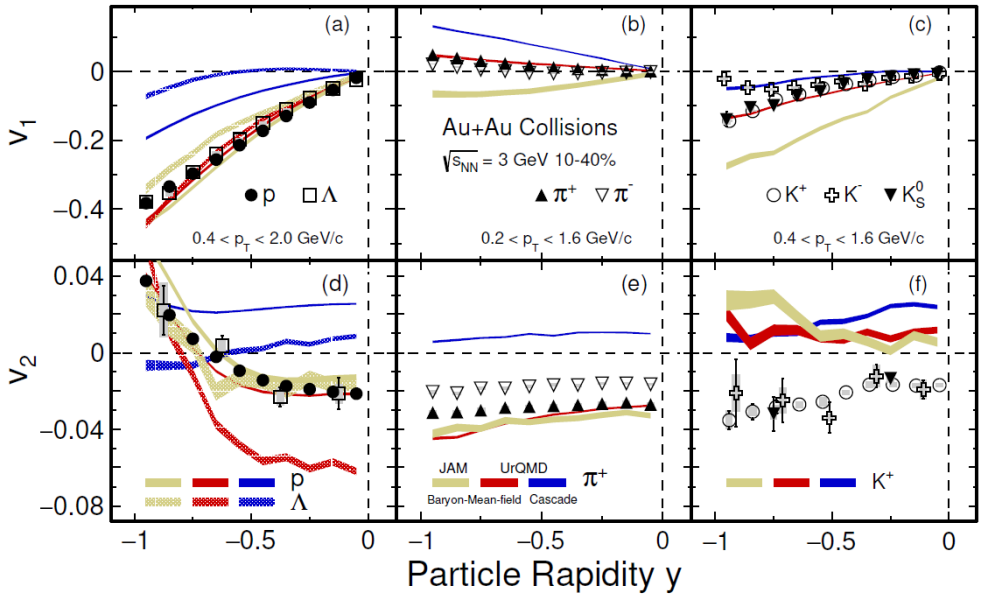

Figure 1.15: Directed and elliptic flow of protons, λ hyperons, pions, and kaons as a function of rapidity (integrated within given range of transverse momentum) measured by STAR collaboration in $10-40\%$ most central $\mathrm{Au}+\mathrm{Au}$ collisions at $\sqrt{s_{\mathrm{NN}}} = 3.0\,\mathrm{GeV}$. The comparison to JAM and UrQMD models (both cascade and mean-field mode with incompressibility $\kappa = 380\,\mathrm{MeV}$) is included for selected hadrons. Figure taken from [152].

lisions at the Relativistic Heavy-Ion Collider at Brookhaven National Laboratory, NY USA. It started operations in 2002 with the intention "to investigate the behavior of strongly interacting matter at high energy density and to search for signatures of quark-gluon plasma (QGP) formation" [149] and the first results (showing evidence for the first observation of QGP) are summarized in [150]. Afterwards, the focus of the STAR experiment turned to the search of the critical point using the Beam Energy Scan (BES) [151]. The first successful measurements in collider mode were extended to a fixed target mode since 2018 [139] where the lowest collision energy is $\sqrt{s_{\mathrm{NN}}} = 3.0\,\mathrm{GeV}$. Thanks to the many upgrades of the original STAR detector high precision for measurement of reaction plane was achieved and combined with the particle identification made it possible to obtain results on flow of all kaons, see figure 1.15. The comparison with JAM and two versions of UrQMD models for K^+ is present as well, suggesting a good agreement with UrQMD using the mean field in the directed flow but completely missing the data points of the elliptic flow. One can also observe that data points of K^+ and $\mathrm{K}^0_{\mathrm{S}}$ match perfectly and moreover negative kaons exhibit very similar flow patterns too. All of these results are integrated over $0.4 < p_{\mathrm{T}} < 1.6\,\mathrm{GeV}/c$ and correspond to $10-40\%$ of the most central Au+Au collisions.

Summary of experimental results on Kaon Flow

Our up-to-date experimental knowledge on kaon flow in heavy-ion collisions is based on a very limited data set. These published results are either for smaller systems slightly above the kaon production threshold or for the same system as presented in this thesis (Au+Au) but significantly higher collision energy. In

summary, the results on K^+ show antiflow pattern at $p_T < 0.4\,\mathrm{GeV}/c$ changing to negative directed flow for higher transverse momenta. The results for neutral short-lived kaons reveal the same nature as positively charged kaons, while there are only weak indications of similar behaviour for K^-. All experiments observed perpendicular elliptic flow of K^+ with respect to reaction plane, the values of v_2 for K^- are mostly consistent with zero within error bars.

There has never been an analysis focusing on the subthreshold energy region, however, the importance of different undergoing processes is very much influenced by the energy region as well as the collision system size, e.g., probability of rescattering, multistep processes to produce strangeness. Thus, the presented, moreover, differential analysis of kaon flow including the comparison to different models predictions might shed some light on the topic of KN potentials and the properties of the equation of state of nuclear matter.

Chapter 2

HADES

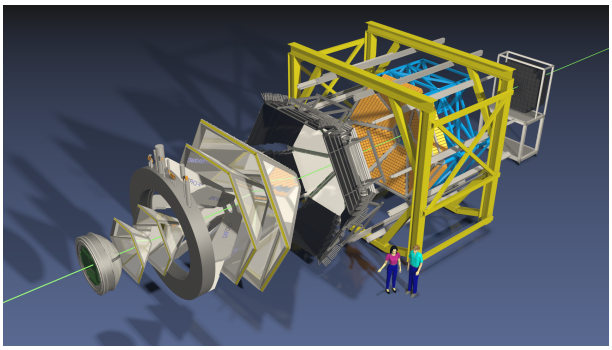

Recently, in 2019, the HADES collaboration celebrated already its 25$^{\text{th}}$ anniversary. This collaboration, consisting of 130 scientists from 20 institutes across Europe, has its roots at a *3*$^{\text{rd}}$ *workshop on real photon/dilepton program for SIS* where the results [153] from **D**i-**L**epton **S**pectrometer (DLS) located at Bevalac accelertor in Berkeley, California USA, were discussed and new a detector for the newly constructed accelerator SIS18 (**S**chwer**i**onen**s**ynchrotron 18)[1] at GSI Helmholtzzentrum für Schwerionenforschung in Darmstadt, Germany, was proposed. The major improvements compared to the pioneering DLS experiment [155] were greater acceptance (85 % in azimuth angle and interval $18° < \theta < 85°$ in polar angle , more than 100-times larger)[2] and better mass resolution ($\delta m/m \approx 2\% \rightarrow$ 10-times smaller), see figure 2.1.

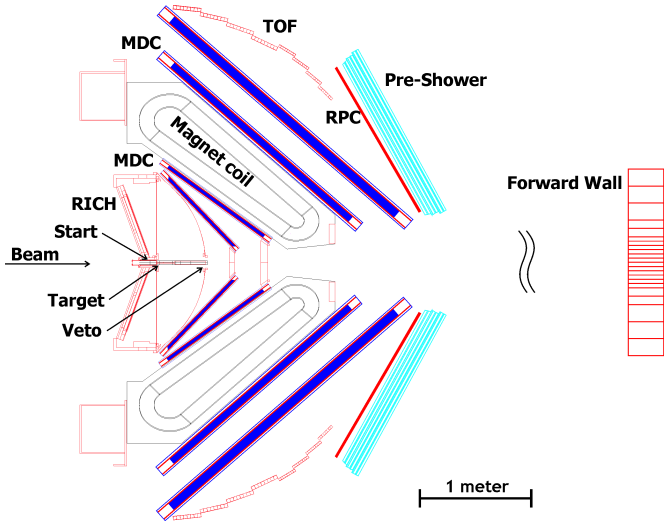

Figure 2.1: Cross-section of HADES spectrometer. Taken from [156].

The main purpose of this detector is to study in medium modifications of the properties (mass, mean lifetime, etc.) of the light vector mesons[3] ρ, ω, ϕ by measuring e^+e^- pairs originating from their decay. These pairs are excellent

[1]Number 18 in the name of this heavy-ion synchrotron designate the bending power of installed magnets 18 Tm, the circumference of the accelerator is 216.72 m [154].

[2]From that comes the name HADES which means **H**igh-**A**cceptance **DiE**lectron **S**pectrometer.

[3]The lifetimes of these mesons correspond to the duration of the compression phase of the HIC with kinetic energy of the beam $1 - 2\,A$GeV.

probes, as they can pass hot and dense baryonic matter undisturbed because a strong interaction does not act on them. Unfortunately, these leptonic decays are strongly suppressed compared to other decay channels. To obtain a sufficiently large data set in a reasonable timescale, one needs to have a spectrometer built out of fast subdetectors and electronics (to decrease dead-time and increase the rate of recorded events). Additionally, the background reduction, coming from real photon conversion, is important and therefore the spectrometer is built with low-material-budget subdetectors. Thanks to the excellent identification of charged particles, the HADES spectrometer is also an excellent tool for studying rarely produced hadrons at low energies, like kaons.

The last important ingredient for the unique results from HADES is the capability of the spectrometer[4] to measure the products of various interactions from elementary pion- or proton-induced reactions up to heavy-ion collisions. All production runs are summarized in table 2.1.

Some parts of the following sections are taken from my diploma thesis [157].

Year	Colliding system	$\sqrt{s_{NN}}$[GeV]	$N_{\text{events rec.}}[\times 10^9]$
2002	C + C	2.70	0.25
2004	$p + p$	2.77	0.44
2004	C + C	2.32	0.50
2005	Ar + KCl	2.61	0.93
2006	$d + p$	2.37	0.85
2007	$p + p$	2.42	1.70
2007	$p + p$	3.18	1.18
2008	p + Nb	1.93	4.21
2012	Au + Au	2.42	7.31
2014	π^- + C	1.98	0.40
2014	π^- + W	1.89	
2014[5]	$\pi^- + \mathbf{p}$(PE − 2C)	1.47 − 1.56	1.23
2019	Ag + Ag	2.55	13.61

Table 2.1: Overview of HADES experiments carried up to 2020 with important information about individual beam times.

2.1 Target

It was already mentioned that HADES is a fixed target experiment [158]. Expect for the liquid hydrogen target and polyethylene target used in the elementary reaction physics program, the used targets are segmented into several thin cylinders (the gold beam time target was divided into 15 segments with a total width of 3 mm) that are glued to a kapton foil which is fixed to the carbon support structure, see figure 2.2. Segmentation is necessary to decrease the probability

[4] As well as the ability of the accelerator to provide primary proton to heavy-ions and also secondary pion beams.

[5] Instead of liquid hydrogen target, two targets (polyethylen and carbon) were used for the π^- beam scan in the region of nucleon resonance region, for example $N(1520)$.

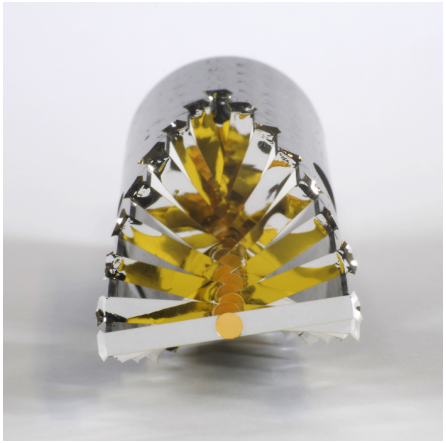

Figure 2.2: Photo of the segmented gold target used during the gold beam time. Source [156].

of interaction of the produced particles with the target material. The target is inserted into a beam pipe, and the air is sucked out. The standard interaction probability is approximately 2 %.

2.2 START and VETO detectors

The START and VETO detectors are diamond-based detectors used for triggering data acquisition, measuring t_0 of the interactions needed for the final time of flight and VETO, mainly for the cleaning of recorded events, see 3.2. The position of the START detector is less than 5 cm in front of the target inside the beam pipe, the VETO detector is much further behind the target (in the case of Au + Au experiment, it was located 70 cm behind the last segment of the target). The radiation in this place is very intensive, but still it causes only small damage to the diamond material [159]. Due to the trigger purpose of the START detector, it is essential to keep the detection efficiency as high as possible, therefore, the position of the START detector was changed 8 times during the gold campaign. In case of the pion beam, such an action was not needed because a pion with an energy of several hundreds of MeV is a minimum ionizing particle.

The advantage of diamond material is the very large energy gap between valence and conducting level (band gap = 5.5 eV), this means that there is no need for detector cooling and there will still be no noise at room temperature. Another advantage is the high electron drift velocity (220 km/s) which results in good time resolution (well below 50 ps) and high count rate capability (up to 10^8 parts/s/mm^2). Finally, due to the low $Z = 6$ of carbon and the technical opportunity to make very fine diamond plates, there is no problem with multiple scattering with these detectors.

The START detector used during the gold beam time was a monocrystalline diamond (made by a process called Chemical Vapour Deposition) of square shape with a side length of 4.7 mm and thickness of 50 μm. The diamond was coated with 16 golden strips on both sides with a width of 200 μm and a width of 90 μm gap between strips [156]. On one the division was horizontal and on the other vertical, allowing also position measurement, see figure 2.3. The time resolution

of START was below 50 ps. The VETO was 100 μm thick polycrystalline diamond and size of $8 \times 8\,\mathrm{mm}^2$.

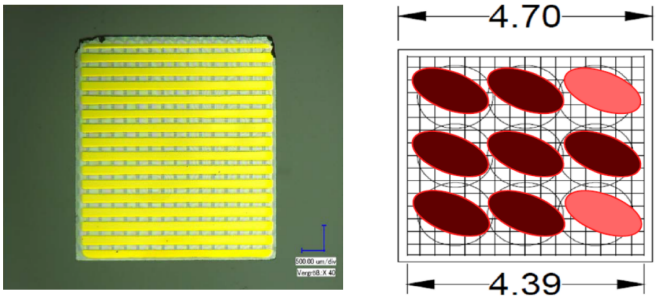

Figure 2.3: Photo of the START detector with visible gold strips and schematics of the 9 positions where the accelerated gold ions passed through during the experiment. Source [156].

2.3 RICH detector

The **R**ing **I**maging **CH**erenkov detector is used to identify relativistic $e^{\pm}$ [160] and is supposed to be hadron-blind[6]. The functionality of RICH detectors is found on the discovery that charged particles with a speed greater than the phase speed of light in the medium of refractive index n emit photons under the angle θ_C with respect to their trajectory. The angle is related to the speed of the charged particle $\beta = \sqrt{1 - \frac{1}{\gamma^2}}$ through the relation

$$\cos\theta = \frac{1}{\beta n}. \tag{2.1}$$

As was mentioned, there was a hadron-blind requirement for the RICH detector. In the simulations, the threshold for $\gamma_{\mathrm{tr}} \approx 12$ was determined (based on the typical speed of the electrons and hadrons emitted from collisions). Among other requirements, the position of photon detectors must be upstream of the target to keep the amount of material in the electron path as low as possible. This leads to the layout which is presented on figure 2.4. As the gas radiator was chosen C_4F_{10} with $\gamma_{\mathrm{tr}} = 18$, and with a high transmission for the ultra-violet vacuum (VUV) wavelength region (up to $\lambda = 145\,\mathrm{nm}$). The emitted Cherenkov light is then reflected on the spherical mirror with radius $R = 871\,\mathrm{mm}$ and continues through the CaF_2 window to the detector gas (very pure CH_4). The pads with photon detector (Multi-Wire Proportional Chamber) are inclined by 20° because the position of the target is not exactly in the centre of the spherical mirror. The principle of photon detection is shown in the detail picture 2.4. There is a certain probability, determined by quantum efficiency, that the electron would be released by collision of a photon with CsI via the photoelectric effect. This electron is attracted to anode wire and creates an avalanche of positive ions that drift back to the cathode pad where they are registered. From the tests, the

[6]This means that hadrons should not create Cherenkov radiation. In case of the lightest charged hadrons $\pi^{\pm}$ the minumum momentum that would lead to Cherektov radiation is $p_{\pi\mathrm{tr}} \approx 2.1\,\mathrm{GeV/c}$ which makes it very improbable to occur in HIC at SIS18 energy.

single-electron detection efficiency was determined at $\varepsilon \approx 95\%$. The entire RICH detector consists of 4712 cathode pads per sector. The ring finder algorithm is later used in low-level data analysis to identify lepton tracks. The backtracking method was developed with the aim of increasing the detection efficiency for close pairs [161].

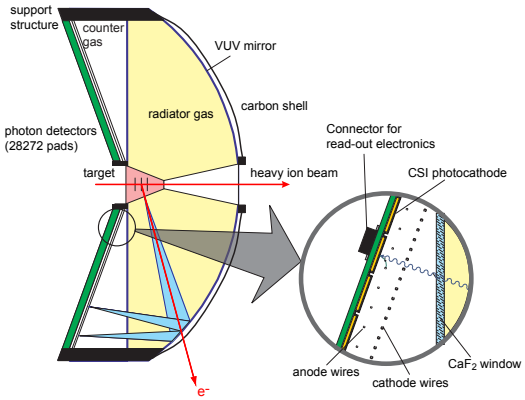

Figure 2.4: RICH detector with detail on the photon detector. Taken from [162].

2.3.1 Upgrade of RICH photon detector

After the pion beam time performed in summer 2014, a long accelerator break was expected, and that time was used by the HADES collaboration for various upgrades of the spectrometer. One of such upgrades was the replacement of the RICH photon detector with a new one based on multi-anode PMTs (Hamamatsu H12700) because it was observed that the overall response of the original photon detector with MWPC decreased by more than 40 % over the 15 years of operation [163]. The front area of these MAPMTs is 2×2 inches in size and is divided into 64 individual channels. In total, 428 MAPMTs were placed in the new photon detector and successfully operated during the silver experiment in 2019, see figure 2.5.

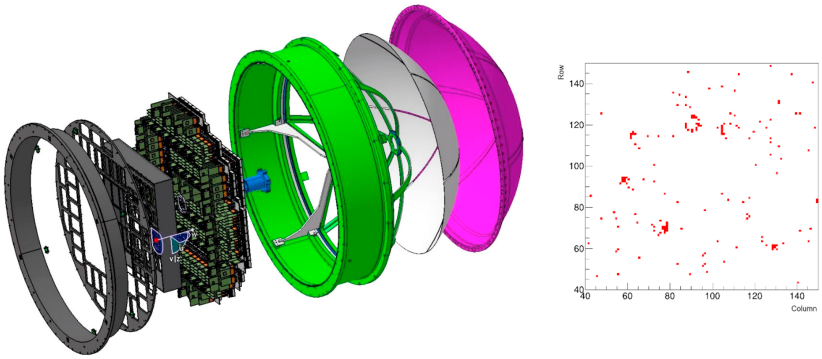

Figure 2.5: Sketch of the upgraded HADES RICH detector and online detection of rings. Taken from [163] and [164].

2.4 Tracking system for momentum determination

HADES spectrometer tracking is based on the Multiwire Drift Chambers (MDC) and superconductiong magnet calles ILSE. Both of these two systems will be described in the following and the procedure of momentum reconstruction will be given in 3.5.

2.4.1 Magnet

To be able to identify particles, the momentum determination is crucial, resulting in the need of a magnetic field to bend the particle tracks and measure the positions before and after the magnetic field. During the design stage, several requirements on the properties of the magnetic field were defined:

- the strength of the magnetic field in combination with the MDC position measurement should enable a momentum resolution for the electron better than $\frac{\sigma_p}{p} < 2\,\%$,
- acceptance in phase space $p = 0.1 - 2\,\mathrm{GeV/c}$, $18^\circ < \theta < 85^\circ$ and almost full azimuth coverage,
- no magnetic field in RICH subdetector.

From simulations for the energy region of the SIS18 accelerator, it became clear that the transverse momentum kick of $p_{\mathrm{kick}} = 0.1\,\mathrm{GeV/c}$ for the high-momentum particles is needed [158]. Since there is a relation between kick momentum p_{kick}, magnetic field intensity B, and length of particle trajectory inside of the magnetic field L

$$p_{\mathrm{kick}} \sim B \cdot L, \tag{2.2}$$

one gets a clear limit for the intensity $B \leq 0.9\,\mathrm{T}$ if we want to keep the spectrometer compact($L \simeq 0.4\,\mathrm{m}$). Subsequently, the requirements on the MDC subdetector are: two planes of chambers on both sides of the magnetic field with a distance between $d = 0.3\,\mathrm{m}$ and a position resolution better than $150\,\mu\mathrm{m}$. To satisfy the demand on zero magnetic field in RICH, a toroidal magnetic field was chosen with six superconducting coils placed in the vertices of imaginary hexagon, see figure 2.6. Thanks to this geometry, there is no additional matter in the particle path that might cause unwanted multiple scattering. Each coil has 140 turns and in full operational mode there is a current of 3464 A. To keep the coils in the superconducting state, liquid nitrogen cooling (85 K) is used for the coil shielding and the conductors themselves are cooled down to 4.7 K with liquid helium. Some problems with cooling might occur if there were a bubble inside the tubes that carries helium to the coils. To avoid these problems, helium is compressed to 0.29 MPa when the critical point of helium at 4.7 K is 0.23 MPa. When the helium gas enters the coils it expands to 0.13 MPa and is liquefied.

The field map which was calculated (and is displayed on figure 2.7) is in excellent agreement with the measurements (after corrections to the Earth magnetic field) that were done with the Hall probe and the optical position system.

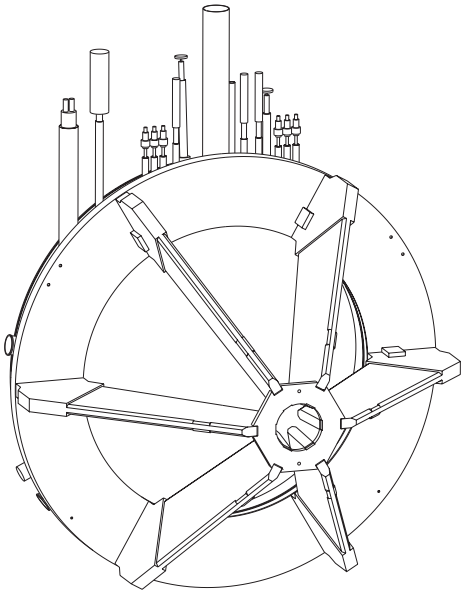

Figure 2.6: Scheme of ILSE (Iron-Less Superconducting Electromagnet) construction. Taken from [156].

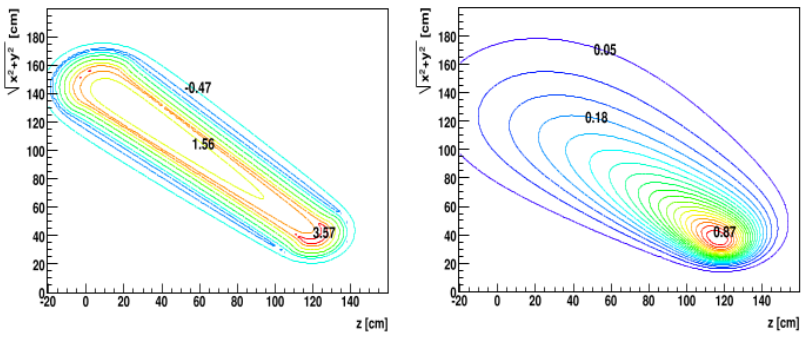

Figure 2.7: Magnetic field in contour lines. Left picture is for $\phi = 30°$ where the coil is placed and right is for $\phi = 0°$. Along the beam we use the z-direction. Taken from [158].

2.4.2 Multiwire Drift Chambers

As was already mentioned in section 2.4.1, the subdetector MDC consists of four planes, two in front of the magnet and two behind. Furthermore, the requirement for position resolution better than 150 μm was mentioned above. Among other demands on detector performance belong especially high efficiency and keeping detector thickness as low as possible to restrict multiple scattering (for this reason only very thin Mylar foil is covering the chambers). The shape of the chambers is trapezoidal to fit in the spaces of hexagonal layout of the spectrometer, see figure 2.8. In the same figure, one can see that in each chamber there are six layers of wires with different orientation ($\pm 0°, \pm 20°, \pm 40°$) [165]. The size of chambers varies from 0.35 m^2 to 3.2 m^2 and each of them is divided into 1100 drift cells. The chambers are filled with a mixture of helium and isobutane ($He : C_4H_{10} = 60 : 40$). The diameter of potential and cathode wires (made of aluminium) is between 80 μm and 100 μm, the initial tension on these wires is in the range $80 - 120$ cN. Meanwhile, the sense wires, for the detail of wires disposition see figure 2.9, are made from gold and tungsten with diameter 20 μm (planes I-III) and 30 μm (plane IV) with initial tension $40 - 110$ cN.

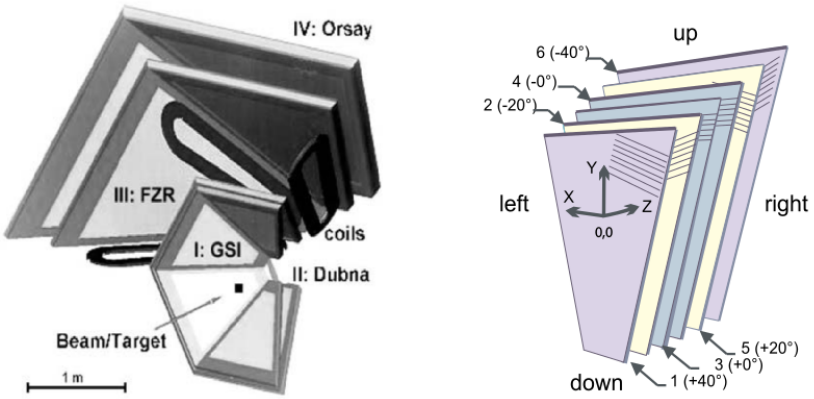

Figure 2.8: In the left picture is the MDC layout with the name of institutions that made the according plane. The picture on the right shows the scheme of the inner structure of one MDC chamber. Taken from [158].

To achieve the desired position resolution, it is needed to align the detectors (not only MDC chambers), which is usually done in the first step using stereo photometry, afterwards with cosmic rays, and finally using straight trajectories from collisions with the magnetic field switched off. This procedure allows us to set the correct position with an accuracy of 0.1 mm. The particle detection efficiency is about 90 % for plane I, 97 % for plane II, and close to 100 % for planes III and IV. The lower efficiency for the first two planes is due to the dependence of the efficiency on the applied high voltage. Optimal efficiency is achieved for 2000 V, but due to the non-stability of this setting, the value of HV is lower during experiments to 1800 V. Due to this effect, the efficiency of track reconstruction is 86 %. In figure 2.10 is shown the results of time respective position resolution, one can notice that the requirement on position resolution is accomplished.

From the measurement of time over the threshold (ToT, effectively the width of signals), it is possible to get information about energy losses $\frac{\mathrm{d}E}{\mathrm{d}x}$ for the reconstructed track, that is, we can deduce the particle species in combination with

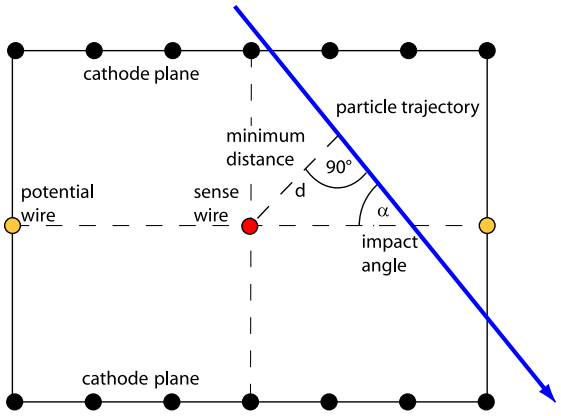

Figure 2.9: Detail on wires disposition with example of particle track. Taken from [156].

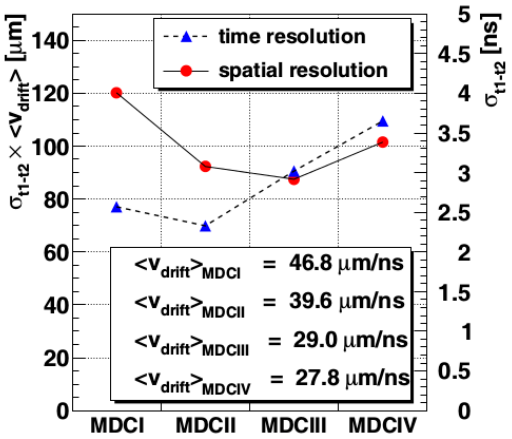

Figure 2.10: Spatial and time resolution for all MDC planes. Taken from [158].

the particle momentum p. The relation between ToT and energy loss can be described by

$$\mathrm{ToT} = c_0 + c_1 \left[\log_{10} \left(\frac{\mathrm{d}E}{\mathrm{d}x} + c_3 \right) \right]^{c_2}, \tag{2.3}$$

where c_i for $i = 0, .., 3$ are the fit parameters. These parameters were obtained from the elastic scattering of the proton on the proton, see figure 2.11. There is also shown excellent agreement of the measured data with theoretical calculations from the Bethe-Bloch formula.

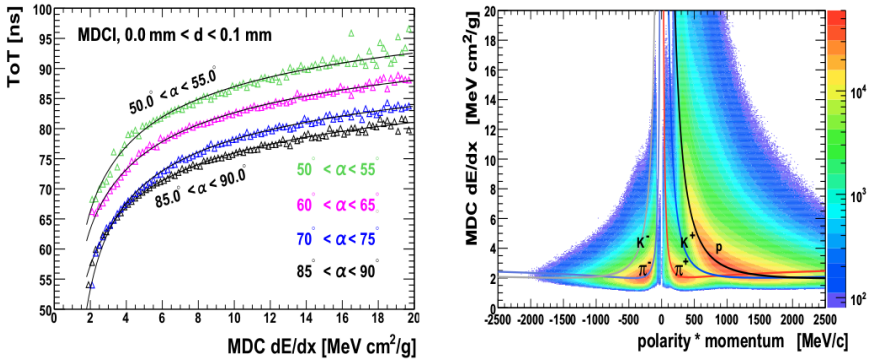

Figure 2.11: Left picture shows the results of the fitting dependence of ToT on energy losses (for protons and different incidence angles α) according to (2.3). Right picture shows the measured energy losses dependent on the momentum of the particle multiplied by its charge sign. Taken from [158].

2.5 META detectors

To improve particle identification (not to be dependent only on energy loss and momentum from MDC), the **M**ultiplicity **E**lectron **T**rigger **A**rray following the outermost MDC plane is part of the HADES spectrometer[7]. Originally, there were two scintillator-based time-of-flight detectors (TOF, described in 2.5.1 and TOFino) and the Shower detector (see section 2.5.3), see [158] for more details. To enable the measurement of high particle track density events from heavy-ion collisions, the inner TOFino detector was replaced by a 50 times more segmented RPC detector, and more details will be given in 2.5.2. This configuration was used during the two analysed experiments. During the mentioned break in accelerator operation, the Shower detector was replaced by an Electromagnetic Calorimeter (a short description is part of 2.5.3).

[7]Before the upgrade of DAQ system used by HADES spectrometer in 2010, there were two levels of trigger in order to select mainly events where the probability of dilepton pair creation is high (this also helped to keep the amount of written data to tapes small. The first trigger level usually consists of beam particle detection with START and reaction detection using TOF and TOFino detectors. The first level trigger started the image processing unit (IPU) of the RICH detector (ring finder), IPU of the Shower detector (determining the size of detected particle shower), and IPU of the TOF detector (fast particles). When the information from IPUs in the Matching Unit, the decision of whether electrons were detected was made and the Central Trigger Unit started the transmission of data from the detector buffers to the event builders. Therefore, the name of this group of detectors is META, nowadays only level one trigger is used.

2.5.1 Time Of Flight chambers

TOF is a scintillator wall divided into eight modules, each module consists of eight scintillator rods (this is for each of the six sectors), that is, in total there are 384 rods. On both ends of these scintillator rods are photomultipliers (PMT), which allows us to calculate the position of hits from the time difference

$$x = \frac{1}{2}\left(t_{\text{right}} - t_{\text{left}}\right) \cdot v_{\text{g}}, \tag{2.4}$$

where v_{g} is the group velocity of light in the scintillator material and t_{PMT} is the time of photon registration in each PMT. The time resolution, which determines also the spatial resolution x (along the scintillator rod), is $\sigma_t = 150\,\text{ps}$, i.e., the spacial resolution $\sigma_x \approx 2.5\,\text{cm}$ (from testing each rod group velocity $v_{\text{g}} = (15.4 \pm 0.2)\,\text{cm/ns}$ was determined [166]). In the other two coordinates, the spatial resolution is determined by the cross-section of the rod, which is $3 \times 3\,\text{cm}^2$ for the 192 outermost rods and $2 \times 2\,\text{cm}^2$ for the 192 inner ones. Additionally, the length L of the rods differs from 1 m up to 2 m. The time-of-flight t is calculated as

$$t = \frac{1}{2}\left(t_{\text{right}} + t_{\text{left}} - \frac{L}{v_{\text{g}}}\right) - t_0, \tag{2.5}$$

where t_0 is the time measured by the START detector. One can also gain information about the energy loss of a particle in the scintillator that might be useful in the particle identification process

$$\Delta E = k\sqrt{a_{\text{right}} \cdot a_{\text{left}} \cdot e^{-\frac{L}{\lambda_{\text{att}}}}}, \tag{2.6}$$

where a_{PMT} are the amplitudes of PMT signals, λ_{att} is the attenuation length of light in the scintillator, and k is constant. TOF covers the polar angle between $44° < \theta < 88°$ and the whole azimuth angle. The detector is shown on figure 2.12.

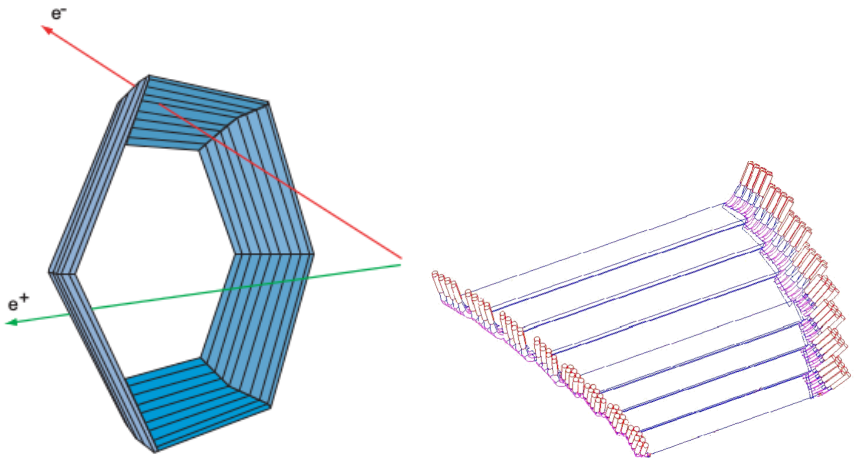

(a) (b)

Figure 2.12: (a) Scheme layout of the TOF detector with example of the registration electron and positron. (b) Technical drawing of one sector. Figures taken from [162, 167].

2.5.2 Resistive Plate Chambers

The second detector for time-of-flight measurement is Resistive Plate Chambers (RPC). This technique for registering particles is rather new, the first RPCs were used in 1980's [168]. In principle, passing particles ionise the gas between two electrodes covered by a high-resistance plate. Originally, these plates were made of a phenolic resin (Bakelite), but nowadays they are usually made from soda-line glass, which is very commonly produced (its volume resistivity is $\rho \approx 10^{12}\,\Omega\mathrm{m}$). There are two types of operational modes of RPCs:

- streamer mode: register the stream of charges thanks to high secondary ionisation (used for triggering),
- avalanche mode: register the charge of electrons and ions in the avalanche (used in timing RPCs).

The typical gas mixture is 85 % of $C_2H_2F_4$, 10 % of SF_6, and 5 % of iso $- C_4H_{10}$. Each gas has some purpose: in $C_2H_2F_4$ the electron avalanche is well propagated, SF_6 extend the so-called streamer-free zone, and iso $- C_4H_{10}$ is UV quencher.

To improve the properties of RPC detectors, a multigap design was developed. Between two metal electrodes with a large electric potential difference is placed the glass plate as an electrically floating electrode. Improvement is in detection efficiency

$$\varepsilon_N = 1 - (1 - \varepsilon_1)^N\,, \tag{2.7}$$

where ε_i is the detection efficiency of RPC with i gas gaps and N is the number of gaps. In addition, the time resolution σ is improved

$$\sigma_N = \frac{\sigma_1}{\sqrt{N}}. \tag{2.8}$$

The RPCs used in the HADES setup have 4 gas gaps (that are very thin - 270 μm) divided by 2 glass and 3 aluminium electrodes, all with a thickness of 2 mm, see figure 2.13. The gas mixture used is a little different (90 % of $C_2H_2F_4$ and 10 % of SF_6). The nominal high voltage on the aluminium electrode is 5.5 kV. This detector covers an area of 8 m^2 in polar angle $12° < \theta < 45°$ and almost full azimuth angle. Due to the high rate and multiplicity of detected particles (up to 1 $\mathrm{kHz/cm}^2$) and required detection efficiency and maximal occupancy of one RPC chamber, the detector is divided into 1116 cells. Each of the 6 sectors has 2 layers of cells in 3 columns where each one has 31 cells, see figure 2.14. The experimental time resolution is $\sigma_t = 70$ ps.

2.5.3 Shower detector

Another detector besides RICH with the purpose of distinguishing electrons from fast hadrons is Shower [158]. It covers the region of polar angle $18° < \theta < 45°$ and full azimuth angle (it is also divided into six sectors, and so between them is a small dead area). From the position of the Shower detector, one can deduce that it will detect particles with large momentum, which also means large energy ($E \gg 10$ MeV). Identification of electrons based only on time-of-flight measurement is problematic because of very fast pion contamination. Electrons interacting with

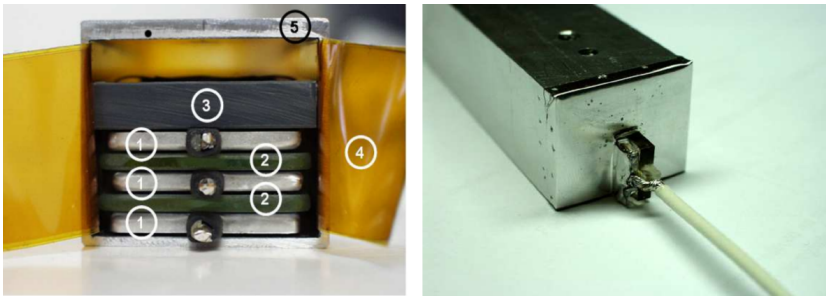

Figure 2.13: Internal layout of one RPC cell. On the left picture: 1 - Al electrodes, 2 - glass electrodes, 3 - pressure plate, 4 - kapton insulation and 5 - Al shielding. Taken from [168].

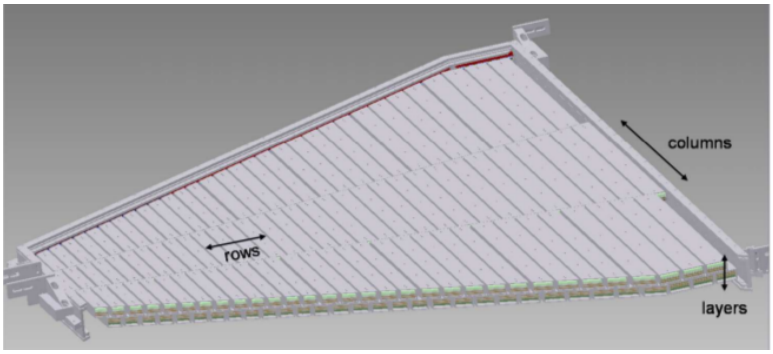

Figure 2.14: Cell distribution of one RPC sector. Taken from [168].

matter at high energy have the highest probability of creating electromagnetic showers (via Bremsstrahlung and photon conversion to e^+e^- pairs, see figure 2.15) that are the detected signatures of electrons. The cross-section of the Shower detector is shown on figure 2.16.

The physics background of electron identification in the Shower detector is based on detecting an electromagnetic shower which is much more probable to develop if electrons pass through than hadrons. They can create hadronic showers, but the chance of such scenario is kept low due to the adjusted thickness of the lead plates (their thickness is 1.2 cm, which corresponds to the radiation length $\frac{X}{X_0} \approx 2$). The prospective hadronic shower is narrower than the electromagnetic shower, which enables the identification of the type of particle passing. Particles passing through the Shower are detected in the wire chambers (two types of wires are included: grounded field wires with 125 μm in diameter and potential wires with high voltage up to 3500 V and thickness of 25 μm) filled with isobutan-based gas mixture. These chambers are operated in the so-called self-quenching streamer mode, which has the advantage that the collected charge is independent of specific particle losses, although the charge is correlated with the number of particles passing through the chamber. To achieve good granularity, the read-out plane is divided into 942 pads whose area is chosen so the geometrical acceptance of pads is the same with respect to the target position. The electron recognition algorithm then just compares the multiplicity of one hitted pad plus eight surrounding ones in the prechamber with its corresponding nine pads in the post1 and post2 chambers. In case of a rising number of hits (according to the function that was determined from simulations), the particle is identified as an electron.

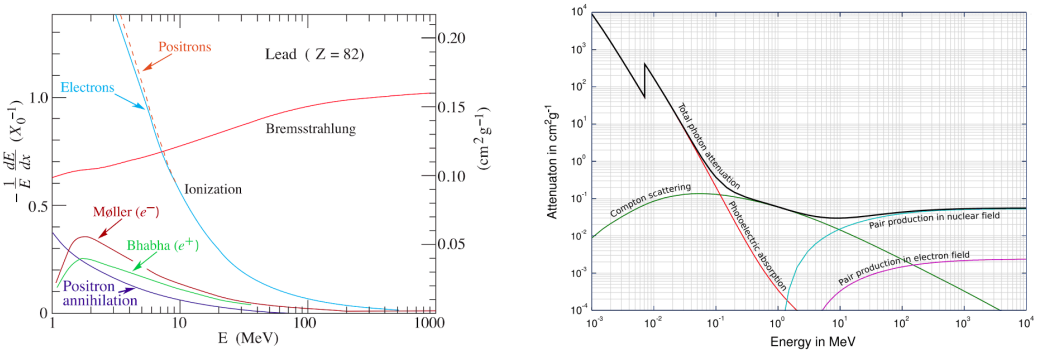

Figure 2.15: Cross sections of different interactions of electrons and photons with matter. Taken from [12] and https://www.nuclear-power.net/nuclear-power/reactor-physics/interaction-radiation-matter/interaction-gamma-radiation-matter/ .

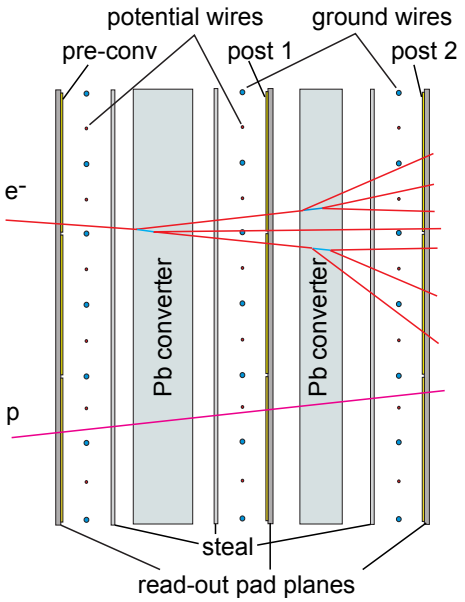

Figure 2.16: Cross-section of Shower detector. Taken from [162].

Electromagnetic calorimeter upgrade

To extend the HADES detection capability to real photon detection, the ageing Shower detector was replaced by an Electromagnetic calorimeter (ECAL). The layout of the ECAL is shown on the left side of figure 2.17. Each sector is equipped with 163 modules, and their internal structure is displayed on the right side of figure 2.17. Most of the module space is taken by the lead glass with radiation length $X_0 = 2.51\,\text{cm}$, Moliére radius 3.6 cm, and dimensions $92 \times 92 \times 420\,\text{mm}^3$ which is wrapped by TYVEK paper to enhance the light reflection [169]. As a photon detector the photomultiplier tubes are used (the aim is to use in all modules Hamamatsu R6091, but currently there are two sectors with older EMI 9903KB with slightly worse energy resolution than Hamamatsu PMTs). Due to the enormous weight of the lead glass (one module weighs over 15 kg) compared to the rest of the HADES spectrometer, a special support construction was installed in the cave. The planned energy resolution of $\frac{\sigma_E}{E} = \frac{5\,\%}{\sqrt{E\,[\text{GeV}]}}$ is believed to be achievable[8] based on several tests with cosmic muons and photon beam experiments performed at Mainz microtron MAMI [170].

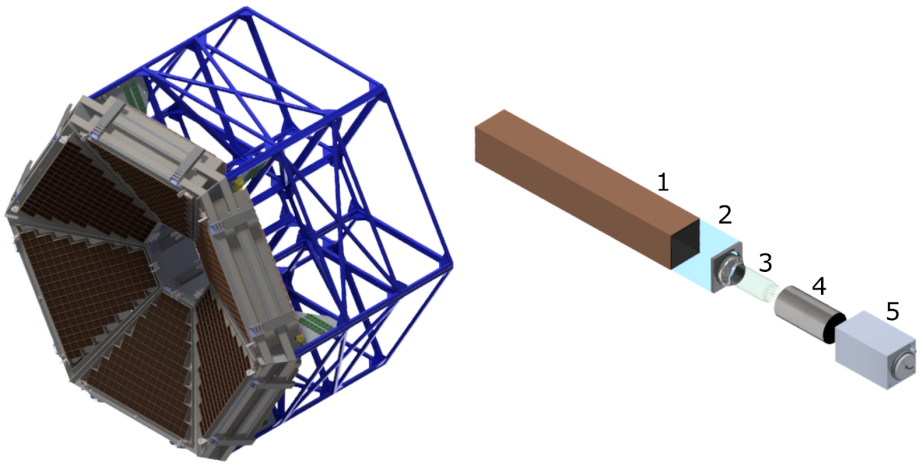

Figure 2.17: ECAL. Taken from [171].

2.6 Forward Wall

The Forward hodoscope Wall (FW) is used during the experiments with heavy ions and its position is 7 m behind the target, so it covers the polar angle $0.33° < \theta < 7.17°$. It is made from plastic scintillators divided into 140 small cells ($4 \times 4\,\text{cm}^2$), 64 middle cells ($8 \times 8\,\text{cm}^2$), and 84 big cells ($16 \times 16\,\text{cm}^2$) [172]. Each cell has its own photomultiplier for the signal read out. The granularity is chosen so that the dimension of cells grows with the growing distance from the beam spot, see figure 2.18. This detector measures the orientation of reaction plane in azimuth angle and enables us to study particle flow (because of a large gap in rapidity between FW and the rest of HADES spectrometer, there

[8]Since the lead glass modules were previously used in the OPAL experiment at LEP accelerator at CERN where this energy resolution was achieved only with different photon detector system.

is no issue with autocorrelation between reaction plane angle determination and particle flow measurement). For that, it registers spectator nucleons and fragments emitted from the heavy-ion collision. The experimental time resolution is $\sigma_t = 500\,\text{ps} \Rightarrow \frac{\sigma_p}{p} = 11\,\%$, and the angular resolution $\sigma_\phi \approx 45°$ (however, this is strongly dependent on the collision centrality).

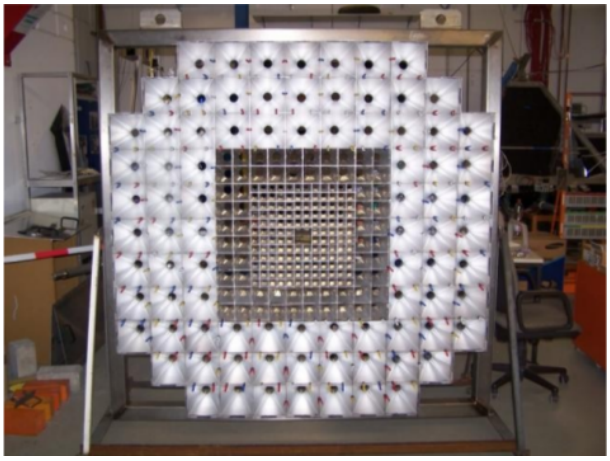

Figure 2.18: The photo of the uncovered Forward Wall. During measurement there is a black foil on the whole detector to reduce the number of photons from the background, and to protect the sensitive photon detectors. Taken from [156].

2.7 Data Acquisition System

Reading out all information from already mentioned detectors is the job of the **D**ata **A**c**Q**uisition system (DAQ). In total, the DAQ must transfer information from 30 000 time-to-digital converters (TDCs) and 50 000 analogue-to-digital converters (ADCs) [173]. Data transfer is asynchronous due to different speed of response and different dead times from the detectors. The DAQ system can handle without problems an event rate of a few tens of kHz (up to peak 50 kHz) and a typical data rate of 300 MB/s. Signals from detectors first go to Front-End Electronics (FEE boards), which usually contain some TDCs and ADCs, the information is then processed in Read-Out boards (in most cases Trigger and Read-Out Boards - TRBs) and through the network infrastructure the data are sent to the Central Trigger System (CTS) or to Slow Control System for online monitoring during data taking or finally to Event Builders (EB) that takes the correct information together and store them on server discs and tapes, see figure 2.19. The correct running of the system is controlled by 550 Field Programmable Gate Arrays (FPGAs), integrated circuits which can be programmed to provide any logical function. The overview of the DAQ system is shown on figure 2.20. The boards connect 7 km of optical cables to cope with this very high event and data rate.

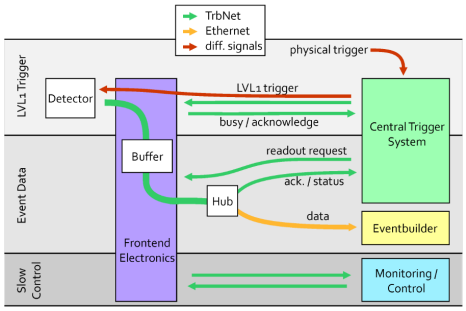

Figure 2.19: Scheme of communication between detector, Central Trigger System, Slow Control Systém, and Event Builders. Taken from [173].

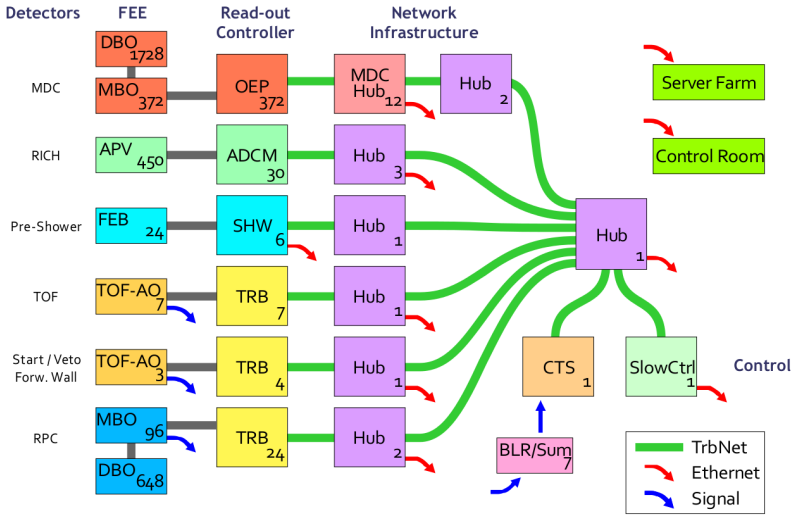

Figure 2.20: DAQ system layout. Taken from [173].

2.8 Calibration of TOF detector

It is usual in HADES collaboration that students participate in so-called Low-Level Analysis before (or during) their involvement in the physics analysis. My duty from the low-level analysis point of view was the calibration of the TOF detector.

Since this detector is not new to the HADES setup, the procedure for calibration is well established. First, some preliminary calibration parameters are prepared during the first days of beam time, particularly the time and position offsets, as well as the scaling constant of the deposited energy for each scintillator rod. Later, one can check if the original set of parameters can be used for the whole beam time or different sets must be prepared for different days due to some instability, e.g., temperature inside the cave tends to rise which affects the sensitive read-out electronics. Important measures that control the rightness of the parameters are the time of flight and energy loss of negative pions (almost all negative tracks) and the difference between the position calculated by (2.4) and the reconstructed position from the tracking algorithm for all tracks, see figure 2.21.

When the stability of calibration is achieved during the whole beam time, one should continue with time-walk correction[9]. This procedure was upgraded by G. Kornakov [174], I carefully applied it on the pion beam data. The scintillator rod are subdivided (only virtually in the analysing macro) into 20 same cells along the longest side of the rod. Within each cell, the correlations of the charge registered by left and by right PMT (which corresponds to time-over-thershold ToT) and time difference between expected time-of-flight for certain particle specie (only tracks with highest quality of recontruction are used) and the time registered by left and right PMT are studied (all combinantions: ΔT_Rvs.Q_R, ΔT_Rvs.Q_L, ΔT_Lvs.Q_R and ΔT_Lvs.Q_L), see figure 2.22. These correlations are then fitted with the following function

$$\langle \Delta T \rangle (Q) = \begin{cases} p_2 + p_0 \exp(p_1 Q) & \text{if } Q < p_8 \\ p_7 + p_3 \exp(p_4 Q) + p_5 Q^{p_6} & \text{if } Q \geq p_8, \end{cases} \tag{2.9}$$

where p_i are fit parameters, Q is the charge (depicted on figure 2.22 as Q2W [ns]). Due to the rather large amount of parameters, a human check of the fit quality is needed (observe the function displayed on top of the data points, see figure 2.23, as well as check on the fit residuals). If the fit is found to be satisfactory, then the fit parameters are saved, otherwise an additional restriction on the limits of individual parameters are set by hand.

[9]Due to the necessity of setting up some threshold value under which any signal is considered just for noise, the real time of particle registration is hidden because of this threshold. Fortunately, from the correlation of the time when signal crosses the threshold and so called time-over-threshold (difference between times of rising edge and trailing edge) one can partialy correct the time measurement.

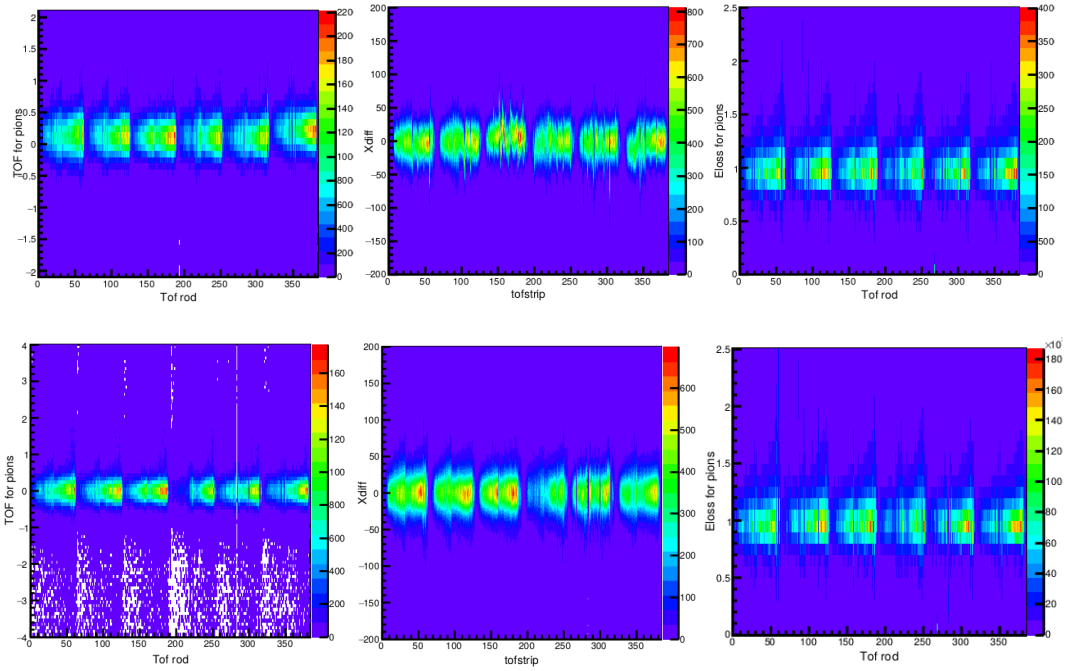

Figure 2.21: The figures in the upper row are before careful calibration was performed, and the figures in the lower row are after this procedure.

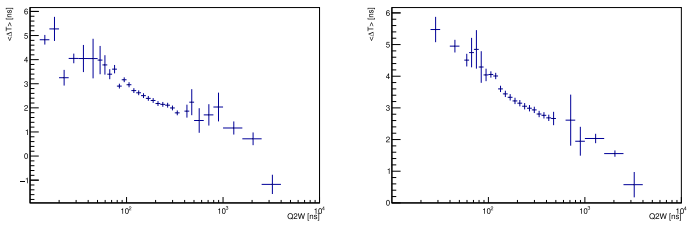

(a) ΔT_Lvs.Q_L (b) ΔT_Rvs.Q_R

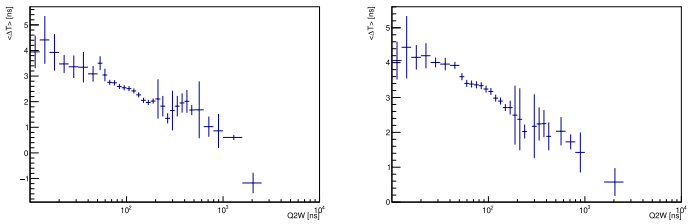

(c) ΔT_Lvs.Q_R (d) ΔT_Rvs.Q_L

Figure 2.22: Mean value and its uncertainty of $\langle \Delta T \rangle$ dependend on the charge (ToT) for one virtual cell inside the TOF scintillator rod.

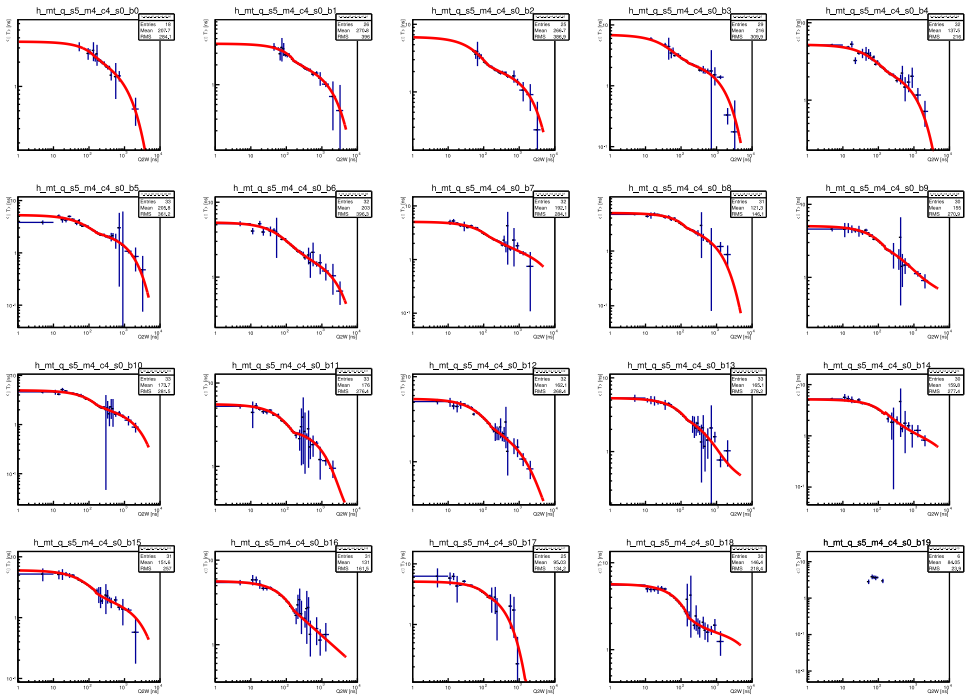

Figure 2.23: Example of checking the goodness of the fits. The last histogram was not fitted due to insufficient statistics.

Chapter 3

Event selection and track reconstruction

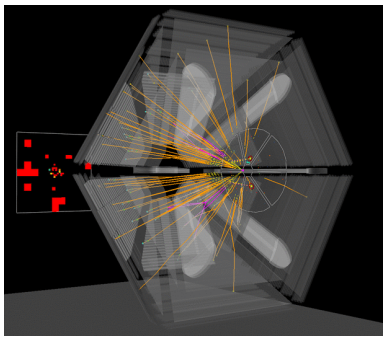

The third chapter of this thesis is dedicated to explaining how the collected data are being processed to obtain useful physical information about the measured particles. First, the overview of the experiment is described in section 3.1, followed by the data cleaning process called event selection 3.2. Since the properties of hot and dense baryonic matter produced in heavy-ion collisions may vary significantly depending on the size of the nuclei overlap, the characteristic called centrality is studied, and its determination is given in section 3.3. Then the construction of objects called particle candidates is detailed in three sections 3.4, 3.5, and 3.6. Afterwards, one can deduce the particle type which passed through the HADES spectrometer using one or both particle identification methods, see section 3.7. Finally, Monte Carlo simulations are described in 3.8 which are used to extrapolate the measurements to uncovered regions and to validate the results.

3.1 Beamtime overview

During two months (April and May) of 2012, the HADES experiment measured for the first time a heavy collision system. This was possible mainly thanks to the upgrade of time-of-flight detector for smaller polar angles (from 18° to 45°) where the original Tofino detector (scintillator based detector splitted into 24 pads with time resolution 400 ps) by RPC detector with more than 1000 cells and much better time resolution, more details are given in section 2.5.2. The colliding nuclei were gold ions. The target was segmented into 15 stripes of 25 μm thick circles with a diameter of 2.2 mm and separated by 4.5 mm. The kinetic energy of beam $^{197}_{79}\mathrm{Au}^{69+}$ gold ions was $E_{\mathrm{beam}} = 1.23\,A\mathrm{GeV}$ and the beam intensity provided by the SIS18 accelerator was $I_{\mathrm{beam}} = (1.2 - 1.5) \times 10^6\,\mathrm{s}^{-1}$.

The read-out trigger was based on the raw charged hit multiplicity in the META wall, i.e., multiplicity in the TOF detector. Most recorded events were triggered by Physical Trigger 3 (PT3), which requires $Mult_{\mathrm{TOF}} > 20$. There were also recorded events with PT2 $Mult_{\mathrm{TOF}} > 5$, but they were not analyzed in this thesis. In addition to that, the so-called minimum bias trigger where a signal from START detector is required only. The events were registered at an average trigger rate of 8 kHz with a duty cycle of 50 % and recorded on tape at a data rate of 200 MByte/s. After 557 hours of data taking, 7.31×10^9 events have been

collected, from which 2.2×10^9 events were marked as good for further physics analysis (removed pile-up, interactions outside the target region, etc.).

3.1.1 Data processing

The data acquisition system was described in detail in section 2.7. The recorded events are written to HLD files with a unique identifier in the form of DT (Data Type), YY (last two digits of the current year), DAY of the year (recorded days 096–126), HHMMSS (time of the day in 24-hours format) and EB (number of event builder that processed corresponding data, range 01–08), for example *be1210819121502.hld*. Due to this unique identification, each file can be related to the actual performance of each subdetector, which is monitored with a slow control system. For successful data analysis, precise calibration of all detector systems is mandatory, using the Oracle system database, several sets of parameters can be defined for different periods of beam time. When the calibration parameters are available, mass production of Data Summary Tapes (DST) files is executed using the HYDRA framework[1] [175]. In the case of the discussed beam time, the total disk space used by DST files is above 140 TByte. Inside these files one can already find the fully reconstructed track candidates with all relevant physics observables.

During the data taking, online event analysis is performed to monitor the quality (QA[2]) and if some major discrepancies are observed from the expected detector behaviour, the shift crew should take the appropriate steps. Significant drops in high voltage were observed in the drift chambers of sector 2 ($240° \leq \phi \leq 300°$) during almost the whole beam time. To guarantee a high-quality data set with stable detector performance, a careful scan of all files was performed, and a list of well-functional sectors was made. If two maliciously working sectors were found, sector 2 and any additional one, this file was excluded from the analysis.

3.2 Event selection

If one wants to provide the highest quality measurements, the first thing to do is clean up the data sample. It was already mentioned above that only files with stable spectrometer performance are taken into account, in the next step the cleaning at the individual event level is needed. There are several sources which might be able to compromise our analysis, the main ones are pile-up events and interactions with other materials than gold target. The pile-up events occur when more than one beam particle interacts with material at the target region within the time window of data acquisition, see figure 3.1. Therefore, one cannot distinguish which particles are coming from which reaction and the time measurement of these produced particles is therefore wrong, i.e., the particle species would not

[1] HYDRA stands for **H**ades s**Y**stem for **D**ata **R**eduction and **A**nalysis. This analysis software developed under ROOT framework is used for the so-called unpacking of the raw data and the digitization of simulated response, more details on simulation can be found in section 3.8. After this first step, the track, ring, and META-hit finding algorithms are used to determine the response of individual detectors, followed by the matching procedure to obtain full information of whole tracks, which are latter called particle candidates.

[2] Quality Assessment

be correctly determined. The second main source of undesirable events is a collision of accelerated ions with other materials than gold plates, e.g., carbon target holder, kapton foils holding the gold plates, or event START detector. For event selection, we use the following criteria which results in a decrease of the number of events used for further analysis (see figure 3.2):

- To ensure that a time-of-flight measurement is started, at least one hit is made in one of the two START detector modules (*selectStart*).
- To minimize the probability of pile-up events, a condition (*StartPileUp*) that only one hit cluster of the START detector (correlated hits in two modules) is registered inside the time window $-5\,\text{ns} < t_0 < 15\,\text{ns}$.
- If there would be a particle registered in VETO detector 15 ns around the START time, the event is refused based on *NoVeto* flag because it is very probable that the beam particle did not interact with the target.
- If a second START hit without correlated VETO hit is detected after the triggered START time t_0 between times 15 ns and 350 ns, the event is excluded (*GoodVetoStart*).
- There are two criteria for a reconstructed event vertex, which is expected to be in the region of $-65\,\text{mm} < z < 0\,\text{mm}$ and $\sqrt{(x-x_0)^2+(y-y_0)^2} < 4\,\text{mm}$ in the laboratory coordinate system, namely *GoodCandVertex* and *GoodClusterVertex*. The first one requires that at least two reconstructed particle candidates are coming from this vertex, the second at least one reconstructed track from MDC is connected to the vertex.
- Finally, the condition of the second START hit that has correlated hits in META detector and arrives in the time window from 80 ns to 350 ns after t_0 can discard an event (*GoodStartMeta*). Although the time-of-flight measurement would not be corrupted because at all these times META hits would result in nonphysical particles, the multiplicity measurement is influenced, and therefore also the centrality determination would not be correct (as will be explained later).

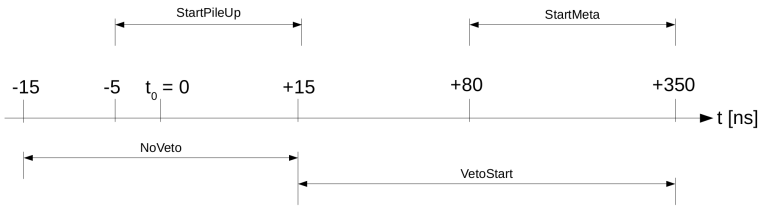

Figure 3.1: Overview of time windows used for event selection criteria.

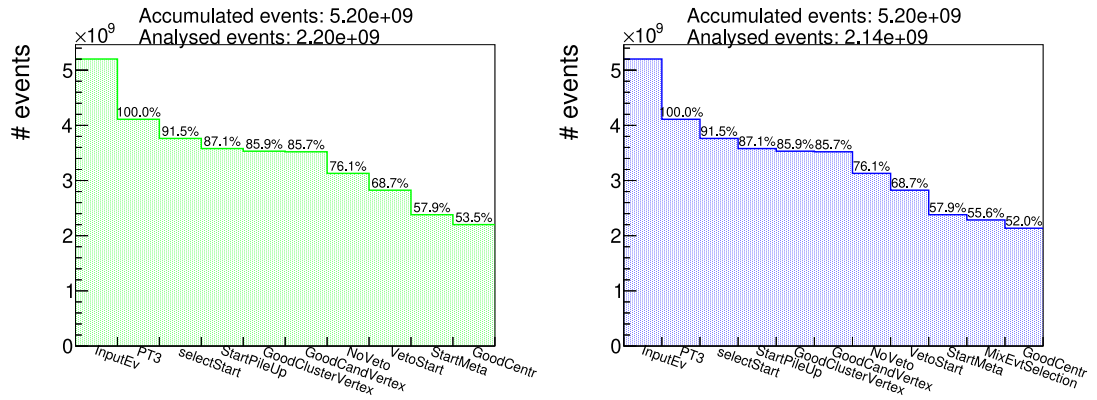

(a) (b)

Figure 3.2: Histogram showing the number of events accepted after each step of event selection. This is already after the cleaning procedure of DST-files in which less than 5 sectors were stably operating. In figure (a) is shown the selection for the analysis of charged kaons and in (b) for the neutral kaons, respectively.

3.3 Centrality determination

Many of the physical observables of HIC depend on the centrality of the collision. In the experiments, there are usually defined centrality classes which correspond to a certain interval of impact parameter b (a transverse distance of the centers of colliding nuclei). A detailed description of how centrality determination is realized in the case of the HADES Au + Au experiment can be found in [176], therefore only a brief summary would be included here. Since direct observation of the impact parameter is impossible due to the high inelasticity of HIC at relativistic energies, indirect observables like the number of participating nucleons in the reaction N_{part} are linked to b via the Glauber model [18, 177]. Based on Glauber Monte Carlo simulations, one can calculate the averaged number of charged particles N_{ch} (which would in experiment transform to the number of TOF and RPC hits $N_{\mathrm{hits}}^{\mathrm{TOF+RPC}}$), additionally to allow event-by-event fluctuation around the averaged number of charged particles per participant nucleon is sampled by negative binomial probability distribution with mean value μ and dispersion parameter k thus we get $\langle N_{\mathrm{ch}} \rangle = \mu \langle N_{\mathrm{part}} \rangle$[3]. To take into account the non-linear response of the detector, the obtained distribution is further folded with a phenomenological efficiency function $\varepsilon(\alpha) = 1 - \alpha \cdot N_{\mathrm{part}}^2$. The simulated spectra are then compared to the measured one, and the intervals of $N_{\mathrm{TOF+RPC}}$ for centrality classes are introduced, see figure 3.3 and summary table 3.1.

[3]The number of TOF and RPC its needs to be fitted separately and the resulting values of parameters are: $\mu_{\mathrm{TOF}} = 0.20$, $k_{\mathrm{TOF}} = 6.36$, $\mu_{\mathrm{RPC}} = 0.50$, $k_{\mathrm{RPC}} = 29.06$ and $\alpha_{\mathrm{TOF}} = \alpha_{\mathrm{RPC}} = 1.64 \times 10^{-6}$

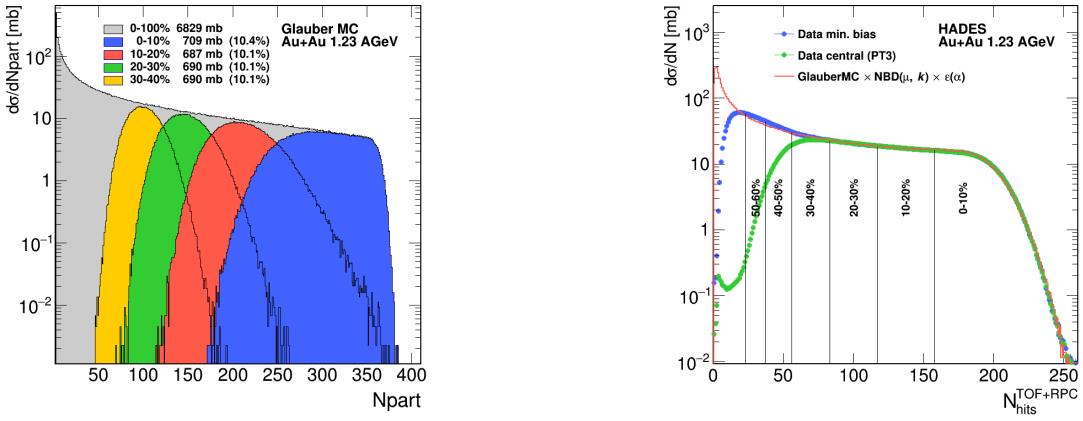

(a) (b)

Figure 3.3: (a) Number of participant nucleons in Au + Au collision at kinetic energy 1.23 AGeV as described by the Glauber Monte Carlo model with colored distributions representing four most central 10% classes. (b) Differential cross-section as a function of $N_{\text{hits}}^{\text{TOF+RPC}}$. Comparison between minimum bias (blue), PT3 trigger (green), and weighted simulated Glauber model spectra is shown. Figures taken from [176].

Centrality [%]	b_{max}[fm]	$\langle b \rangle$[fm]	$\langle N_{\text{part}} \rangle$	$N_{\text{min}}^{\text{TOF+RPC}}$	$N_{\text{max}}^{\text{TOF+RPC}}$
0 – 10	4.70	3.14	303.0	157	312
10 – 20	6.60	5.70	213.1	117	156
20 – 30	8.10	7.38	149.8	82	116
30 – 40	9.30	8.71	103.1	55	81

Table 3.1: Centrality classes and the corresponding values of the maximal impact parameter, mean value of the impact parameter, mean value of the number of participating nucleons, and the range for the number of hits in TOF and RPC. Values taken from [176].

3.4 Track reconstruction

The tracking algorithm used for charged particles that pass through HADES spectrometer is rather complex and complicated, and thus only a short introduction will be given here. A nice overview of the algorithm is displayed in figure 3.4. We will try to outline the individual steps below. The underlying physical principle of particle detection is the ionization of gas inside MDC chambers (see section 2.4.2). After the drifting electrons are registered on the sense wire, we call it the fired wire.

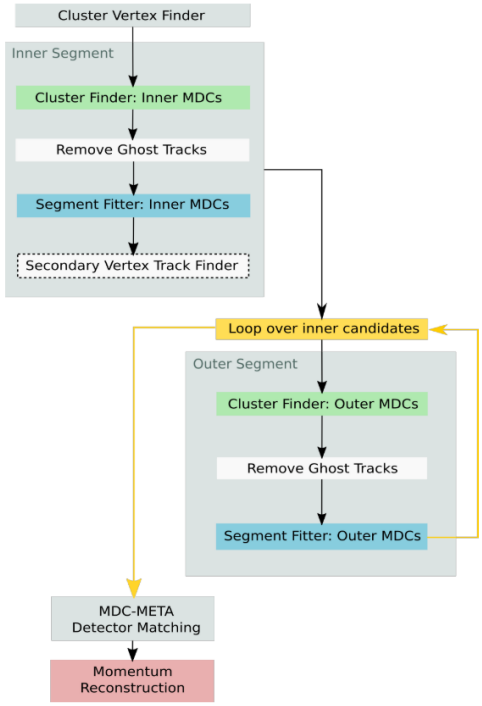

Figure 3.4: Flow chart of track reconstruction with individual steps specified in the text. Figure taken from [178].

The starting point is to determine inside which segment of the gold target the interaction most likely occurred. For that purpose, the Cluster Vertex Finder is called, and the fired wires are projected to each target segment and the one with the best projection resolution is further used as a reaction vertex. To find the position of the tracks, we define common planes (one for two inner MDCs and one for two outer MDCs), and all fired wires from both chambers are projected to that plane. Then we can observe a local maxima on the crossing of the fired wires where the particle went through (there are together 12 planes in two chambers and therefore the value of the crossing might be up to 12 to call the maxima a true cluster when a certain threshold is reached, usually > 9). To define the inner segment of the track, we use these true clusters and the reaction vertices, which are connected by a straight line since there is no magnetic field between the MDC I and II. This line is prolonged to the so-called kick plane, see figure 3.5, which is located in the region of maximum magnetic field. The intersection is then used as a starting point of a line that goes through the true clusters of the second common plane between the MDC III and IV. However, the number of

wrongly fired wires due to the noise and questionable cluster assignment can be very significant (about 50 %), and removal of such false segments (ghost tracks) is necessary. Luckily, they can be identified because of the smaller average number in fired wires of the cluster and the smaller number of unique fired wires. Still, there is an important improvement, the usage of the measured drift time. This significantly reduces the size of the projection on the common plane and therefore improves the determination of track position (the track segments are fitted to the drift cells).

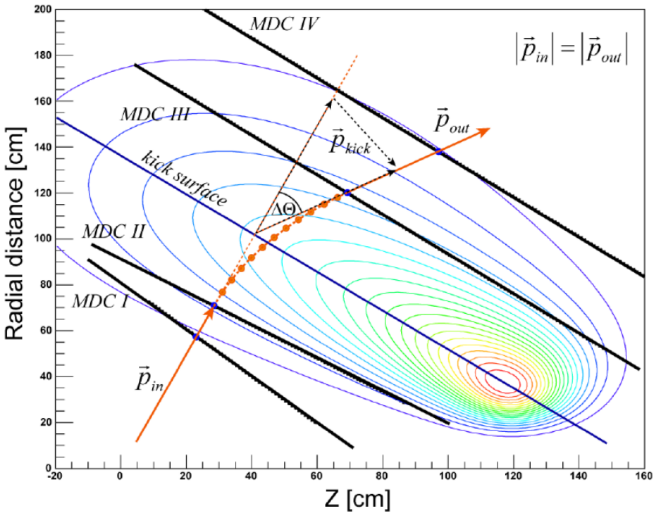

Figure 3.5: Example of a track in the HADES magnetic field with kick plane and cubic spline momentum determination methods. Figure taken from [158].

A fairly new feature of the tracking algorithm is the secondary vertex track finder. In this procedure, the tracking algorithm takes a look at the fired wires that are not used in the fitted inner segments, selects a good quality two-wire crossing (one from MDC I and the second from MDC II), connects them with a line, and tries to find other fired wires around this line. If at least 7 such wires are found, then the connected line is fitted to the drift cell as described above, and such a segment is added to the list of reconstructed inner segments with a special off-vertex flag. This procedure increases the number of reconstructed weakly decaying particles like K^0_S by more than 10 %.

3.5 Momentum determination

Charged particle trajectories are bent in the magnetic field due to the effect of the Lorentz force

$$\vec{F}_L = q(\vec{v} \times \vec{B}), \tag{3.1}$$

where q is the charge of the particle with velocity $\vec{v}$ and $\vec{B}$ is the magnetic flux density of the field. The integrated effect of the magnetic field along the entire path is the total momentum deflection which we might express using (3.1)

$$\Delta\vec{p} = \vec{p}_{\text{out}} - \vec{p}_{\text{in}} = \int_{\vec{p}_{\text{in}}}^{\vec{p}_{\text{out}}} \mathrm{d}\vec{p} = \int_{t_0}^{t_1} \vec{F}_L \mathrm{d}t = -q \int_{\text{path}} \vec{B} \times \mathrm{d}\vec{s}. \tag{3.2}$$

As one can see from figure 3.5, this integration can be substituted by a virtual single kick on the particle trajectory, making the virtual particle change its polar angle by $\Delta\theta$ connected to the momentum deflection $\sin\frac{\Delta\theta}{2} = \frac{\Delta\vec{p}}{2p}$ where $p = |\vec{p}_{\text{in}}| = |\vec{p}_{\text{out}}|$.

The momentum determination is achieved using the so-called Runge-Kutta method, which is a technique used to obtain an approximate numerical solution of differential equations (in this case the equation of motion). As input, this method takes the momentum value calculated by the spline method (in short, this method solves the equation of motion at several points between MDC II and III and connects these with splines, but still assumes a straight track between MDC I and II, respectively, between MDC III and IV), x and y coordinate at $z = 0$ and two cosines for initial direction. These are iteratively optimized to fit the measured spatial points with MDCs. The resulting momentum p and initial direction are stored in DST files together with a specific χ^2_{RK} value (the sum of squared differences between RK fit and the actual position of MDC hits weighted with errors of the positions - these are in some cases rather small causing large χ^2) which is later used as the track quality criterion. More details can be found in [158].

3.6 META matching

By extrapolation of the outer segments to the META detector, we get an idealized position of the META hit, see figure 3.6. Matching to a fired META hit is done based on the difference in the y-direction (which is preferred over x due to the natural geometry of META cells), where the maximal difference is a momentum-dependent value up to 4 mm for high-momentum tracks. The quality of this matching is defined as $\chi^2_{\text{MM}} = \frac{\delta x}{\sigma_x}$, where δx is the difference between the extrapolation of the Runge-Kutta track and the fired META hit. At the DST level, all combinations of tracks and META hits within $\chi^2_{\text{MM}} < 5$ are stored.

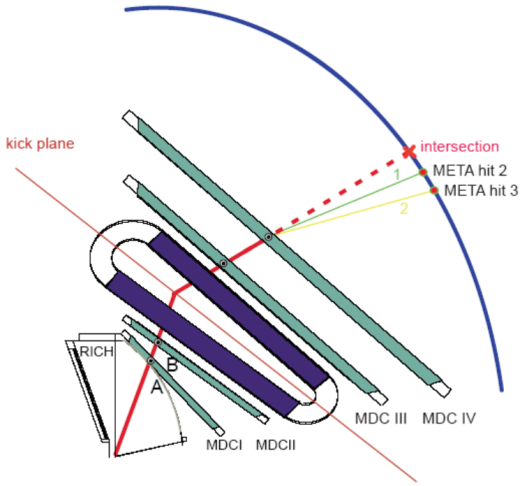

Figure 3.6: Sketch of META matching. Figure taken from [161].

3.7 Particle identification

The next step towards physics analysis of particle candidates is creating the track candidates. The track candidates are made from the Runge-Kutta track and matched META hits, but due to the great number of such combinations (especially in case of central collisions) very generous criteria have to be fulfilled:

- META hits must correspond to time-of-flight below 60 ns,
- the momentum reconstruction must give a value greater than zero,
- both χ^2 of the inner segment and complete RK are smaller than 1000,
- matching of META hit must give χ^2 smaller than 3.

After this rough cleaning, combinations of inner track segments with outer segments and META hits are generated, allowing the sharing of all three components according to the following rules:

- one inner segment can be followed by one or more outer segments,
- one or more outer segments may be matched with one or more META hits.

The sharing of track segments and META hits of the produced track candidates clearly depends on the centrality of the collision. For peripheral collisions ($30 - 40\,\%$), the level of sharing of track segment is around $10\,\%$ and the sharing of META hit at $5\,\%$, in case of central collisions ($0 - 10\,\%$), these levels go up to $30\,\%$ for the sharing of inner segment, $20\,\%$ for the outer segment, and $25\,\%$ for META hit sharing, more details in [179]. However, for physics analysis it is needed that only unique tracks, i.e., without any sharing, are used. Thus, a second cleaning procedure is needed where the tracks that share any item are sorted with respect to the lowest χ^2_{RK} and only the best track is saved to the `HParticleCand` container which is the starting point of physics analysis. Any user can define its own sorting criteria, but the quality of Runge-Kutta track is used in this thesis.

3.7.1 Charged particle identification

Long-lived[4] charged particles are being identified either by time-of-flight and momentum measurements or via specific energy losses.

Identification based on time-of-flight and momentum measurement

Thanks to the Runge-Kutta track fitting, we have a good understanding of the length of the particle trajectory s and its direction of bending in the magnetic field. During the Au + Au experiment, the magnetic field forced the positive

[4]With respect to the size of HADES spectrometer where the usual path length is below 2.5 m and therefore the life-time of light mesons $(c\tau)_{\pi^\pm} = 7.8\,\mathrm{m}$ and $(c\tau)_{\mathrm{K}^\pm} = 3.7\,\mathrm{m}$ [12] is enough for them to be registered. Beside these stable particles like protons, electrons and light fragments of HIC are registered with HADES. Other particles must be reconstructed using their decay products, e.g. mesons π^0, $\mathrm{K}^0_{\mathrm{S}}$, η, ρ; baryon resonances and hyperons.

particles to bend in and negative out of the direction of the beam axis. Joined with the time-of-flight $\Delta t = t_1 - t_0$, using START time t_0 and META hit time t_1, this provides us information about the velocity of the particle

$$\beta = \frac{v}{c} = \frac{s}{c\Delta t}. \tag{3.3}$$

Moreover, using the Runge-Kutta method, the momentum of the particle is reconstructed and using the relation $p = m\beta\gamma c$, where $\gamma = 1/\sqrt{1-\beta^2}$ denotes Lorentz factor, we can calculate the mass of the particle which is the unique property we are after. However, the uncertainty of time-of-flight measurement might result in nonphysical $\beta > 1$ and the latter relation would give us imaginary masses. To avoid this unpleasant situation, a square of the mass is used. Additionally, to distinguish between positive and negative particles, the charge in multiples of the positron charge $q = \frac{Q}{e}$ is added as follows:

$$m^2 \frac{1}{q} = \frac{p^2}{\beta^2\gamma^2 c^2} \frac{1}{q}. \tag{3.4}$$

The measured particle's velocity versus momentum divided by its charge is displayed on figure 3.7. Due to the difference in time resolution, the TOF and RPC detectors are shown separately. The corresponding mass spectrum is plotted on figure 3.8.

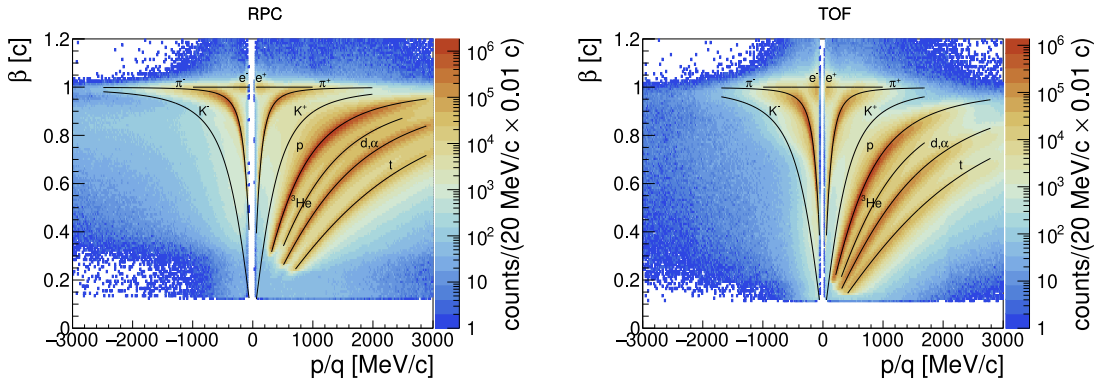

Figure 3.7: Measured correlations of velocity and momenta scaled by particle's charge in Au + Au collisions at $E_{\text{kin}} = 1.23A\,\text{GeV}$, using RPC and TOF detector for time-of-flight measurement on the left and right side, respectively.

Identification via specific energy loss

The second method used for charge particle identification uses the specific energy loss per unit path length in MDC and TOF detectors. The mean energy loss per unit path length is prescribed by the Bethe equation[5] [12]

$$-\left\langle \frac{\mathrm{d}E}{\mathrm{d}x} \right\rangle = Kz^2 \frac{Z}{A} \frac{1}{\beta^2} \left[\frac{1}{2} \ln \frac{2m_e c^2 \beta^2 \gamma^2 T_{\max}}{I^2} - \beta^2 - \frac{\delta(\beta\gamma)}{2} \right], \tag{3.5}$$

[5]In some literature other designation might be found, e.g. Bethe's stopping power formula, Bethe-Bloch formula (Bloch indeed contributed, but he found second order corrections proportional to z^4, first order correction proportional to z^3 are called Barkas-Andersen-effect).

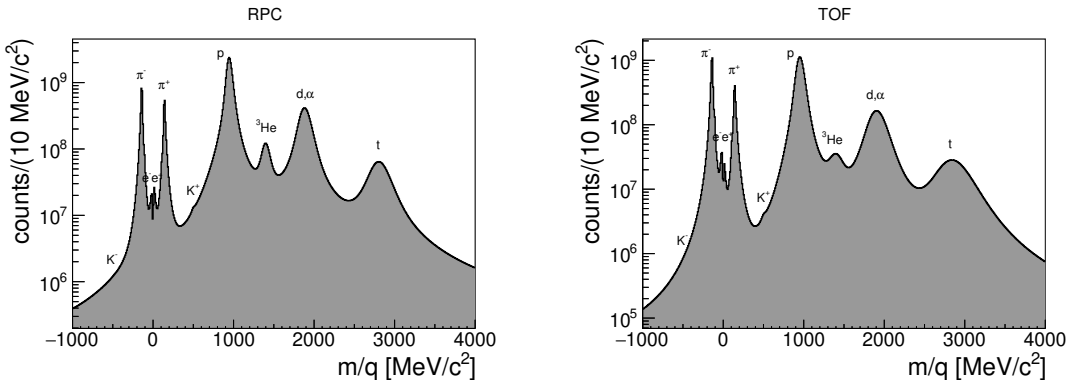

Figure 3.8: Measured spectrum of the particle's mass scaled by its charge in Au + Au collisions at $E_{\mathrm{kin}} = 1.23A\,\mathrm{GeV}$, using RPC and TOF detector for time-of-flight measurement on the left and right side, respectively.

where the coefficient $K = 4\pi N_A r_e^2 m_e c^2 = 0.307\,\mathrm{mol}^{-1}\mathrm{cm}^2$ (classical electron radius $r_e = \frac{e^2}{4\pi\epsilon_0 m_e c^2} = 2.818\,\mathrm{fm}$, electron rest mass $m_e c^2 = 0.511\,\mathrm{MeV}$, Avogadro's number $N_A = 6.022 \times 10^{23}\,\mathrm{mol}^{-1}$), z is particle charge number, Z and A are atomic number respectively mass of absorber, I mean excitation energy in eV, $\delta(\beta\gamma)$ is density effect correction and finaly $T_{\mathrm{max}} = \frac{2m_e c^2\beta^2\gamma^2}{1+2\gamma m_e/M+(m_e/M)^2}$ is maximum energy trasnfer in a single collision for particle with mass M. This equation is valid with an excellent accuracy of a few % for $0.1 \leq \beta\gamma \leq 1000$ for intermediate Z materials. Below this limit, the particle velocity would be similar to the electron velocity bound in atoms, and above it the radiative effects become significant. For the range of momenta accepted by the HADES spectrometer and the masses of charged particles created in HIC at SIS18 energy, the Bethe equation gives proper predictions as can be seen from figures 3.9 and 3.10, where the measured energy losses within MDC and TOF from the experiment are compared with the model predictions from the Bethe equation.

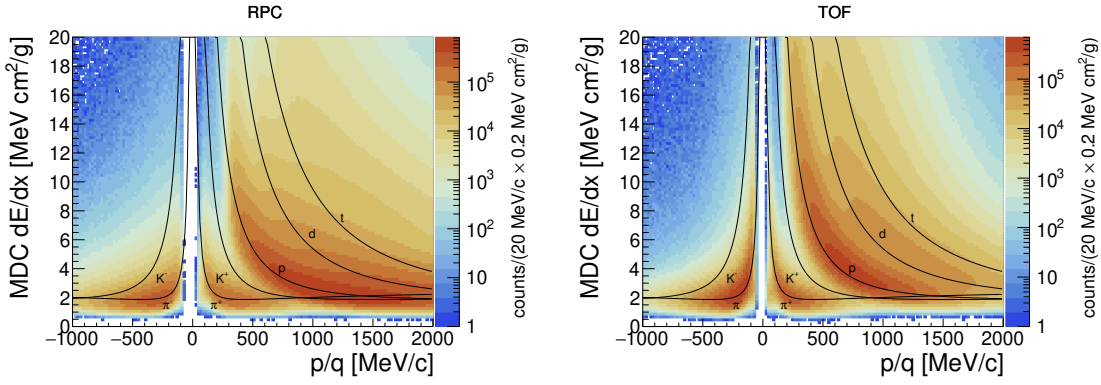

Figure 3.9: Measured correlations of energy losses within the MDC detector and momenta scaled by particle charge in Au + Au collisions at $E_{\mathrm{kin}} = 1.23A\,\mathrm{GeV}$, for particles registered with the RPC and TOF detector on the left and right sides, respectively.

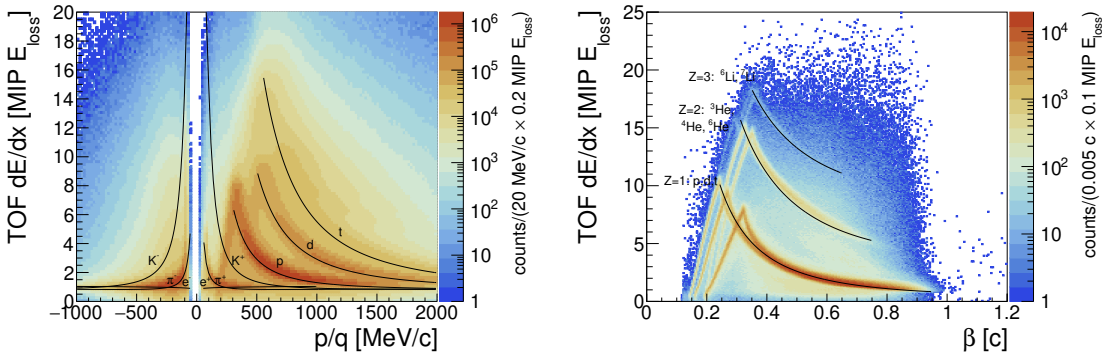

(a) (b)

Figure 3.10: (a) Measured correlations of energy losses within the TOF detector and momenta scaled by particle charge. (b) Measured correlations of energy losses within the TOF detector and velocity. The visible decrease in energy losses for small velocity is due to stopping of the particle within the scintillator material.

3.7.2 Decaying particle identification

In the past, the HADES capability to reconstruct decayed particles from its charged products is being extended to real photons and partially neutrons due to the ongoing upgrades of the spectrometer, like the inclusion of ECAL, more details were presented in section 2.5.3. However, during the Au + Au campaign, only charged particles from the decay could be reconstructed.

When the daughter particles are identified, they can be combined, and using the four-momentum algebra, the invariant mass of the mother particle might be calculated (for simplicity, we will present here only the case of two particles which is also the analysed case of K^0_S in this thesis). The nominal masses m_i of the daughter particle species, taken from [12], are assigned to the reconstructed and identified tracks and together with their momentum $\vec{p}_i$ from Runge-Kutta method gives us the desired invariant mass

$$\begin{aligned} M^2_{\text{inv}} &= (P_1 + P_2)^2 \\ &= (E_1 + E_2)^2 - |\vec{p}_1 + \vec{p}_2|^2 \\ &= E_1^2 - p_1^2 + E_2^2 - p_2^2 + 2E_1E_2 - 2\vec{p}_1 \cdot \vec{p}_2 \\ &= m_1^2 + m_2^2 + 2\sqrt{m_1^2 + p_1^2}\sqrt{m_2^2 + p_2^2} - 2p_1p_2 \cos\Delta\omega_{12}, \end{aligned}$$

where $\Delta\omega_{12}$ is the opening angle between the daughter particle tracks.

Background

There are usually many possible combinations of the charged decay products (in the case of $K^0_S \to \pi^+\pi^-$ coming from Au + Au collisions at $\sqrt{s_{NN}} = 2.42\,\text{GeV}$ on average there are 7 π^- and 4 π^+ [180], i.e. 28 combinations) resulting in the so-called combinatorial background. In the spectrum of invariant mass, there are four sources [181]:

Signal selected tracks come from one decay of the particle of our interest, their invariant mass would be around the nominal mass of the mother (smearing

due to finite spectrometer resolution and width of the decayed particle is expected).

Uncorrelated background selected tracks do not have a common mother particle, therefore, their invariant mass is defined by the phase space and the HADES acceptance.

Correlated background selected tracks originate from one decay but not the particle that we intend to study (e.g., Λ or $\Delta^0(1232) \to p\pi^-$).

Misidentification one of the selected tracks was misidentified, e.g., in reality it was a proton but due to incorrect META matching was labeled as π^+.

The challenge of a perfect description of the background is of utter importance, because if it is successful, then the pure signal would be left and the precise results of physics analysis would be obtained. A powerful method for background estimation is the **Mixed-Event technique**. As the title suggests, it combines the daughter particles of one kind from one event with the daughter particles of a second kind from another event. This approach ensures that the combination would give us uncorrelated pairs and if certain conditions are met, like both events are from the same class of events, therefore the kinematic properties should be similar, a good approximation[6] of the same event, the uncorrelated background is retrieved. Afterwards, the disentanglement of the signal from the correlated background might be required, for which purpose model predictions are helpful. A big advantage is the high statistics of mixed-event spectra, thus, no significant additional uncertainty is introduced by its subtraction.

Machine Learning

With the rise of computational power and the corresponding rise of data storage possibilities, the influence of artificial intelligence or machine learning (a very comprehensive textbook on machine learning [182]), respectively, is increasingly visible in many fields of human activity[7]. There are in general three types of machine learning, see figure 3.11:

Supervised learning algorithm is trained on human-labeled data, i.e., the result is known, and during training, the algorithm optimises the inner parameters to get the required result.

[6] Only normalization of the mixed-event spectrum to same-event spectrum is usually needed because the number of combinations in case of mixed-event overcome the number of combinations from same-event.

[7] One of these areas is board games where the evaluation is quite simple and well defined. Until very recently, the game of Go was seen as a major challenge for the machine to master since the human intuition plays a significant role in the decision making process about the next moves. Contrary to expectation of the Go community, the match between AlphaGo and Lee Sedol in 2016 end up with human defeat 4 to 1. This program was first supervised learnt on human vs. human games of Go masters and later the reinforcement learning process of self-playing was used to boost the performance. Later the same group of scientists developed an even stronger algorithm called AlphaGo Zero which was introduced only with the rules of the game and learned the game purely on self-playing [183] which beat AlphaGo in all 100 games.

Unsupervised learning there is no human input and the algorithm only groups the inputs based on similarity, e.g., as an output the user gets sets of pictures in which the program identifies dogs, cats, cars, etc.

Reinforcement learning program is evaluated after some training time and selects the best ones from many results for the next training phase, e.g., the program should navigate the car around some track, but the track is not known to the program in advance.

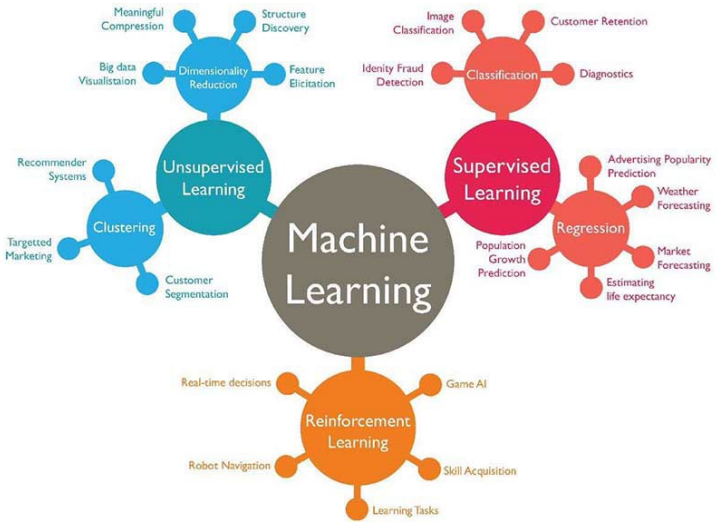

Figure 3.11: Three types of machine learning with examples of usage. Taken from [184]

In nuclear and particle physics, machine learning is also used more frequently nowadays. In the case of the analysis in this thesis, the TMVA [185] toolkit in ROOT [186] framework was used thanks to its simple implementation and many provided options. Supervised learning was performed with simulated K^0_S as pure signal and mixed-event pion pairs as background in both training and testing samples for multilayer perceptron neural network (MLP NN), more details about the particular usage in this thesis will be given in section 3.7.2.

3.8 Simulations

In addition to real experimental data, it is needed to analyse in the same way also Monte Carlo (MC) simulations. The scheme of the entire analysis procedure is shown in figure 3.12. The necessity of MC simulations comes from the inaccessibility of some physical variables in the experiment, e.g., impact parameter (see section 3.3), or the evaluation might be too complicated due to the entanglement between different components of the spectrometer, e.g. detection efficiency (see section 4.4). Both examples mentioned are mandatory for the comparison of experimental measurements with theoretical models. There is also an advantage that during the analysis of simulations one can check the influence of any step on the final observable thanks to the known complete information about the system after the freeze-out.

To achieve a as precise description of the detector in the simulation as possible, a careful alignment of the spectrometer consisting of several steps (photogrammetry, measurement of cosmic rays, and measurement of collisions without magnetic field) is executed before and after each experiment. Knowledge of the materials used in the detectors is also needed, as it is part of the input for any simulation. Finally, the response of the detectors to the passage of different particle species must be understood in detail to mimic the algorithms.

The first steps in the simulation chain, shown in figure 3.12, are the event generators. In the case of the HADES experiment with Au + Au collisions, three generators were used:

Pluto Rather fast MC generator [187] developed under ROOT [186] framework. As it was developed by colleagues from the HADES collaboration, it is very easy to use, however, it is limited to lower energies. The particles are generated according to statistical models from a thermal source with arbitrary angular and momentum distributions.

UrQMD The kinetic transport model UrQMD [79], used in version 3.4, provides a detailed space-time evolution of HIC, which enables a deeper study of some effects, but is also more demanding on the computational time. More details on microscopic models are given in 1.4.

SMASH The recently developed hadronic transport model [95] is nowadays used either for full collision simulation in the case of lower energies ($\sqrt{s} \lesssim 20\,\mathrm{GeV}$) or as a hadronic afterburner for higher energies (where hydrodynamical evolution is essential). In contrast to UrQMD, SMASH is solving the relativistic Boltzmann equation using the test particles (MC approach).

The virtual HADES spectrometer is defined in HGeant, a program based on the Geant 3.21 software package [188]. This version of Geant is written in FORTRAN language because it was developed in CERN before the rise of ROOT data analysis framework fully developed with C++ language. Therefore, HGeant has an interface which enables us to convert Geant output into ROOT file format. All components of the HADES spectrometer have to be defined as a volume of a specific material with well-defined space coordinates. Geant then propagates the particles from the event generators through these materials and the magnetic fields, allowing interactions between the particles and their decays.

The next step is called digitizer and is executed under the HYDRA framework, and it means that the imprints of particles passing through the virtual spectrometer are transformed into measured properties by individual detectors in real experiments. The details of the digitization procedure are nicely elucidated in [167]. Afterwards, the simulation events are processed in the same way as the acquired experimental data, i.e., hits in META detectors, rings in RICH detector, and tracks in MDC are found; the matching of this information is applied to get full tracks also called particle candidates, which are stored in DST-files.

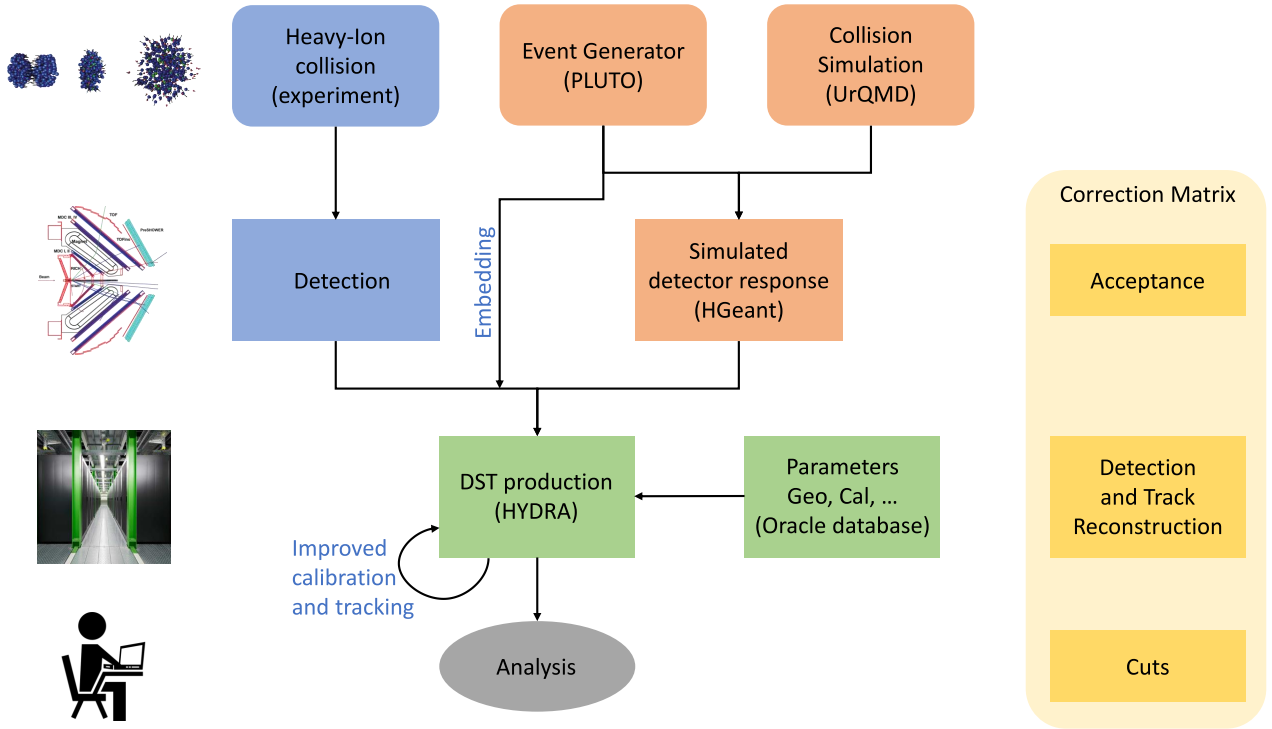

Figure 3.12: Flow chart of the analysis scheme showing individual steps and required tools. At each step, separate parts of the correction matrix are displayed.

Chapter 4

Kaon reconstruction

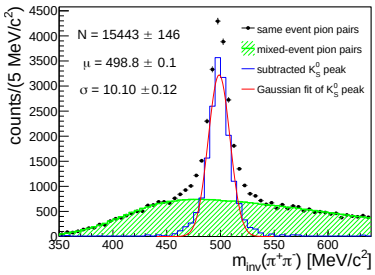

In this chapter, I will focus on the individual steps on how to reconstruct the emitted kaons from gold-gold collisions. In the first part, I will concentrate on charged kaons whose mean lifetime is long enough to reach all parts of the HADES detector. The second part will be dedicated only to K^0_S because the lifetime of its CP symmetry counterpart K^0_L is too long for HADES to register its decay (see table 4.1).

particle	K^+ and K^-	K^0_S	K^0_L
mass m[MeV/c^2]	493.68	497.61	
mean life τ[ns]	12.38	89.5×10^{-3}	51.1
mean life $c\tau$[m]	3.712	2.68×10^{-2}	15.34
main decay channels (BR)	$\mu^\pm\nu_\mu(63.6\%)$ $\pi^0\pi^\pm(20.7\%)$ $\pi^+\pi^-\pi^\pm(5.6\%)$ $\pi^0 e^\pm\nu_e(5.1\%)$ $\pi^0\mu^\pm\nu_\mu(3.4\%)$	$\pi^+\pi^-(69.2\%)$ $\pi^0\pi^0(30.7\%)$ $\pi^+\pi^-\gamma(0.1\%)$	$\pi^\pm e^\mp\nu_e(40.6\%)$ $\pi^\pm\mu^\mp\nu_\mu(27.0\%)$ $3\pi^0(19.5\%)$ $\pi^0\pi^+\pi^-(12.5\%)$

Table 4.1: Table of selected kaon properties. Values taken from [12].

4.1 Charged kaons

Each detected charged particle and its reconstructed track obtain the calculated mass (see section 3.7.1, equation (3.4)). If one would directly take a look at the mass spectra displayed on figure 3.8 and with additional momentum information on figure 4.1, only the most abundant particles like pions, protons, and light nuclei are visible. Since kaons are rarely produced in analysed HICs at subthreshold energy, it is necessary to make additional selection criteria. Due to the fact that charged kaons are sitting on the non-Gaussian tails[1] of surrounding particles (π^- for negatively charged kaons and π^+ and protons for positively charged kaons) it is desirable to apply strong cuts on the track quality parameters χ^2_{RK} and χ^2_{MM}. In addition to that, specific energy losses inside the MDC and TOF are used. A

[1]The origin of these tails is mainly in resolution of momentum and time-of-flight measurement.

lot of details of the cut optimization can be found in [179]. The summary table with the selection criteria used is in table 4.2.

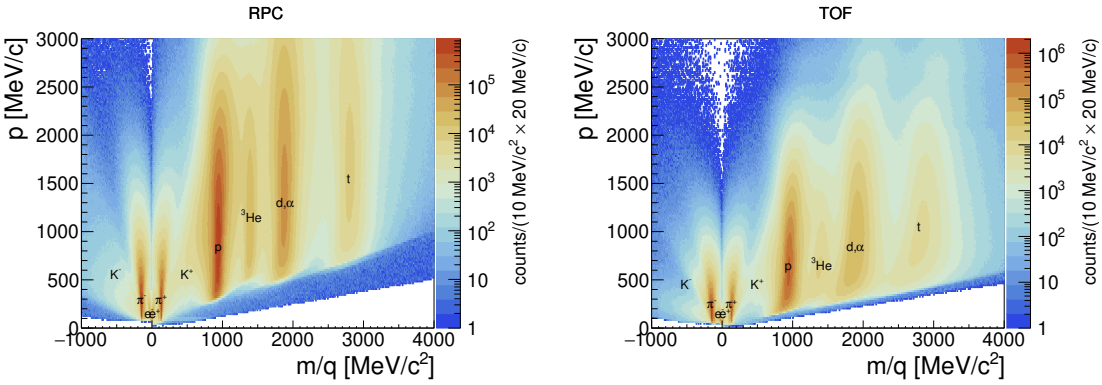

Figure 4.1: Measured correlations of momenta and mass scaled by particle's charge in Au + Au collisions at $E_{\mathrm{kin}} = 1.23A\,\mathrm{GeV}$, using RPC and TOF detector for time-of-flight measurement on the left and right side, respectively.

variable	criteria
χ^2_{RK}	< 100
χ^2_{MM}	< 2
$\mathrm{d}E/\mathrm{d}x$ in MDC	graphical cut
$\mathrm{d}E/\mathrm{d}x$ in TOF	graphical veto cut

Table 4.2: Summary of selection criteria used for charged kaon identification.

4.1.1 Track quality cuts

As was already mentioned, the kaon mass region is highly populated by the tails of the mass spectra of surrounding particles. The two main track quality parameters χ^2_{RK} and χ^2_{MM} available in the analysed data at particle track level are used for the background suppression[2]. The comparison of track quality parameters for different particle species is shown in figure 4.2. One can see that kaons have much larger tails with high χ^2 due to the population of their mass region in the tails as described above. However, due to the problem of simulations not perfectly reproducing the experimental distributions[3] of track quality, we cannot apply too strong cuts because the efficiency corrections of such cuts would have a significant uncertainty. A compromise was selected between the purity of the kaon samples and a good description of the experimental results via simulation was selected: $\chi^2_{\mathrm{RK}} < 100$ and $\chi^2_{\mathrm{MM}} < 2$.

[2]Defined in 3.4: χ^2_{RK} is sum of squared differences of the measured position and Runge-Kutta interpolation, χ^2_{MM} is difference between extrapolated Runge-Kutta track and recorded position by META detector normalized by standard deviation.

[3]We observe a small deviation of the simulation from the experimental data in case of the number of all and selected candidate tracks as well as in the track quality parameter distribution. More details in [179].

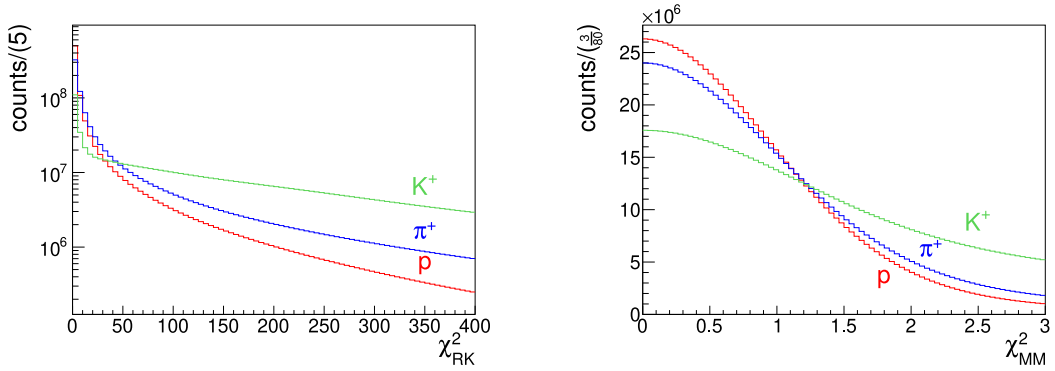

(a) (b)

Figure 4.2: (a) Comparison of tracks χ^2 of Runge-Kutta method for different particle species. (b) Comparison of tracks χ^2 of META match for different particle species. Particle species are distinguished by mass cuts: $m_{\pi^+} \in (50; 300)\,\mathrm{MeV}/c^2$, $m_{\mathrm{K}^+} \in (300; 700)\,\mathrm{MeV}/c^2$, and $m_{\mathrm{p}} \in (700; 1200)\,\mathrm{MeV}/c^2$.

4.1.2 Energy loss in MDC

From the Bethe equation (3.5) and from figure 3.9 we expect the specific kaon energy loss in MDC to be between pion and proton losses in the $\frac{\mathrm{d}E}{\mathrm{d}x}(p)$ representation. However, the resolution of MDC $\frac{\mathrm{d}E}{\mathrm{d}x}$ is not sufficient to obtain the pure kaon signal. Therefore, the cuts are based on simulations with 2σ width around the mean value in one momentum bin. The width was broadened because it was found that the energy losses for easily identified negative pions and protons are wider in real data than in simulations. The cuts were broadened with the averaged ratio as for these other hadrons, see figures 4.3.

4.1.3 Energy loss in TOF

Wrong matching of pion tracks with META hits from proton or some other light nuclei is the cause of the ghost correlation visible in mass-momentum correlation in figure 4.1 which originates at low momentum at pion nominal mass but with increasing momentum the mass is increasing as well. Thanks to the fact that protons and light nuclei have higher energy losses in the material (see figure 3.10), it is possible to cut out the region of high $\frac{\mathrm{d}E}{\mathrm{d}x}$ and velocity β for charge $|Z| = 1$, see figure 4.4. This selection is particularly strong in the case of K^- as one can see in figure 4.5 where the mass distribution after each cut application is shown.

4.1.4 Background subtraction

Even after careful track selection, we can observe significant background contamination in the mass spectra shown in figure 4.5. Its subtraction is a decisive step in the present analysis. In the case of positively charged kaons, there are two sources of contamination (protons and π^+) whose relevance is changing depending on the track momentum vector. For negatively charged kaons, there is only contamination from π^- tracks, due to insufficient collision energy to produce antiprotons, however, their production is suppressed by two orders of magnitude

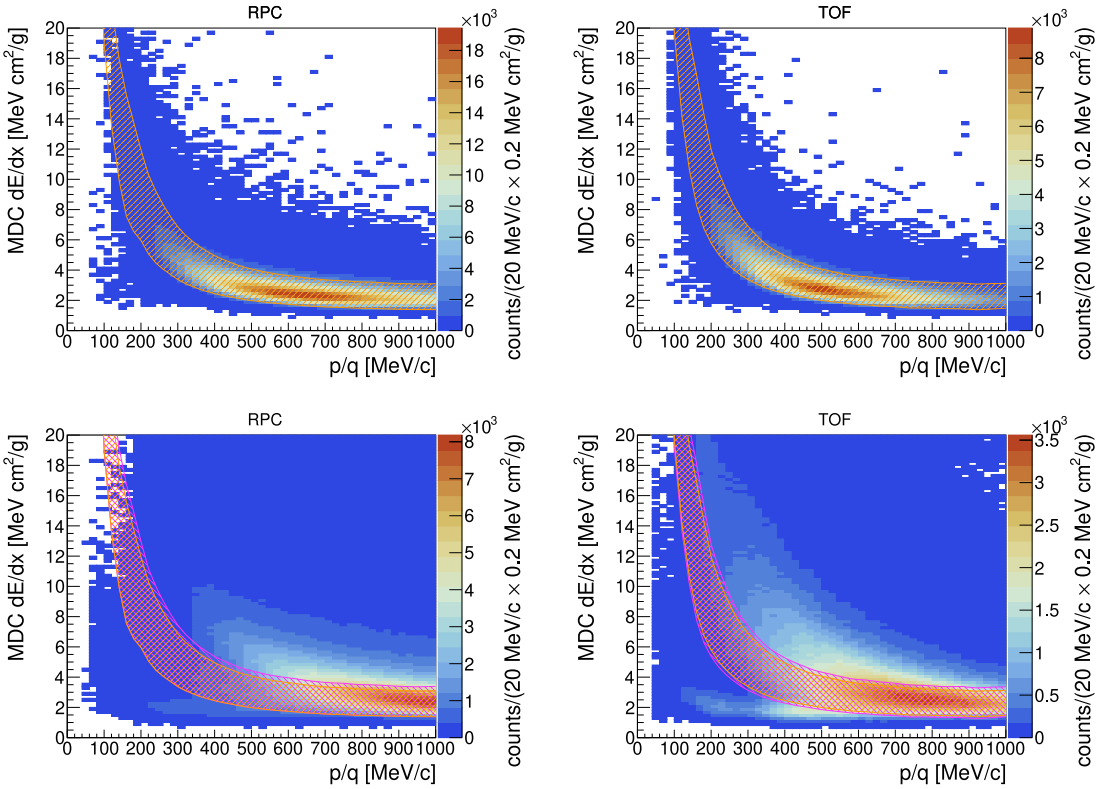

Figure 4.3: Energy losses within MDC for simulated K^+ track (upper row) and measured tracks after track quality ($\chi^2_{\mathrm{RK}} < 100$ and $\chi^2_{\mathrm{MM}} < 2$) and mass cuts ($m_{\mathrm{K}^+} \in (300; 700)\,\mathrm{MeV}/c^2$) are applied (lower row). Orange hatched area shows the cuts based on simulation and with magenta hatched area is displayed the broadened region for real data analysis.

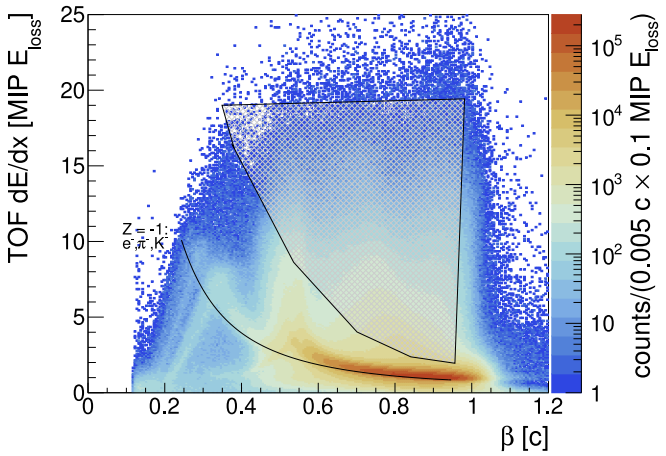

Figure 4.4: Measured correlations of energy losses within the TOF detector and velocity for particles with negative electric charge. The solid black line shows the theoretical values calculated with (3.5). In the gray hatched region are particles with mismatched META hit, see text for more details.

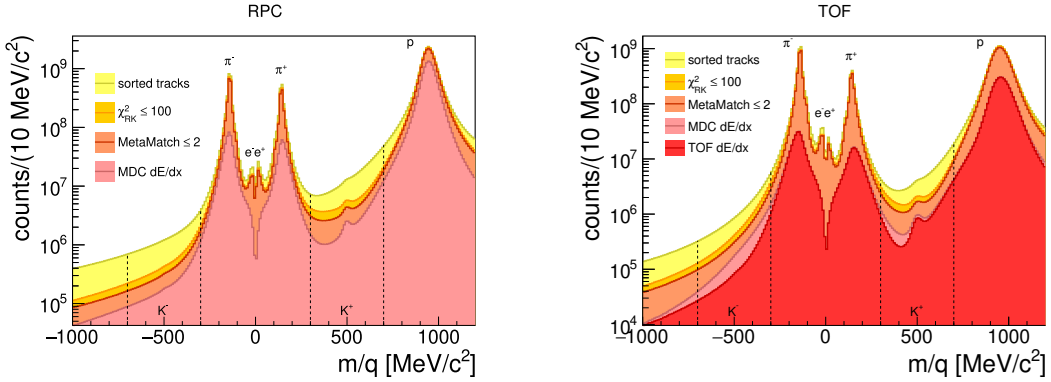

Figure 4.5: Measured spectra of mass scaled by particle's charge in Au + Au collisions at $E_{\text{kin}} = 1.23A$ GeV with selection criteria applied in steps (only region important for charged kaon identification is shown), using RPC and TOF detector for time-of-flight measurement on the left and right sides, respectively.

due to higher threshold energy.

The cubic polynomial function was selected as the best candidate for background description together with the Gaussian function for the kaon peak of the mass spectra. Because of the importance of this step for flow analysis, careful check of the fit parameters, as well as eye inspection, was used to avoid any obvious errors. Examples of the fitted mass spectra are presented in figure 4.6. The signal is obtained by summing the measured spectra of the selected tracks ($\mathrm{d}N/\mathrm{d}m$) within the 3σ width intervals around the mean value of the Gaussian fit function. Due to the finite binning of the mass histograms, the actual sum is from the bin where the value $\mu - 3\sigma$ belongs up to the bin that contains $\mu + 3\sigma$. From this sum, the integral of the background function from the low edge of the first bin included in the sum to the low edge of the first bin not included in the sum is subtracted[4]. The statistical uncertainty of the determined number of kaons σ_S is calculated as the square root of the sum of squares σ_{S+B} and σ_B, where σ_{S+B} is computed using error propagation from the bin errors assuming that all bins are uncorrelated, and σ_B is calculated from the parameter uncertainties and their covariance matrix (taken from ROOT documentation). Different background functions are studied and included within the systematic uncertainty (see section 6.2.2).

4.1.5 Phase space distribution

After the above mentioned steps are performed, we can make the charged-kaon phase space distribution which is displayed in figure 4.7 together with the signal-to-background ratio of the kaon mass peak. Only values for the centrality class for

[4]The overall mathematical prescription is the following

$$S = S + B - B = \sum_{j=i_{\mu-3\sigma}}^{i_{\mu+3\sigma}} N_j - \frac{1}{\Delta m} \int_{m_{\text{low}}(i_{\mu-3\sigma})}^{m_{\text{low}}(i_{\mu+3\sigma}+1)} c_0 + c_1 m + c_2 m^2 + c_3 m^3 \mathrm{d}m,$$

where i_{x} stands for the bin index where mass x belongs, Δm is the bin width, $m_{\text{low}}(i)$ is the mass that corresponds to the low edge of i bin.

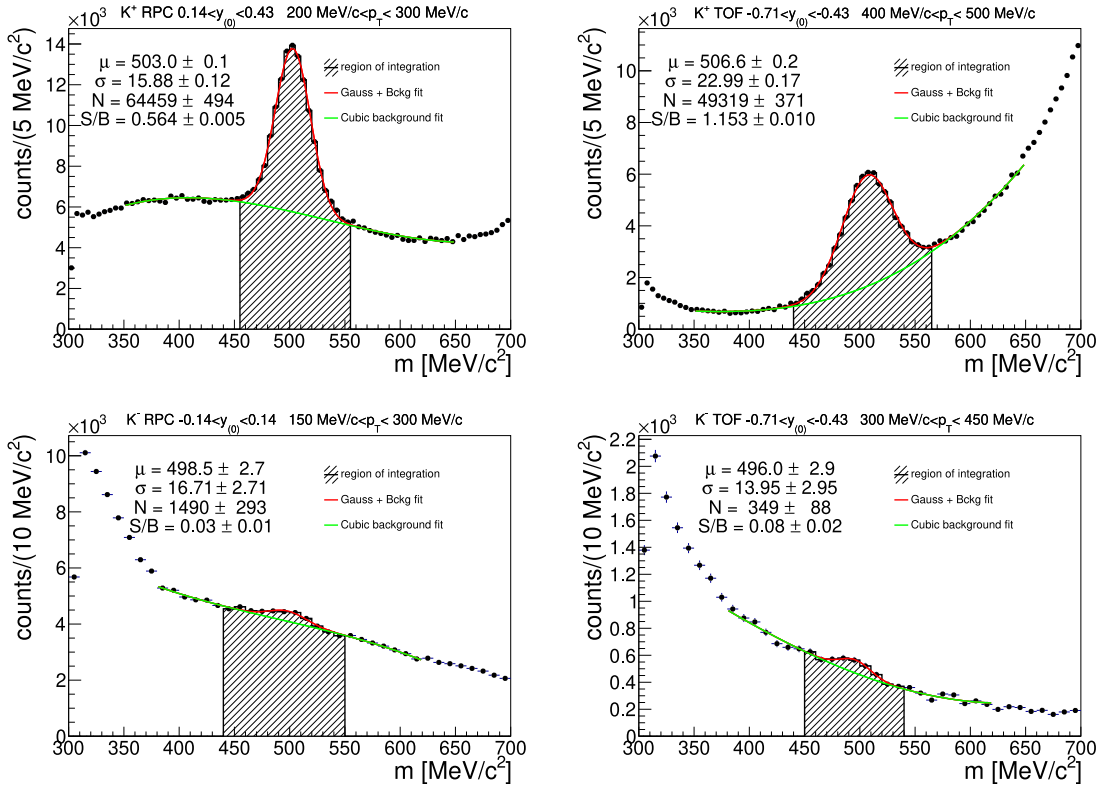

Figure 4.6: Example of charged kaon mass spectra fitted with Gaussian added to cubic polynomial function.

20%−30% most central collisions are shown, the rest is presented in attachment A in figures A.1 to A.12. One can easily see that the flow analysis for negatively charged kaons would require integration over a large phase space, otherwise the results would be influenced by very large statistical uncertainties.

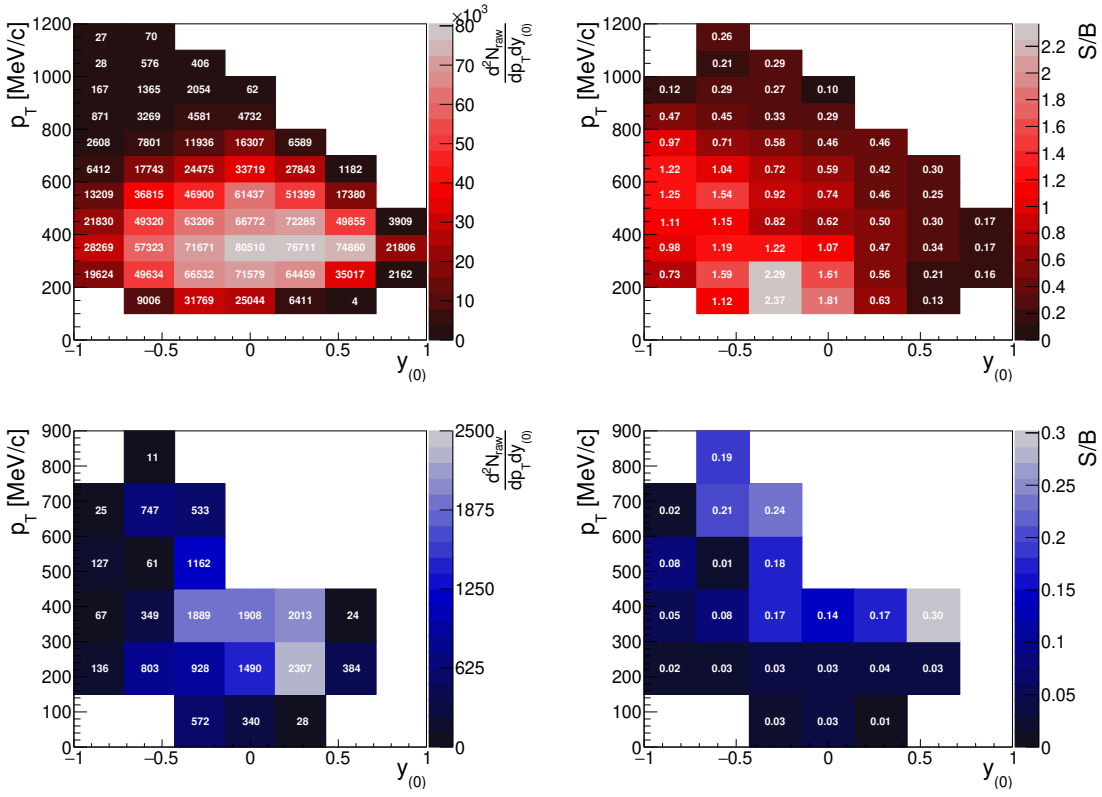

Figure 4.7: Charged kaon phase space distribution and signal-to-background ration of the kaon peak in mass spectra in $20\% - 30\%$ most central collisions. Upper row is for K^+, lower for K^-.

4.2 Neutral kaons

As one of the weakly decaying strange hadrons, neutral kaons live sufficiently long enough to escape from the fireball created in HIC and decay far enough from its spatial point of origin to allow us to distinguish between these two vertices. The procedure of finding these secondary vertices is described in section 3.4 and in the following we will try to introduce a procedure of selection of the pion pairs with high probability to originate from the neutral kaon decay. The summary table with the selection criteria used is in table 4.3.

variable	criteria
χ^2_{RK} for both π^+ and π^-	< 400
χ^2_{MM} for both π^+ and π^-	< 3
$\left\lvert\frac{m}{q}\right\rvert$	> 0 and $< 300\,\mathrm{MeV}/c^2$
topology precuts	defined in (4.1)
$\Omega_{\mathrm{MLP}}\,(d_1, d_2, d_3, d_{\mathrm{ver}}, d_{\mathrm{min}}, p_{\mathrm{mother}})$	> 0.975

Table 4.3: Summary of selection criteria used for neutral kaon identification.

4.2.1 Identification of decay products

It was already visible in figure 3.8 that pions are the second most abundant particle species at SIS18 energy. Due to their long lifetime ($c\tau = 7.8\,\mathrm{m}$), only a very small fraction would decay before being detected with the HADES spectrometer. Although there are well-visible correlations in β versus $\frac{p}{q}$ plots (see figure 3.7), we use a broad mass cut $0 < \left\lvert\frac{m}{q}\right\rvert < 300\,\mathrm{MeV}/c^2$ displayed on the figure 4.8 together with a general track quality selection $\chi^2_{\mathrm{RK}} < 400$ and $\chi^2_{\mathrm{MM}} < 3$, because it was found that selection of the mentioned correlations creates a bias for the neutral kaons [178].

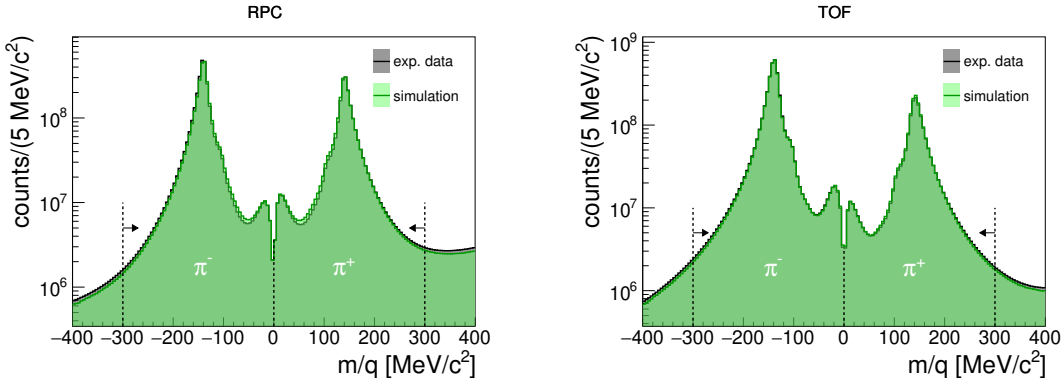

Figure 4.8: Measured spectra of mass scaled by particle's charge in Au + Au collisions at $E_{\mathrm{kin}} = 1.23A\,\mathrm{GeV}$ (only region important for charged pion identification is shown). On the left side RPC detector was used for time-of-flight measurement, and on the right TOF detector.

4.2.2 Topology of the decay

The schematic view of K^0_S decay is displayed in figure 4.9. As was already mentioned, the production probability of K^0_S is rather low in the analysed Au+Au collisions at $E_{kin} = 1.23A\,\mathrm{GeV}$ compared to the number of possible pairs of charged pions. For that reason, we must introduce the so-called topology cuts, i.e., a set of limitations for the variables d_x that are shown in figure 4.9. For clarity, their definitions are:

- d_1 and d_2 are the minimal distances of charged pion tracks to the event vertex (also referred to as global vertex),
- d_3 is the minimal distance of the combined track of the charged pion pair to the event vertex,
- d_{ver} is the distance between the event vertex and point where the two charged pion tracks are closest to each other (the so-called decay vertex),
- d_{min} is the minimal distance between the two charged pion tracks.

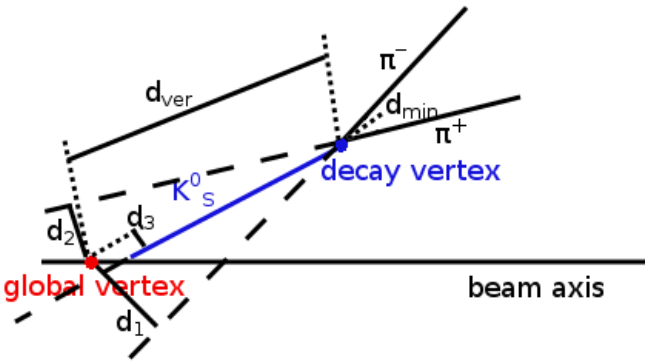

Figure 4.9: Schematic drawing of neutral kaon into charged pion decay topology.

The power of topology cuts can be seen from figure 4.10, where the invariant mass spectra of charged pion pairs from the same event are displayed using different topology selection criteria. Although it is possible to define cuts on variables d_x so-called by hand[5], a much better way is to use dedicated tools for such optimization tasks as TMVA (see section 3.7.2). However, it is very difficult for the algorithm to search for such a hidden signal as neutral kaons, therefore, a set of precuts for d_x variables were introduced to decrease the number of pion pair combinations, see figure 4.10. The values implemented in the present analysis are

$$d_1 > 6\,\mathrm{mm}, \quad d_2 > 6\,\mathrm{mm}, \quad d_3 < 12\,\mathrm{mm}, \quad d_{ver} > 17\,\mathrm{mm}, \quad d_{min} < 13\,\mathrm{mm}. \tag{4.1}$$

[5]This means to generate a procedure where all reasonable combinations $[d_1, d_2, d_3, d_{ver}, d_{min}]$ are tested with respect to the out coming number of identified K_s^0 and the significance of the peak in invariant mass spectra. This test was carried out with 45 000 combinations of d_x variables. The results we sorted by significance and 5 selected combinations were compared with the MLP NN results as a part of study of the systematical uncertainty.

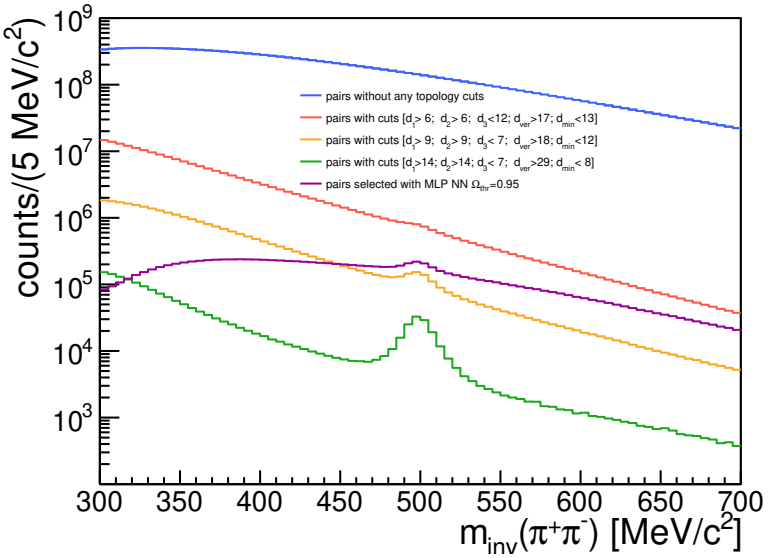

Figure 4.10: Invariant mass spectrum of charged pion pairs for multiple sets of topology cuts: the black line shows the spectra for all possible combinations (no cuts), the blue lines correspond to the topology precuts defined in (4.1), green line refers to cuts optimized for $S/\sqrt{S+B}$, red line is for a very high S/B ratio, and the purple line spectra was obtained with MLP NN.

Multivariate Data Analysis

As was mentioned in the presented analysis, we used supervised learning of MLP NN with simulated K^0_S tracks embedded into real data to get as similar conditions as possible during the training phase and the actual application. Moreover, the reconstructed momentum of the neutral kaon candidate p_{mother} was added to the set of variables, the values of which are optimized.

The performance of MLP NN can be studied using the testing samples (created in the same way as the training sample, i.e., K^0_S tracks from the simulation embedded into real data as signal entries and mixed event pion pairs as background entries) and compared to the application on real data, see figure 4.11.

Finally, it is necessary to determine the threshold value for the MLP output Ω_{thr}. If the neural network output $\Omega > \Omega_{\text{thr}}$ for the input d_x and p_{mother} variables of the pion pair, then this pair will be marked as K^0_s candidate and will be passed into the next steps of analysis, otherwise it will be discarded. Because we analyse well-known decay $K^0_S \to \pi^+\pi^-$ we need to maximize the expected value of significance $S/\sqrt{S+B}$, where S stands for the number of signal entries and B for the number of background entries[6]. The optimal value of the threshold value for MLP output was found $\Omega_{\text{thr}} = 0.975$ as one can see from figure 4.12.

[6]In more detail, we expect the signal to be proportional to S and the estimated error of the signal to be $\sqrt{S+B}$, which is the expected fluctuation of the total number of entries (Poisson distribution). Other view on this can be described with N_S being the true number of signal entries, ϵ efficiency: $S = \epsilon N_S$. Then the so-called merit figure, which we want to maximize, would be $\sqrt{N_S}\sqrt{\epsilon S/(S+B)}$, where $S/(S+B)$ is the signal purity. The intuitive trade-off between efficiency and signal purity is visible in this expression since there is an upper limit of such FOM. [189]

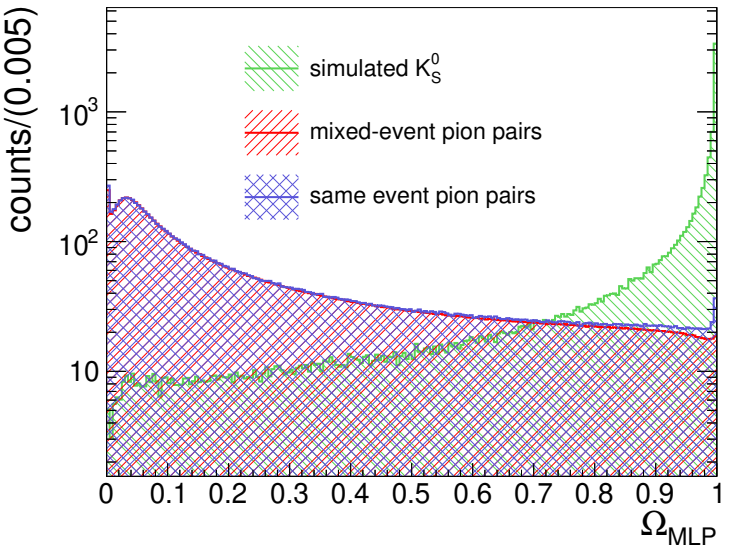

Figure 4.11: Number of entries (pairs of charged pions) with their evaluated output value of MLP NN for simulated neutral kaons signal, mixed-event background pairs (both scaled for the same integral over the whole range of Ω_{MLP}), and pion pairs from measured Au + Au collisions (scaled to background in the range $0.02 < \Omega_{\mathrm{MLP}} < 0.1$).

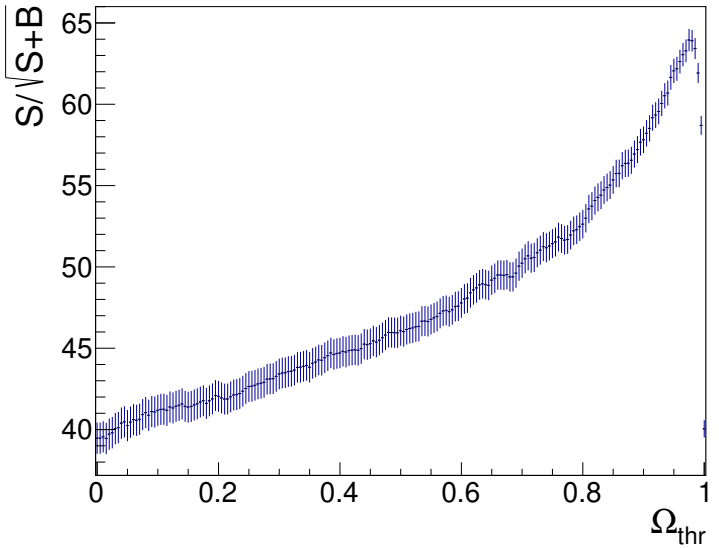

Figure 4.12: Significance of K^0_S peak in invariant mass spectra of charged pion pairs as a function of threshold value of MLP NN output.

4.2.3 Background contributions

Different contributions in the invariant mass spectrum of charged pion pairs were defined in section 3.7.2. Due to the fact that there are no other particle species which decay into two charged pions at around the nominal mass of neutral kaons, there should be no correlated background contributing to our invariant mass spectra. The misidentification origin mainly from $\pi^+ \leftrightarrow$ p however both pions and protons have purity above 95 %, therefore the only relevant source is the uncorrelated pion pairs. For that type of background, the Mixed-Event technique is used with very good results. However, one will have to pay attention to several event characteristics, which might influence the properties of pion tracks that are combined. Classification of events based on these event properties is therefore introduced, and only pions from the same class are combined. The relevant characteristics are found to be:

Time of event recording might influence the performance of the spectrometer, since it was changing slightly during the beam time (e.g., the performance of MDC as discussed in section 3.1.1). Thus, to ensure that we mix pion pairs with similar performance of the detectors, one class is only for several minutes of data taking.

Centrality is one of the variables for which we study the dependence of the flow parameters. It also influences the phase space distribution of pions and their multiplicity in one event [180]. Therefore, it is also one of the classification criteria.

Event Vertex position is the last criterion. Because the total length of the segmented gold target is almost 60 mm (see section 2.1), it matters in which segment reaction happened due to the difference in magnetic field strength for the same pion polar angle but different event vertices (see figure 2.7). Therefore, even for the completely same interactions, the resulting particles would end up in different parts of the spectrometer with possibly different detection efficiency.

The algorithm then mixes pions with opposite charges from different events, which are stored in the buffer, and continues with the analysis with the same steps as if they were from the same event.

4.2.4 Signal acquisition

Finally, it is necessary to scale the mixed-event invariant mass spectra to the integrated number of events in the intervals around the peak[7] of K^0_s as the same-event spectra. The exact edges of the scaling intervals are determined with an educated guess because the perfect match between mixed-event background and the background part of the same-event invariant mass spectra was not possible.

[7]Because of the shape of the spectra, where there are more pion pair combinations for lower invariant mass, the interval on the left side of the peak is slightly smaller than the one on the right side to have roughly the same number of entries in both intervals. The edges of the intervals close to the peak position are in both cases more than 3σ away from the peak maximum.

To achieve the best background description in the signal region, the scaling intervals should be as close as possible to the signal region but at least 3σ away from the K^0_s mass peak maximum to include utmost 0.3 % of signal entries. Different scaling intervals are studied, and the differences with primarily used values are included in the systematic uncertainty (see section 6.2.3). The invariant mass spectrum for pion pairs satisfying the condition $\Omega > \Omega_{\text{thr}}$, together with the corresponding mixed event background, is displayed on figure 4.13.

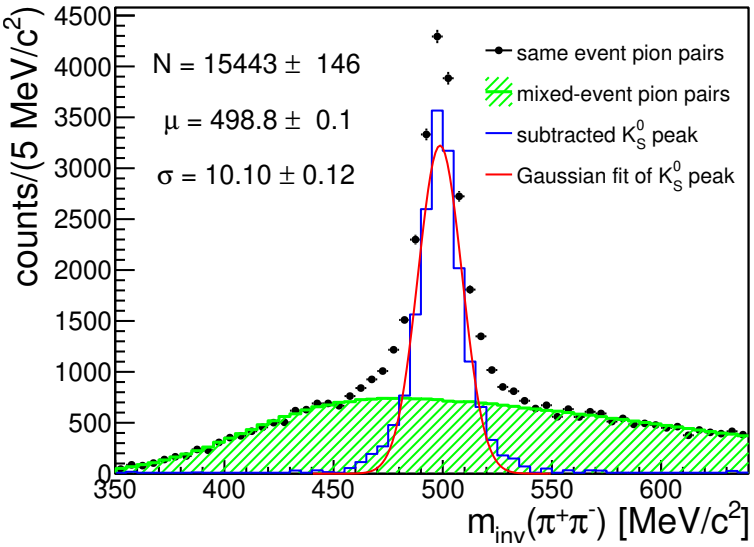

Figure 4.13: Example of charged pion pairs invariant mass spectrum with mixed-event background.

After the mixed-event background is subtracted from the same event invariant mass spectra, the number of signal K^0_S is extracted in the 2σ region around the mean value mean value μ of the Gaussian function fit of the peak. Different widths of signal regions were tested as well as the background subtraction method based purely on fitting the same event invariant mass spectra with a function, and all these variations are part of systematic uncertainty. Statistical uncertainty is calculated as $\sigma_N = \sqrt{\sigma^2_{\text{SE}} + \sigma^2_{\text{ME}}}$, where both σ_{SE} and σ_{ME} are computed using error propagation from the bin errors of invariant mass histograms assuming that all bins are uncorrelated. Due to the much larger statistics of mixed-event spectra (by a few orders), the statistical uncertainty is dominated by the same event spectrum uncertainty.

4.2.5 Phase space distribution

K^0_S phase space distribution, shown in figure 4.14 together with the signal-to-background ratio of the kaon mass peak, immediately points out that due to smaller statistics, the flow analysis of the neutral kaon would suffer from large uncertainties. However, in comparison to K^- we observe much larger S/B ratios which give us a better chance for differential flow analysis. Only values for the centrality class for $20\% - 30\%$ most central collisions are shown, the rest is presented in attachment A in figures A.17 to A.20.

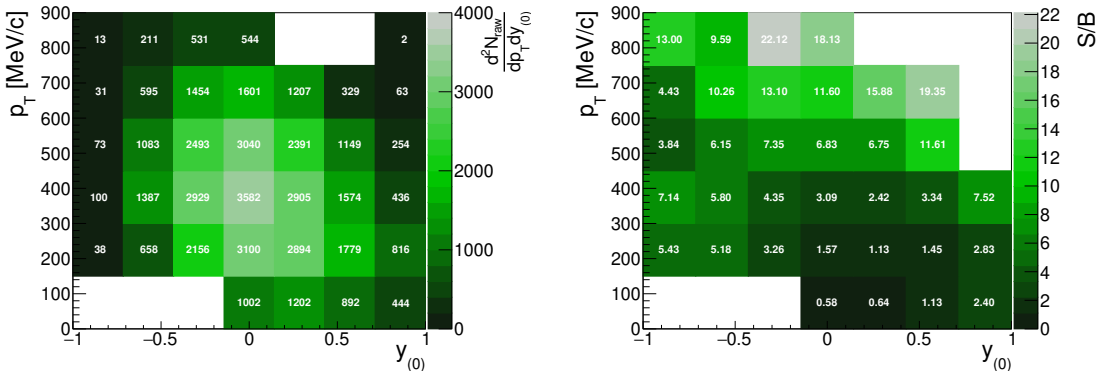

Figure 4.14: Neutral kaon phase space distribution and signal-to-background ration of the kaon peak in mass spectra in 20% – 30% most central collisions.

4.2.6 Decay curve test

Independent test of a possible bias introduced by decay topology selection (outlined in section 4.2.2) and the spectrometer acceptance and reconstruction efficiency corrections (defined in section 3.8) is the reconstruction of the decay curve and measurement of the lifetime of the reconstructed K^0_s.

The number of K^0_s after time t of their existence in their rest frame follows the law of exponential decay

$$N(t) = N_0 \cdot \exp^{-t/\tau}, \tag{4.2}$$

where N_0 is the number of decaying particles at time $t = 0$, and τ is the mean lifetime of the particle species. With the detectors, we are able to measure the laboratory time-of-flight t_{lab} which is connected to the time-of-flight in the particle rest frame with the well-known STR relation $t_{\text{lab}} = t'\gamma$. The laboratory time-of-flight can also be characterized as the length of the particle path divided by its velocity $t_{\text{lab}} = \frac{l}{\beta c}$. By joining these expressions and realizing that the size of the momentum vector of a relativistic particle can be denoted as $|\vec{p}| = mc\beta\gamma$ we derive the formula for the time-of-flight in the particle rest frame

$$t' = \frac{l \cdot m}{|\vec{p}|}, \tag{4.3}$$

where m is the nominal mass of the particle. In our case of decaying K^0_s, the path length is the variable d_{ver} introduced in figure 4.9, the mass value is taken from the table 4.1 and $|\vec{p}|$ is calculated from the charged pion momenta $|\vec{p}| = |\vec{p_{\pi^-}} + \vec{p_{\pi^+}}|$. To find the value of mean life time from the experiment, we need to create a histogram of the number of kaons $N_{K^0_s}$ as a function of t', the details of this procedure can be found in section 4.2.4.

To verify this method, we have tested it on the Monte Carlo simulation data set, where a nice exponential decay curve is observed, see figure 4.15a. From this test, we observed $\tau_{\text{primary}} = 89.38 \pm 0.42\,\text{ps}$ that agrees with $\tau_{\text{PDG}} = 89.5\,\text{ps}$ from the table 4.1. When we analyze the simulated K^0_S with our algorithm, where the precuts (4.1) introduce a gap in the spectra for low t'[8], we obtain the spectra

[8] For an average value of momenta $\langle p \rangle \approx 500\,\text{MeV}/c$ the precut $d_{\text{ver}} > 17\,\text{mm}$ corresponds to $t' > 85\,\text{ps}$.

displayed on figure 4.15b with $\tau_{\mathrm{sim,reco}} = 86.2 \pm 1.1\,\mathrm{ps}$ that is only slightly below the expected value. With this successful result, we moved on to use it for the acceptance and reconstruction efficiency corrected data. To constrain the range of t' used for fit, we have calculated the significance $S/\sqrt{S+B}$ in each bin, see figure 4.16a, and used only part of the spectra where the significance was high. The final value of mean life time $\tau_{\mathrm{exp}} = 87.9 \pm 2.2\,\mathrm{ps}$ is within 1σ from τ_{PDG} which we consider a great agreement.

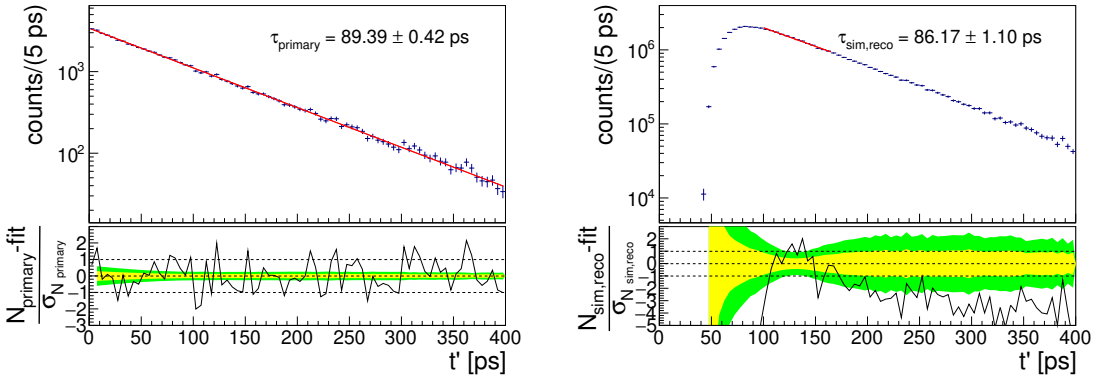

(a) (b)

Figure 4.15: (a) Spectrum of primary neutral kaons dependent on their rest frame time fitted with function (4.2). Both l and $|\vec{p}|$ (needed for calculation of t') are taken directly from Monte Carlo simulations. (b) Number of reconstructed K^0_S in the simulated data set as a function of time in their rest frame fitted with function (4.2). The residuals of the fit are also shown together with the confidence intervals of 1σ and 2σ.

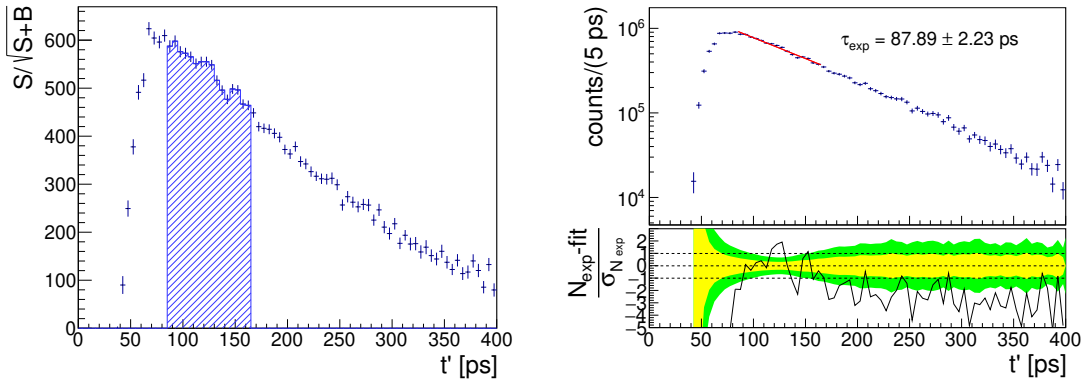

(a) (b)

Figure 4.16: (a) Calculated significance of K^0_S peak in the invariant mass spectra of charged pion pairs as a function of t'. The selected region for fitting $N_{\mathrm{exp}}(t')$ spectra is shown with infill. (b) Number of identified neutral kaons as a function of time in their rest frame fitted with the function (4.2). The residuals of the fit are also shown together with the confidence intervals of 1σ and 2σ.

4.3 Comparison of experimental data and simulation

Simulations are necessary for almost any particle data analysis nowadays for the reasons mentioned in section 3.8. It is essential that the virtual spectrometer in simulation has as similar performance as possible to the real HADES spectrometer, especially in the case of analysis of rare probes that are kaons, because the correction factors coming from detector acceptance and reconstruction efficiency might reach values above 100. Therefore, a careful comparison is made between the simulation and the experimental data for each variable used for kaon identification. The usage of variables that have different simulated and experimental spectra would lead to a deviation of the efficiency corrections.

One of the first applied selections on the tracks are cuts on quality parameters χ^2_{RK} and χ^2_{MM}. In the case of charged kaons, the selection was more strict than in the case of pions coming from neutral kaon decay to suppress the tails in the mass spectra of pions and protons. For pions, the selection was broadened to avoid possible bias. As one can see from figures 4.17 and 4.18, there are small discrepancies between the spectra for experimental data and simulation. Both parameters χ^2_{RK} and χ^2_{MM} have a slightly narrower distribution (the spectra are more peaked towards zero values) in the case of simulation. However, the shapes of the spectra are very similar, thus the adjusted rather large values of χ^2_{RK} and χ^2_{MM} cuts do not introduce a big bias on the integrated number of kaons.

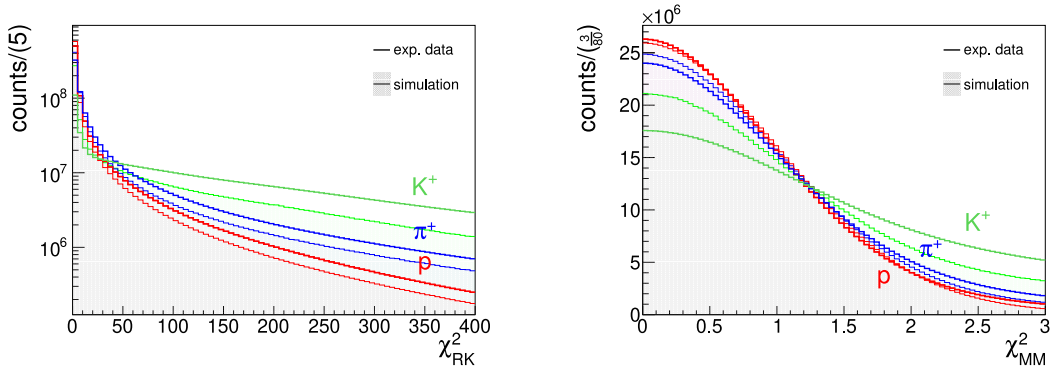

(a) (b)

Figure 4.17: (a) χ^2 from Runge-Kutta momentum reconstruction method is compared for three particle species distinguished by mass selection ($m_{\pi^+} \in (50; 300)\,\mathrm{MeV}/c^2$, $m_{\mathrm{K}^+} \in (300; 700)\,\mathrm{MeV}/c^2$, and $m_{\mathrm{p}} \in (700; 1200)\,\mathrm{MeV}/c^2$) between data displayed with wide full lines and simulations with filled histograms. (b) Similar to (a) only for χ^2 of META matching.

The second group of cuts used for charged kaon identification uses the information on energy losses within MDC and TOF detectors. The case of MDC detector was already discussed in section 4.1.2 and the difference between the selected regions for K^+ for simulation and experimental data is visible in figure 4.3, and more details on this topic can be found in [179]. For the TOF detector, the comparison between simulation and measured data for energy loss of particles

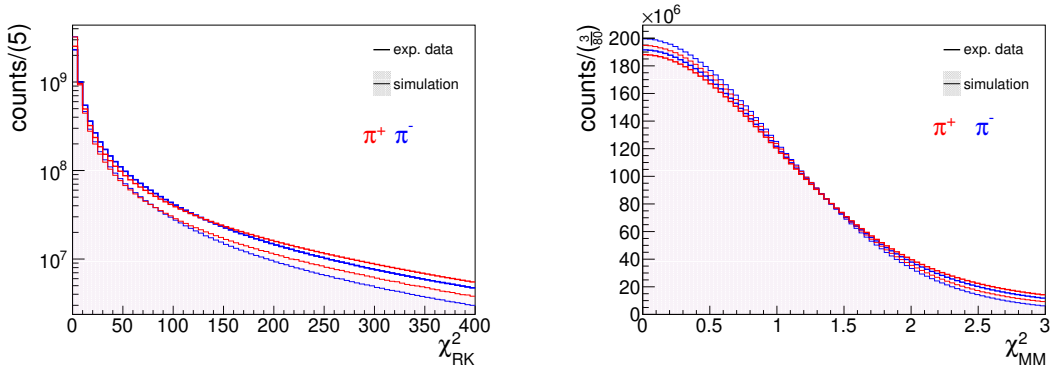

(a) (b)

Figure 4.18: (a) χ^2 from Runge-Kutta momentum reconstruction method is compared for charged pions identified with mass to charge ratio ($0 < |m/q| < 300\,\mathrm{MeV}/c^2$) between data displayed with wide full lines and simulations with filled histograms. (b) Similar to (a) only for χ^2 of META matching.

with negative electric charge is presented in figure 4.19. In both cases, the incorrect correlations at high velocity and large deposited energy are present, and the graphical veto cut eliminates them.

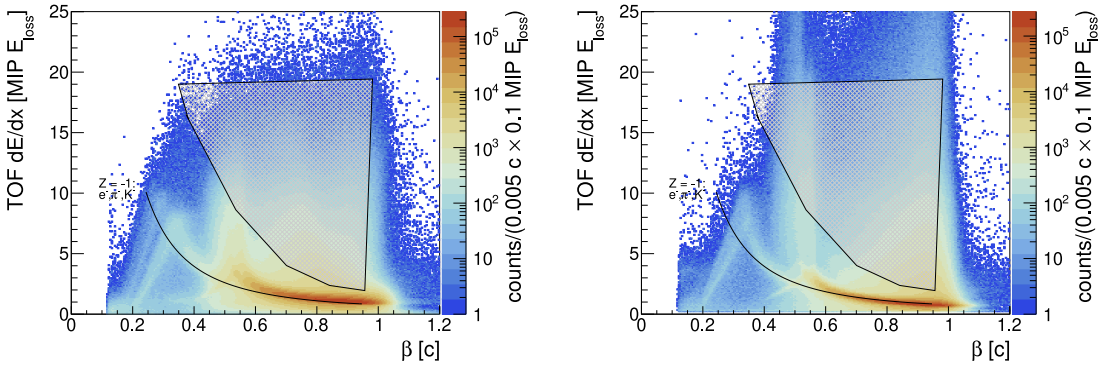

(a) Experimental data (b) Simulation

Figure 4.19: Measured correlations of energy losses within the TOF detector and velocity for particles with negative electric charge. The solid black line shows the theoretical values calculated with (3.5). In the gray hatched region are particles with mismatched META hit, see the text for more details.

In the case of neutral kaons, the second step of the selection procedure of pion pairs is the topology precuts. Due to the low interaction energy below the strangeness production threshold, only a very small number of identified charged pions would originate from weakly decaying hadrons, e.g., neutral kaons or lambda hyperons. Thus, in both the data and simulations, the distribution of d_x would be dominated by background. We can, however, also include d_x spectra from the reconstructed simulated signal of neutral kaons to explore the effectiveness of the applied precuts. The distributions for one million pion pairs are shown in figure 4.20. We observe that the spectrum of d_x from the data and simulation agrees rather well, only small discrepancies are visible for d_1 and d_ver. The pion

pairs that originate from neutral kaon decay have a very similar distribution of d_3 (distance of K^0_S track from the global vertex) and d_{min} (minimal distance of the two charged pion tracks), which is not too surprising as these variables are basically measures of the quality of the track reconstruction. The others (d_1, d_2, and d_{ver}) are selecting off-global vertex tracks that are probable to come from weakly decaying hadrons, therefore the differences between background and signal pion pairs are desirable.

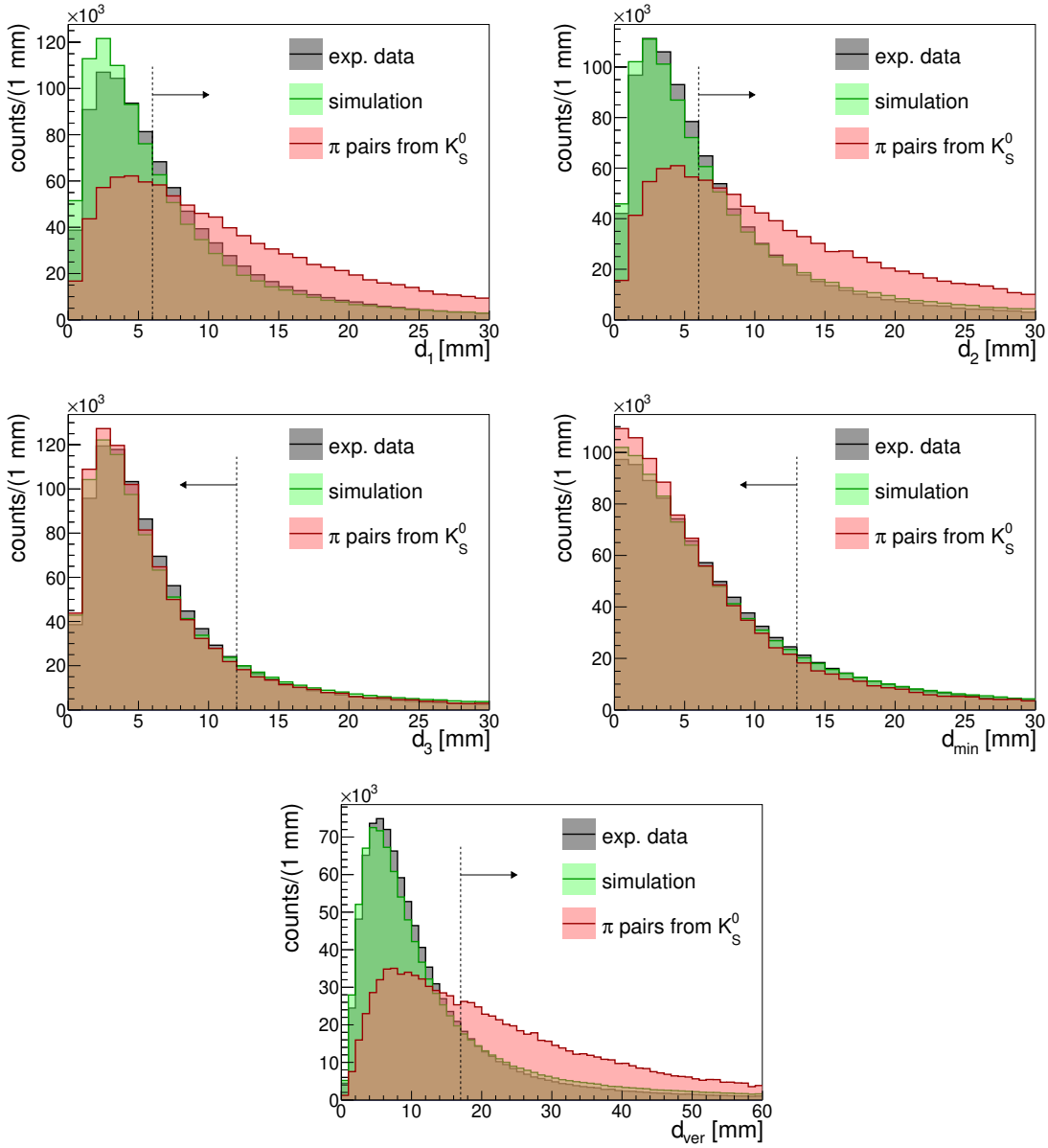

Figure 4.20: Comparison of topology cut variables spectra between data, simulations, and signal pion pairs.

After the precuts were applied, multivariate data analysis was used to distinguish uncorrelated pion pairs and those originating from neutral kaon decay. As it was already shown in figure 4.11, where we observe a very good agreement between same-event pion pairs from measured Au + Au collisions and the spectra of mixed-event pair for small values of Ω_{MLP} where the domination of the

background is expected. The simulated signal spectra could be scaled down to the integral difference between the same and mixed event pion pairs spectra and then compared with the experimental spectra, see figure 4.21. Excellent agreement is achieved up to $\Omega_{\mathrm{MLP}} = 0.975$ (where the ratio is 0.937) and then the simulation overshoots the experimental measurement. However, this overshoot is not so important for our analysis since we determined exactly the threshold value $\Omega_{\mathrm{thr}} = 0.975$ based on the highest significance of $\mathrm{K}^0_{\mathrm{S}}$ peak in the invariant mass spectra.

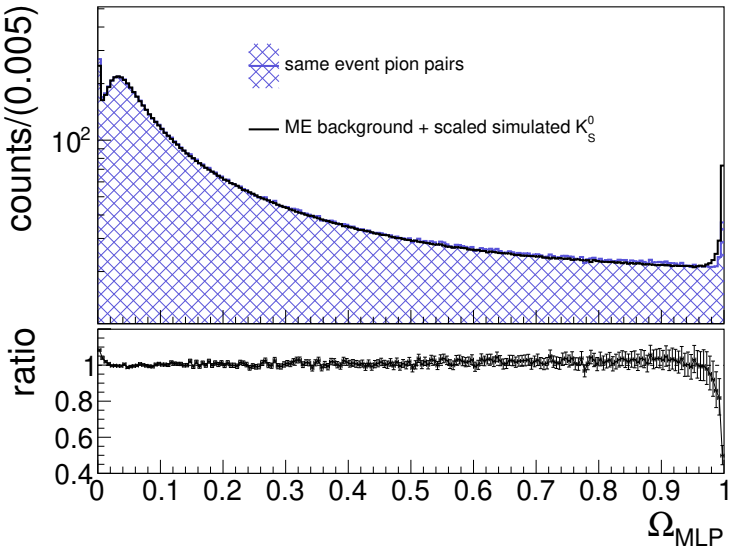

Figure 4.21: Comparison of measured same event pion pairs with scaled simulated neutral kaons signal (to the integral of difference between same event and mixed event pairs for $\Omega_{\mathrm{MLP}} > 0.5$) added on top of mixed-event background spectra.

4.4 Acceptance and Reconstruction Efficiencies

In the case of charged kaon azimuthal anisotropy analysis, we might avoid the need of phase space dependent acceptance and reconstruction efficiency corrections simply by limiting the analysis to small phase space regions, where the effect of acceptance and reconstruction probability is approximately constant. However, due to the small number of reconstructed kaons (resulting from the subthreshold collision energy), we may need to integrate over large intervals of normalized rapidity $y_{(0)}$ and/or transverse momenta p_{T}[9].

For neutral kaons reconstructed via their decay products, charged pions, we have to calculate the corrections for these products since there are two degrees of freedom for the two-particle decay problem, i.e. there is a continuum of combinations of their phase space variables for a particular phase space interval of the neutral kaon.

[9]Definition of rapidity $y = \frac{1}{2}\ln\left[(E + p_z)/(E - p_z)\right]$. If we denote projectile rapidity as y_{proj} (in case of analysed Au + Au collisions at $E_{\mathrm{kin}} = 1.23A\,\mathrm{GeV}$ its value is $y_{\mathrm{proj,Au}} = 1.48$), we can express the rapidity in the center-of-mass system as $y_{\mathrm{cm}} = y_{\mathrm{lab}} - \frac{1}{2}y_{\mathrm{proj}}$ and normalized rapidity $y_{(0)} = y_{\mathrm{lab}}/y_{\mathrm{proj,cm}} - 1$. Definition of transverse momenta $p_{\mathrm{T}} = \sqrt{p_x^2 + p_y^2}$.

Simulations play a key role in the determination of these corrections. In Pluto generator, we define the basic properties (mainly temperature) of a fireball that is created when the gold nuclei collide and ask for the kaon phase space distribution. Then we take one kaon track and embed it into the measured events (one kaon track per one event), which we then pass to the HGeant and HYDRA algorithms. Since we know the number of embedded tracks N_{input} and their phase space distribution, we can compare it to the number of accepted tracks N_{acc} (we ask that the simulated track has at least 4 hits in each MDC plane and one META hit)

$$\varepsilon_{\text{acc}}(y_{(0)}, p_{\text{T}}, \mathcal{C}) = \frac{N_{\text{acc}}}{N_{\text{input}}}, \tag{4.4}$$

where we define the acceptance $\varepsilon_{\text{acc}}(y_{(0)}, p_{\text{T}}, \mathcal{C})$ dependent on the phase space variables and the centrality of the event $\mathcal{C}$. Similarly, the reconstruction efficiency, which covers all effects originating from the tracking algorithm and selection criteria (track quality, energy loss, topology cut, etc.), is determined as

$$\varepsilon_{\text{reco}}(y_{(0)}, p_{\text{T}}, \mathcal{C}) = \frac{N_{\text{reco}}}{N_{\text{acc}}}, \tag{4.5}$$

where N_{reco} is the number of reconstructed and selected kaon tracks (the same analysis code is used for simulations as for the measured data). Finally, the combined efficiency, which inverse value is later used as the track weight,[10] is defined as the product of the two above, i.e., track weight $w = (\varepsilon_{\text{acc}} \cdot \varepsilon_{\text{reco}})^{-1}$.

In the case of $20\% - 30\%$ the most central collisions, the acceptance and reconstruction efficiencies for charged and neutral kaons are depicted in figures 4.22,4.23 and 4.24. The efficiencies for other analysed centrality classes are presented in attachment A in figures A.5 to A.24.

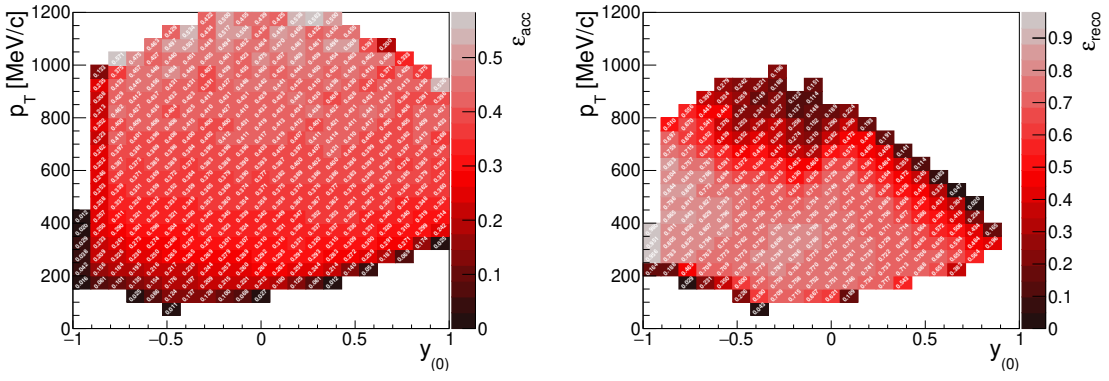

(a) (b)

Figure 4.22: K^+ acceptance in (a) and reconstruction efficiency in (b) for $20-30\,\%$ centrality class.

[10] This weight is used when the track is filled into invariant mass histograms with the corresponding rapidity, transverse momenta, and event centrality.

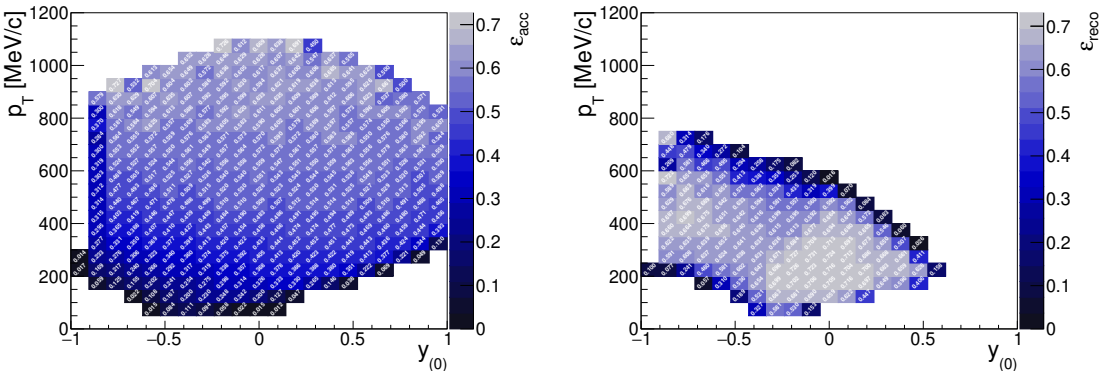

(a) (b)

Figure 4.23: K^- acceptance in (a) and reconstruction efficiency in (b) for 20−30 % centrality class.

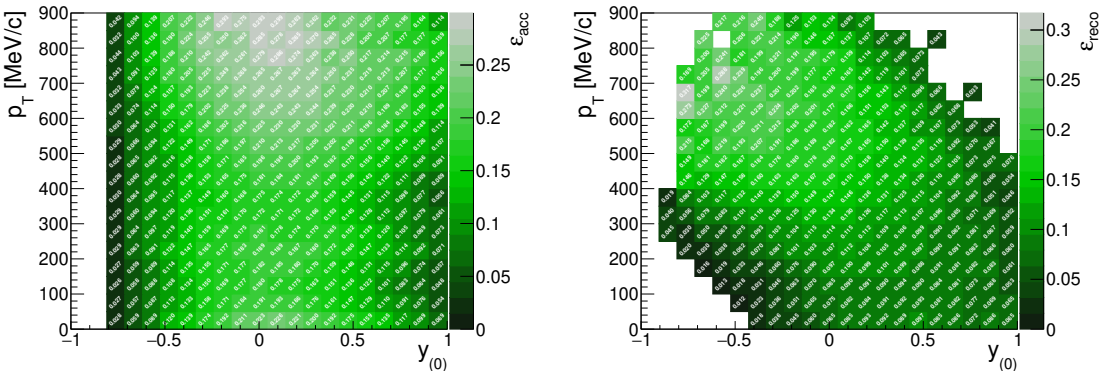

(a) (b)

Figure 4.24: K^0_S acceptance in (a) and reconstruction efficiency in (b) for 20−30 % centrality class.

Chapter 5

Measurement of collective flow

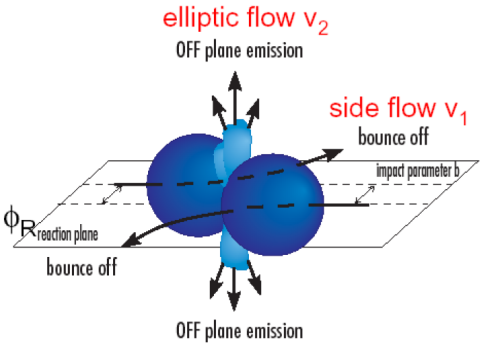

First, in this chapter, I would like to introduce a little bit of history of what is today called flow analysis, section 5.1, because it is quite important for the understanding of motivation of the techniques used in the analysis presented in this thesis. Detailed description of the method used for the kaon flow analysis will follow, see section 5.2.

As was already mentioned in the first chapter, the generic term flow would be used later on in the sense of observed azimuthal angle correlations between particles radiated from heavy-ion collisions, also referred to as transverse flow. Apart from this nomenclature, flow is related also to the longitudinal and radial expansion of the created hot and dense matter.

5.1 Development of the flow analysis

The importance of flow measurement[1] consist in the direct indication of collective phenomena in relativistic heavy-ion collisions compared to an original view on such systems as a simple overlap of many NN scatterings [190].

5.1.1 Relativistic collisions

The first theoretical models of describing HIC in terms of fluid dynamics [191, 192] (with the advantage of easily incorporating the equation of state), and as a cascade of binary on-shell NN collisions [193] (which opens the possibility to track the influence of individual NN collisions) gave predictions of shock waves caused by the compression of nuclear matter. There were also thermodynamical fireball model [194] requiring thermal equilibrium of the overlap region in the collision, and classical many-body calculations [195] exploiting measured NN scattering data that were able to predict particle multiplicities.

The experimentalists, on the other hand, achieved major success with the proof of collective flow effect [196] which we now call directed transverse flow. In this work the authors used sphericity tensor method suggested in [197] and improved in [198]. The idea of defining second order momentum tensor was already used by Bjorken and Brodsky [199] which they used to study hadron jets

[1] In this section, the kaon flow is not discussed, but mainly flow of protons and pions.

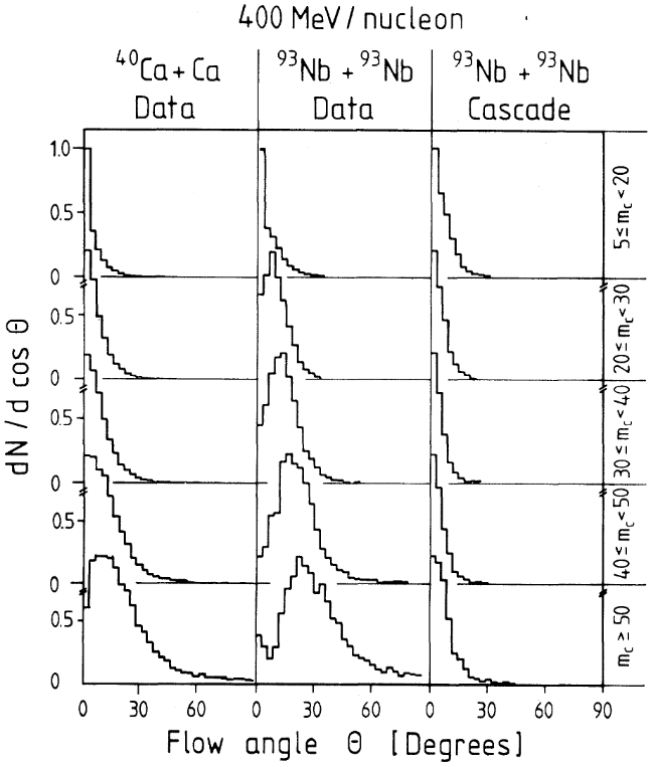

Figure 5.1: Frequency distribution of the flow angle for different multiplicity bins in measured data and cascade prediction. Figure taken from [196].

in high-energy electron-positron collisions. The sphericity tensor is defined as

$$F_{ij} = \sum_{\nu=1}^{N} \omega_\nu p_i(\nu) p_j(\nu), \tag{5.1}$$

where $p_i/j(\nu)$ are the components of the measured final momenta $\vec{p}$ of the fragment ν in the event with N fragments in the final state, ω_ν are weights of the fragments. If these weights are constant, then the tensor F_{ij} is called the sphericity tensor, for the choice of $\omega_\nu = \frac{1}{2m_\nu}$ (m_ν is the mass of the fragment ν) leads to a kinetic flow tensor. From the eigenvalues f_n and eigenvectors $\vec{e}_n$ of this tensor one can construct flow angle θ_{F} (in fact this is a polar and not azimuthal angle, however, in the first experiments at low energy the event shape was studied not only in the transverse plane) and the kinetic flow ratios f_1/f_3 and f_2/f_3, for details see [198]. The nonzero flow angle value of the maxima of event distribution shown on figure 5.1 was the obvious hint for the collective effect in heavy-ion collisions.

The increase of projectile kinetic energy leads to a decrease of momentum transfer into transverse direction by γ^{-2} of Lorentz factor (due to decrease of passing time and longitudinal contraction of nuclei) [190]. A new method developed by Danielewicz and Odyniec [200] (originally suggested in [201], elaborated in great detail in [202]) which use only the transverse component of fragment momenta to define $\vec{Q}$-vector (nowadays also denoted as directivity)

$$\vec{Q} = \sum_{\nu=1}^{N} \omega_\nu \vec{p}_{\mathrm{T}}(\nu), \tag{5.2}$$

where again ω_ν are the weights of the fragments and $\vec{p}_{\mathrm{T}}(\nu)$ are the transverse component of the momenta of the fragment. The choice of weigths was the following $\omega_\nu = 1$ for baryons with rapidity $y > y_{\mathrm{c}} + \delta$, $\omega_\nu = -1$, for baryons with rapidity $y < y_{\mathrm{c}} - \delta$, and $\omega_\nu = 0$ for pions and baryons with $y_{\mathrm{c}} - \delta < y < y_{\mathrm{c}} + \delta$. In case of symmetric collisions, the critical rapidity is the rapidity of the overall center-of-mass of the system $y_{\mathrm{c}} = y_{\mathrm{proj}}/2$. With such weights, it is possible to remove so-called autocorrelations (particles around midrapidity do not contribute to the determination of the reaction plane and only cause its fluctuation). This vector can then be used to estimate the reaction plane[2] azimuthal angle $\tan \Psi_{\mathrm{RP}} = \frac{Q_y}{Q_x}$ (or one can even define for particle μ its own $\vec{Q}_\mu = \sum_{\mu \neq \nu} \omega_\nu \vec{p}_{\mathrm{T}}(\nu)$ which is used for the estimation of the reaction plane for this particle). In the latter paper [202] corrections are applied for azimuthal acceptance of the detector and for conservation of transverse momentum. Moreover, in [200] the authors investigate the precision of reaction plane determination by randomly dividing the measured fragments into two groups (called subevents) and for each vector $\vec{Q}_{\mathrm{I}}$, resp. $\vec{Q}_{\mathrm{II}}$, is calculated. From these the difference of the azimuthal angles of the subevent reaction planes $\Delta\Psi_{\mathrm{RP}} = |\Psi_{\mathrm{RP,I}} - \Psi_{\mathrm{RP,II}}|$ is studied and used for the correction of reaction plane resolution. This revolutionary method was quickly accepted by the scientific community for its superior ability to distinguish between dynamical effects and statistical fluctuations even for a very small number of analysed events (in both mentioned cases the number of events was only around 500). The main difference in contrast to the sphericity tensor method (which studies single-particle effect incorporated in many particle distribution of the eigenvectors of the tensor) is in the summation of two-particles correlation due to the existence of reaction plane.

Using the novel transverse momentum method, the experiments were able to identify new component of collective flow [203] which we now call elliptic flow. Contrary to previously observed directed flow (at that time this effect was called bounce-off and side-splash), which take place in the direction of the reaction plane, the elliptic flow (in the mentioned paper referred to as squeeze-out) is perpendicular to reaction plane and pronounced mainly in the midrapidity region, see figure 5.2. From the agreement with hydrodynamic model prediction and fireball model picture, this observable was used for the extraction of details about the nuclear equation of state ever since.

5.1.2 Ultra-relativistic collisions

On the theory side, Jean-Yves Ollitrault published in year 1992 article [204] predicting in-plane elliptic flow in ultra-relativistic HIC, in which most of the center-of-mass energy would remain in the longitudinal direction (along beam) due to nuclear transparency (therefore $\theta_{\mathrm{F}} \to 0$). He introduced two scenarios:

- The collisions are view as superpositions of many independent NN collisions (no collective effect), which would lead to isotropic momentum distribution.
- If thermal equilibrium is restored in the overlap region, the pressure gradient

[2]The reaction plane is defined by the vector of impact parameter $\vec{b}$ and momenta of the projectile $\vec{p}_{\mathrm{beam}}$.

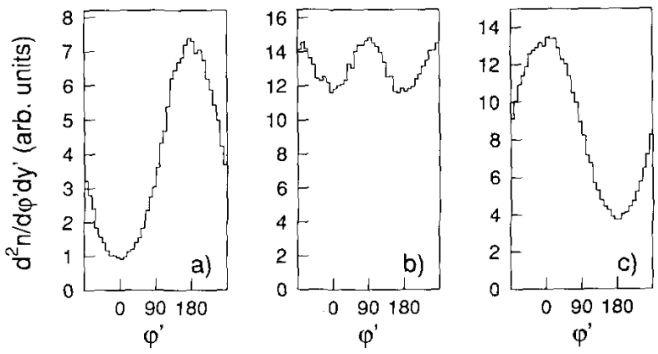

Figure 5.2: Distribution of the fragment azimuthal angle w.r.t. the reaction plane for (a) target- (b) mid- and (c) projectile rapidity region in Au + Au collisions at 400A MeV. Figure taken from [203].

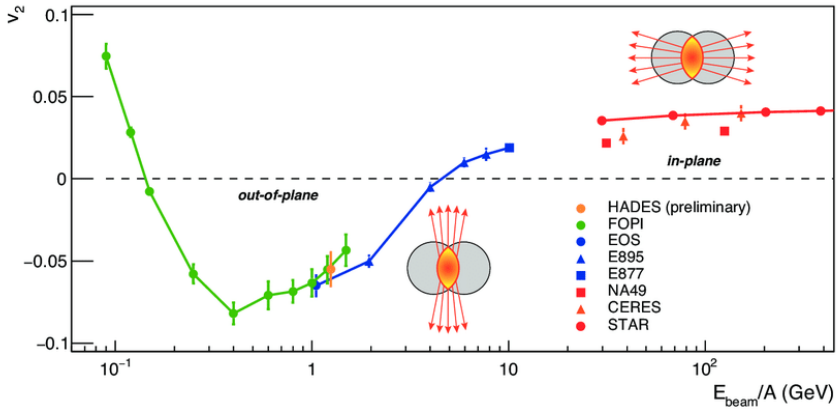

Figure 5.3: The excitation function of elliptic flow (v_2 in modern nomenclature) measured in semicentral heavy-ion collisions at midrapidity. Figure taken from [206].

is the largest along the impact parameter vector and according to the Euler equation the collective flow would occur in this direction.

One year later the in-plane elliptic flow was indeed observed by E877 collaboration [205] at AGS accelerator in BNL, see figure 5.3. In the same article, the sphericity tensor method is revisited to be applicable also in the ultra-relativistic energy region, where the main idea is to eliminate the longitudinal and focus on transverse part $S^{\perp}_{ij} = \sum_{\nu=1}^{N} p_i(\nu)p_j(\nu)$ with $i, j = 1, 2$. The dimensionless observable $\alpha = \left[1 - (4 \det S^{\perp})/(\mathrm{tr}S^{\perp})^2\right]^{1/2}$ is introduced as a natural measure of the anisotropy in transverse momenta. Similar observable can be introduced also for spatial anisotropy α_s and argue that the initial spatial anisotropy influences the hydrodynamic flow, i.e., is the origin of transverse momentum anisotropy (qualitative agreement of curves on figure 5.4).

With the growing number of experiments and development of different methods of the event shape analysis (or flow analysis) suggesting many observables, the situation was a little confusing, until the emerge of Fourier expansion of azimuthal particle distribution in [207]. The authors propose a systematic description of observer azimuthal particle distribution on the event-by-event basis with and even without prior estimation of the reaction plane angle. They recom-

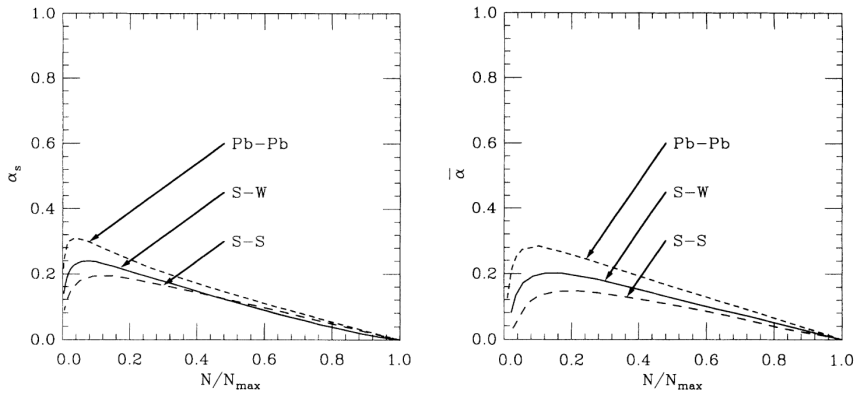

Figure 5.4: On the left figure the spatial anisotropy α_s as a function of centrality for different collision systems. On the right the transverse momentum anisotropy $\bar{\alpha} = \left(\langle p_x^2\rangle - \langle p_y^2\rangle\right) / \left(\langle p_x^2\rangle + \langle p_y^2\rangle\right)$, where averaging runs over a large number of fragments, as a function of centrality for different collision systems. Figure taken from [204].

mend to divide the (pseudo)rapidity into smaller bins and study the azimuthal corrections in each separately enabling reconstruction of three-dimensional event shape as it is done in [208]. A quantity of azimuthal distribution is expressed with $r(\phi) = \mathrm{d}p_\mathrm{T}/\mathrm{d}\phi$ which is periodical by definition and can be written in the form of Fourier expansion

$$r(\phi) = \frac{x_0}{2\pi} + \frac{1}{\pi}\sum_{n=1}^{\infty}\left[x_n\cos(n\phi) + y_n\sin(n\phi)\right], \tag{5.3}$$

$$x_n = \int_0^{2\pi} r(\phi)\cos(n\phi)\mathrm{d}\phi = \sum_{\nu=1}^{N_\eta} r_\nu\cos(n\phi_\nu), \tag{5.4}$$

$$y_n = \int_0^{2\pi} r(\phi)\sin(n\phi)\mathrm{d}\phi = \sum_{\nu=1}^{N_\eta} r_\nu\sin(n\phi_\nu), \tag{5.5}$$

where the integrals become sums over particles in selected (pseudo)rapidity window because of a finite number of particles in the real events. If there was no azimuthal anisotropy, all x_n and y_n would be zero, otherwise nonzero values would lead to, what the authors call, "n-th type flow" characterised by magnitude $v_n = \sqrt{x_n^2 + y_n^2}$ and angle $\psi_n \in (0; \frac{2\pi}{n})$:

$$x_n = v_n\cos(n\psi_n) \qquad y_n = v_n\sin(n\psi_n). \tag{5.6}$$

The designation directed to v_1 and elliptic flow to v_2 were used for the first time in this article due to obvious geometrical interpretation. Furthermore, the authors elucidated the connection of their new method to the two commonly used methods of Danielewicz and Odyniec [200] respective Ollitrault [204]. In the first case, the $\vec{Q} = \sum_\nu \omega_\nu \vec{p}_\mathrm{T}(\nu)$ vector coincides with $\vec{v}_1 \equiv (v_1, \phi_1)$ for the choice $\omega_\nu = 1$. The second connection to the transverse sphericity tensor $S_{ij}^\perp \equiv \sum_\nu \omega_\nu p_i(\nu)p_j(\nu)$ or in other notation $S^\perp = \frac{T}{2}\begin{pmatrix} 1+\varepsilon\cos 2\theta & \varepsilon\sin 2\theta \\ \varepsilon\sin 2\theta & 1-\varepsilon\cos 2\theta \end{pmatrix}$ is by choice of weights $\omega_\nu = r_\nu/p_\mathrm{T}^2(\nu)$. The trace of the tensor is then $T = \mathrm{tr}S_{ij}^\perp = \sum_\nu r_\nu = v_0$ and from eigenvalues we can obtain eccentricity $\varepsilon = v_2/v_0$ and angle $\theta = \psi_2$. This method

was further developed by Poskanzer and Voloshin in [209], which is often referred to as the standard method, will be discussed in detail in section 5.2 as it is the method I used for the kaon flow analysis.

Recent development of flow analysis focuses mainly on separation of collective (flow) and few particle correlations, and also the event-by-event fluctuation of flow [190]. The underlying idea is the utilization of so-called cumulants [210], that subtract the nonflow contribution to the first order (can be improved by the so-called Lee-Yang zeros method to all orders [211]). It uses the idea of omitting the estimation of reaction plane using the particle-pair [212] (or multi-particle) correlations for the flow harmonic determination. In the standard analysis [213] the Fourier coefficients are defined $v_n \equiv \langle \cos\left[n(\phi - \Psi_{\mathrm{RP}})\right]\rangle = \langle e^{in(\phi-\Psi_{\mathrm{RP}})}\rangle$. However, the determination of the exact angle of reaction plane is impossible in a real experiment, and only estimation can be used, which implies inaccuracy. One can use the particle correlations instead

$$\begin{aligned}\left\langle\left\langle e^{in(\phi_1-\phi_2)}\right\rangle_{\text{particles}}\right\rangle_{\text{events}} &= \left\langle\left\langle e^{in(\phi_1-\Psi_n-(\phi_2-\Psi_n))}\right\rangle\right\rangle \\ &= \left\langle\left\langle e^{in(\phi_1-\Psi_n)}\right\rangle\left\langle e^{in(\phi_2-\Psi_n)}\right\rangle\right\rangle = v_n^2, \end{aligned} \tag{5.7}$$

where ϕ_j denotes the azimuthal angle of j-particle, Ψ_n is the estimate of the reaction plane for n-th flow harmonic. This can be generalized to $2k$-particle correlations. The problems of (5.7) arise from trivial self-correlations, physical correlations (like HBT effect [214]) and detector effects (acceptance). Therefore, we define (second order) cumulants

$$\left\langle\left\langle e^{in(\phi_1-\phi_2)}\right\rangle\right\rangle_{\mathrm{c}} \equiv \left\langle\left\langle e^{in(\phi_1-\phi_2)}\right\rangle\right\rangle - \left\langle\left\langle e^{in\phi_1}\right\rangle\right\rangle\left\langle\left\langle e^{-in\phi_2}\right\rangle\right\rangle, \tag{5.8}$$

where the brackets on the RHS mean averaging over all particle-pairs and over all events. If one imagines a perfect detecor with isotropic acceptance then $\langle e^{in\phi_j}\rangle = 0$ and the cumulant is directly connected to the v_n^2. For realistic detector the cumulant retains the physical correlations of particle pairs since if ϕ_1 and ϕ_2 are uncorrelated (no collective effect), the cumulant is zero. The non-flow but physical contribution to the cumulant is generally isotropic and would scale with multiplicity as $1/M$ [214]. Since the calculated harmonic of cumulants is affected by fluctuations[3] and non-flow effects new notation is used $v_n\{2\} \equiv \sqrt{\left\langle\left\langle e^{in(\phi_1-\phi_2)}\right\rangle\right\rangle_{\mathrm{c}}}$. This procedure can be generalized as mentioned for more than one particle pair [215].

With the immense increase of collected data in heavy-ion experiments, the dominant source of total uncertainty of measured flow harmonics became systematic uncertainty. The cumulant method of flow analysis partially solves this issue by clearly separating the flow and non-flow effects if one possesses large enough data sample (in order of millions of events). This method is important mainly in case of high energy heavy-ion collisions, e.g. experiments at SPS, RHIC and LHC accelerator, where the multiplicity in one event reaches above 1000 particles and the dominant particles are pions (which are influenced also by non-flow effects [214]). In comparison HADES operates at intermediate energy

[3]It was shown in [215] that in the case of the mean value of the flow moment $\langle v\rangle$ and its variance σ_v^2 the two-particle cumulant is enhanced by fluctuactions $v\{2\} \approx \langle v\rangle + \frac{1}{2}(\sigma_n^2/\langle v\rangle$ but the four-particle cumulant is suppressed $v\{4\} \approx \langle v\rangle - \frac{1}{2}(\sigma_n^2/\langle v\rangle$. Thus the true value of flow moment lies between these two estimates.

where baryons are the dominant particles and most of the background sources are suppressed.

5.2 Standard flow method

As was mentioned earlier in this section, the method published in the article of Poskanzer and Voloshin [209] would be summarised, and its actual application for HADES will be given in detail. The method presented is divided into several steps: the first is reaction plane estimation (so-called event plane), evaluation of Fourier coefficients in the expansion of the azimuthal distribution of particles with respect to the event plane, correction of these coefficients for the finite number of detected particles (division by the event plane resolution, which is estimated using the sub-event method).

5.2.1 Estimation of reaction plane

In case of differential flow analysis we study triple differential distribution

$$E\frac{\mathrm{d}^3N}{\mathrm{d}p^3} = \frac{1}{2\pi}\frac{\mathrm{d}^2N}{p_\mathrm{T}\mathrm{d}p_\mathrm{T}\mathrm{d}y}\left(1+\sum_{n=1}^{\infty}2v_n\left(p_\mathrm{T},y\right)\cos\left[n(\phi-\Psi_\mathrm{RP})\right]\right), \tag{5.9}$$

where Ψ_RP is the azimuthal angle of the reaction plane, and the Fourier coefficients v_n are easy to interpret as $v_n = \langle\cos\left[n(\phi-\Psi_\mathrm{RP})\right]\rangle$ where the brackets represent averaging over all particles in all events. As the reaction plane is not accessible in the experiment (since the actual vector of impact parameter is unknown), we must use only estimates of Ψ_RP. These estimates are usually called event planes, and for their determination the anisotropic flow is used. The event flow vector Q_n and the event plane angle Ψ_n is calculated for each harmonic independently using a set of equations

$$Q_n\cos(n\Psi_n) \quad = X_n \quad = \sum_i \omega_i\cos(n\phi_i), \tag{5.10}$$

$$Q_n\sin(n\Psi_n) \quad = Y_n \quad = \sum_i \omega_i\sin(n\phi_i), \tag{5.11}$$

where we might select only some particles i with weights ω_i for the event plane determination. One example of the determination of different harmonics for one simulated heavy-ion collision is shown on figure 5.5.

The selection of particles, which we use to determine the event plane, and particles whose anisotropic flow is under study, might lead to autocorrelations. In most of the experiments this effect is avoided with (pseudo-)rapidity separation of these sets of particles. In case of HADES the Forward-Wall (FW) detector (see section 2.6) is used for event plane determination. It detects projectile spectators, mostly protons and light ions, and their position (consequently azimuthal angle $\phi_{\mathrm{FW},i}$) together with their charge used as weight $\omega_i = |Z_i|$ defines the event plane (see figure 5.6)

$$Q_n\cos(n\Psi_n) \quad = \tfrac{1}{N_\mathrm{FW}}\textstyle\sum_{i=1}^{N_\mathrm{FW}}|Z_i|\cos(n\phi_{\mathrm{FW},i}), \tag{5.12}$$

$$Q_n\sin(n\Psi_n) \quad = \tfrac{1}{N_\mathrm{FW}}\textstyle\sum_{i=1}^{N_\mathrm{FW}}|Z_i|\sin(n\phi_{\mathrm{FW},i}). \tag{5.13}$$

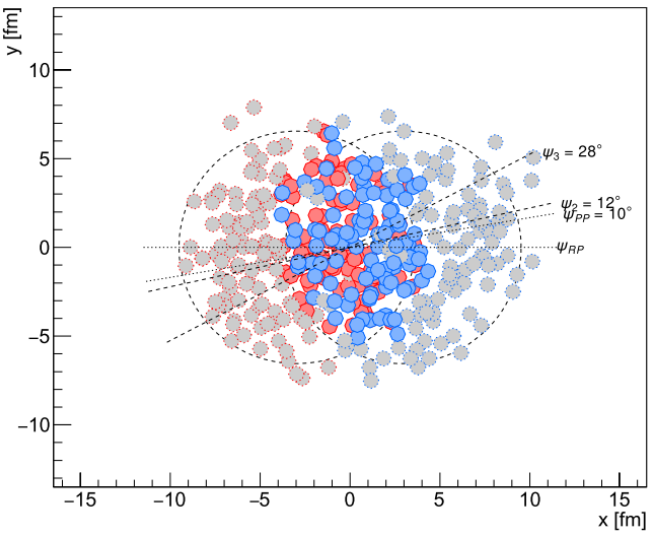

Figure 5.5: Example of the azimuthal angle of different event plane harmonics Ψ_n, the participant plane Ψ_{PP}, and the actual reaction plane angle Ψ_{RP} in one Au+Au collision at $b = 5.9\,\mathrm{fm}$. Figure taken from [206].

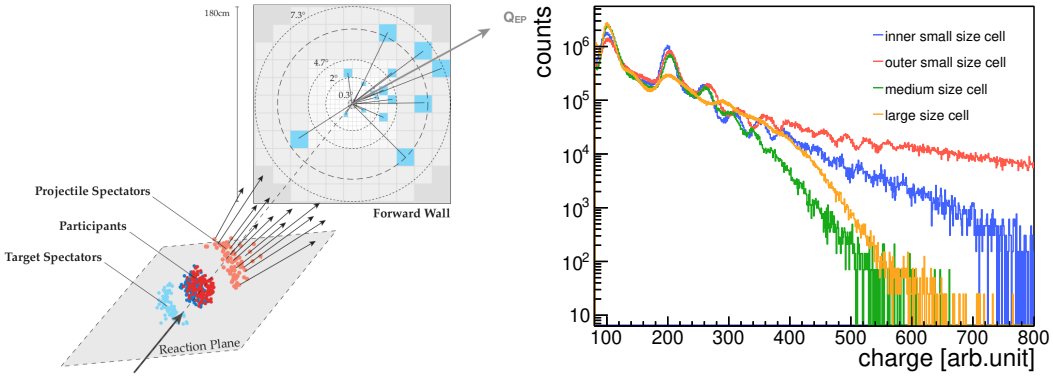

Figure 5.6: (a) Sketch of event plane determination used by HADES collaboration [156] (Credit: B. Kardan). (b) Fragment charge distribution in different Forward Wall cells.

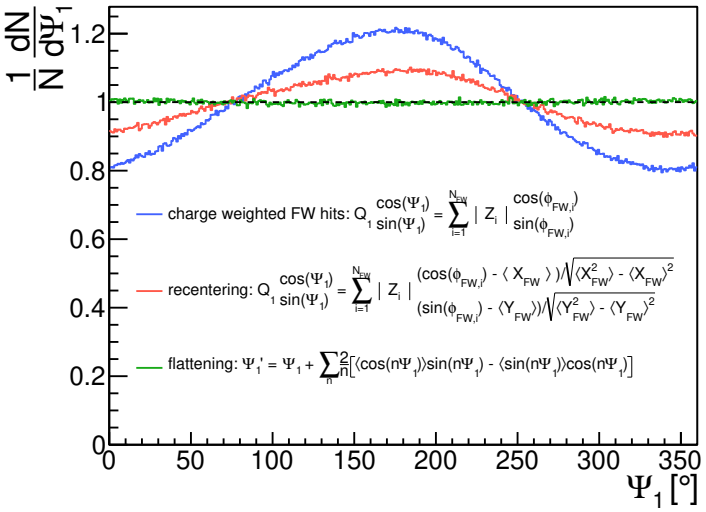

Figure 5.7: Comparison of the azimuthal angle distribution of the event plane at different stages of the flattening procedure.

In the real experiment, circumstances might arise and the distribution of the event plane azimuthal angle would not be flat as expected. This could be caused by non-uniform acceptance or possibly misalignment of the beam. In that case the first correction used by HADES [208] and other collaborations [216] is re-centering, i.e., for the HADES case each FW hit is shifted by the mean value $\langle X_{\mathrm{FW}}\rangle$ and $\langle Y_{\mathrm{FW}}\rangle$ in a certain period of time (changes might occur due to possible beam tuning during experiment or broken FW channels) and divided by square root of variances $\sqrt{\langle X_{\mathrm{FW}}^2\rangle - \langle X_{\mathrm{FW}}\rangle^2}$ respective $\sqrt{\langle Y_{\mathrm{FW}}^2\rangle - \langle Y_{\mathrm{FW}}\rangle^2}$. However this would not remove higher harmonics and additional flattening is needed. One possibility is to use measured $\frac{1}{N}\frac{\mathrm{d}N}{\mathrm{d}\Psi_n}$ distribution for weight definition (inverse values). In HADES we use the approach detailed in appendix of [216]. The calculated Ψ_1 is shifted $\Psi_1' = \Psi_1 + \Delta\Psi_1$, where

$$\Delta\Psi_1 = \sum_n \left[A_n \cos(n\Psi_1) + B_n \sin(n\Psi_1)\right]. \tag{5.14}$$

One can require the vanishing of n-th Fourier moments of the new $\frac{1}{N}\frac{\mathrm{d}N}{\mathrm{d}\Psi_1'}$ distribution, which leads to

$$A_n = -\tfrac{2}{n}\langle \sin(n\Psi_1)\rangle_{\mathrm{events}} \tag{5.15}$$

$$B_n = \tfrac{2}{n}\langle \cos(n\Psi_1)\rangle_{\mathrm{events}}. \tag{5.16}$$

Using this procedure, we can get the event plane azimuthal angle distribution flat within 1%, see figure 5.7.

5.2.2 Fourier decomposition with respect to Ψ_n

One can study the Fourier coefficients v_n using any harmonic m of the reaction plane estimation if $n \geq m$, and n must be a multiple of m, e.g. Ψ_1 can be used for any v_n, Ψ_2 only for even n, Ψ_3 for $v_{3,6,\ldots}$, etc. The Fourier decomposition from (5.9) thus changes to

$$\frac{\mathrm{d}(wN)}{\mathrm{d}(\phi - \Psi_m)} = \frac{\langle wN\rangle}{2\pi}\left(1 + \sum_{k=1}^{\infty} 2v_{km}^{\mathrm{obs}} \cos\left[km(\phi - \Psi_m)\right]\right), \tag{5.17}$$

where the general weights w are equal to p_{T} in the case of transverse momentum flow analysis, but could also be unity for the study of flow of a number of particles. In HADES case we are using only the first harmonic Ψ_1 as event plane for all v_n because at rather low energy HIC the multiplicity of particles is much smaller compared to experiments at RHIC and LHC, and the Fourier coefficients for higher harmonics are small too, see [206, 208].

The coefficients $v_n^{\mathrm{obs}} = \langle \cos\left[n(\phi - \Psi_m)\right]$ are always smaller than the true v_n, implying the necessity of the so-called event plane resolution correction

$$v_n = \frac{v_n^{\mathrm{obs}}}{\langle \cos\left[km(\Psi_m - \Psi_{\mathrm{RP}})\right]\rangle}. \tag{5.18}$$

5.2.3 Event plane resolution

The event plane resolution $\langle \cos\left[km(\Psi_m - \Psi_{\mathrm{RP}})\right]\rangle$ depends on the harmonic m used for event plane determination as well as on the order n of Fourier coefficients. For the analytical calculation of the resolution (performed in [207]) one starts with a probability distribution

$$\frac{\mathrm{d}\mathcal{P}}{\mathrm{d}\left[m(\Psi_m - \Psi_{\mathrm{RP}})\right]} = \int \frac{v_m' \mathrm{d}v_m'}{2\pi\sigma^2} \exp\left(-\frac{v_m^2 + v_m'^2 - 2v_m v_m' \cos\left[m(\Psi_m - \Psi_{\mathrm{RP}})\right]}{2\sigma^2}\right), \tag{5.19}$$

where the parameter $\sigma^2 = \frac{1}{2M}(\langle w^2\rangle / \langle w\rangle^2)$ and M is the number of particles used for event plane determination. After analytical integration one gets the resolution

$$\langle \cos\left[km(\Psi_m - \Psi_{\mathrm{RP}})\right]\rangle = \frac{\sqrt{\pi}}{2\sqrt{2}} \chi_m \exp(-\chi_m^2/4) \left[I_{\frac{k-1}{2}}(\chi_m^2/4) + I_{\frac{k+1}{2}}(\chi_m^2/4)\right], \tag{5.20}$$

where $\chi_m \equiv v_m/\sigma$ and I_ν is the modified Bessel function of order ν.

To overcome the inaccessibility of the reaction plane in experiments, two independent sets a, b of particles (either from different phase space windows or a random distribution of the so-called sub-events introduced in [200]). From trigonometry one easily deduces

$$\begin{aligned} \langle \cos\left[n(\Psi_m^a - \Psi_m^b)\right]\rangle &= \langle \cos\left[n(\Psi_m^a - \Psi_{\mathrm{RP}})\right]\rangle \times \langle \cos\left[n(\Psi_m^b - \Psi_{\mathrm{RP}})\right]\rangle \Rightarrow \\ \Rightarrow \langle \cos\left[km(\Psi_m - \Psi_{\mathrm{RP}})\right]\rangle &= \sqrt{2\langle \cos\left[km(\Psi_m^a - \Psi_m^b)\right]\rangle}, \end{aligned} \tag{5.21}$$

where the factor of 2 under the square root comes from the fact that the number of particles in sub-events is $M/2$ and the χ_m is proportional to $\sqrt{M}$.

The complicated relation (5.20) can be simplified in the case of two limits:

1. Weak flow ($\chi_m \ll 1$, i.e. low event plane resolution) where for mostly used cases $k = 1, 2$ we obtain

$$\begin{aligned} \langle \cos\left[m(\Psi_m - \Psi_{\mathrm{RP}})\right]\rangle &\approx \sqrt{\tfrac{\pi}{8}}\chi_m, \\ \langle \cos\left[2m(\Psi_m - \Psi_{\mathrm{RP}})\right]\rangle &\approx \chi_m^2/4. \end{aligned}$$

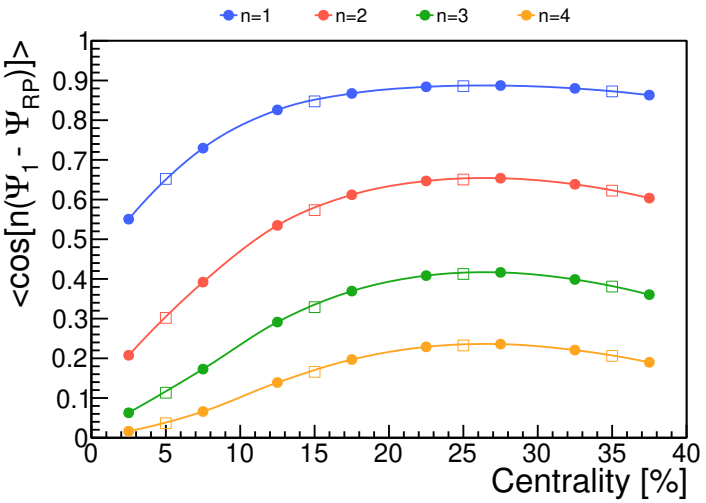

Figure 5.8: Event plane resolution $\langle \cos[n(\Psi_1 - \Psi_{\mathrm{RP}})]\rangle$ for different harmonics of Fourier decomposition as a function of centrality. Full circles are for 5% and open squares for 10% centrality classes, lines are only to guide the eyes.

2. Strong flow ($\chi_m \gg 1$, usually for low-energy collisions) where the interpolation technique results in approximate equations (valid for $\chi_m < 3$)

$$\begin{aligned}\langle \cos[m(\Psi_m - \Psi_{\mathrm{RP}})]\rangle = \; & 0.626657\chi_m - 0.09694\chi_m^3 + 0.02754\chi_m^4 \\ & -0.002283\chi_m^5, \\ \langle \cos[2m(\Psi_m - \Psi_{\mathrm{RP}})]\rangle = \; & 0.25\chi_m^2 - 0.011414\chi_m^3 - 0.034726\chi_m^4 \\ & +0.006815\chi_m^5.\end{aligned}$$

Different approximate method introduced in [217] is using the ratio of events in which the gap between the two subevent event planes is greater than $\pi/2$ to the number of all events

$$\frac{N\left(m\left|\Psi_m^a - \Psi_m^b\right| > \pi/2\right)}{N_{\mathrm{total}}} = \frac{\exp(-\chi_m^2/4)}{2}. \tag{5.22}$$

The calculated χ_m from this relation is then inserted into (5.20) and the resolution is calculated for any k. However, equation (5.22) is valid also only for not too large χ_m due to the exponential decrease of the right-hand side with increasing χ_m leading to very small values with large statistical fluctuation.

Since HADES is using directed flow of projectile spectators for event plane determination for all harmonics of Fourier decomposition of the azimuthal angle distribution, the resolution corrections are slightly higher than they could be in the case of using higher harmonics also for event plane determination. The values obtained from equations (5.20) and (5.22)[4] are displayed on figure 5.8.

[4]The condition on smallness of χ_m is satisfied within $\chi_m < 2.5$.

Chapter 6

Results on kaon flow

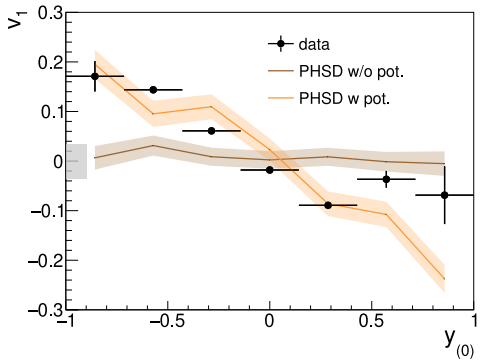

This chapter is dedicated to the results of the kaon flow analysis. It will start with the description of the individual steps towards flow coefficients v_n (in the section 6.1). Then the evaluation of systematic uncertainty will be the content of section 6.2. The obtained results will be given in the section 6.3 and the closing part would contain a comparison with microscopic transport model predictions (section 6.4).

6.1 Application in differential kaon flow analysis

In this section, I will briefly summarize steps how the coefficients $v_n(\mathcal{C}, p_\mathrm{T}, y_{(0)})$ are obtained from the analysis of data collected from Au+Au collisions at $\sqrt{s_\mathrm{NN}} = 2.42\,\mathrm{GeV}$.

The first step is the data cleaning procedure described in 3.1.1 followed by the event selection detailed in 3.2. For each selected event, the centrality $\mathcal{C}$ is determined using the comparison with Glauber model simulations, see section 3.3 or [176]. Using the detected projectile fragments in the Forward Wall, the azimuthal angle of the event plane is estimated and its resolution is calculated as described above in sections 5.2.1 and 5.2.3.

All reconstructed particle tracks are examined and kaon candidates are selected via the methods depicted in chapter 4. Candidates are classified based on their transverse momentum p_T, normalized rapidity $y_{(0)}$, difference in azimuthal angle with respect to the event plane $\Delta\phi = \phi_\mathrm{K} - \Psi_1$, and the centrality of the event $\mathcal{C}$. For each group of kaon candidates, the background tracks are subtracted and the cleaned number of kaons is used for $\mathrm{d}N(\mathcal{C}, p_\mathrm{T}, y_{(0)})/\mathrm{d}\Delta\phi$ distribution, see figure 6.1. These spectra are then fitted with Fourier decomposition (5.17) with $m = 1$ and $k \leq 4$, and the obtained values v_{1-4}^obs are corrected for the event plane resolution (5.18). To get the final results for $v_n(\mathcal{C}, p_\mathrm{T}, y_{(0)})$ one must do the systematic uncertainty study. However, it was found that the very high multiplicity environment is influencing the performance of the HADES spectrometer, which required the introduction of so-called occupancy corrections.

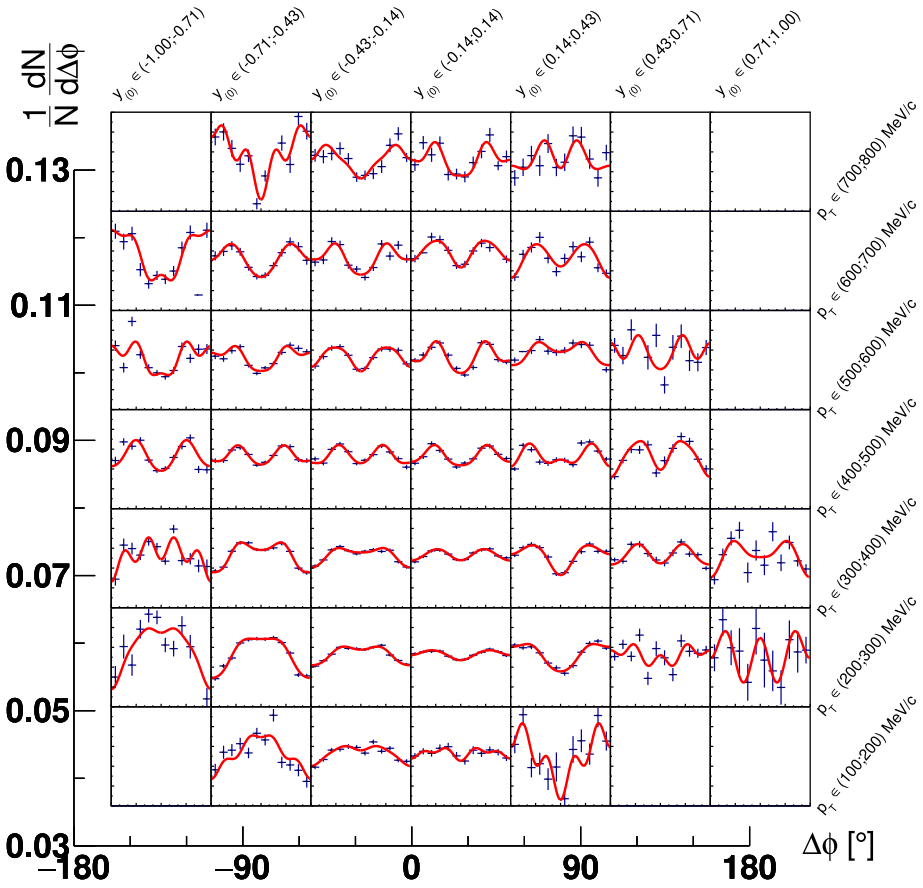

Figure 6.1: K^+ normalized azimuthal angle distributions w.r.t. event plane for centrality class $20-30\%$ and each phase space bin fitted with function (5.17) up to fourth order. For better readability, the enlarged axes are displayed on the side.

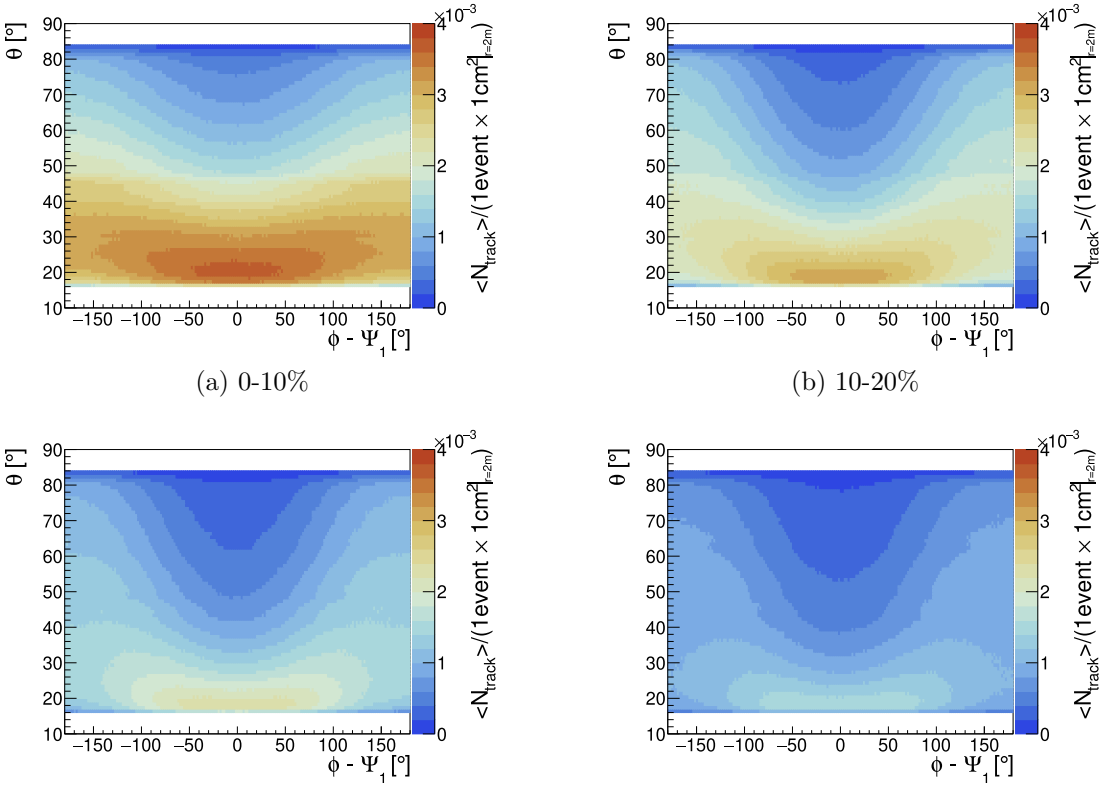

(a) 0-10%

(b) 10-20%

(c) 20-30%

(d) 30-40%

Figure 6.2: Distribution of track density for each analysed centrality class as a function of polar angle θ and azimuthal angle difference with respect to event plane angle $\phi - \Psi_1$.

6.1.1 Occupancy corrections

As already mentioned, the actual efficiency of track reconstruction in central collisions is decreasing with the impact on flow measurement due to the higher concentration of tracks around the reaction plane[1]. The density of tracks per event and $1\,\mathrm{cm}^2$ at a distance of $2\,\mathrm{m}$ from the target is displayed on figure 6.2 separately for each centrality class but keeping the same scale of the color axis. It is obvious from the figures that due to the higher density of tracks close to the azimuthal angle of the event plane (which we use as an approximation to the true inaccessible reaction plane angle), and for lower polar angles the effect on the measured tracks will differ significantly. It should be mentioned that this is not a problem of HADES spectrometer alone, but similar corrections were implemented in other experiments too, e.g. FOPI [218] and PHOBOS [219].

The effect of track density around a particular track of interest was studied using the HGeant simulations, however, the obtained corrections were not able to fully compensate the observed effect. Thus, a data-driven approach was developed using an assumption of a linear or quadratic dependency of the track reconstruction efficiency on the track density $\langle \rho_{\mathrm{track}} \rangle = N_{\mathrm{track}}/(1\,\mathrm{event} \times 1\,\mathrm{cm}^2|_{r=2m})$

[1]The origin of the loss of tracks lies in the ambiguity of the assignment of firing drift cells to a given track. Within a certain cut window, the tracking algorithm is not able to distinguish between two tracks within a very small space-time window.

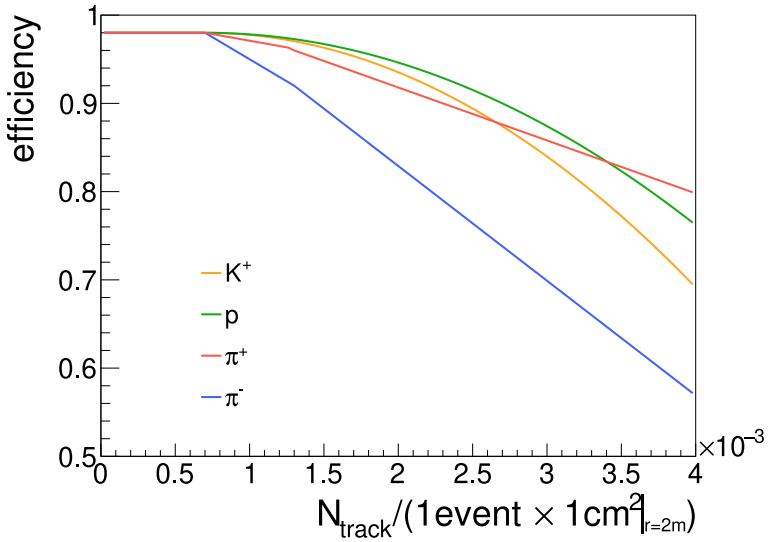

Figure 6.3: Functional dependence $\varepsilon_{\text{occup}}(\langle\rho_{\text{track}}\rangle)$ for selected particle species.

$$\varepsilon_{\text{occup}}(\langle\rho_{\text{track}}\rangle) = \varepsilon_{\text{max}} - C(\langle\rho_{\text{track}}\rangle - \rho_0)^{1 \text{ or } 2}, \tag{6.1}$$

where we know from the simulations that for $\langle\rho_{\text{track}}\rangle < \rho_0$ there is no decrease of efficiency due to track density and therefore $\varepsilon_{\text{occup}} = \varepsilon_{\text{max}}$. The values $\rho_0 = 7.\times10^{-4}$ and $\varepsilon_{\text{max}} = 0.98$ were obtained from simulations. Due to different dynamics of each particle species, these corrections have to be also particle dependent and thus the value of constant C has to adjusted respectively (pions [156, 220], electrons [221], protons [156] and Lambda hyperons [222]). The functional dependence of the applied corrections for selected particle species is shown on figure 6.3. For decaying particles like K^0_S and Λ the efficiency is calculated as a multiple of the efficiencies of the decay products.

The requirement given for the determination of a constant C is the symmetry of directed flow expressed in the form of $v_1(\mathcal{C}, p_\text{T}, y_{(0)} = 0) = 0$. This ideal state is, however, difficult to achieve with just one parameter, thus we actually want to obtain a smaller directed flow after the correction than it was before $\left|v_1^{\text{corr}}(y_{(0)} = 0)\right| < \left|v_1^{\text{raw}}(y_{(0)} = 0)\right|$. Different values of coefficient and also linear dependence were tested as a part of systematical uncertainty evaluation. Each track is finally weighted with the inverse of the efficiency $w_{\text{occup}} = 1/\varepsilon_{\text{occup}}$. The comparison of directed flow measurements before and after correction is presented on figure 6.4.

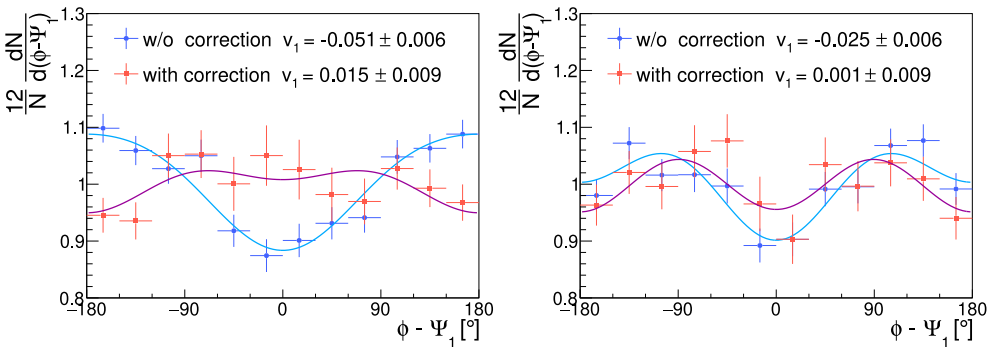

(a) 0-10% (b) 20-30%

Figure 6.4: Positively charged kaon azimuthal angle distribution w.r.t. event plane with and without the occupancy corrections for the midrapidity bin ($y_{(0)} \in (-0.14; 0.14)$) and low transverse momenta ($p_{\mathrm{T}} \in (200; 300)\,\mathrm{MeV}/c$). These values correspond to $\theta \approx 30°$ through an equation $\tan^2\theta = p_{\mathrm{T}}^2 / \left[\sinh^2 y\,(p_{\mathrm{T}}^2 + m^2)\right]$.

6.2 Systematic uncertainty evaluation

To evaluate the systematic uncertainty of the flow coefficients $v_n(\mathcal{C}, p_{\mathrm{T}}, y_{(0)})$ I made several changes in the analysis procedure or varied the values of some parameters and observed how they affect the coefficients. Due to rather large statistical fluctuations, I averaged the differences $\delta v_n = \left|v_n - v_n^{\mathrm{varied}}\right|$ over all phase space bins ($N_{\mathrm{PSB}} = N_{p_{\mathrm{T}}}^{\mathrm{bins}} \cdot N_{y_{(0)}}^{\mathrm{bins}}$) in one centrality class

$$\sigma_{\mathrm{sys}}(\mathrm{variation}) = \frac{1}{N_{\mathrm{PSB}}} \sum_{i=1}^{N_{\mathrm{PSB}}} \frac{\left|v_n - v_n^{\mathrm{varied}}\right|}{\sqrt{\sigma_{\mathrm{stat}}^2(v_n) + \sigma_{\mathrm{stat}}^2(v_n^{\mathrm{varied}})}}. \tag{6.2}$$

The total systematic error is then calculated as the square root of the sum of squares over all variations

$$\sigma_{\mathrm{total\ sys}} = \sqrt{\sum_{\mathrm{variations}} \sigma_{\mathrm{sys}}^2(\mathrm{variation})}. \tag{6.3}$$

The obtained values are summarized in tables 6.1 and 6.2.

6.2.1 Alternative flow methods

One of the arbitrary choices made in the analysis is the choice of a standard (event plane) flow analysis method, see section 5.2. There are other methods, as was presented in 5.1.

The first of the two alternative methods used for systematic uncertainty study is called the invariant mass method and is based on the article [223]. Originally it was suggested for the study of short-lived particles, e.g., Λ hyperon or $\mathrm{K}^0_{\mathrm{S}}$ meson, but it is applicable as well for directly measured particles like charged kaons if one can assume the number of background particles and their flow coefficients behave as smooth functions. The invariant mass spectrum is assumed to consist of background entries (uncorrelated pion pairs or tails of other particle species)

collision centrality	v_1				v_2			
	$0-10\%$	$10-20\%$	$20-30\%$	$30-40\%$	$0-10\%$	$10-20\%$	$20-30\%$	$30-40\%$
flow methods	0.012	0.011	0.010	0.011	0.019	0.013	0.018	0.021
number of $\Delta\phi$ bins	0.003	0.003	0.003	0.003	0.008	0.006	0.005	0.007
number of harmonics	0.001	0.001	0.001	0.001	0.002	0.002	0.002	0.003
kaon identification	0.015	0.021	0.023	0.015	0.020	0.013	0.013	0.017
track quality cuts	0.011	0.010	0.011	0.012	0.019	0.009	0.009	0.013
occupancy corrections	0.013	0.008	0.004	0.003	0.006	0.005	0.003	0.003
background subtraction	0.017	0.021	0.021	0.020	0.012	0.007	0.006	0.009
total	0.031	0.035	0.035	0.030	0.037	0.023	0.025	0.032

Table 6.1: Summary table of the influence of individual variations on the directed and elliptic flow of K^+, respectively.

collision centrality	v_1				v_2			
	$0-10\%$	$10-20\%$	$20-30\%$	$30-40\%$	$0-10\%$	$10-20\%$	$20-30\%$	$30-40\%$
flow methods	0.018	0.013	0.017	0.016	0.031	0.033	0.020	0.032
number of $\Delta\phi$ bins	0.006	0.003	0.004	0.007	0.026	0.011	0.010	0.012
number of harmonics	0.001	0.001	0.001	0.002	0.002	0.002	0.002	0.004
pion identification	0.018	0.012	0.011	0.013	0.024	0.012	0.014	0.022
topology selection	0.023	0.019	0.015	0.019	0.059	0.030	0.022	0.031
topology precuts	0.016	0.009	0.009	0.009	0.020	0.016	0.014	0.017
MLP threshold value	0.014	0.009	0.008	0.012	0.029	0.017	0.012	0.017
occupancy corrections	0.017	0.015	0.007	0.006	0.014	0.009	0.005	0.008
background subtraction	0.025	0.016	0.020	0.017	0.054	0.028	0.022	0.018
total	0.051	0.036	0.036	0.037	0.100	0.061	0.045	0.060

Table 6.2: Summary table of the influence of individual variations on the directed and elliptic flow of K^0_S, respectively.

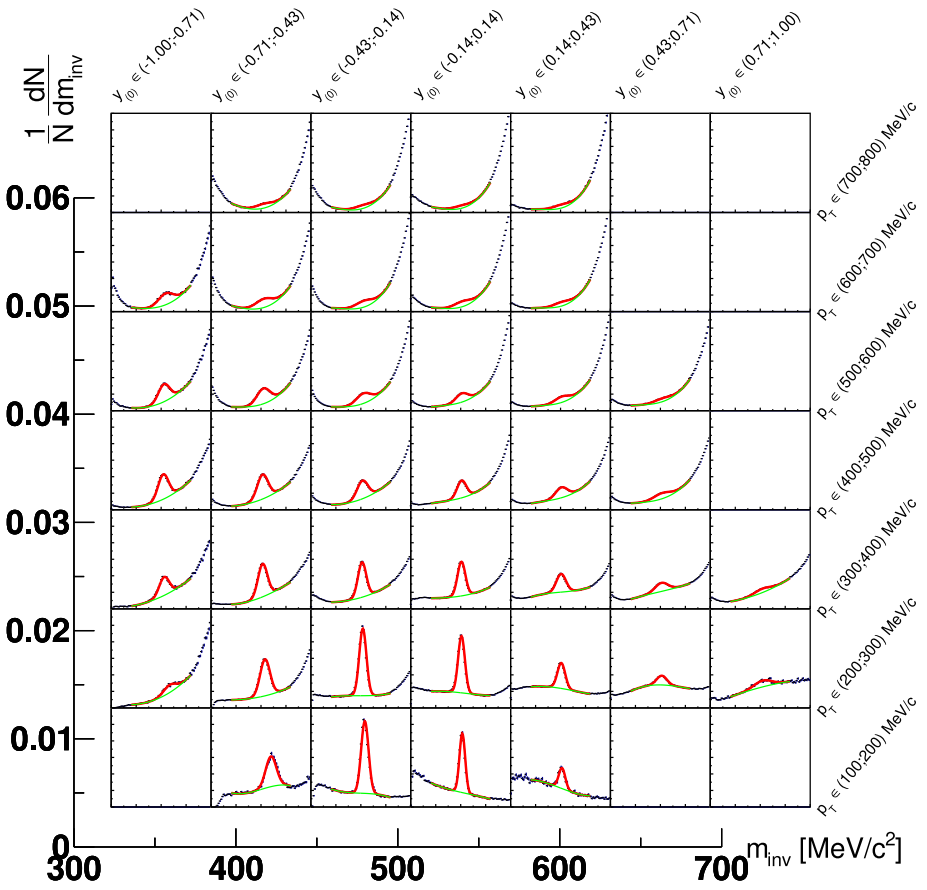

Figure 6.5: K^+ normalized invariant mass distributions for centrality class 20 – 30% and each phase space bin fitted with sum of Gaussian and cubic polynomial functions. For better readability, the enlarged axes are displayed on the side.

and signal entries (represented by a peak in the spectrum) $N_{\text{candidates}}(m_{\text{inv}}) = N_{\text{S}}(m_{\text{inv}}) + N_{\text{B}}(m_{\text{inv}})$. Then one can make a decomposition, using the assumption of smoothness as mentioned above, of the observed mean value over all candidates in all events

$$v_{n,\text{S+B}}^{\text{obs}}(m_{\text{inv}}) = \langle \cos[n(\phi_{\text{K}} - \Psi_1)] \rangle (m_{\text{inv}}) \tag{6.4}$$

$$v_{n,\text{S+B}}^{\text{obs}}(m_{\text{inv}}) = v_{n,\text{S}}^{\text{obs}} \left[\frac{N_{\text{S}}}{N_{\text{S}}+N_{\text{B}}} \right] (m_{\text{inv}}) + v_{n,\text{B}}^{\text{obs}}(m_{\text{inv}}) \left[\frac{N_{\text{B}}}{N_{\text{S}}+N_{\text{B}}} \right] (m_{\text{inv}}), \tag{6.5}$$

where we assume a polynomial function for $v_{n,\text{B}}^{\text{obs}}(m_{\text{inv}}) = \sum_i p_i m_{\text{inv}}^i$. The observed values must be still corrected for the event plane resolution in the same way as in the case of the standard method. In practice, we fill `TProfile` histograms in ROOT with the calculated $\cos[n(\phi_{\text{K}} - \Psi_1)]$ for each selected track and its weight (occupancy correction, etc.). Alongside we also fill invariant mass histograms which are used as well in standard method for the extraction of the number of signal entries (for each invariant mass bin, we need to know N_{S} and N_{B}, see 4.1.4 and 4.2.4), see figure 6.5. Then we fit `TProfile` histograms with function corresponding to formula (6.5) and assuming cubic polynomial function for background $v_{n,\text{B}}^{\text{obs}}(m_{\text{inv}})$, which is also used for the background estimation in the invariant mass spectrum, see figures 6.6 and 6.7.

The second method is based on the comparison between quarters of the azimuthal angle distribution with respect to the event plane. Similarly to the

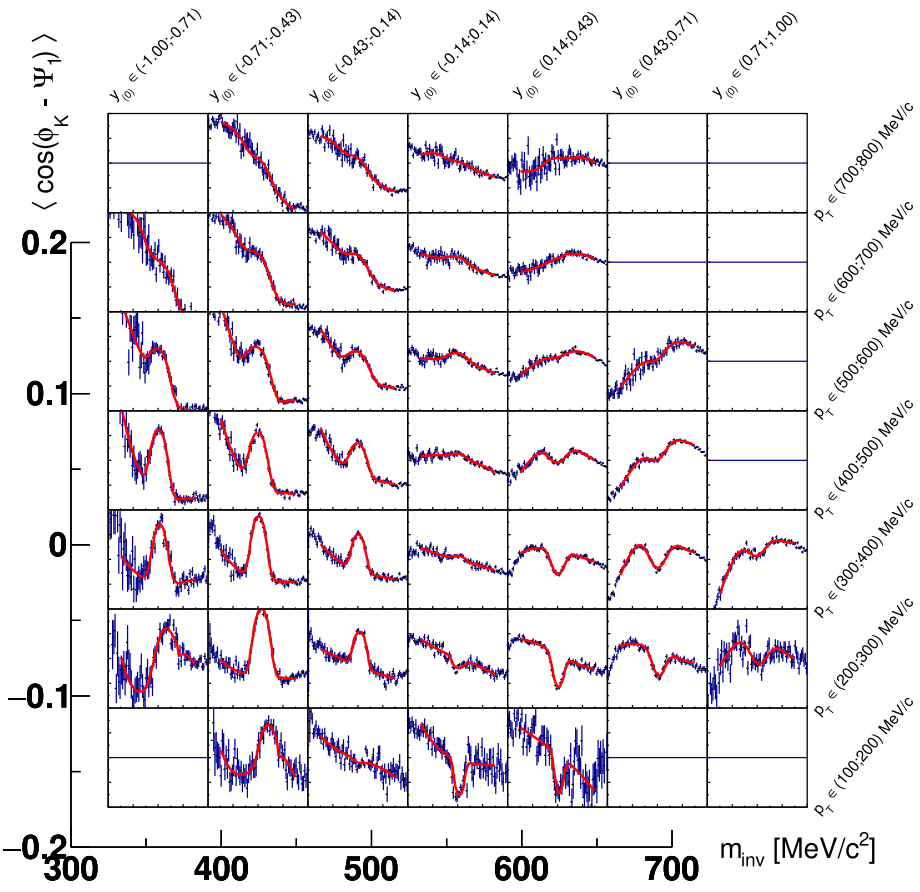

Figure 6.6: Mean values of $\cos(\phi_{\mathrm{K}^+} - \Psi_1)$ for centrality class $20 - 30\%$ and each phase space bin fitted with function (6.5). For better readability, the enlarged axes are displayed on the side.

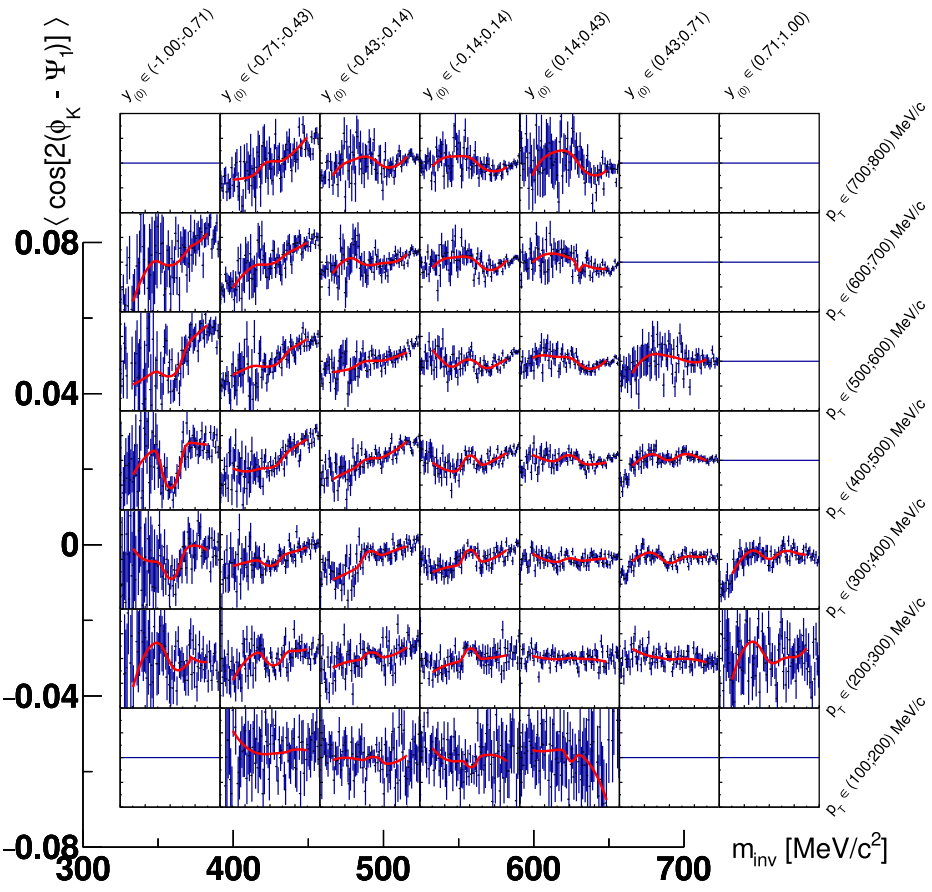

Figure 6.7: Mean values of $\cos[2(\phi_{\mathrm{K}^+} - \Psi_1)]$ for centrality class $20-30\%$ and each phase space bin fitted with function (6.5). For better readability, the enlarged axes are displayed on the side.

standard method, we study the distribution $\mathrm{d}N(\mathcal{C}, p_\mathrm{T}, y_{(0)})/\mathrm{d}\Delta\phi$ but the width of $\Delta\phi$ bin is 90° and they are centered around the major axis of the virtual ellipse of the overlap region (first bin corresponds to $-45° \leq \Delta\phi < 45°$, second bin $45° \leq \Delta\phi < 135°$, etc.). We designate the number of kaons within one quarter with the corresponding difference of azimuthal angles $\Delta\phi = \phi_\mathrm{K} - \Psi_1$ of the center of the bin ($N_0 \sim -45° \leq \Delta\phi < 45°$). Then we can use the ratios [217]

$$R_{\mathrm{in-plane}} = \frac{N_0}{N_{180}} \tag{6.6}$$

$$R_{\mathrm{squeeze}} = \frac{N_{90} + N_{270}}{N_0 + N_{180}} \tag{6.7}$$

together with the trimmed Fourier decomposition of the azimuthal angle distribution[2]

$$\frac{\mathrm{d}N}{\mathrm{d}\Delta\phi} \approx \mathrm{const}\left(1 + 2v_1^{\mathrm{obs}}\cos(\Delta\phi) + 2v_2^{\mathrm{obs}}\cos(2\Delta\phi)\right). \tag{6.8}$$

Using these equations, one can derive

$$v_2^{\mathrm{obs}} = \frac{1}{2}\frac{1 - R_{\mathrm{squeeze}}}{1 + R_{\mathrm{squeeze}}} \tag{6.9}$$

$$v_1^{\mathrm{obs}} = \frac{1}{2}\frac{(1 + 2v_2^{\mathrm{obs}})(R_{\mathrm{in-plane}} - 1)}{1 + R_{\mathrm{in-plane}}}, \tag{6.10}$$

which are necessary to correct for the event plane resolution to obtain v_1 and v_2.

The comparison of K^+ differential flow $v_{1,2}(p_\mathrm{T}, y_{(0)})$ for collision centrality $20 - 30\%$ is shown on figures 6.8 and 6.9.

Furthermore, I tried to vary the number of $\Delta\phi$ bins used in histograms displayed on figure 1.12b, so the bin width would change from 30° to 20° and 40° respectively. Likewise, I tested the dependency of $v_{1,2}^{\mathrm{obs}}$ from standard flow method on the number of harmonics used in the Fourier decomposition 5.17. Both of these changes have only a very small impact on the value of $v_{1,2}$ as can be seen from tables 6.1 and 6.2.

6.2.2 Charged kaon systematic study

Among the different flow methods and changes in the parameters of the standard method, I studied the influence of the different choices I made in the procedure of extracting the number of kaons. As already illustrated via the values in table 6.1 there were decisions which had a smaller or bigger influence on the observed Fourier coefficients.

One of the strongest effects was found to come from the identification of kaon candidates. The original was described in 4.1 and the alternative approach was based on the work of a colleague from the HADES collaboration. He suggested to use instead of graphical cuts on the specific energy losses, fixed cut values on the variables products of the energy losses in MDC drift chambers and TOF scintillator rods on the particle momentum p, respectively, a multiple of relativistic factors $\beta\gamma$. The actual values used in this alternative way are summarised in

[2]This simplification can be justified based on the results from the standard method, where higher coefficients $v_{3,4}$ are comparable with zero within statistical uncertainties.

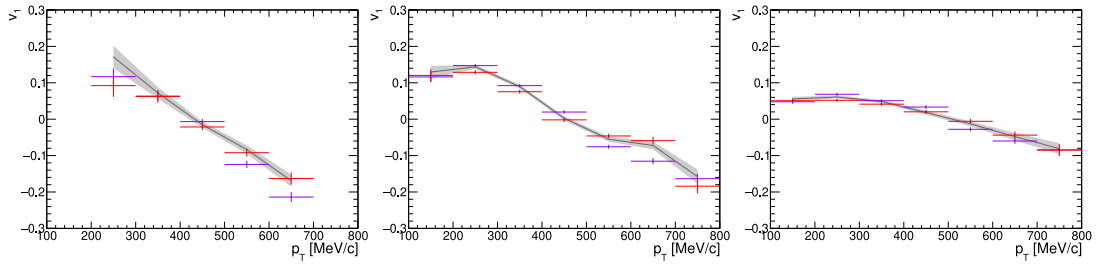

(a) $y_{(0)} \in (-1.00; -0.71)$ (b) $y_{(0)} \in (-0.71; -0.43)$ (c) $y_{(0)} \in (-0.43; -0.14)$

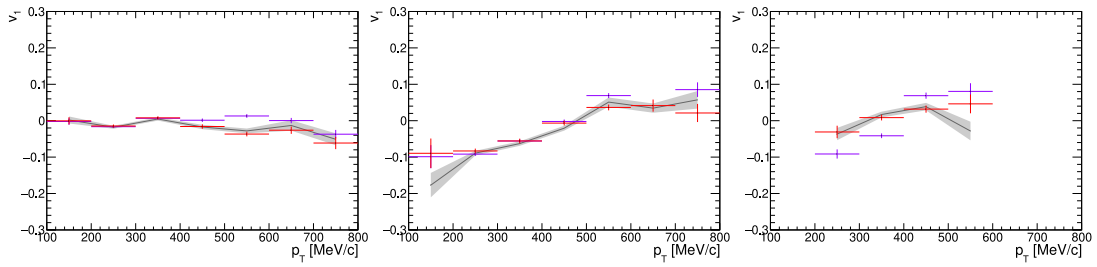

(d) $y_{(0)} \in (-0.14; 0.14)$ (e) $y_{(0)} \in (0.14; 0.43)$ (f) $y_{(0)} \in (0.43; 0.71)$

Figure 6.8: Differential directed flow of K^+ in collisions with $20-30\%$ centrality determined using 3 methods described in the text. The standard method is represented with a gray line and shaded area, blue points are for the invariant mass method and red points for the quarters method.

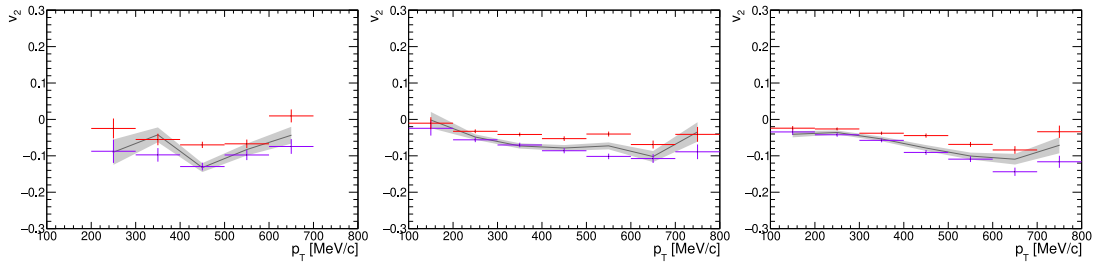

(a) $y_{(0)} \in (-1.00; -0.71)$ (b) $y_{(0)} \in (-0.71; -0.43)$ (c) $y_{(0)} \in (-0.43; -0.14)$

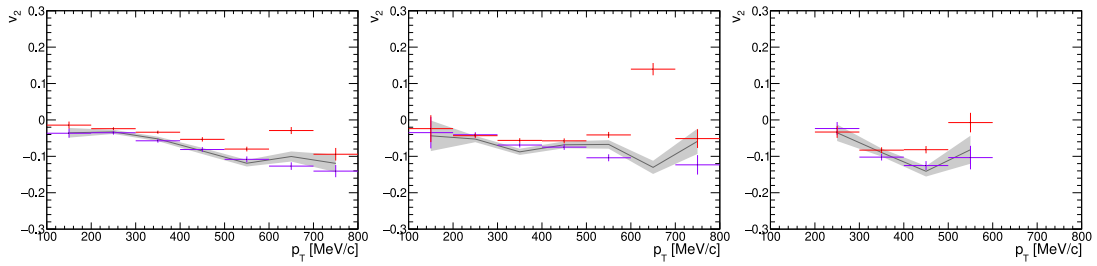

(d) $y_{(0)} \in (-0.14; 0.14)$ (e) $y_{(0)} \in (0.14; 0.43)$ (f) $y_{(0)} \in (0.43; 0.71)$

Figure 6.9: Differential elliptic flow of K^+ in collisions with $20-30\%$ centrality determined using 3 methods described in the text. The standard method is represented with a gray line and shaded area, blue points are for the invariant mass method and red points for the quarters method.

		$\mathrm{d}E_{\mathrm{MDC}}/\mathrm{d}x$	$\mathrm{d}E_{\mathrm{MDC}}/\mathrm{d}x \cdot p$	$\mathrm{d}E_{\mathrm{TOF}}/\mathrm{d}x \cdot \beta\gamma$	$p[\mathrm{MeV}/c]$
K^+	RPC	< 40	$[550; 10\,000]$		$[200; 1\,200]$
K^-	RPC		> 800		$[250; 700]$
K^+	TOF	$[1.1; 60]$	$[500; 15\,000]$	$[0.3; 3.2]$	$[150; 900]$
K^-	TOF	> 2.5	> 500	$[1.0; 2.2]$	$[250; 650]$

Table 6.3: Table of cut values used for both charged kaons registered within the specified META detector.

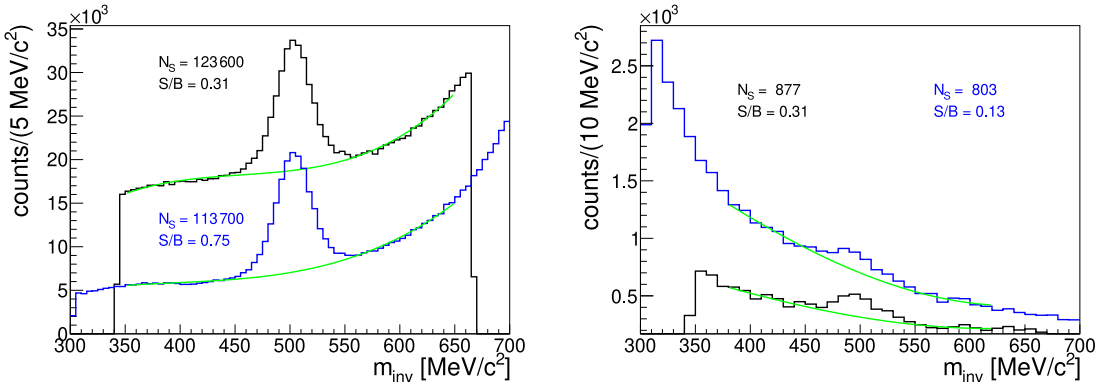

(a) K^+ (b) K^-

Figure 6.10: Comparison of two charged kaon identification methods. The original approach is shown in blue, and the alternate is in black.

table 6.3. The advantages of both ways are visible from figure 6.10. One can see that the original way is better suited for positively charged kaons and the alternative for negative ones (for which it is, however, very difficult to obtain sufficient statistics to perform flow analysis).

Other substantial systematical uncertainty comes from the background subtraction, namely, from the function used for background description in the fitting procedure of mass spectra. From figure 6.11 one can observe that in some cases the influence is not that big, but for another set of transverse momentum and normalized rapidity the difference in the number of reconstructed kaons is significant.

Only a moderate influence on the values of $v_{1,2}$ originates from the values of track quality cuts. I made one set with weaker criteria ($\chi^2_{\mathrm{RK}} < 400$ and $\chi^2_{\mathrm{MM}} < 3$) and another with stronger selection ($\chi^2_{\mathrm{RK}} < 60$ and $\chi^2_{\mathrm{MM}} < 1.5$). No bias introduced by these criteria was observed in both cases.

Finally, I tried to modify the occupancy corrections which resulted in a small bias in the case of directed flow (this effect is not surprising since these corrections are introduced to correct the midrapidity value of the directed flow) and almost no effect in the case of elliptic flow (which is again expected thanks to symmetry reasons).

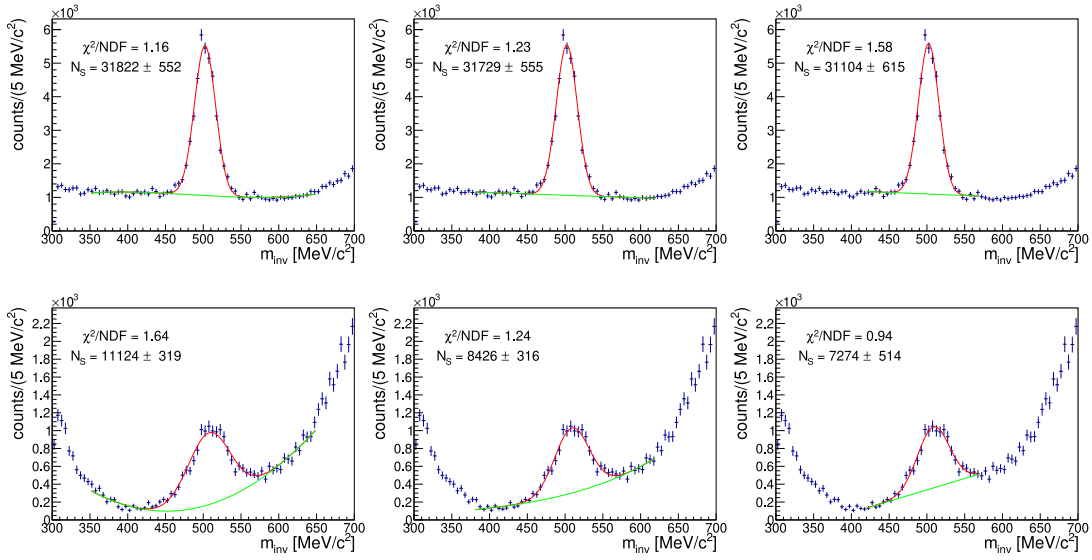

Figure 6.11: Comparison of functions used for description of background.

6.2.3 Neutral kaon systematic study

In the case of neutral kaon flow, the dominant role in the total value of systematic uncertainty, in addition to the flow methods discussed, belongs to the decay topology selection criteria and background subtraction.

The neutral kaon candidates are primarily identified based on the decision of a neural network (specifically multilayer perceptron), however, one can use sets of fixed values of decay topology variables d_{x}. This approach is compared with the outcome of the neural network on figure 6.12 together with different threshold values of Ω_{MLP}. It is obvious that we can select d_{x} in a way that almost no background uncorrelated pion pairs would pass the conditions, however, this would also decrease the number of signal (correlated) pairs, which is undesirable effect since the number of reconstructed neutral kaons is rather small compare to K^{+}. On the other hand, we can choose different values of d_{x} which would result in similar number of signal entries, however, the amount of background would increase accordingly too. A similar effect can be seen from the variation of the applied threshold value of Ω_{MLP}, see figure 6.12, however the effect on the Fourier coefficients $v_{1,2}$ is a bit smaller. For comparison, I also used a different set of topology precuts, which was applied in the analysis published in [224], with an aggregate effect similar to the variation of the neural network threshold value. Overall, the selection of neutral kaon candidate selection has a dominant role in systematic uncertainty, but it is not significantly greater than statistical uncertainty.

The background entries of the pion pair invariant mass spectra are subtracted using the mixed-event (ME) background technique. An important step in this approach is the scaling of ME spectra outside the peak that corresponds to the correlated pairs. Therefore, I tried to modify the intervals used for the scaling, which is demonstrated on figure 6.13. On the same figure is also shown the spectrum of the same event pion pairs, which were fitted with Gaussian added to

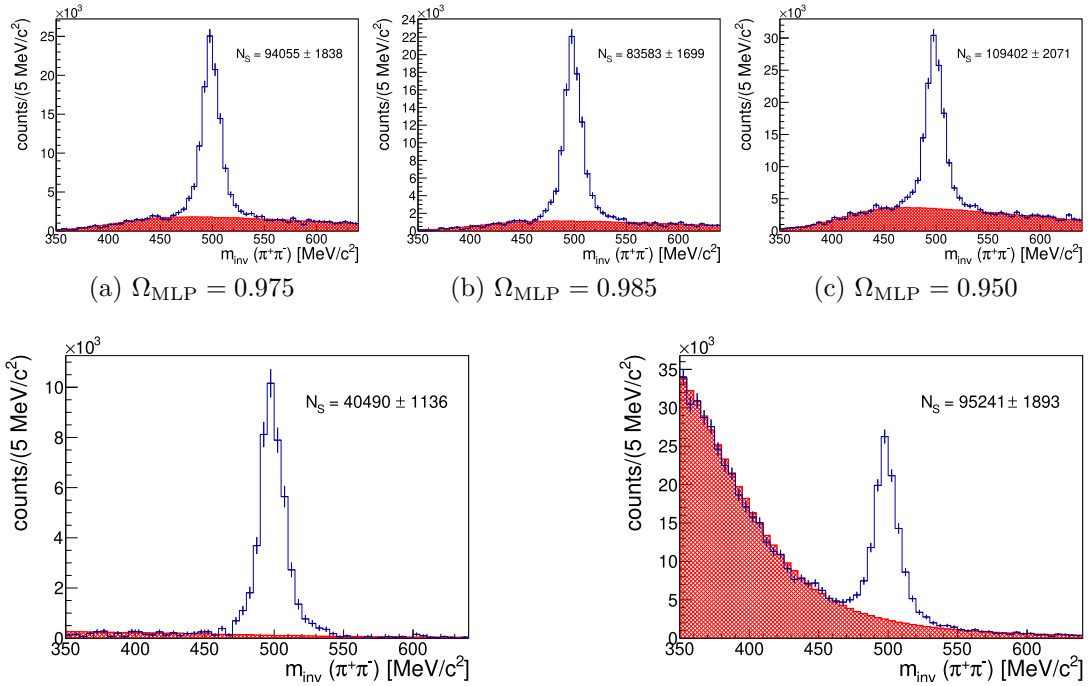

(a) $\Omega_{\mathrm{MLP}} = 0.975$ (b) $\Omega_{\mathrm{MLP}} = 0.985$ (c) $\Omega_{\mathrm{MLP}} = 0.950$

(d) $d_{\mathrm{x}} = \{16, 16, 5, 17, 10\}$ mm (e) $d_{\mathrm{x}} = \{9, 9, 7, 27, 17\}$ mm

Figure 6.12: Comparison of neutral kaon candidates invariant mass spectra identified with different sets of decay topology variables.

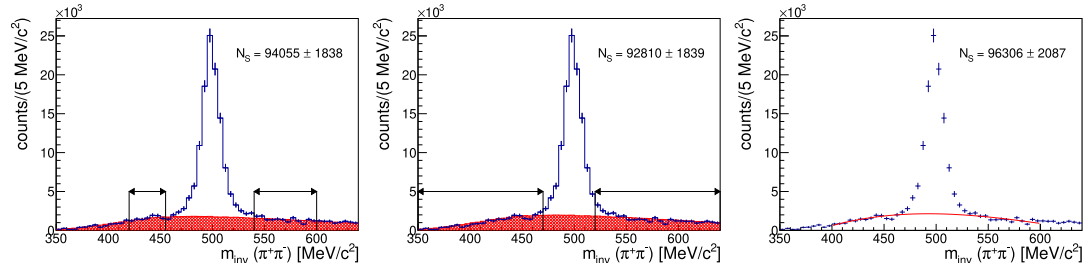

Figure 6.13: Illustration of the influence of different methods used for subtraction of uncorrelated pion pairs in the invariant mass spectra.

the cubic polynomial function. The integral of the polynomial within the 2σ or 3σ region was then used for the background subtraction (the exact procedure was described in 4.1.4). The use of fitted functions for the background subtraction has a greater effect on the number of reconstructed $\mathrm{K}^0_{\mathrm{S}}$ than different scaling intervals of the ME invariant mass spectrum.

The second method of pion identification, already discussed in 4.2.1 and based on the relation $\beta(p)$ and visible region of correlation between these variables of the reconstructed tracks (figure 3.7), have a moderate effect on the measurement of flow. However, there is no bias coming from this method, see figures 6.14 and 6.15. In these figures, the effect of occupancy correction is shown as well. As already mentioned above, the usage of occupancy correction, in this case a product of individual pion corrections, introduces a bias for directed flow but has little effect on the elliptic flow.

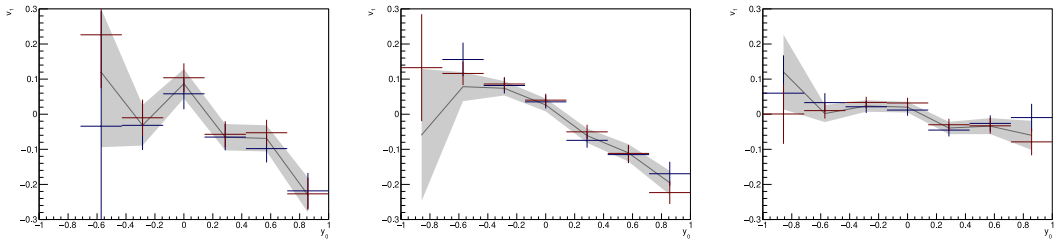

(a) $p_{\mathrm{T}} \in (0; 150)\,\mathrm{MeV}/c$ (b) $p_{\mathrm{T}} \in (150; 300)\,\mathrm{MeV}/c$ (c) $p_{\mathrm{T}} \in (300; 450)\,\mathrm{MeV}/c$

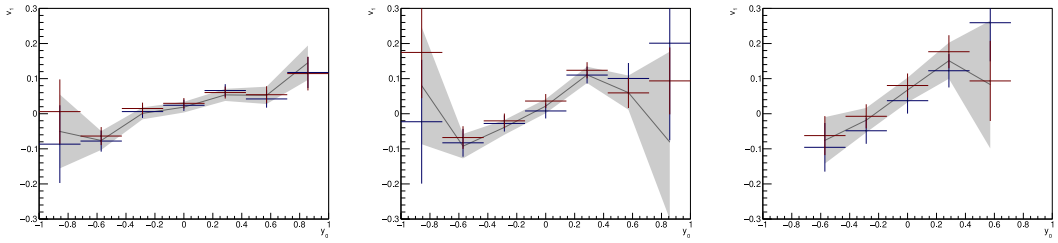

(d) $p_{\mathrm{T}} \in (450; 600)\,\mathrm{MeV}/c$ (e) $p_{\mathrm{T}} \in (600; 750)\,\mathrm{MeV}/c$ (f) $p_{\mathrm{T}} \in (750; 900)\,\mathrm{MeV}/c$

Figure 6.14: Directed flow of $\mathrm{K}^0_{\mathrm{S}}$ in collisions with centrality of $20 - 30\%$ determined using the alternate pion identification method (blue points) and without occupancy corrections (red points), details are described in the text. The results obtained with the procedure described in 4.2 are represented with a gray line and a shaded area.

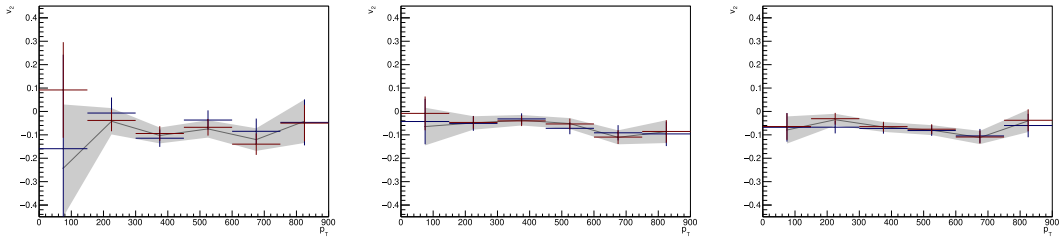

(a) $y_{(0)} \in (-0.71; -0.43)$ (b) $y_{(0)} \in (-0.43; -0.14)$ (c) $y_{(0)} \in (-0.14; 0.14)$

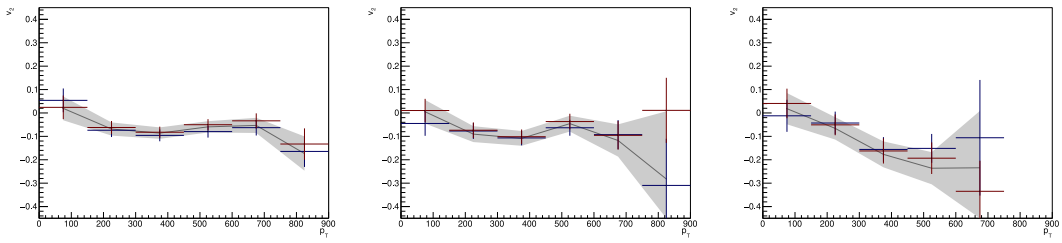

(d) $y_{(0)} \in (0.14; 0.43)$ (e) $y_{(0)} \in (0.43; 0.71)$ (f) $y_{(0)} \in (0.71; 1.00)$

Figure 6.15: Differential elliptic flow of $\mathrm{K}^0_{\mathrm{S}}$ in collisions with $20 - 30\%$ centrality determined using alternate pion identification method (blue points) and without occupancy corrections (red points), details are described in the text. The results obtained with procedure described in 4.2 are represented with a gray line and a shaded area.

6.3 Results of differential kaon flow analysis

The final results of the differential kaon flow analysis obtained via the procedures described in the previous sections and chapters would be presented only for K^+ and K^0_S. The negatively charged kaon production is too low for differential analysis, which is impeded because of background contamination. The obtained results for K^- and the integrated phase space will be mentioned at the end of this section.

I will start the presentation of the mentioned results with more summary plots and go into more details afterwards. The two most compact representations of directed and elliptic flow analysis findings are the slope dependence of the directed flow $\left.\frac{\mathrm{d}v_1}{\mathrm{d}y_{(0)}}\right|_{y_{(0)}=0}$ plotted on figure 6.16, and rapidity integrated elliptic flow shown on figure 6.17 (both as a function of transverse momenta p_T for different centrality classes). The slope values of v_1 at midrapidity are obtained by fitting the individual directed flow spectra $v_1(y_{(0)})$ with a linear function in $y_{(0)}$ in the range $-0.4 < y_{(0)} < 0.4$. As the centrality of the collision decreases the magnitude of the slope increases. Except the agreement between K^+ and K^0_S one can observe that for low transverse momenta the slope is negative and with higher p_T it is rising and changes its sign always around $p_\mathrm{T} \approx 480\,\mathrm{MeV}/c$. The significant dependence observed for kaon flow on transverse momentum p_T was the original motivation for the differential analysis. From the flow symmetry requirement for the symmetrical collision system $v_1(y_{(0)} = 0) = 0$ and the observed rising trend of the directed flow slope, one can conclude that kaons (K^+ and K^0_S) exhibits positive directed flow for low p_T, the so-called antiflow. This opens the possibility of interpreting our results with the repulsive kaon-nucleon potential V_KN. The same outcome can be derived from the measured negative rapidity integrated elliptic flow, i.e. kaons are squeezed out of the collision zone. The absolute value of the potential is possible to deduce from the comparison with dedicated simulations using microscopic kinetic transport models. The parameter v_2 is slightly decreasing (or in absolute value increasing) with increasing transverse momenta. This behaviour is more pronounced with decreasing centrality, i.e. the slope of $v_2(p_\mathrm{T})$ is larger in semiperipheral collisions compared to most central collisions.

The results for neutral kaons are loaded with bigger uncertainties and distortion, when compared to positively charged kaons, however, as can be seen from figures 6.18 and 6.19 the general trends are the same. In comparison to K^+ the acceptance for neutral kaons is more forward rapidity oriented and extends to smaller and even larger transverse momentum, which has an influence on the shape of the flow spectra. Even with this small limitation, the comparison of differential directed and elliptic flow for both kaons shows very good agreement (all values are inline within the uncertainties). The conclusion we can deduce is that thanks to the content of the strange quark, both mentioned kaons behave similarly in the nuclear medium. The comparison for the other centrality classes is given in attachment B on figures B.1 up to B.6.

When studying the centrality dependence of K^+ flow results, one will notice that the flow patterns are less pronounced with increasing centrality of the collisions. This behaviour can be seen in figure 6.20 especially for low transverse

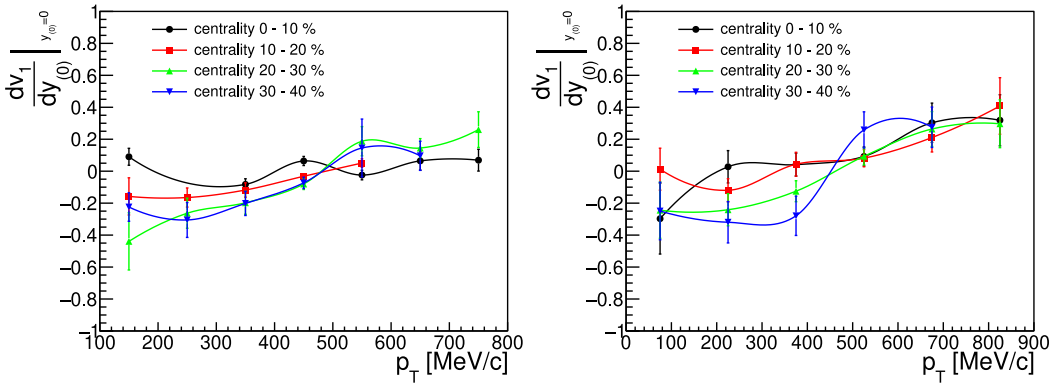

(a) K^+ (b) K^0_S

Figure 6.16: Dependence of the slope of the directed flow at midrapidity on the transverse momentum for different centrality classes.

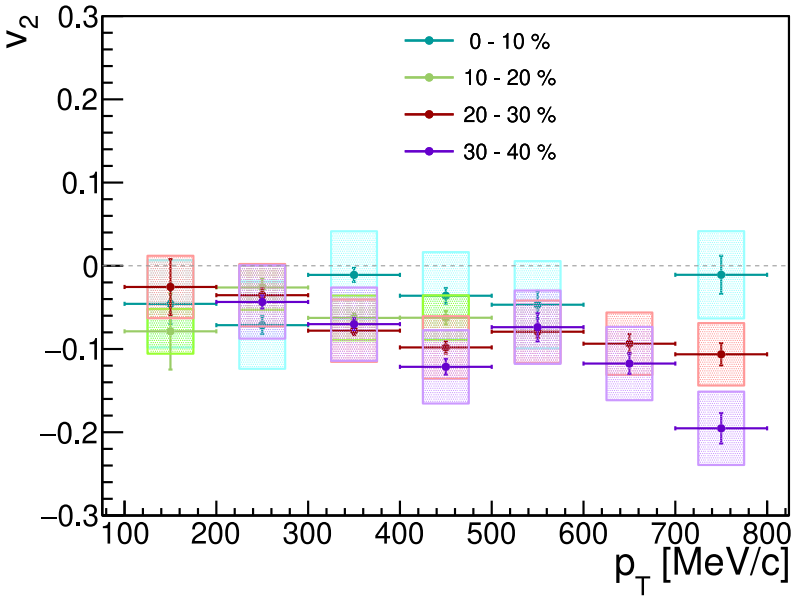

Figure 6.17: Comparison of rapidity integrated elliptic flow of K^+ for various collision centrality. The error bars displayed with lines indicate statistical uncertainties, and the boxes are for systematic uncertainties.

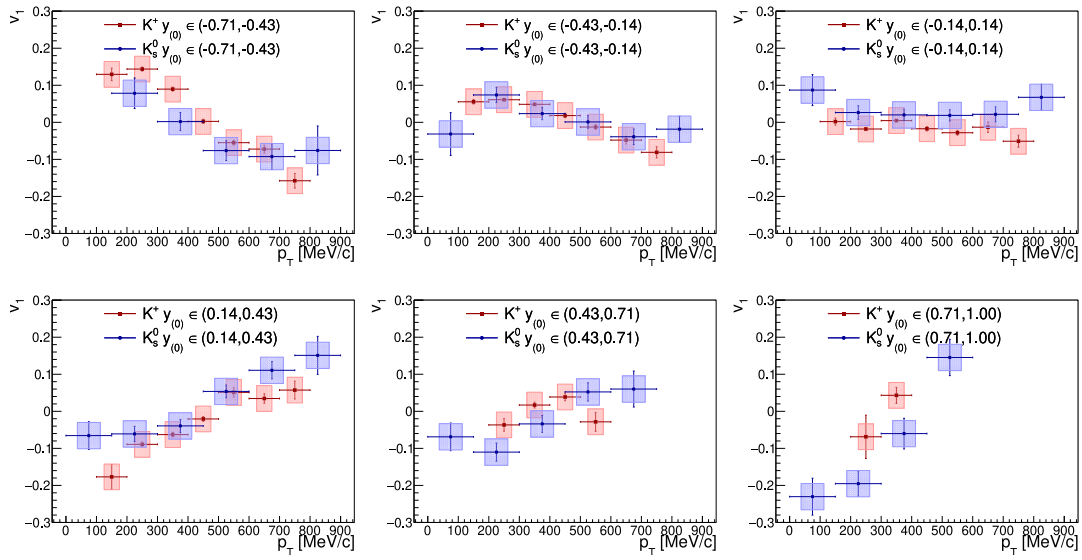

Figure 6.18: Comparison of differential directed flow of K^+ and K^0_S in collisions with $20-30\%$ centrality. The error bars displayed with lines indicate statistical uncertainties, and the boxes are for systematic uncertainties.

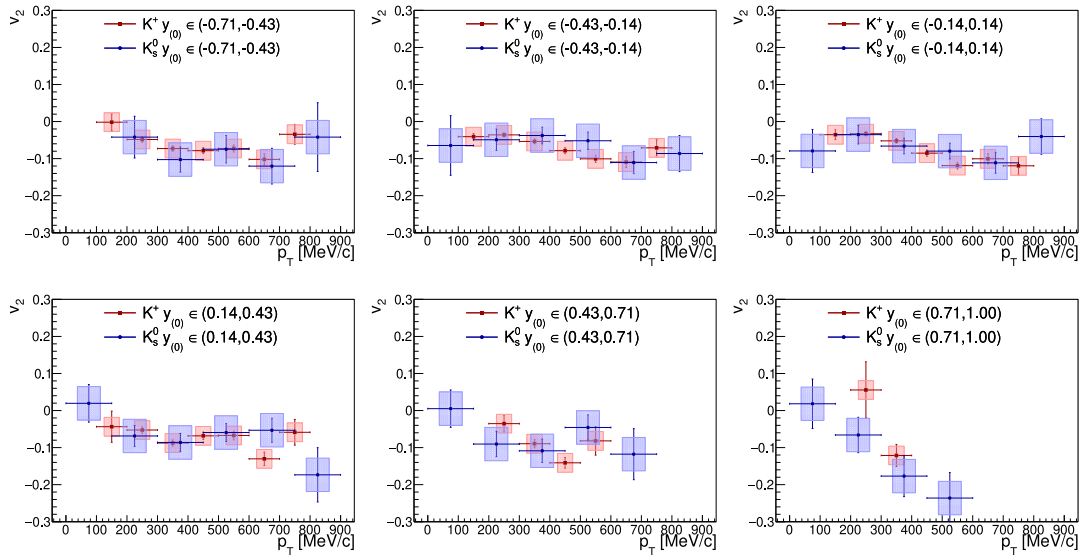

Figure 6.19: Comparison of differential elliptic flow of K^+ and K^0_S in collisions with $20-30\%$ centrality. The error bars displayed with lines indicate statistical uncertainties, and the boxes are for systematic uncertainties.

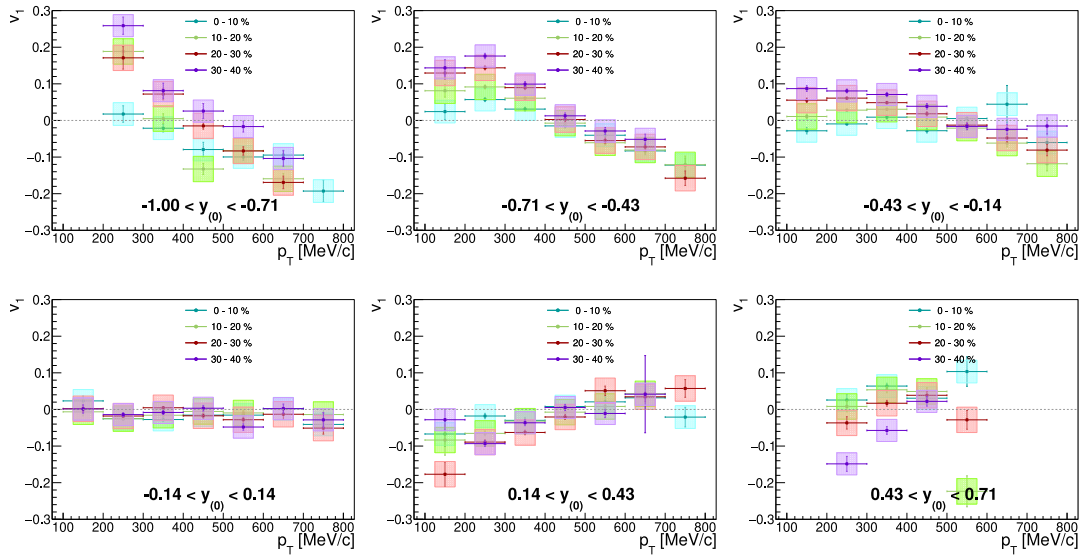

Figure 6.20: Comparison of differential directed flow of K^+ for various collision centrality. The error bars displayed with lines indicate statistical uncertainties, and the boxes are for systematic uncertainties.

momentum, where the absolute value of v_1 in most central collisions $(0-10\%)$ is systematically smaller than the values of directed flow in semi-peripheral collisions $(30-40\%)$. The same holds true also for elliptic flow, only in this case we always observe v_2 either comparable to zero within the uncertainties or negative value. Analogous trends are also observed for protons [156]. This centrality behaviour probably originates from the shape of the collision region and partially also from the shadowing effect, when the passing spectators influence the particles emitted from the created fireball. This effect is considered only for relativistic collisions, where the passing time is comparable to the lifetime of the fireball.

In attachment B there are additional overview figures of the directed and elliptic flow for the studied kaons, starting with figure B.7 up to figure B.10. Both dependencies of $v_{1,2}$ on transverse momentum and normalized rapidity are presented for all centrality classes. The noticed independence of elliptic flow on rapidity motivated the earlier presentation of the rapidity integrated values of v_2.

Unfortunately, the results on the differential flow of K^- were impossible to obtain. Although the absolute yield is not too distant from the yield of neutral kaons, the very low signal-to-background ratio makes this analysis futile. The remaining possibility was to integrate over the variables. Therefore, I select the centrality window $10-40\%$ (to omit the most central collisions where the event plane determination is problematic) and in the case of directed flow, the integration goes also over the transverse momentum and the elliptic flow is integrated over the rapidity, see figure 6.21. On that figure is also presented a comparison with the same integrated flow coefficients for K^+. However, it is difficult to make a strong statement on this comparison between charged kaons due to the size of uncertainties, the general trend is suggestive of being the same for both particle species. This finding is rather unexpected as the potentials V_{KN} and $V_{\overline{\mathrm{K}}\mathrm{N}}$ are predicted to be of opposite sign.

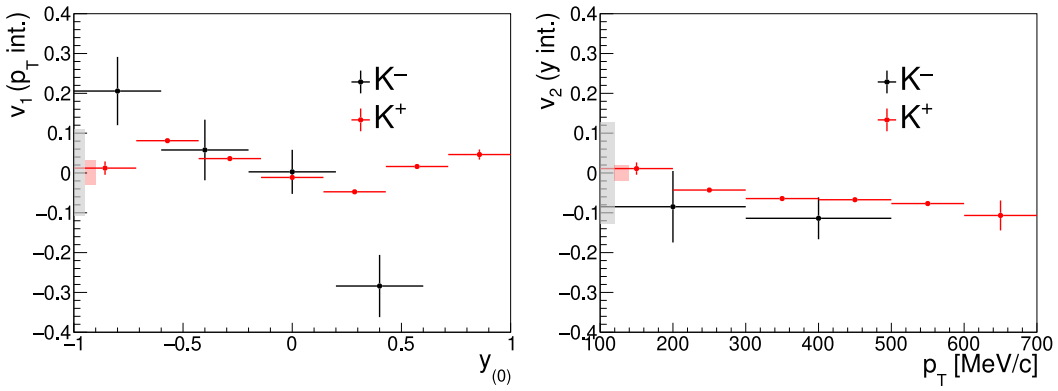

Figure 6.21: Measured p_{T}-integrated directed and rapidity integrated elliptic flow for K^- (black) and K^+ (red) in $10-40\%$ most central Au + Au collisions at $\sqrt{s_{\mathrm{NN}}} = 2.42\,\mathrm{GeV}$. Rectangles represent systematic uncertainty.

6.3.1 Summary of presented results

In this section, a summary of the previously presented differential analysis of the flow of kaons and the integral flow of antikaons is given.

We did not observe significant difference between K^+ and $\mathrm{K}^0_{\mathrm{S}}$. The antiflow of kaons is observed for low transverse momenta region, while for high p_{T} region the directed flow is similar to the flow of nucleons. The negative elliptic flow is independent of rapidity and decreases with increasing transverse momenta up to saturation value about $v_{2,\mathrm{max}} \approx -0.1$. A decrease of the absolute value of both directed and elliptic flow is observed when going from semi-peripheral to central collisions.

The antikaon directed flow shows an antiflow pattern as well, although these are transverse momentum integrated spectra (it should be noted that the phase space distribution of K^- is dominated in the region $p_{\mathrm{T}} \in (150; 450)\,\mathrm{MeV}/c$). The elliptic flow of K^- indicates squeeze-out similarly to kaons, but these values are also comparable to $v_2 = 0$ within the uncertainties.

6.4 Comparison with models

Several transport model simulations (see a brief introduction in section 1.4.2) were performed either by the theoretical group developing a particular model or by HADES collaboration members with advice on input parameter settings by the aforementioned groups. In the following, I refer to these simulations with these abbreviations:

SMASH cascade for SMASH v1.5 run in cascade mode (i.e., no potentials),

SMASH with EoS for SMASH v1.8 with middle Skyrme equation of state[3],

[3]The prescription of Skyrme potential $U_{\mathrm{Skyrme}} = \alpha(\rho/\rho_0) + \beta(\rho/\rho_0)^\tau$ comprises three parameters α, β, τ. These parameters are connected through (1.12) with κ. In the community of transport models, three set of parameters are used for three EoS (soft,hard,middle): $\alpha_{\mathrm{soft}} = -356\,\mathrm{MeV}, \beta_{\mathrm{soft}} = 303\,\mathrm{MeV}, \tau_{\mathrm{soft}} = 1.17, \kappa_{\mathrm{soft}} = 200\,\mathrm{MeV}$, $\alpha_{\mathrm{mid}} = -209\,\mathrm{MeV}, \beta_{\mathrm{mid}} = 156\,\mathrm{MeV}, \tau_{\mathrm{mid}} = 1.35, \kappa_{\mathrm{mid}} = 240\,\mathrm{MeV}$ and $\alpha_{\mathrm{hard}} = -124\,\mathrm{MeV}, \beta_{\mathrm{hard}} = 71\,\mathrm{MeV}, \tau_{\mathrm{hard}} =$

UrQMD cascade for UrQMD v3.4 run in cascade mode (that is, without potentials),

UrQMD with EoS for UrQMD v3.4 with a hard Skyrme equation of state,

PHSD for PHSD v4.5 **with/without** (anti)kaon-nucleon scalar potentials [225],

GiBUU for GiBUU version 2019 patch 5 with non-relativistic **Skyrme**-type potentials or **R**elativistic **M**ean **F**ields.

First, the assumption of similarity between K^+ and K^0_S is tested in the models. The agreement in flow observables in case of these two kaons is satisfactory, as one can see on figures 6.22 and 6.23, where the directed flow as a function of transverse momentum and rapidity integrated elliptic flow is shown in case of two selected models (namely PHSD with kaon-nucleon potentials and SMASH with equation of state). Since similarly good agreement was observed in the experimental data (shown on figures 6.18 and 6.19), there will be presented only a comparison between model prediction and experimental data for K^+ kaons which exhibit significantly smaller experimental uncertainties.

Because we have a non-trivial number of different theoretical models and multi-differential measurement of kaon flow in experimental data, it is needed to select only a few observables which would be able to emphasize the important aspects and differentiate the model predictions. In the case of elliptic flow, the natural selection was the rapidity integrated v_2 as we observe no strong dependence of v_2 on the rapidity. The directed flow shows a more complex behaviour with respect to transverse momentum and rapidity. The directed flow as a function of rapidity in three transverse momentum bins was finally selected as a good observable. The selected p_T bins compress the important aspect of the differential directed flow: at low p_T the directed flow has a negative slope, at mid p_T the $v_1 \approx 0$, and at high transverse momentum the slope of the directed flow is positive. Moreover, for comparison with model prediction, the centrality class $20 - 30\%$ is selected due to its good event plane resolution, which in turn affects the size of the error bars. The centrality dependent results would be presented only for the slope of directed flow and rapidity integrated elliptic flow. Additional figures will be part of appendix C.

In figure 6.24 the comparison of measured directed flow and the model predictions is presented. One can observe that most of the models predict, in agreement with HADES measurements, a rising trend of v_1 for high transverse momentum around mid-rapidity. On the other hand, only two models (GiBUU and PHSD) predict for low p_T the opposite, i.e., a decreasing trend which is observed in the experiment. Particularly good agreement in $v_1(y_{(0)})$ between data and model is achieved for PHSD with kaon-nucleon potential, which can be also seen in the comparison of slope of directed flow at midrapity displayed on figure 6.25. Pure cascade simulations, which do not contain this type of potential, are not able to reproduce the directed flow at low p_T. The addition of Skyrme potentials through the equation of state does not fundamentally change the outcome of the simulations. The UrQMD and SMASH models use high-mass nucleon resonances

$2.0, \kappa_{\text{hard}} = 380\,\text{MeV}$. Except for U_{Skyrme} there is also included (isospin) symmetry potential $U_{\text{sym}} = \pm S_{\text{pot}} \rho_{I_3}/\rho$.

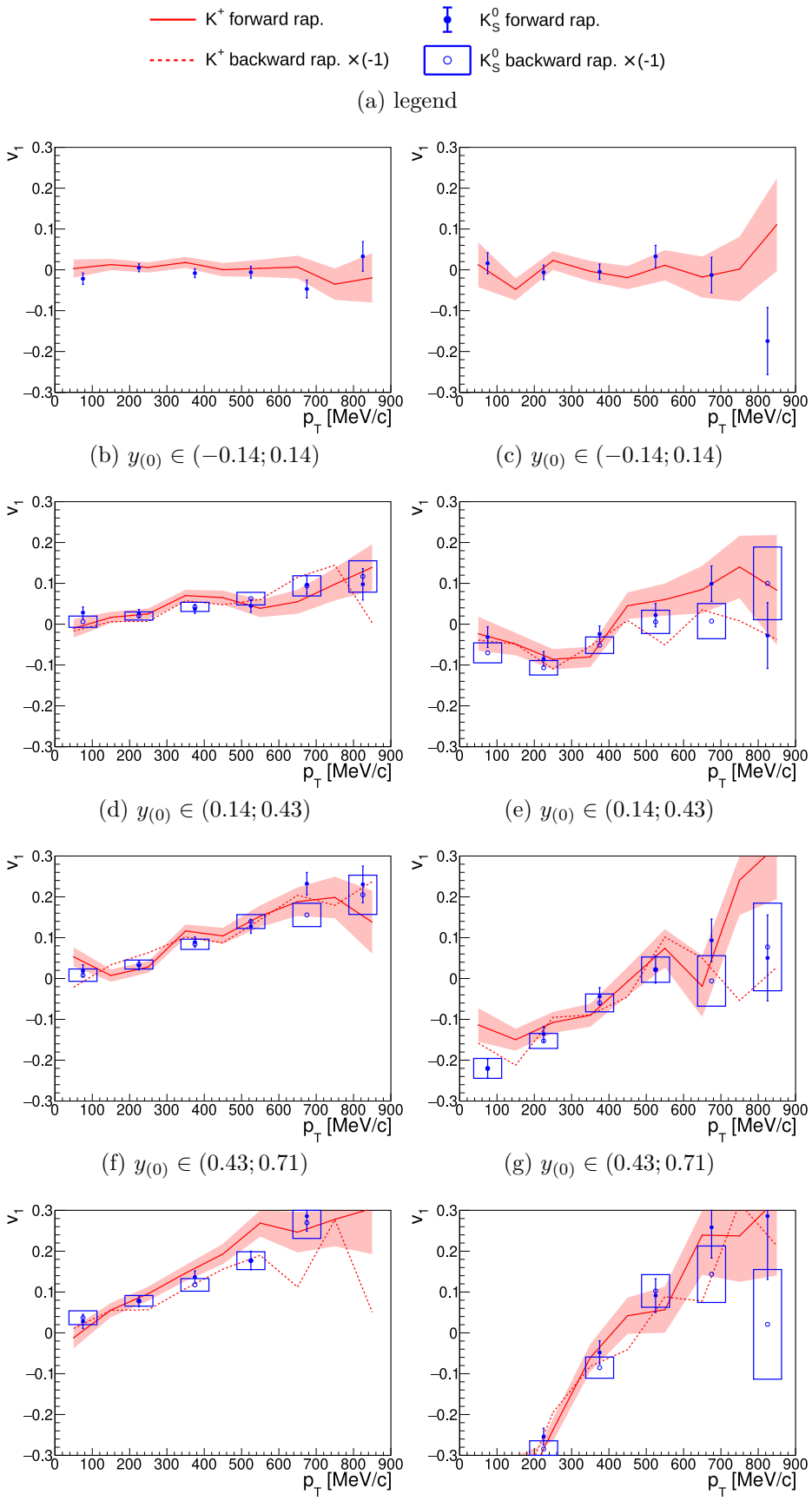

(a) legend

(b) $y_{(0)} \in (-0.14; 0.14)$

(c) $y_{(0)} \in (-0.14; 0.14)$

(d) $y_{(0)} \in (0.14; 0.43)$

(e) $y_{(0)} \in (0.14; 0.43)$

(f) $y_{(0)} \in (0.43; 0.71)$

(g) $y_{(0)} \in (0.43; 0.71)$

(h) $y_{(0)} \in (0.71; 1.00)$

(i) $y_{(0)} \in (0.71; 1.00)$

Figure 6.22: Simulated directed flow of K^+ and K^0_S in $20-30\%$ most central $Au+Au$ collisions. Left plots are from SMASH with Skyrme EoS, right plots are from PHSD with KN potential.

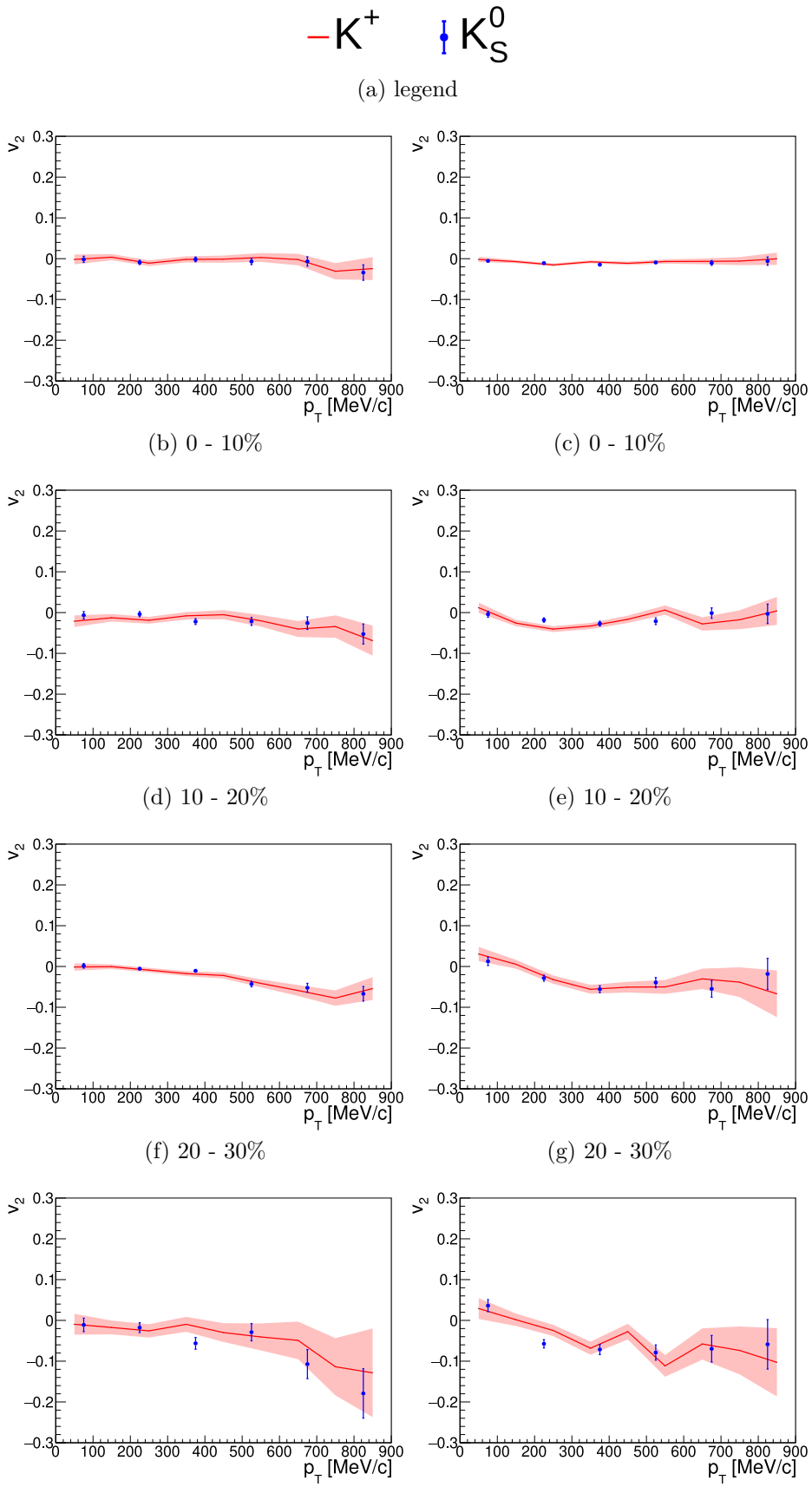

(a) legend

(b) 0 - 10%

(c) 0 - 10%

(d) 10 - 20%

(e) 10 - 20%

(f) 20 - 30%

(g) 20 - 30%

(h) 30 - 40%

(i) 30 - 40%

Figure 6.23: Simulated rapidity integrated elliptic flow for K^+ and K^0_S. Left plots are from SMASH with Skyrme EoS, right plots are from PHSD with KN potential.

for the strangeness production, and kaon propagation is then governed only by the scattering of other particles [226]. These observations lead us to the conclusion that the incorporation of additional kaon-nucleon potentials into the model improves agreement with the directed flow measured by HADES.

The elliptic flow predictions are set side by side with the HADES measurement on figure 6.26. Similar findings to directed flow can be derived. The UrQMD model predicts zero v_2 independent of the simulation type. The SMASH cascade again agrees with UrQMD cascade, however, the inclusion of EoS squeezes the kaons slightly out of the dense environment resulting in a small negative elliptic flow especially at high transverse momentum. The GiBUU model with Skyrme type potentials follows well the trend of experimental data but significantly undershoots the elliptic flow at the quantitative level. On the other hand, when the RMF mode of simulation is used (which also includes the KN potential), the best agreement with the experimental data is achieved. In the case of the PHSD model, the inclusion of the KN potential does not play as an important role as it did in the directed flow. The qualitative agreement between the data and the PHSD is very good, but the experimental data suggest a slightly stronger kaon squeeze-out. The centrality dependence of the rapidity integrated elliptic flow is the subject of the figure 6.27 where the GiBUU RMF model was selected as it was found to best describe the experimental data.

The analysis of the flow of antikaons, as was mentioned earlier, was much more complicated for experimental data, and thus the integration over centrality and transverse momentum for v_1, respective rapidity for v_2 was unavoidable. The model prediction with the same assumptions is shown on figure 6.28. Although the statistical and systematic uncertainties of the experimental data points are significant, one can make an interesting observation: contrary to the case of K^+ directed flow where SMASH and UrQMD curves were quite distant from the HADES measurement (see figure 6.29), the antikaons are well described by these models even in the cascade mode where no potentials are included. The same holds true for PHSD models where the option without the KN potential is in better agreement with the data points than the PHSD with the KN potential. The elliptic flow is very close to zero in almost all transport models, where the data points suggest a small squeeze-out of antikaons (negative v_2). The case of negative kaons is very intricate not only due to limited statistics and thus large uncertainty, but also due to the fact that a considerable fraction ($\approx \frac{1}{2}$) of K^- originates from ϕ meson decay [227].

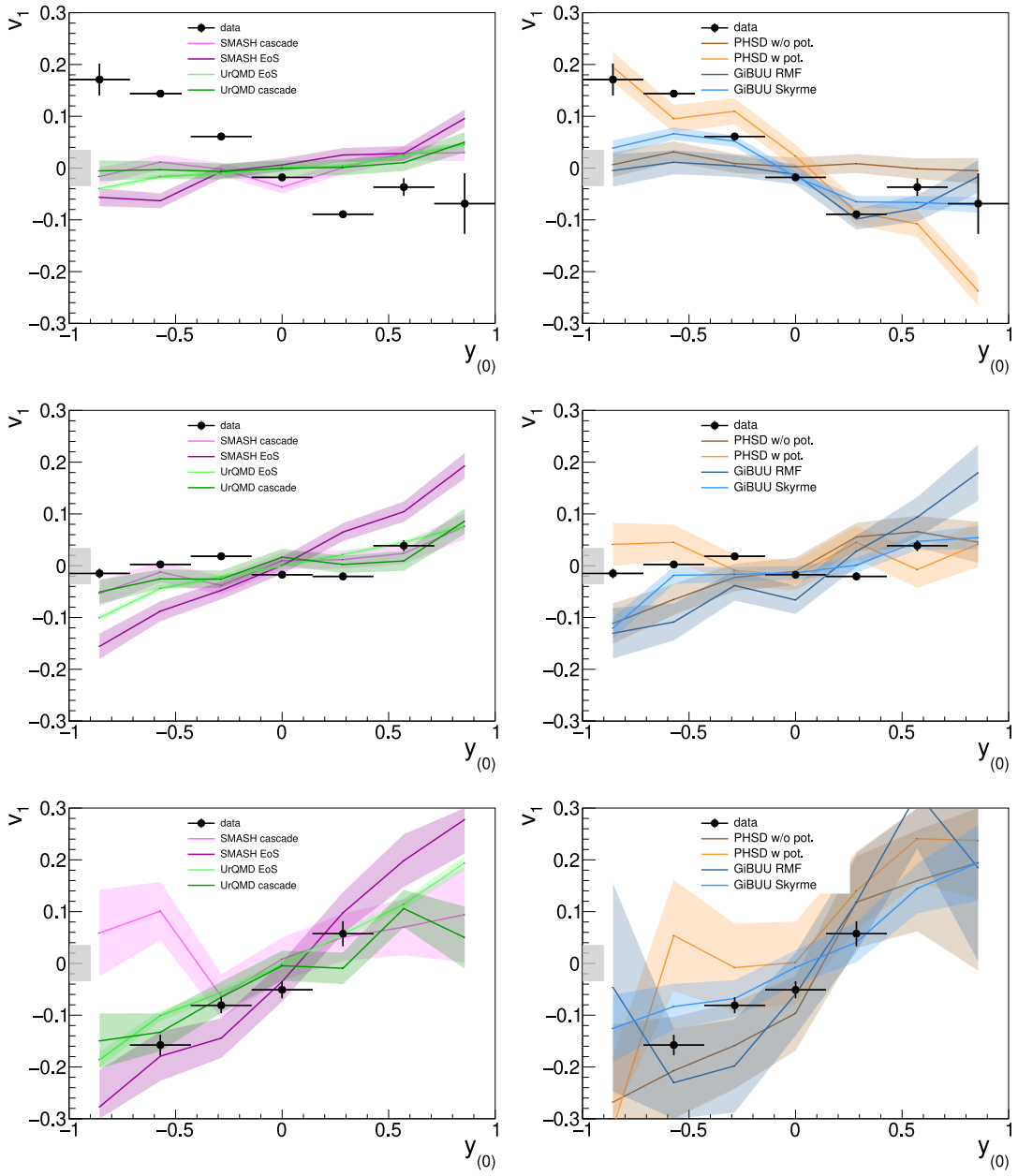

Figure 6.24: Close comparison of the results of the data analysis and the predictions of the directed flow for selected models. Upper row is for $p_{\mathrm{T}} \in (200, 300)\,\mathrm{MeV}/c$, middle row $p_{\mathrm{T}} \in (400, 500)\,\mathrm{MeV}/c$ and lower row $p_{\mathrm{T}} \in (700, 800)\,\mathrm{MeV}/c$. The gray box indicates the size of the systematic uncertainty of the data points.

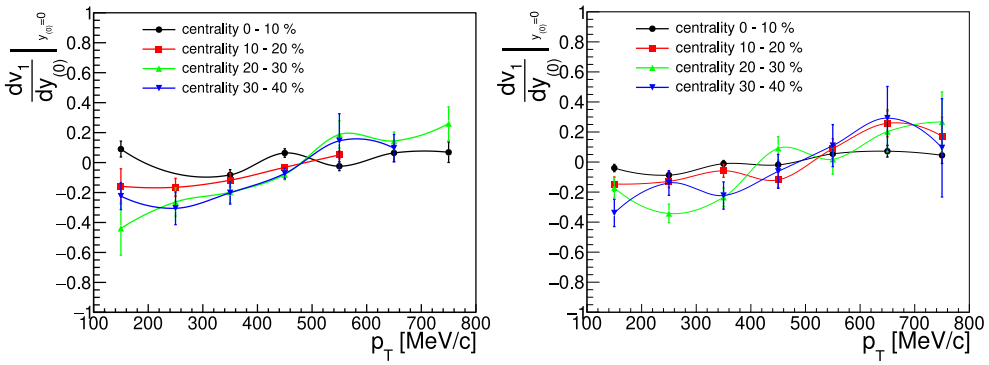

(a) experimental data (b) PHSD with KN pot.

Figure 6.25: The transverse momentum dependence of the slope of directed flow at midrapidity for different centrality classes. The experimental measurements on the left side and the prediction of the PHSD model on the right.

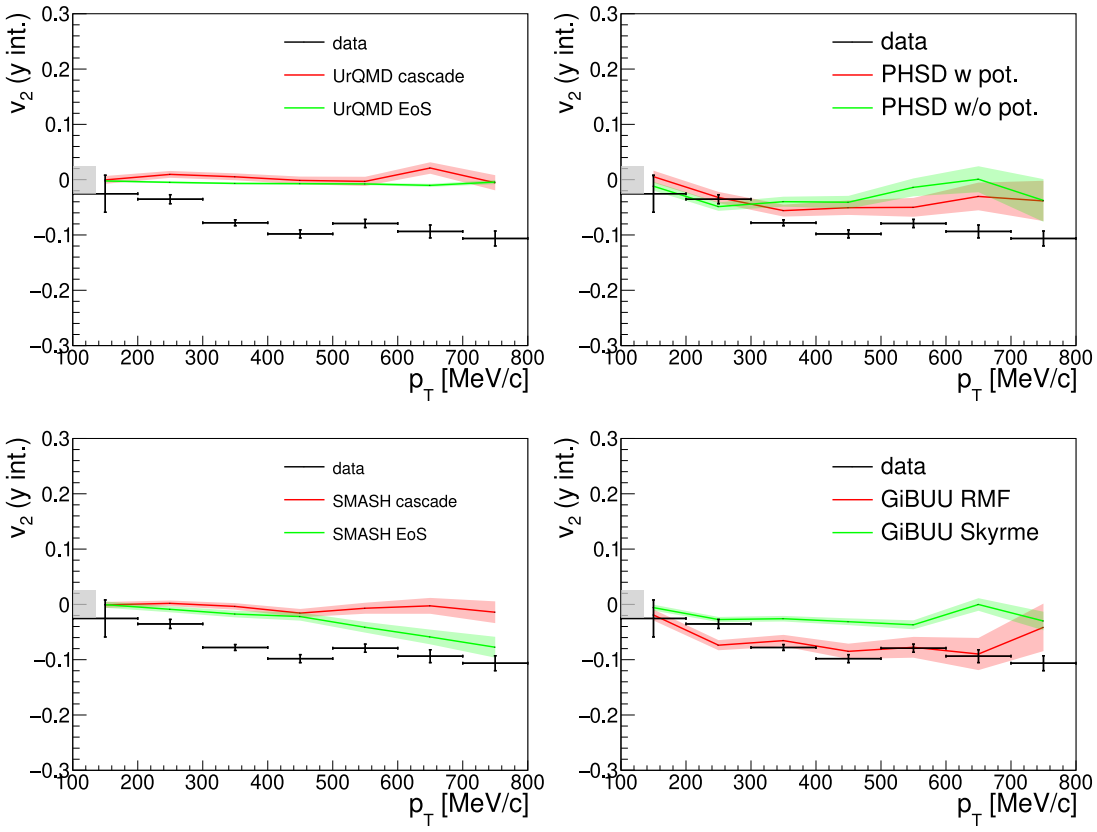

Figure 6.26: Elliptic flow of positively charged kaons measured in $20-30\%$ most central Au + Au collisions at beam energy $1.23A$ GeV confronted with selected transport model simulations. The gray box indicates the size of the systematic uncertainty of the data points.

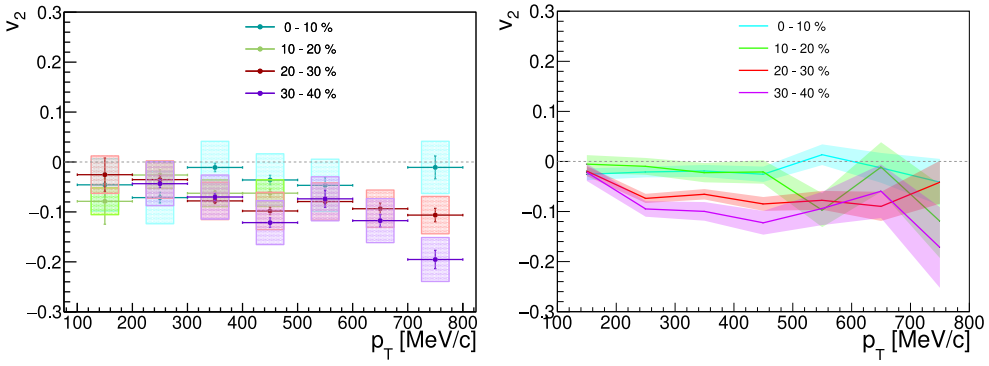

(a) experimental data (b) GiBUU RMF

Figure 6.27: The transverse momentum dependence of the rapidity integrated elliptic flow for different centrality classes. The experimental measurements on the left side and the prediction of the GiBUU model on the right.

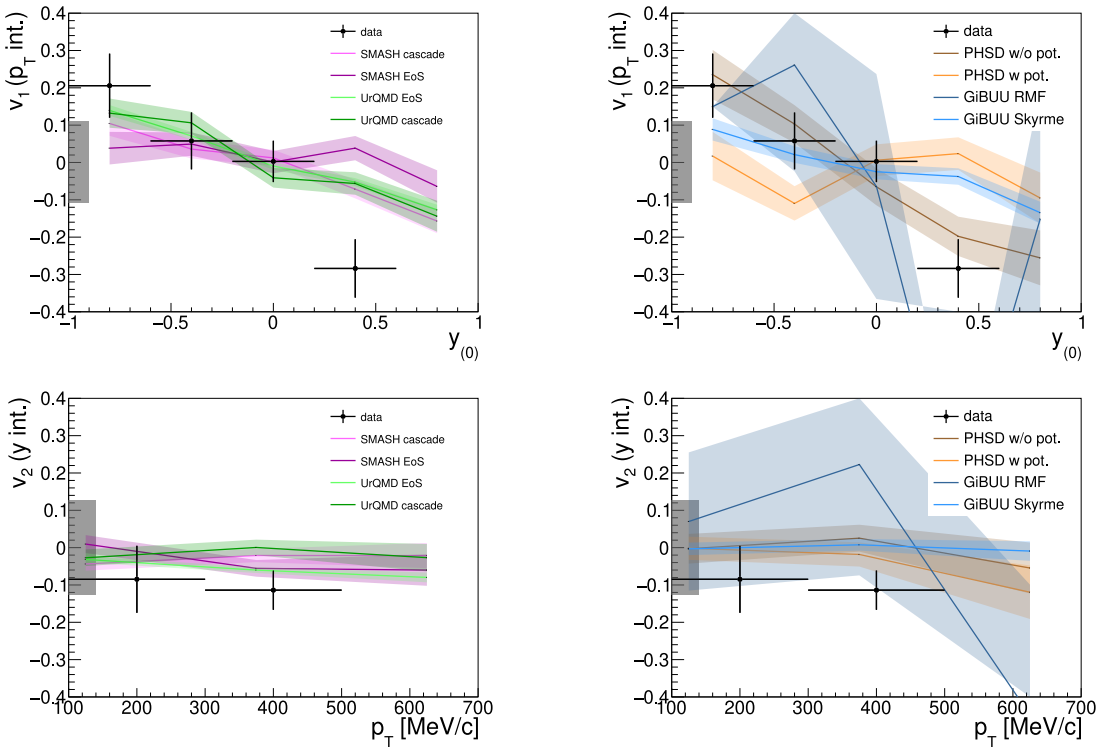

Figure 6.28: Measurements of directed and elliptic flow for K^- are set side by side to simulations obtained from selected models. The gray box indicates the size of the systematic uncertainty of the data points.

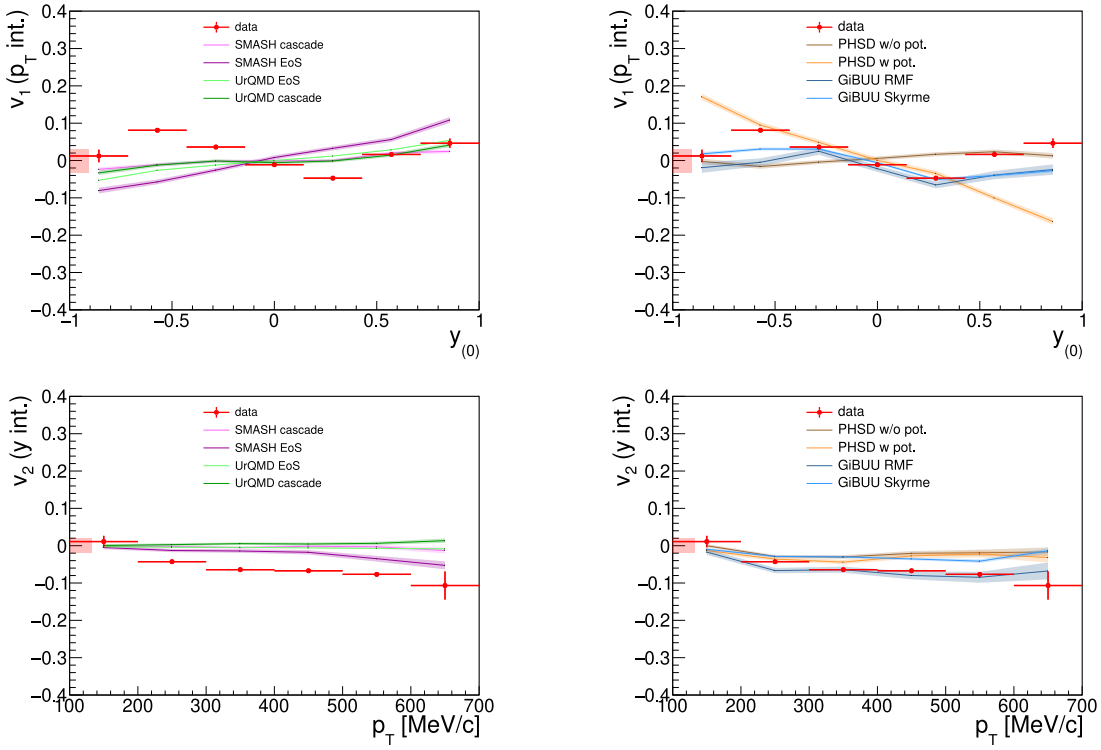

Figure 6.29: K^+ measured and model predicted directed and elliptic flow within the range of integration of flow measurement for K^-. The red box indicates the size of the systematic uncertainty of the data points.

Conclusion

In this thesis, I focused on the analysis of kaon flow in Au + Au collisions at kinetic beam energy 1.23A GeV measured with the HADES spectrometer during April and May 2012.

The study of strangeness around the NN threshold energy is one of the pillars of the HADES collaboration physics program, since the strange hadrons are considered a good probe of the processes taking place inside the hot and dense nuclear matter. Thanks to the nowadays solitary investigation of heavy-ion collisions at $\sqrt{s_{\mathrm{NN}}} \approx 2.5\,\mathrm{GeV}$ (apart from experiments with SIS18 at GSI, there were pioneering experiments at Bevalac/LBL in the 1980s and 1990s), it gives HADES a unique opportunity to study very rare probes for the first time or at least significantly improve the existing results. The spectrometer is continuously upgraded to provide further insight on the interesting state of strongly interacting matter, which can also be observed not only in our laboratory but in the Universe as well, e.g., in the neutron star merge.

During the mentioned gold beam time, HADES has recorded over 7 billion events from which 2.2 billions were selected for physics analysis. This remarkable data set allowed one to study very sensitive observables such as differential transverse flow even for subthreshold-produced kaons. After careful cleaning of the recorded events and sorting of the identified tracks, the kaons were identified. The charged kaon candidates were chosen on the basis of the track quality parameters and specific energy losses in the MDC and TOF detectors. The neutral kaon candidates were reconstructed using their decay products (the charged pion channel is the most convenient from an experimental point of view), and for the pion pair selection, machine learning algorithms were trained and applied. The background tracks were subtracted with the fitting procedure and the mixed event technique for charged and neutral kaons, respectively. The azimuthal angle distributions of kaons with respect to the first harmonic of the reaction plane were later fitted with Fourier decomposition and the obtained coefficients v_n^{obs} were corrected for the event plane resolution. Systematic uncertainties were determined from the variation of several values of the analysis parameters.

From the results on the directed and elliptic flow of (anti)kaons, I made the following observations:

- directed flow of K^+ is strongly dependent on transverse momentum,
- both $|v_1|$ and $|v_2|$ of K^+ is decreasing with increasing collision centrality,
- elliptic flow of K^+ is approximately constant as a function of rapidity and decreases towards higher transverse momentum,
- there is no significant difference in flow of K^+ and $\mathrm{K}^0_{\mathrm{S}}$,
- directed flow of K^- integrated over transverse momentum exhibits antiflow pattern,
- elliptic flow of K^- is not significantly different from zero (probably is slightly negative).

Although it is not appropriate to compare these results directly with other measurements done by KaoS, FOPI, and STAR collaborations (due to slightly different kinetic beam energy and/or due to different collision system sizes), they can be viewed as useful guidelines. The results of kaon flow presented in this thesis are in good qualitative agreement with the published data reviewed in section 1.7.1. In particular, there is agreement with all experiments that the elliptic flow of K^+ is negative and approximately constant function of rapidity. One can also see a correspondence with FOPI that the directed flow of K^+ is positive for low transverse momentum and drops to negative values for $\frac{p_T}{m} > 1$, available results from STAR are for higher p_T where a similarity can be found in the rising trend of $v_1(y)$ of kaons. The identical observed flow patterns of K^+ and K^0_S are confirmed with the STAR measurements, together with qualitatively very similar tendencies of K^- flow. The decreasing trend of the absolute value of transverse flow for more central collisions was also found by the FOPI collaboration, as well as the observation of antiflow for K^-.

Additionally, I made a comparison with the selected kinetic transport models: SMASH, UrQMD, PHSD, and GiBUU. For the positively charged kaons, the best agreement with the presented experimental data belongs to PHSD with the KN potential switched on. On the opposite side are models which do not use any potentials (the simulations were performed in the so-called cascade mode). A surprise was to find that for K^- these models (where no potentials were used) predict the closest values to the HADES measurements. More detailed understanding of why some models work better for K^+ and not so well for K^- and vice versa is desirable.

Finally, the HADES collaboration recorded during March 2019 about two times more collisions of Ag + Ag at $\sqrt{s_{NN}} = 2.55\,\text{GeV}$ which exactly corresponds to K^+ production threshold energy. The analysis of these data might be thus very interesting and can provide even more precise and differential results on kaon flow in heavy-ion collisions.

Bibliography

[1] M. Gell-Mann. The Eightfold Way: A theory of strong interaction symmetry. *Report CTSL* (20). 1961.

[2] M. Gell-Mann. A schematic model of baryons and mesons. *Physics Letters* **8** (3): 214 - 215. 1964.

[3] G. Zweig. An SU(3) model for strong interaction symmetry and its breaking. *CERN Report* (8182): TH-401. 1964.

[4] R. Aaij *et al.* (LHCb collaboration). Observation of structure in the J/ψ-pair mass spectrum. `arXiv:2006.16957`.

[5] R. Aaij *et al.* (LHCb Collaboration). Observation of a Narrow Pentaquark State, $P_c(4312)^+$, and of the Two-Peak Structure of the $P_c(4450)^+$. *Physical Review Letters* **122** : 222001. 2019.

[6] M. Aker *et al.* (KATRIN collaboration). Improved Upper Limit on the Neutrino Mass from a Direct Kinematic Method by KATRIN. *Physical Review Letters* **123** (22): 221802. 2019.

[7] F. An *et al.* (Daya Bay collaboration). New Measurement of Antineutrino Oscillation with the Full Detector Configuration at Daya Bay. *Physical Review Letters* **115** (11): 111802. 2015.

[8] M. Acero *et al.* (NOvA collaboration). First measurement of neutrino oscillation parameters using neutrinos and antineutrinos by NOvA. *Physical Review Letters* **123** (15): 151803. 2019.

[9] G. Aad *et al.* (ATLAS collaboration). Observation of a new particle in the search for the Standard Model Higgs boson with the ATLAS detector at the LHC. *Physics Letters B* **716** (1): 1–29. 2012.

[10] S. Chatrchyan *et al.* (CMS collaboration). Observation of a new boson at a mass of 125 GeV with the CMS experiment at the LHC. *Physics Letters B* **716** (1): 30–61. 2012.

[11] Wikipedia contributors. Standard Model — Wikipedia, The Free Encyclopedia. `https://en.wikipedia.org/w/index.php?title=Coupling_constant&oldid=891630615`. [Online; accessed 3-February-2020].

[12] M. Tanabashi *et al.* (Particle Data Group). Review of Particle Physics. *Physical Review D* **98** : 030001. 2018.

[13] J. Rafelski. Melting hadrons, boiling quarks. *European Physical Journal A* **51** (9): 114. 2015.

[14] B. P. Abbott *et al.* (LIGO Scientific Collaboration and Virgo Collaboration). GW170817: Observation of Gravitational Waves from a Binary Neutron Star Inspiral. *Physical Review Letters* **119** : 161101. 2017.

[15] Particle Data Group. History of the Universe. `https://particleadventure.org/images/history-of-the-universe-2015.pdf`. [Online; accessed 5-March-2020].

[16] T. Galatyuk, P. M. Hohler, R. Rapp, F. Seck, and J. Stroth. Thermal dileptons from coarse-grained transport as fireball probes at SIS energies. *European Physical Journal A* **52** (5). 2016.

[17] V. Pospíšil. *Experimentální studium relativistických jádro-jaderných srážek s pomocí di-leptonového spektrometru HADES*. Master's thesis. Prague: Czech Technical University in Prague, Faculty of Nuclear Sciences and Physical Engineering. 2005.

[18] M. L. Miller, K. Reygers, S. J. Sanders, and P. Steinberg. Glauber Modeling in High-Energy Nuclear Collisions. *Annual Review of Nuclear and Particle Science* **57** (1): 205-243. 2007.

[19] S. Mandelstam. Determination of the Pion-Nucleon Scattering Amplitude from Dispersion Relations and Unitarity. General Theory. *Physical Review* **112** : 1344–1360. 1958.

[20] H. Oeschler. Strangeness production at 1-2 A GeV. *Progress in Particle and Nuclear Physics* **62** (2): 433–438. 2009.

[21] C. M. Ko. Effect of final state interactions on subthreshold K^- production in heavy-ion collisions. *Physics Letters B* **138** (5-6): 361–364. 1984.

[22] D. B. Kaplan and A. E. Nelson. Strange goings on in dense nucleonic matter. *Physics Letters B* **175** (1): 57–63. 1986.

[23] G. Brown, K. Kubodera, and M. Rho. Strangeness condensation and "clearing" of the vacuum. *Physics Letters B* **192** (3-4): 273–278. 1987.

[24] C. H. Lee, G. E. Brown, and M. Rho. Kaon condensation in "nuclear star" matter. *Physics Letters B* **335** (3-4): 266–272. 1994.

[25] T. Muto and T. Tatsumi. Theoretical aspects of kaon condensation in neutron matter. *Physics Letters B* **283** (3-4): 165–170. 1992.

[26] M. Lutz, A. Steiner, and W. Weise. Kaons in baryonic matter. *Nuclear Physics A* **574** (4): 755–787. 1994.

[27] H. Yabu, S. Nakamura, F. Myhrer, and K. Kubodera. Effective kaon mass in baryonic matter and kaon condensation. *Physics Letters B* **315** (1-2): 17–23. 1993.

[28] C. Blume and C. Markert. Strange hadron production in heavy ion collisions from SPS to RHIC. *Progress in Particle and Nuclear Physics* **66** (4): 834–879. 2011.

[29] I. G. Bearden *et al.* (BRAHMS Collaboration). Charged Meson Rapidity Distributions in Central Au + Au Collisions at $\sqrt{s_{NN}} = 200\,\mathrm{GeV}$. *Physical Review Letters* **94** : 162301. 2005.

[30] P. Chung *et al.* (E895 Collaboration). Near-Threshold Production of the Multistrange Ξ^- Hyperon. *Physical Review Letters* **91** : 202301. 2003.

[31] B. B. Back *et al.* (E917 Collaboration). Production of ϕ mesons in Au + Au collisions at $11.7A\,\mathrm{GeV}/c$. *Physical Review C* **69** : 054901. 2004.

[32] L. Ahle *et al.* (E802 Collaboration). Kaon production in Au+Au collisions at $11.6A\,\mathrm{GeV}/c$. *Physical Review C* **58** : 3523–3538. 1998.

[33] L. Ahle *et al.* (E866 and E917 Collaboration). An excitation function of K^- and K^+ production in Au + Au reactions at the AGS. *Physics Letters B* **490** (1): 53–60. 2000.

[34] L. Ahle *et al.* (E802 Collaboration). Particle production at high baryon density in central Au+Au reactions at $11.6A$ GeV/c. *Physical Review C* **57** : R466–R470. 1998.

[35] J. L. Klay *et al.* (E895 Collaboration). Charged pion production in $2A$ to $8A$ GeV central Au + Au Collisions. *Physical Review C* **68** : 054905. 2003.

[36] C. Alt *et al.* (NA49 Collaboration). Ω^- and $\overline{\Omega}^+$ Production in Central Pb + Pb collisions at 40 and $158A$ GeV. *Physical Review Letters* **94** : 192301. 2005.

[37] C. Alt *et al.* (NA49 Collaboration). Energy dependence of ϕ meson production in central Pb + Pb collisions at $\sqrt{s_{NN}} = 6$ to 17 GeV. *Physical Review C* **78** : 044907. 2008.

[38] C. Alt *et al.* (NA49 Collaboration). Energy dependence of Λ and Ξ production in central Pb + Pb collisions at $20A, 30A, 40A, 80A$, and $158A$ GeV measured at the CERN Super Proton Synchrotron. *Physical Review C* **78** : 034918. 2008.

[39] S. V. Afanasiev *et al.* (NA49 Collaboration). Energy dependence of pion and kaon production in central Pb+Pb collisions. *Physical Review C* **66** : 054902. 2002.

[40] C. Alt *et al.* (NA49 Collaboration). Pion and kaon production in central Pb + Pb collisions at $20A$ and $30A$ GeV: Evidence for the onset of deconfinement. *Physical Review C* **77** : 024903. 2008.

[41] J. Adamczewski-Musch *et al.* (HADES collaboration). Sub-threshold production of K^0_s mesons and Λ hyperons in Au + Au collisions at $\sqrt{s_{NN}} = 2.4\,\mathrm{GeV}$. *Physics Letters B* **793** : 457 - 463. 2019.

[42] J. Adamczewski-Musch *et al.* (HADES Collaboration). Strong Absorption of Hadrons with Hidden and Open Strangeness in Nuclear Matter. *Physical Review Letters* **123** : 022002. 2019.

[43] J. Adamczewski-Musch *et al.* (HADES Collaboration). Charged pion production in Au + Au collisions at $\sqrt{s_{NN}} = 2.4\,\mathrm{GeV}$. *European Physical Journal A* **56** : 259. 2020.

[44] P. Senger and H. Ströbele. Hadronic particle production in nucleus-nucleus collisions. *Journal of Physics G* **25** (5): R59–R131. 1999.

[45] S. Leupold, V. Metag, and U. Mosel. Hadrons in strongly interacting matter. *International Journal of Modern Physics E* **19** (02): 147-224. 2010.

[46] R. Rapp. Dileptons and Medium Effects in Heavy-Ion Collisions. *Nuclear Physics A* **782** (1): 275 - 282. 2007.

[47] J. Adamczewski-Musch *et al.* (HADES collaboration). Probing dense baryon-rich matter with virtual photons. *Nature Physics* **15** (10): 1040–1045. 2019.

[48] W. Marciano and H. Pagels. Quantum chromodynamics. *Physics Reports* **36** (3): 137 - 276. 1978.

[49] D. J. Gross and F. Wilczek. Ultraviolet Behavior of Non-Abelian Gauge Theories. *Physical Review Letters* **30** : 1343–1346. 1973.

[50] H. D. Politzer. Reliable Perturbative Results for Strong Interactions?. *Physical Review Letters* **30** : 1346–1349. 1973.

[51] E. Noether. Invariante Variationsprobleme. *Nachrichten von der Gesellschaft der Wissenschaften zu Göttingen, Mathematisch-Physikalische Klasse* **1918** : 235-257. 1918.

[52] V. Koch. Introduction to Chiral Symmetry. `arXiv:nucl-th/9512029`.

[53] P. W. Higgs. Broken Symmetries and the Masses of Gauge Bosons. *Physical Review Letters* **13** : 508–509. 1964.

[54] F. Englert and R. Brout. Broken Symmetry and the Mass of Gauge Vector Mesons. *Physical Review Letters* **13** : 321–323. 1964.

[55] G. S. Guralnik, C. R. Hagen, and T. W. B. Kibble. Global Conservation Laws and Massless Particles. *Physical Review Letters* **13** : 585–587. 1964.

[56] R. Rapp and J. Wambach. Chiral Symmetry Restoration and Dileptons in Relativistic Heavy-Ion Collisions. *Advances in Nuclear Physics* **25** : 1–205. 2005.

[57] P. Braun-Munzinger, K. Redlich, and J. Stachel. *Particle production in heavy ion collisions* (World Scientific, 2004), pp. 491–599. `https://www.worldscientific.com/doi/pdf/10.1142/9789812795533_0008`.

[58] B. Borasoy. Introduction to chiral perturbation theory. *Springer proceedings in physics* **118** : 1–26. 2008.

[59] A. E. Nelson and D. B. Kaplan. Strange condensate realignment in relativistic heavy ion collisions. *Physics Letters B* **192** (1): 193 - 197. 1987.

[60] G. Brown, K. Kubodera, M. Rho, and V. Thorsson. A novel mechanism for kaon condensation in neutron star matter. *Physics Letters B* **291** (4): 355 - 362. 1992.

[61] G. Brown, C.-H. Lee, M. Rho, and V. Thorsson. From kaon-nuclear interactions to kaon condensation. *Nuclear Physics A* **567** (4): 937 - 956. 1994.

[62] N. Kaiser, P. Siegel, and W. Weise. Chiral dynamics and the low-energy kaon-nucleon interaction. *Nuclear Physics A* **594** (3): 325 - 345. 1995.

[63] M. Lutz. Nuclear kaon dynamics. *Physics Letters B* **426** (1): 12 - 20. 1998.

[64] G. Mao *et al.*. Kaon effective mass and energy from a novel chiral SU(3)-symmetric Lagrangian. *Physical Review C* **59** : 3381–3385. 1999.

[65] G. Q. Li and C. M. Ko. Kaon flow in heavy-ion collisions. *Nuclear Physics A* **594** (4): 460–482. 1995.

[66] S. Weinberg. Pion Scattering Lengths. *Physical Review Letters* **17** : 616–621. 1966.

[67] Y. Tomozawa. Axial-vector coupling constant renormalization and the meson-baryon scattering lenghts. *Il Nuovo Cimento A* **46** (4): 707–717. 1966.

[68] P. B. Demorest, T. Pennucci, S. M. Ransom, M. S. E. Roberts, and J. W. T. Hessels. A two-solar-mass neutron star measured using Shapiro delay. *Nature* **467** (7319): 1081–1083. 2010.

[69] P. Braun-Munzinger, I. Heppe, and J. Stachel. Chemical equilibration in Pb + Pb collisions at the SPS. *Physics Letters B* **465** (1-4): 15–20. 1999.

[70] F. Becattini, M. Gaździcki, and J. Sollfrank. On chemical equilibrium in nuclear collisions. *European Physical Journal C* **5** (1): 143–153. 1998.

[71] S. Wheaton, J. Cleymans, and M. Hauer. THERMUS-A thermal model package for ROOT. *Computer Physics Communications* **180** (1): 84–106. 2009.

[72] G. Torrieri *et al.*. SHARE: Statistical hadronization with resonances. *Computer Physics Communications* **167** (3): 229–251. 2005.

[73] A. Kisiel, T. Tałuć, W. Broniowski, and W. Florkowski. THERMINATOR: THERMal heavy-IoN generATOR. *Computer Physics Communications* **174** (8): 669–687. 2006.

[74] A. Andronic, P. Braun-Munzinger, and J. Stachel. Hadron production in central nucleus–nucleus collisions at chemical freeze-out. *Nuclear Physics A* **772** (3-4): 167–199. 2006.

[75] J. Rafelski and M. Danos. The importance of the reaction volume in hadronic collisions. *Physics Letters B* **97** (2): 279 - 282. 1980.

[76] J. Cleymans, H. Oeschler, K. Redlich, and S. Wheaton. Comparison of chemical freeze-out criteria in heavy-ion collisions. *Physical Review C* **73** : 034905. 2006.

[77] K. Tsushima, S. Huang, and A. Faessler. The role of the Δ (1920) resonance for kaon production in heavy ion collisions. *Physics Letters B* **337** (3-4): 245–253. 1994.

[78] G. Li, C.-H. Lee, and G. Brown. Kaons in dense matter, kaon production in heavy-ion collisions, and kaon condensation in neutron stars. *Nuclear Physics A* **625** (1-2): 372–434. 1997.

[79] S. Bass *et al.*. Microscopic models for ultrarelativistic heavy ion collisions. *Progress in Particle and Nuclear Physics* **41** : 255–369. 1998.

[80] M. Bleicher *et al.*. Relativistic hadron-hadron collisions in the ultra-relativistic quantum molecular dynamics model. *Journal of Physics G* **25** (9): 1859–1896. 1999.

[81] H. Kruse, B. V. Jacak, J. J. Molitoris, G. D. Westfall, and H. Stöcker. Vlasov-Uehling-Uhlenbeck theory of medium energy heavy ion reactions: Role of mean field dynamics and two body collisions. *Physical Review C* **31** : 1770–1774. 1985.

[82] G. Bertsch and S. Das Gupta. A guide to microscopic models for intermediate energy heavy ion collisions. *Physics Reports* **160** (4): 189–233. 1988.

[83] C. M. Ko, Q. Li, and R. Wang. Relativistic Vlasov equation for heavy-ion collisions. *Physical Review Letters* **59** : 1084–1087. 1987.

[84] O. Buss *et al.*. Transport-theoretical description of nuclear reactions. *Physics Reports* **512** (1-2): 1–124. 2012.

[85] B.-A. Li and C. M. Ko. Formation of superdense hadronic matter in high energy heavy-ion collisions. *Physical Review C* **52** : 2037–2063. 1995.

[86] W. Ehehalt and W. Cassing. Relativistic transport approach for nucleus-nucleus collisions from SIS to SPS energies. *Nuclear Physics A* **602** (3-4): 449–486. 1996.

[87] W. Cassing and E. Bratkovskaya. Parton–hadron–string dynamics: An off-shell transport approach for relativistic energies. *Nuclear Physics A* **831** (3-4): 215–242. 2009.

[88] J. Cugnon. Intranuclear cascade model. A review. *Nuclear Physics A* **387** (1): 191–203. 1982.

[89] W. Cassing. Anti-baryon production in hot and dense nuclear matter. *Nuclear Physics A* **700** : 618–646. 2002.

[90] Z. Xu and C. Greiner. Thermalization of gluons in ultrarelativistic heavy ion collisions by including three-body interactions in a parton cascade. *Physical Review C* **71** : 064901. 2005.

[91] J. Aichelin. "Quantum" molecular dynamics—a dynamical microscopic n-body approach to investigate fragment formation and the nuclear equation of state in heavy ion collisions. *Physics Reports* **202** (5-6): 233–360. 1991.

[92] Ch. Hartnack *et al.*. Modelling the many-body dynamics of heavy ion collisions: Present status and future perspective. *European Physical Journal A* **1** (2): 151-169. 1998.

[93] H. Sorge, H. Stöcker, and W. Greiner. Poincaré invariant Hamiltonian dynamics: Modelling multi-hadronic interactions in a phase space approach. *Annals of Physics* **192** (2): 266–306. 1989.

[94] Y. Nara, N. Otuka, A. Ohnishi, K. Niita, and S. Chiba. Relativistic nuclear collisions at 10A GeV energies from p + Be to Au+Au with the hadronic cascade model. *Physical Review C* **61** : 024901. 1999.

[95] J. Weil *et al.*. Particle production and equilibrium properties within a new hadron transport approach for heavy-ion collisions. *Physical Review C* **94** : 054905. 2016.

[96] L. D. Landau. On the multiparticle production in high-energy collisions. *Izvestiya Akademii Nauk SSR, Seriya Fizicheskaya* **17** : 51-64. 1953.

[97] I. Arsene *et al.* (BRAHMS collaboration). Quark–gluon plasma and color glass condensate at RHIC? The perspective from the BRAHMS experiment. *Nuclear Physics A* **757** (1): 1 - 27. 2005.

[98] B. Back *et al.* (PHOBOS collaboration). The PHOBOS perspective on discoveries at RHIC. *Nuclear Physics A* **757** (1): 28 - 101. 2005.

[99] J. Adams *et al.* (STAR collaboration). Experimental and theoretical challenges in the search for the quark–gluon plasma: The STAR Collaboration's critical assessment of the evidence from RHIC collisions. *Nuclear Physics A* **757** (1): 102 - 183. 2005.

[100] K. Adcox *et al.* (PHENIX collaboration). Formation of dense partonic matter in relativistic nucleus–nucleus collisions at RHIC: Experimental evaluation by the PHENIX Collaboration. *Nuclear Physics A* **757** (1): 184 - 283. 2005.

[101] C. Gale, S. Jeon, and B. Schenke. Hydrodynamic modeling of heavy-ion collisions. *International Journal of Modern Physics A* **28** (11): 1340011. 2013.

[102] C. Nonaka and M. Asakawa. Modeling a realistic dynamical model for high energy heavy ion collisions. *Progress of Theoretical and Experimental Physics* **2012** (1). 2012.

[103] P. Braun-Munzinger and J. Wambach. The Phase diagram of strongly interacting matter. *Reviews of Modern Physics* **81** (3): 1031–1050. 2009.

[104] NuPECC. Long Range Plan 2017. `http://www.nupecc.org/?display=lrp2016/main`. [Online; accessed 1-February-2020].

[105] A. Bazavov *et al.* (HotQCD Collaboration). Chiral and deconfinement aspects of the QCD transition. *Physical Review D* **85** : 054503. 2012.

[106] F. R. Brown *et al.*. On the existence of a phase transition for QCD with three light quarks. *Physical Review Letters* **65** : 2491–2494. 1990.

[107] B.-J. Schaefer, J. M. Pawlowski, and J. Wambach. Phase structure of the Polyakov-quark-meson model. *Physical Review D* **76** : 074023. 2007.

[108] M. A. Stephanov. Non-Gaussian Fluctuations near the QCD Critical Point. *Physical Review Letters* **102** : 032301. 2009.

[109] M. Cheng *et al.*. Baryon number, strangeness, and electric charge fluctuations in QCD at high temperature. *Physical Review D* **79** : 074505. 2009.

[110] L. McLerran, K. Redlich, and C. Sasaki. Quarkyonic matter and chiral symmetry breaking. *Nuclear Physics A* **824** (1): 86 - 100. 2009.

[111] B. C. Barrois. Superconducting quark matter. *Nuclear Physics B* **129** (3): 390–396. 1977.

[112] The CBM physics book: Compressed baryonic matter in laboratory experiments. *Lecture Notes in Physics* **814** . 2011.

[113] Blaschke, David *et al.*. Topical issue on Exploring Strongly Interacting Matter at High Densities - NICA White Paper. *European Physical Journal A* **52** (8): 267. 2016.

[114] F. Seck. Thermal dileptons as fireball probes at SIS energies. Talk at Critical Point and Onset of Deconfinement 2016 in Wroclaw. `http://ift.uni.wroc.pl/~cpod2016/slides.php`. [Online; accessed 4-February-2020].

[115] A. A. Penzias and R. W. Wilson. A Measurement of Excess Antenna Temperature at 4080 Mc/s.. *Astrophysical Journal* **142** : 419-421. 1965.

[116] N. Aghanim *et al.*. Planck 2018 results: I. Overview and the cosmological legacy of Planck. *Astronomy and Astrophysics* **641** . 2020.

[117] C. F. v. Weizsäcker. Zur Theorie der Kernmassen. *Zeitschrift für Physik* **96** (7): 431–458. 1935.

[118] H. A. Bethe. Theory of Nuclear Matter. *Annual Review of Nuclear Science* **21** (1): 93–244. 1971.

[119] J. P. Blaizot. Nuclear compressibilities. *Physics Reports* **64** (4): 171–248. 1980.

[120] H. H. Wolter. The nuclear symmetry energy in heavy ion collisions. *Physics of Particles and Nuclei* **46** (5): 781–785. 2015.

[121] R. C. Tolman. Static Solutions of Einstein's Field Equations for Spheres of Fluid. *Physical Review* **55** : 364–373. 1939.

[122] J. R. Oppenheimer and G. M. Volkoff. On Massive Neutron Cores. *Physical Review* **55** : 374–381. 1939.

[123] G. Stoicea *et al.* (FOPI Collaboration). Azimuthal Dependence of Collective Expansion for Symmetric Heavy-Ion Collisions. *Physical Review Letters* **92** : 072303. 2004.

[124] C. Hartnack, H. Oeschler, and J. Aichelin. Hadronic Matter Is Soft. *Physical Review Letters* **96** : 012302. 2006.

[125] P. Russotto *et al.*. Results of the ASY-EOS experiment at GSI: The symmetry energy at suprasaturation density. *Physical Review C* **94** (3): 1–23. 2016.

[126] J. Antoniadis *et al.*. A Massive Pulsar in a Compact Relativistic Binary. *Science* **340** (6131). 2013.

[127] A. Andronic *et al.*. Directed flow in Au+Au, Xe+CsI, and Ni+Ni collisions and the nuclear equation of state. *Physical Review C* **67** : 034907. 2003.

[128] A. Andronic *et al.* (FOPI collaboration). Excitation function of elliptic flow in Au+Au collisions and the nuclear matter equation of state. *Physics Letters B* **612** (3): 173 - 180. 2005.

[129] R. Stock. Particle production in high energy nucleus-nucleus collisions. *Physics Reports* **135** (5): 259–315. 1986.

[130] C. Fuchs and H. H. Wolter. Modelization of the EOS. *European Physical Journal A* **30** (1): 5–21. 2006.

[131] G. Q. Li, C. M. Ko, and B. A. Li. Kaon flow as a probe of the kaon potential in nuclear medium. *Physical Review Letters* **74** (2): 235–238. 1995.

[132] G. Li, C. Ko, and G. Brown. Kaon azimuthal distributions in heavy-ion collisions. *Physics Letters B* **381** (1): 17 - 22. 1996.

[133] Z. S. Wang, C. Fuchs, A. Faessler, and T. Gross-Boelting. Kaon squeeze-out in heavy ion reactions. *European Physical Journal A* **5** : 275–283. 1999.

[134] C. A. Ogilvie (E802 and E917 Collaboration). Kaon production in Au + Au collisions at the AGS. *Nuclear Physics A* **630** : 571C–581C. 1998.

[135] S. Voloshin (E877 Collaboration). Anisotropic flow of identified particles in Au + Au collisions at AGS energy. *Nuclear Physics A* **638** : 455C–458C. 1998.

[136] J. L. Ritman *et al.* (FOPI collaboration). On the transverse momentum distribution of strange hadrons produced in relativistic heavy ion collisions. *Zeitschrift für Physik A Hadrons and Nuclei* **352** (4): 355–357. 1995.

[137] B.-A. Li and A. T. Sustich. Differential Flow in Heavy-Ion Collisions at Balance Energies. *Physical Review Letters* **82** (25): 5004–5007. 1999.

[138] B. A. Li, B. Zhang, A. T. Sustich, and C. M. Ko. Kaon differential flow in relativistic heavy-ion collisions. *Physical Review C* **60** (3): 4. 1999.

[139] M. S. Abdallah *et al.* (STAR Collaboration). Flow and interferometry results from Au + Au collisions at $\sqrt{s_{NN}} = 4.5$ GeV. *Physical Review C* **103** : 034908. 2021.

[140] C. Hartnack, H. Oeschler, Y. Leifels, E. L. Bratkovskaya, and J. Aichelin. Strangeness production close to the threshold in proton–nucleus and heavy-ion collisions. *Physics Reports* **510** (4-5): 119–200. 2012.

[141] P. Senger *et al.* (KaoS collaboration). The kaon spectrometer at SIS. *Nuclear Inst. and Methods in Physics Research, A* **327** (2-3): 393–411. 1993.

[142] A. Förster *et al.* (KaoS collaboration). Review of the results of the KaoS Collaboration. *Journal of Physics G* **31** (6): S693–S700. 2005.

[143] F. Uhlig *et al.* (KaoS collaboration). Observation of Different Azimuthal Emission Patterns of K+ and of K- Mesons in Heavy-Ion Collisions at 1–2A GeV. *Physical Review Letters* **95** (1): 012301. 2005.

[144] A. Gobbi *et al.* (FOPI collaboration). A highly-segmented ΔE-time-of-flight wall as forward detector of the 4π-system for charged particles at the SIS/ESR accelerator. *Nuclear Inst. and Methods in Physics Research, A* **324** (1-2): 156–176. 1993.

[145] J. Ritman (FOPI collaboration). The FOPI Detector at SIS/GSI. *Nuclear Physics B (Proceedings Supplements)* **44** (1-3): 708–715. 1995.

[146] P. Crochet *et al.* (FOPI collaboration). Sideward flow of K+ mesons in Ru+Ru and Ni+Ni reactions near threshold. *Physics Letters B* **486** (1-2): 6–12. 2000.

[147] M. Merschmeyer (FOPI collaboration). Strangeness production close to threshold. *Journal of Physics G* **31** (6): S1147–S1150. 2005.

[148] V. Zinyuk *et al.* (FOPI collaboration). Azimuthal emission patterns of K^+ and of K^- mesons in Ni + Ni collisions near the strangeness production threshold. *Physical Review C* **90** (2): 025210. 2014.

[149] K. Ackermann *et al.* (STAR collaboration). STAR detector overview. *Nuclear Instruments and Methods in Physics Research Section A* **499** (2): 624-632. 2003.

[150] J. Adams *et al.* (STAR collaboration). Experimental and theoretical challenges in the search for the quark–gluon plasma: The STAR Collaboration's critical assessment of the evidence from RHIC collisions. *Nuclear Physics A* **757** (1): 102-183. 2005.

[151] S. Collaboration *et al.* (STAR collaboration). An Experimental Exploration of the QCD Phase Diagram: The Search for the Critical Point and the Onset of De-confinement. `arXiv:1007.2613`.

[152] M. S. Abdallah *et al.*. Disappearance of partonic collectivity in $\sqrt{s_{NN}} = 3$ GeV Au+Au collisions at RHIC. `arXiv:2108.00908v1`.

[153] G. Roche *et al.* (DLS collaboration). First Observation of Dielectron Production in Proton-Nucleus Collisions below 10 GeV. *Physical Review Letters* **61** (9): 1069–1072. 1988.

[154] P. Kienle. The SIS/ESR-project at GSI: Present and future. in *The Nuclear equation of state. Pt. A: Discovery of nuclear shock waves and the EOS. Proceedings, NATO Advanced Study Institute, Peniscola, Spain, May 22 - June 3, 1989*, edited by W. Greiner and H. Stoecker. pp. 463–476. Springer, Boston, MA. 1989.

[155] A. Yegneswaran *et al.* (DLS collaboration). The dilepton spectrometer. *Nuclear Inst. and Methods in Physics Research, A* **290** (1): 61–75. 1990.

[156] HADES collaboration. Internal Materials.

[157] L. Chlad. *HADES - STUDY OF CHANGES OF HADRON'S PROPERTIES*. Master's thesis. Charles University in Prague, Faculty of Mathematics and Physics. 2015.

[158] G. Agakichiev *et al.* (HADES collaboration). The high-acceptance dielectron spectrometer HADES. *European Physical Journal A* **41** (2): 243–277. 2009.

[159] J. Pietraszko *et al.*. Radiation damage in single crystal CVD diamond material investigated with a high current relativistic 197Au beam. *Nuclear Instruments and Methods in Physics Research A* **763** : 1–5. 2014.

[160] L. Fabbietti. *Study of the* e^+e^- *pair acceptance in the dilepton spectrometer HADES*. PhD thesis. Technische Universität München, Physics Department. 2003.

[161] P. Sellheim. *Reconstruction of the low-mass dielectron signal in* 1.23 *A*GeV *Au+Au collisions*. PhD thesis. Johann Wolfgang Goethe-Universität in Frankfurt am Main, Physics Department. 2017.

[162] J. S. Siebenson. *Exclusive analysis of the* $\Lambda(1405)$ *resonance in the charged* $\Sigma\pi$ *decay channels in proton proton reactions with HADES*. Master's thesis. Munich: Technische Universität München, Physics Department. 2010.

[163] C. Pauly *et al.*. Upgrade of the HADES RICH photon detector with H12700 MAPMTs. *Nuclear Instruments and Methods in Physics Research A* **876** : 164–167. 2017.

[164] HADES collaboration. HADES monitoring Ag+Ag 1.58 AGeV. `https://web-docs.gsi.de/~webhades/onlineMon/mar19/hades-online.html`. [Online; accessed 15-February-2020].

[165] H. Alvarez Pol. *On the Multiwire Drift Chambers alignment of the HADES dilepton spectrometer*. PhD thesis. University of Santiago de Compostela, Faculty of Physics. 2002.

[166] T. Marek. *Detekce leptonů v reakcích relativistických těžkých iontů*. Master's thesis. Charles University in Prague, Faculty of Mathematics and Physics. 1998.

[167] J. Bielčík. *Dilepton spectroscopy with HADES*. PhD thesis. Technical University in Darmstadt, Faculty of Physics. 2004.

[168] P. Cabanelas Eiras. *Software development and Performance Analysis of the HADES Resistive Plate Chamber Time-of-Flight Detector at GSI*. PhD thesis. University of Santiago de Compostela, Faculty of Physics. 2011.

[169] O. Svoboda *et al.*. Electromagnetic calorimeter for the HADES@FAIR experiment. *Journal of Instrumentation* **9** (05): C05002–C05002. 2014.

[170] O. Svoboda *et al.*. Verification of electromagnetic calorimeter concept for the HADES spectrometer. *Journal of Physics: Conference Series* **599** (1): 1–6. 2015.

[171] P. Chudoba *et al.* (HADES collaboration). Commissioning of the electromagnetic calorimeter ECAL of the HADES experiment. *Journal of Physics: Conference Series* **1667** (1): 012007. 2020.

[172] O. V. Andreeva *et al.*. Forward scintillation hodoscope for nuclear fragment detection at the high acceptance dielectron spectrometer (HADES) setup. *Instruments and Experimental Techniques* **57** (2): 103–119. 2014.

[173] J. Michel *et al.*. The HADES DAQ System: Trigger and Readout Board Network. *IEEE Transactions on Nuclear Science* **58** (4): 1745–1750. 2011.

[174] G. Kornakov *et al.*. Performance study and calibration strategy of the HADES scintillator TOF Wall with fast digital readout. `arXiv:2103.07416v1`.

[175] M. S. García. *Momentum reconstruction and pion production analysis in the HADES spectrometer at GSI*. PhD thesis. University of Santiago de Compostela, Particle Physics Department. 2003.

[176] J. Adamczewski-Musch *et al.* (HADES collaboration). Centrality determination of Au + Au collisions at 1.23A GeV with HADES. *European Physical Journal A* **54** (5): 85. 2018.

[177] R. J. Glauber. Cross Sections in Deuterium at High Energies. *Physical Review* **100** : 242–248. 1955.

[178] T. Scheib. *Λ and K^0_s Production in Au+Au Collisions at* 1.23 *A*GeV. PhD thesis. Johann Wolfgang Goethe-Universität in Frankfurt am Main, Physics Department. 2017.

[179] H. Schuldes. *Charged Kaon and ϕ Reconstruction in Au+Au Collisions at* 1.23 *A*GeV. PhD thesis. Johann Wolfgang Goethe-Universität in Frankfurt am Main, Physics Department. 2016.

[180] J. Adamczewski-Musch *et al.* (HADES collaboration). Charged pion production in $\mathbf{Au + Au}$ collisions at $\sqrt{\mathbf{s_{NN}}} = 2.4\mathbf{GeV}$. *to be published in EPJA* . 2020.

[181] M. Lorenz. *Vector meson production in* p + Nb *reactions and statistical particle production in* Ar + KCl *collisions*. PhD thesis. Johann Wolfgang Goethe-Universität in Frankfurt am Main, Physics Department. 2012.

[182] C. Bishop. *Pattern Recognition and Machine Learning* (Springer-Verlag New York, 2006).

[183] D. Silver *et al.*. Mastering the game of Go without human knowledge. *Nature* **550** (7676): 354–359. 2017.

[184] H. Heidenreich. The Future with Reinforcement Learning. `https://towardsdatascience.com/the-future-with-reinforcement-learning-877a17187d54`. [Online; accessed 14-May-2020].

[185] A. Hoecker *et al.*. TMVA: Toolkit for Multivariate Data Analysis. *Proceedings of Science* **050** : 040. 2007.

[186] R. Brun and F. Rademakers. ROOT - An object oriented data analysis framework. *Nuclear Instruments and Methods in Physics Research A* **389** (1-2): 81–86. 1997.

[187] I. Froehlich *et al.*. Pluto: A Monte Carlo Simulation Tool for Hadronic Physics. *Proceedings of Science* **050** : 076. 2007.

[188] J. Allison *et al.*. An application of the GEANT3 geometry package to the description of the opal detector. *Computer Physics Communications* **47** (1): 55–74. 1987.

[189] A. J. Bevan *et al.*. The Physics of the B Factories. *European Physical Journal C* **74** (11): 3026. 2014.

[190] L. P. Csernai and H. Stöcker. Global collective flow in heavy ion reactions from the beginnings to the future. *Journal of Physics G* **41** (12): 0–21. 2014.

[191] W. Scheid, H. Müller, and W. Greiner. Nuclear shock waves in heavy-ion collisions. *Physical Review Letters* **32** (13): 741–745. 1974.

[192] H. Stöcker, J. A. Maruhn, and W. Greiner. Collective Sideward Flow of Nuclear Matter in Violent High-Energy Heavy-Ion Collisions. *Physical Review Letters* **44** (11): 725–728. 1980.

[193] J. Cugnon, T. Mizutani, and J. Vandermeulen. Equilibration in relativistic nuclear collisions. A Monte Carlo calculation. *Nuclear Physics A* **352** (3): 505–534. 1981.

[194] G. D. Westfall *et al.*. Nuclear Fireball Model for proton inclusive spectra from relativistic heavy-ion collisions. *Physical Review Letters* **37** (18): 1202–1205. 1976.

[195] J. D. Stevenson. Classical Many-Body Calculation of Relativistic Nuclear Collisions. *Physical Review Letters* **41** (25): 1702–1705. 1978.

[196] H. A. Gustafsson *et al.*. Collective Flow Observed in Relativistic Nuclear Collisions. *Physical Review Letters* **52** (18): 1590–1593. 1984.

[197] J. Cugnon, J. Knoll, C. Riedel, and Y. Yariv. Event by event emission - pattern analysis of the intra-nuclear cascade. in *GSI Scientific Report 1981*, edited by G. Siegert. p. 50. GSI. Darmstadt. 1982.

[198] M. Gyulassy, K. A. Frankel, and H. Stöcker. Do nuclei flow at high energies?. *Physics Letters B* **110** (3-4): 185–188. 1982.

[199] J. D. Bjorken and S. J. Brodsky. Statistical Model for Electron-Positron Annihilation into Hadrons. *Physical Review D* **1** (5): 1416–1420. 1970.

[200] P. Danielewicz and G. Odyniec. Transverse momentum analysis of collective motion in relativistic nuclear collisions. *Physics Letters B* **157** (2-3): 146–150. 1985.

[201] H. H. Gutbrod *et al.*. Observation of strong azimuthal asymmetry between slow and fast secondaries in high energy nuclear collisions in the Plastic Ball. in *GSI Scientific Report 1983*, edited by G. Siegert. p. 50. GSI. Darmstadt. 1984.

[202] H. Stöcker, J. Hofmann, J. A. Maruhn, and W. Greiner. Shock waves in nuclear matter - proof by circumstantial evidence. *Progress in Particle and Nuclear Physics* **4** (C): 133–195. 1980.

[203] H. Gutbrod *et al.*. A new component of the collective flow in relativistic heavy-ion collisions. *Physics Letters B* **216** (3-4): 267–271. 1989.

[204] J. Y. Ollitrault. Anisotropy as a signature of transverse collective flow. *Physical Review D* **46** (1): 229–245. 1992.

[205] J. Barrette *et al.* (E877 collaboration). Observation of Anisotropic Event Shapes and Transverse Flow in Ultrarelativistic Au + Au Collisions. *Physical Review Letters* **73** (19): 2532–2535. 1994.

[206] B. Kardan. Flow harmonics of Au+Au collisions at 1.23 AGeV with HADES. *Journal of Physics: Conference Series* **742** (1). 2016.

[207] S. Voloshin and Y. Zhang. Flow study in relativistic nuclear collisions by Fourier expansion of azimuthal particle distributions. *Zeitschrift fur Physik C* **70** (4): 665–671. 1996.

[208] J. Adamczewski-Musch *et al.* (HADES Collaboration). Directed, elliptic and higher order flow harmonics of protons, deuterons and tritons in Au+Au collisions at $\sqrt{s_{\mathrm{NN}}} = 2.4\,GeV$. *Physical Review Letters* **125** : 262301. 2020.

[209] A. M. Poskanzer and S. A. Voloshin. Methods for analyzing anisotropic flow in relativistic nuclear collisions. *Physical Review C* **58** (3): 1671–1678. 1998.

[210] N. Borghini, P. M. Dinh, and J. Y. Ollitrault. Flow analysis from multiparticle azimuthal correlations. *Physical Review C* **64** (5): 549011–5490123. 2001.

[211] R. S. Bhalerao, N. Borghini, and J. Y. Ollitrault. Analysis of anisotropic flow with Lee-Yang zeroes. *Nuclear Physics A* **727** (3-4): 373–426. 2003.

[212] S. Wang *et al.*. Measurement of collective flow in heavy-ion collisions using particle-pair correlations. *Physical Review C* **44** (3): 1091–1095. 1991.

[213] A. M. Poskanzer and S. A. Voloshin. Methods for analyzing anisotropic flow in relativistic nuclear collisions. *Physical Review C* **58** (3): 1671–1678. 1998.

[214] N. Borghini, P. M. Dinh, and J. Y. Ollitrault. Is the analysis of flow at the CERN Super Proton Synchrotron reliable?. *Physical Review C* **62** (3): 11. 2000.

[215] A. Bilandzic, C. H. Christensen, K. Gulbrandsen, A. Hansen, and Y. Zhou. Generic framework for anisotropic flow analyses with multiparticle azimuthal correlations. *Physical Review C* **89** (6): 064904. 2014.

[216] J. Barrette *et al.* (E877 Collaboration). Proton and pion production relative to the reaction plane in Au + Au collisions at 11 A GeV/ c. *Physical Review C* **56** (6): 3254–3264. 1997.

[217] J.-Y. Ollitrault. Reconstructing azimuthal distributions in nucleus-nucleus collisions. `arXiv:nucl-ex/9711003`.

[218] W. Reisdorf *et al.* (FOPI collaboration). Systematics of pion emission in heavy ion collisions in the 1A GeV regime. *Nuclear Physics A* **781** (3): 459-508. 2007.

[219] B. B. Back *et al.* (PHOBOS collaboration). Pseudorapidity and Centrality Dependence of the Collective Flow of Charged Particles in Au + Au Collisions at $\sqrt{s_{NN}} = 130$ GeV. *Physical Review Letters* **89** : 222301. 2002.

[220] A. Prozorov. Simulation study of effects induced by final granularity of detector in particle flow. *Journal of Physics: Conference Series* **1667** : 012034. 2020.

[221] M. Grunwald. Flow correction for $1.23A\,\mathrm{GeV}$ Au+Au collisions at the HADES experiment. in *Photonics Applications in Astronomy, Communications, Industry, and High Energy Physics Experiments 2020*, edited by R. S. Romaniuk and M. Linczuk. p. 26. SPIE. 2020.

[222] F. J. Kornas. Λ polarization in Au+Au collisions at $\sqrt{s_{\mathrm{NN}}} = 2.4\,\mathrm{GeV}$ measured with HADES. in *The XVIII International Conference on Strangeness in Quark Matter (SQM 2019)*, edited by D. Elia, G. E. Bruno, P. Colangelo, and L. Cosmai. pp. 435–439. Cham. 2020. Springer International Publishing.

[223] N. Borghini and J. Y. Ollitrault. Azimuthally sensitive correlations in nucleus-nucleus collisions. *Physical Review C* **70** (6). 2004.

[224] J. Adamczewski-Musch *et al.* (HADES Collaboration). Sub-threshold production of K^0_S mesons and Λ hyperons in Au+Au collisions at $\sqrt{s_{NN}} = 2.4\,\mathrm{GeV}$. *Physics Letters B* **793** : 457–463. 2019.

[225] T. Song, L. Tolos, J. Wirth, J. Aichelin, and E. Bratkovskaya. In-medium effects in strangeness production in heavy-ion collisions at (sub)threshold energies. *Physical Review C* **103** : 044901. 2021.

[226] V. Steinberg *et al.*. Strangeness production via resonances in heavy-ion collisions at energies available at the GSI Schwerionensynchrotron. *Physical Review C* **99** (6): 064908. 2019.

[227] J. Adamczewski-Musch *et al.* (HADES collaboration). Deep sub-threshold ϕ production in Au+Au collisions. *Physics Letters B* **778** : 403–407. 2018.

List of Abbreviations

HADES	High Acceptance Di-Electron Sectrometer
GSI	Gesellschaft für Schwerionenforschung
BNL	Brookhaven National Laboratory
LBL	Lawrence Berkeley national Laboratory
CERN	Conseil Européen pour la recherche nucléaire
FAIR	Facility for Antiproton and Ion Research
QCD	Quantum Chromo Dynamics
HIC	Heavy-Ion Collision
NN/KN	Nucleon-Nucleon/Kaon-Nucleon
SIS	SchwerIonen Synchrotron
AGS	Alternating Gradient Synchrotron
SPS	Super Proton Synchrotron
RHIC	Relativistic Heavy Ion Collider
LHC	Large Hadron Collider
NICA	Nuclotron-based Ion Collider fAcility
MC	Monte Carlo
ChPT	Chiral Perturbation Theory
(R)VUU	(Relativistic) Vlasov–Ueling–Uhlenbeck
(R)BUU	(Relativistic) Boltzmann–Ueling–Uhlenbeck
GiBUU	Giessen BUU
(P)HSD	(Parton) Hadron String Dynamics
(I)QMD	(Isospin) Quantum Molecular Dynamics
UrQMD	Ultra-Relativistic QMD
JAM	Jet AA Microscopic transport Model
SMASH	Simulating Many Accelerated Strongly-interacting Hadrons
QGP	Quark-Gluon Plasma
CEP	Critical End Point
EOS	Equation Of State (of nuclear matter)
KaoS	Kaon Spectrometer
FOPI	FOur-PI detector system
STAR	Solenoidal Tracker At RHIC
RICH	Ring Imaging CHerenkov detector
MDC	Multiwire Drift Chambers
META	Multiplicity Electron Trigger Array
TOF	Time Of Flight chambers
RPC	Resistive Plate Chambers
ECAL	Electromagnetic CALorimeter
FW	Forward hodoscope Wall
DAQ	Data AcQuisition system
HYDRA	Hades sYstem for Data Reduction and Analysis
DST	Data Summary Tapes file
RK	Runge–Kutta
TMVA	Toolkit for Multivariate Data Analysis
MLP NN	MultiLayer Perceptron Neural Network
ME	Mixed-Event technique

List of publications

Author

- L. Chlad, "Beam detector system for pion beam in HADES at SIS18," Book of Reports - Summer Student Program (2014).
- L. Chlad, J. Pietraszko and W. Koenig, "Secondary pion beam for HADES experiment at GSI," Conference proceedings - 18$^{\text{th}}$ Conference of Czech and Slovak Physicists (2015), ISBN: 978-80-24447-25-4 (CD), 978-80-24447-26-1 (online).
- L. Chlad for the HADES collaboration, "Exploring neutron detection with HADES," **J. Phys. Conf. Ser. 742** (2016) no.1, 012033.
- L. Chlad, A. Kugler, "Using HADES spectrometer for neutron detection," Conference proceedings - 25$^{\text{th}}$ Annual Conference of Doctoral Students – WDS (2016), ISBN 978-80-7378-333-4.
- L. Chlad for the HADES collaboration, "Hidden neutrons in HADES data," Conference proceedings - 19$^{\text{th}}$ Conference of Czech and Slovak Physicists (2017), ISBN: 978-80-89855-04-9.
- L. Chlad for the HADES collaboration, "Strangeness flow in Au+Au collisions at 1.23 AGeV measured with HADES," Conference proceedings - 18$^{\text{th}}$ International Conference on Strangeness in Quark Matter (2019), Springer Proceedings in Physics 250 (2020) 221-224.

Co-author

- P. Rodríguez-Ramos *et al.* [HADES Collab.], "Electromagnetic Calorimeter for HADES Experiment," **EPJ Web Conf. 81** (2014), 06009.
- J. Adamczewski-Musch *et al.* [HADES Collaboration], "Analysis of the exclusive final state npe$^+$e$^-$ in quasi-free np reaction," **Eur. Phys. J. A 53** (2017) no.7, 149. arXiv:1703.08575 [nucl-ex].
- J. Adamczewski-Musch *et al.* [HADES Collaboration], "Deep sub-threshold ϕ production and implications for the K+/K- freeze-out in Au+Au collisions," **Phys. Lett. B 778** (2018), 403. arXiv:1703.08418 [nucl-ex].
- J. Adamczewski-Musch *et al.* [HADES Collaboration], "$\Delta(1232)$ Dalitz decay in proton-proton collisions at T=1.25 GeV measured with HADES," **Phys. Rev. C 95** (2017) no.6, 065205. arXiv:1703.07840 [nucl-ex].
- J. Adamczewski-Musch *et al.* [HADES Collaboration], "A facility for pion-induced nuclear reaction studies with HADES," **Eur. Phys. J. A 53** (2017) no.9, 188.
- J. Adamczewski-Musch *et al.* [HADES Collaboration], "Centrality determination of Au+Au with HADES," **Eur. Phys. J. A 54** (2018) no.5, 85. arXiv:1712.07993 [nucl-ex].
- J. Adamczewski-Musch *et al.* [HADES Collaboration], "Identical pion intensity interferometry in central Au+Au collisions at 1.23 AGeV," **Phys. Lett. B 795** (2019), 446. arXiv:1811.06213 [nucl-ex] (update: 1910.07885 [nucl-ex]).

- J. Adamczewski-Musch *et al.* [HADES Collaboration], "Strong absorption of hadrons with hidden and open strangeness in nuclear matter," **Phys. Rev. Lett. 123** (2019) no.2, 022002. arXiv:1812.03728 [nucl-ex].
- J. Adamczewski-Musch *et al.* [HADES Collaboration], "Sub-threshold production of K^0_s mesons and Λ hyperons in Au+Au collisions at $\sqrt{s_{NN}} = 2.4\,\mathrm{GeV}$," **Phys. Lett. B 793** (2019), 457. arXiv:1812.07304 [nucl-ex].
- J. Adamczewski-Musch *et al.* [HADES Collaboration], "Probing dense baryon-rich matter with virtual photons," **Nature Phys. 15** (2019) no.10, 1040.
- J. Adamczewski-Musch *et al.* [HADES Collaboration], "Identical pion intensity interferometry at $\sqrt{s_{NN}} = 2.4\,\mathrm{GeV}$," **Eur. Phys. J. A 56** (2020) no.5, 140. arXiv:1910.07885 [nucl-ex].
- J. Adamczewski-Musch *et al.* [HADES Collaboration], "Proton number fluctuations in $\sqrt{s_{NN}} = 2.4\,\mathrm{GeV}$ Au+Au collisions studied with HADES," **Phys. Rev. C 102** (2020) no.2, 024914. arXiv:2002.08701 [nucl-ex].
- J. Adamczewski-Musch *et al.* [HADES Collaboration], "Two-pion production in the second resonance region in π^-p collisions with the High-Acceptance Di-Electron Spectrometer," **Phys. Rev. C 102** (2020) no.2, 024001. arXiv:2004.08265 [nucl-ex].
- J. Adamczewski-Musch *et al.* [HADES Collaboration], "Charged-pion production in Au+Au collisions at $\sqrt{s_{NN}} = 2.4\,\mathrm{GeV}$," **Eur. Phys. J. A 56** (2020) no.10, 259. arXiv:2005.08774 [nucl-ex].
- J. Adamczewski-Musch *et al.* [HADES Collaboration], "Directed, elliptic and higher order flow harmonics of protons, deuterons and tritons in Au+Au collisions at $\sqrt{s_{NN}} = 2.4\,\mathrm{GeV}$," **Phys. Rev. Lett. 125** (2020), 262301. arXiv: 2005.12217 [nucl-ex].
- P. Chudoba *et al.* [HADES Collaboration], "Commissioning of the electromagnetic calorimeter ECAL of the HADES experiment," **J. Phys. Conf. Ser. 1667** (2020) no.1, 012007.
- J. Adamczewski-Musch *et al.* [HADES and PANDA Collaborations], "Production and electromagnetic decay of hyperons: a feasibility study with HADES as a phase-0 experiment at FAIR," **Eur. Phys. J. A 57** (2021) no.4, 138. arXiv:2010.06961 [nucl-ex].
- J. Adamczewski-Musch *et al.* [HADES Collaboration], "Correlated pion-proton pair emission off hot and dense QCD matter," **Phys. Lett. B 819** (2021), 136421. arXiv:2012.01351 [nucl-ex].
- G. Kornakov *et al.*, "Performance study and calibration strategy of the HADES scintillator TOF Wall with fast digital readout," submitted to **Nucl. Instrum. Meth. A**. arXiv:2103.07416 [nucl-ex].

Appendix A

Kaons phase space distribution, acceptance and reconstruction efficiencies

A.1 K^+

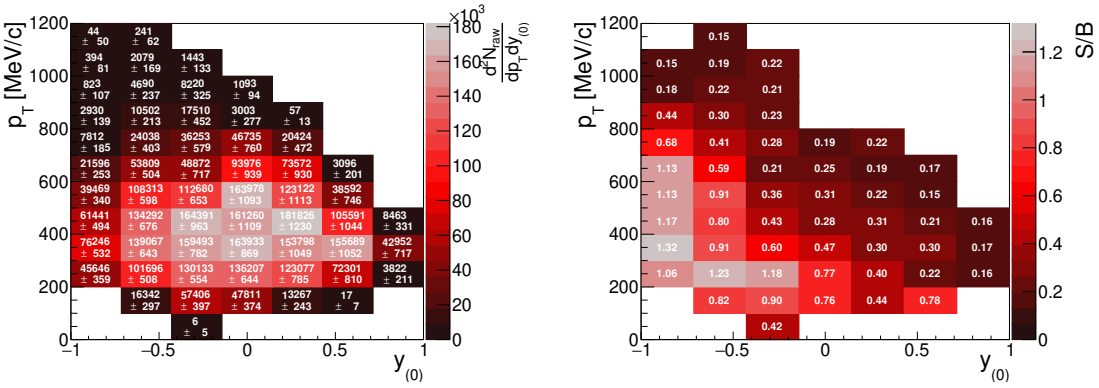

(a) (b)

Figure A.1: K^+ phase space distribution for $0 - 10\,\%$ centrality class shown in (a) and corresponding signal to background ratio in (b).

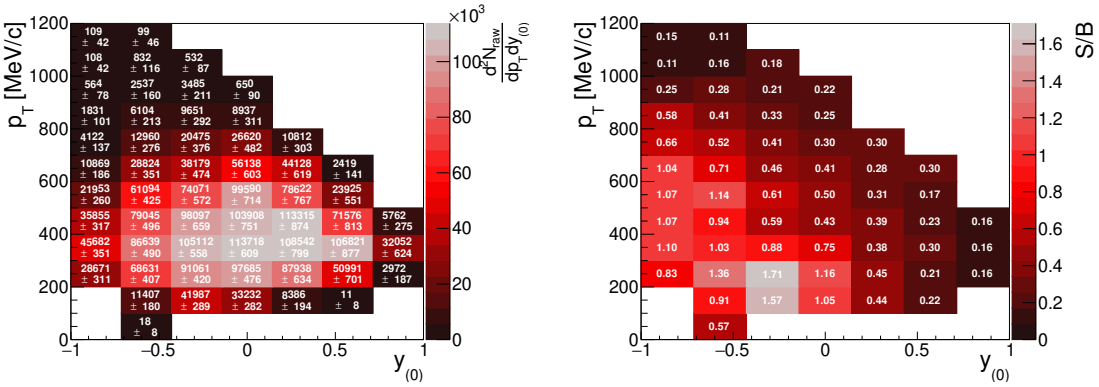

(a) (b)

Figure A.2: K^+ phase space distribution for $10 - 20\,\%$ centrality class shown in (a) and corresponding signal to background ratio in (b).

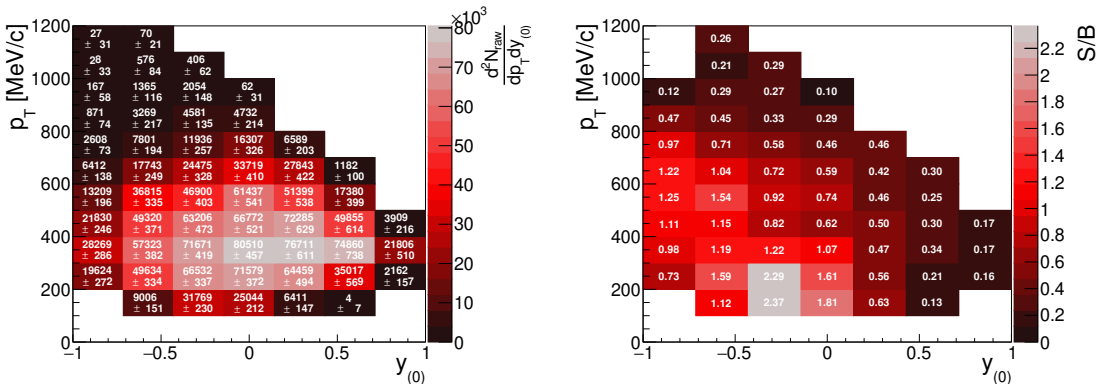

(a) (b)

Figure A.3: K^+ phase space distribution for $20-30\,\%$ centrality class shown in (a) and corresponding signal to background ratio in (b).

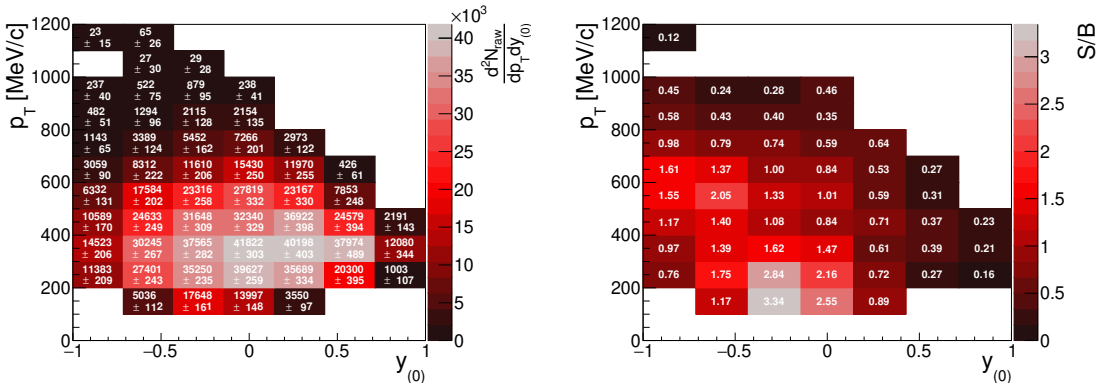

(a) (b)

Figure A.4: K^+ phase space distribution for $30-40\,\%$ centrality class shown in (a) and corresponding signal to background ratio in (b).

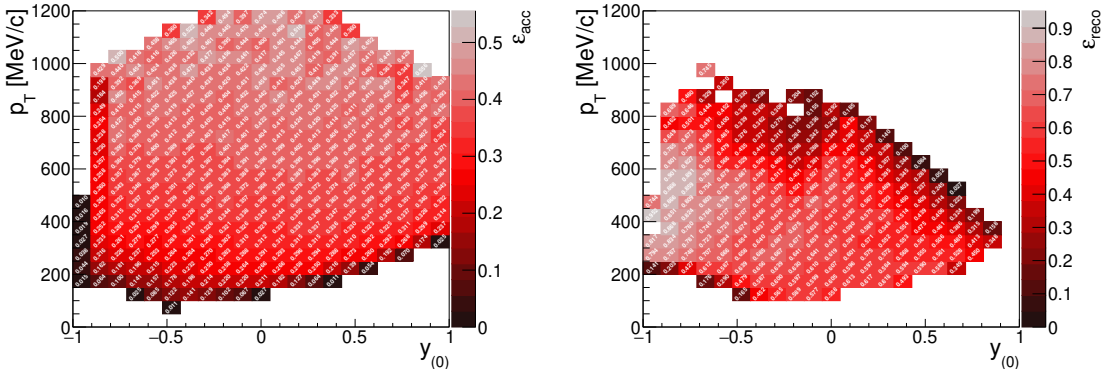

(a) (b)

Figure A.5: K^+ acceptance in (a) and reconstruction efficiency in (b) for $0-10\,\%$ centrality class.

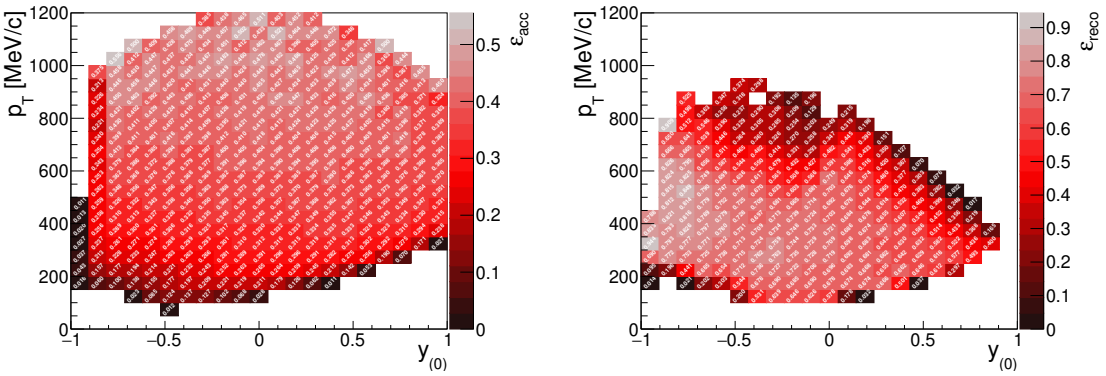

(a) (b)

Figure A.6: K^+ acceptance in (a) and reconstruction efficiency in (b) for $10-20\,\%$ centrality class.

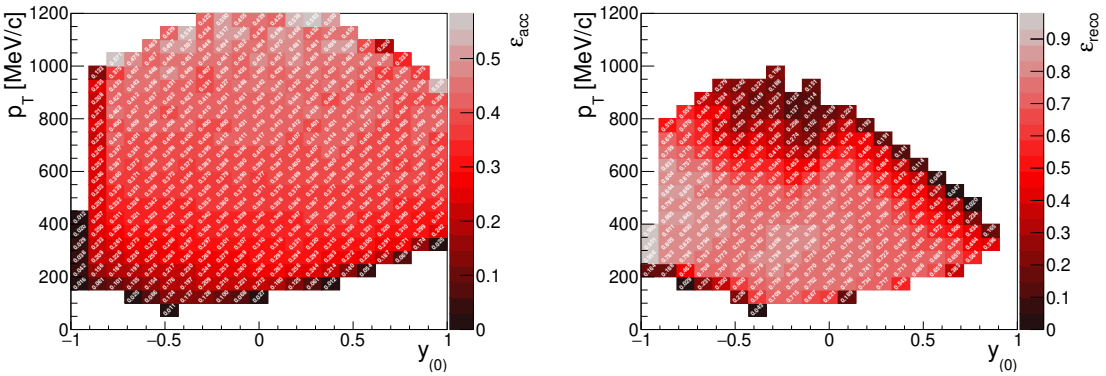

(a) (b)

Figure A.7: K^+ acceptance in (a) and reconstruction efficiency in (b) for $20-30\,\%$ centrality class.

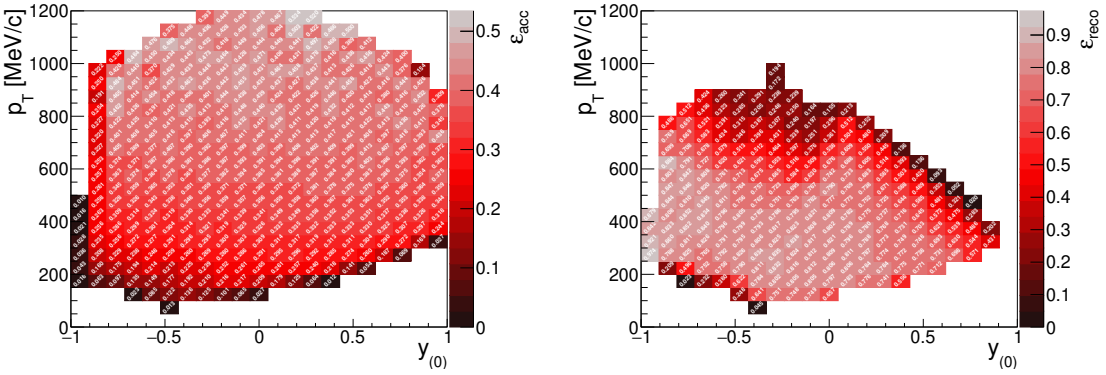

(a) (b)

Figure A.8: K^+ acceptance in (a) and reconstruction efficiency in (b) for $30-40\,\%$ centrality class.

A.2 K^-

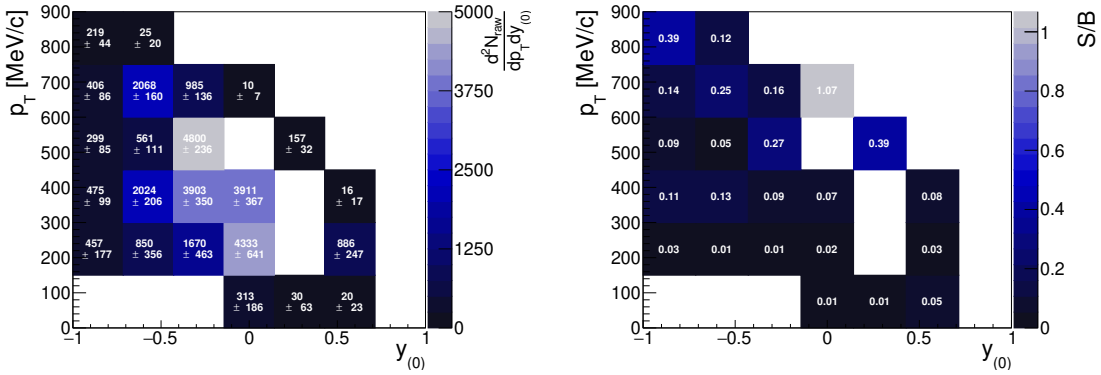

(a) (b)

Figure A.9: K^- phase space distribution for $0 - 10\,\%$ centrality class shown in (a) and corresponding signal to background ratio in (b).

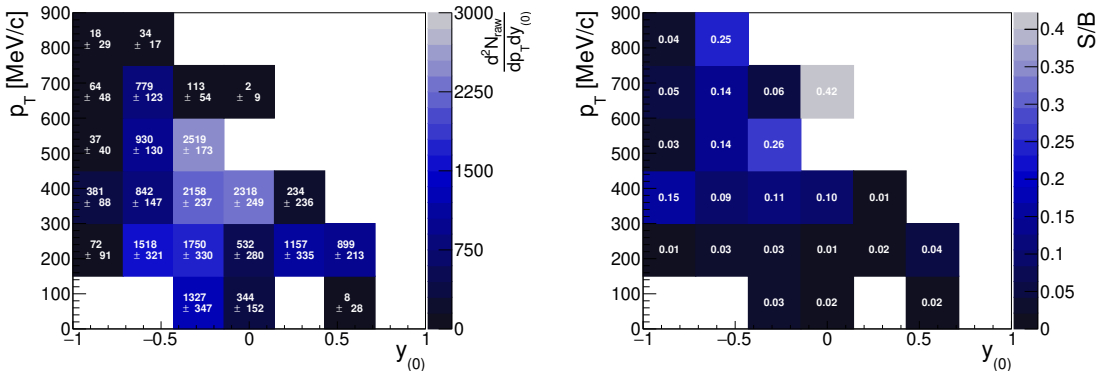

(a) (b)

Figure A.10: K^- phase space distribution for $10 - 20\,\%$ centrality class shown in (a) and corresponding signal to background ratio in (b).

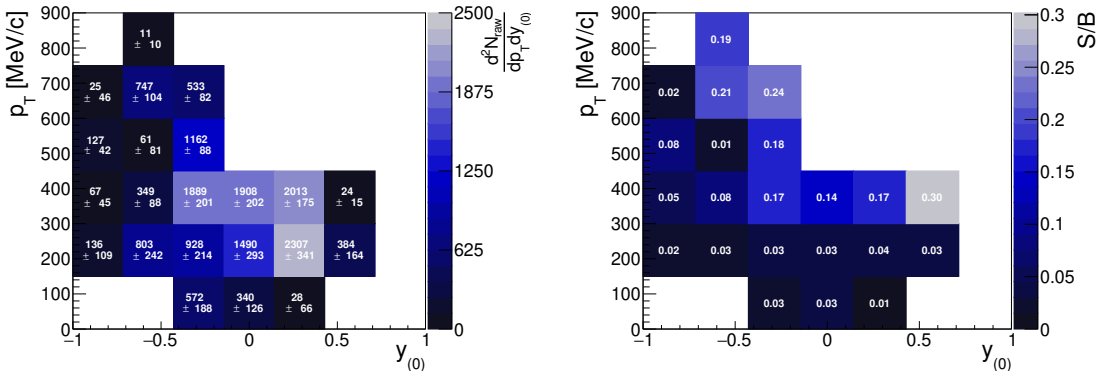

(a) (b)

Figure A.11: K^- phase space distribution for $20-30\,\%$ centrality class shown in (a) and corresponding signal to background ratio in (b).

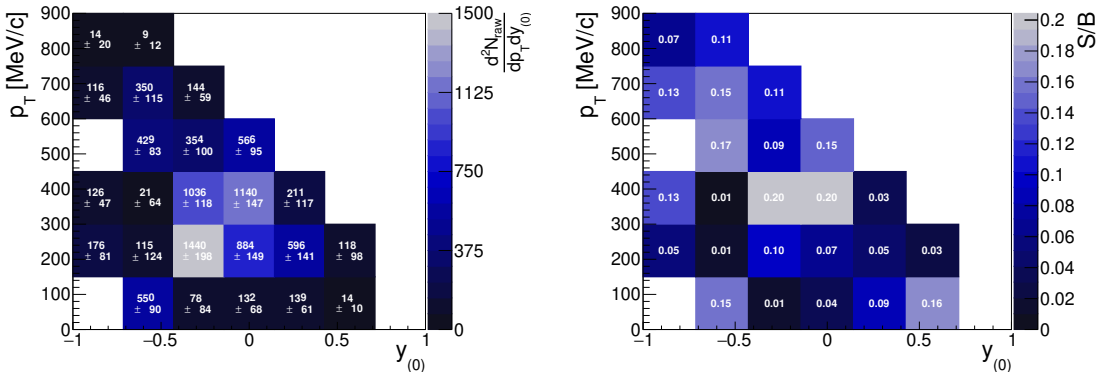

(a) (b)

Figure A.12: K^- phase space distribution for $30-40\,\%$ centrality class shown in (a) and corresponding signal to background ratio in (b).

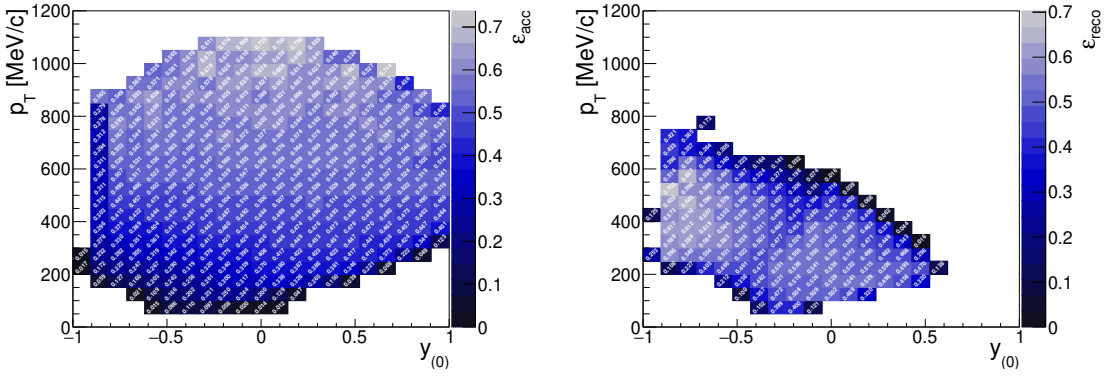

(a) (b)

Figure A.13: K^- acceptance in (a) and reconstruction efficiency in (b) for $0-10\,\%$ centrality class.

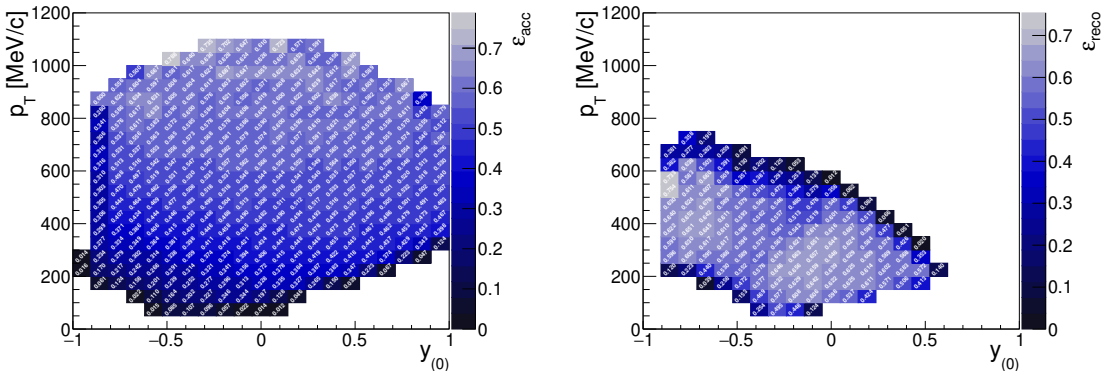

(a) (b)

Figure A.14: K^- acceptance in (a) and reconstruction efficiency in (b) for 10 – 20 % centrality class.

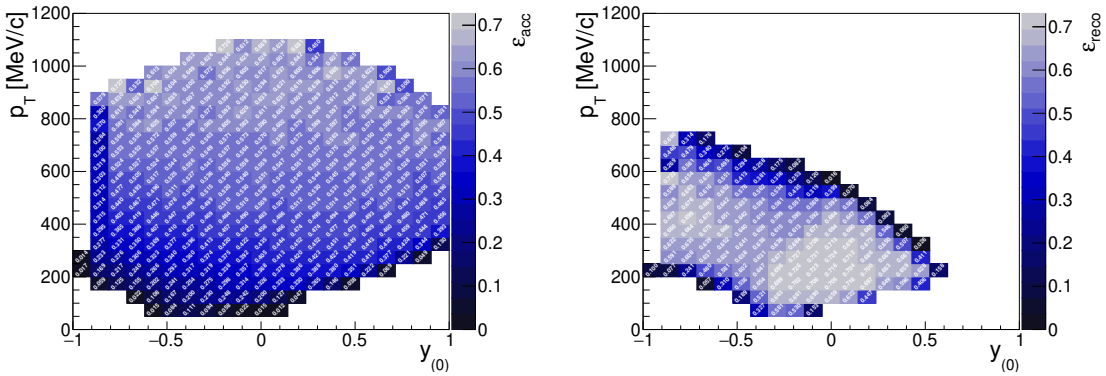

(a) (b)

Figure A.15: K^- acceptance in (a) and reconstruction efficiency in (b) for 20 – 30 % centrality class.

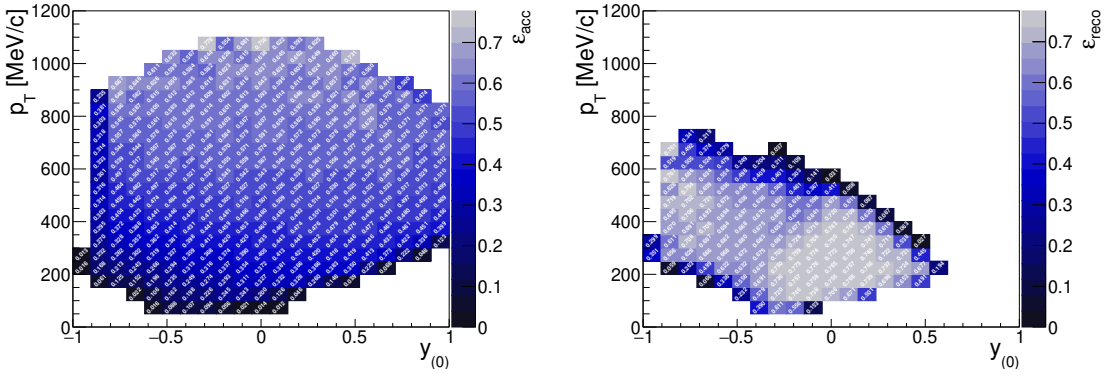

(a) (b)

Figure A.16: K^- acceptance in (a) and reconstruction efficiency in (b) for 30 – 40 % centrality class.

A.3 K^0_S

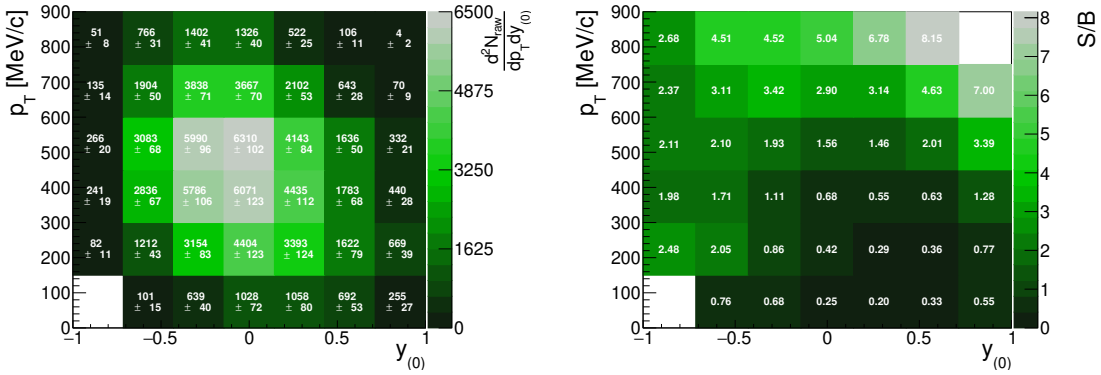

(a) (b)

Figure A.17: K^0_S phase space distribution for $0 - 10\,\%$ centrality class shown in (a) and corresponding signal to background ratio in (b).

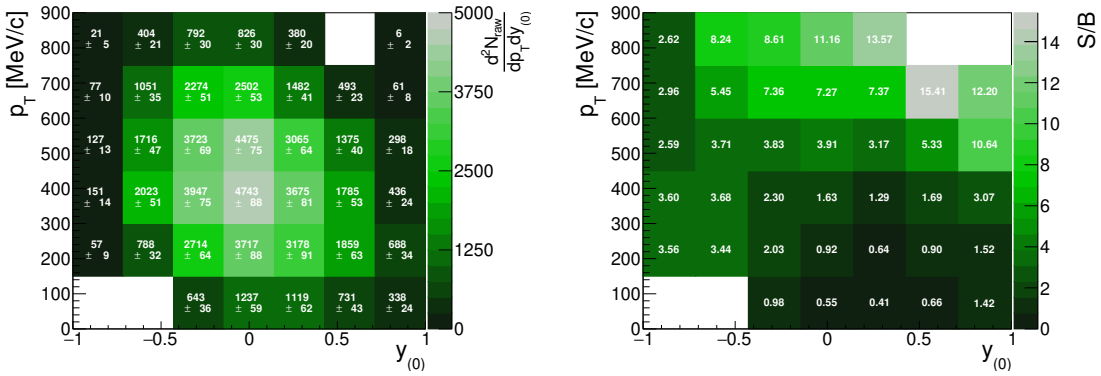

(a) (b)

Figure A.18: K^0_S phase space distribution for $10 - 20\,\%$ centrality class shown in (a) and corresponding signal to background ratio in (b).

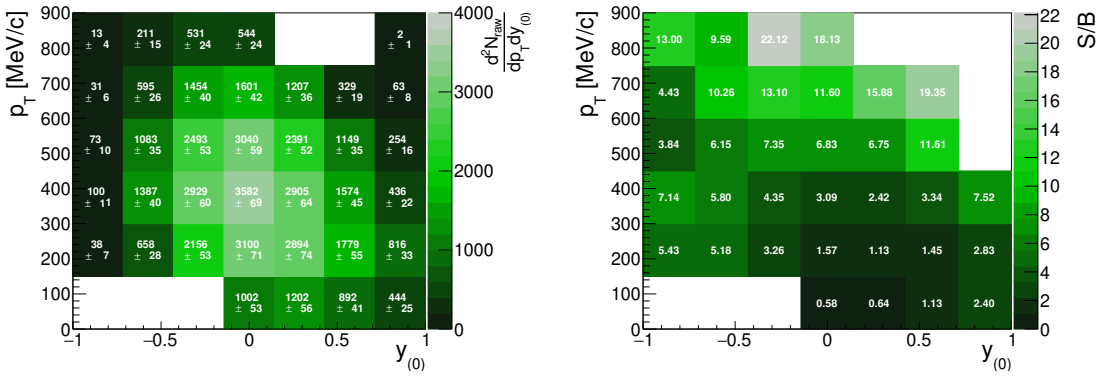

(a) (b)

Figure A.19: K^0_S phase space distribution for $20-30\,\%$ centrality class shown in (a) and corresponding signal to background ratio in (b).

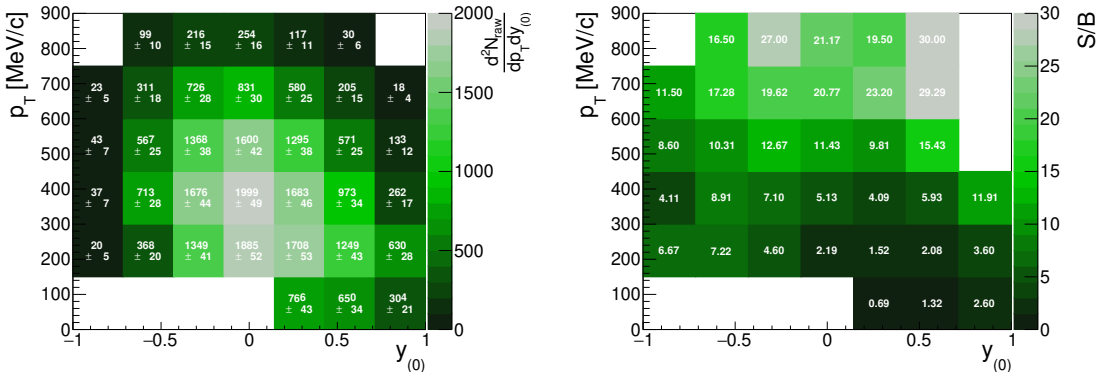

(a) (b)

Figure A.20: K^0_S phase space distribution for $30-40\,\%$ centrality class shown in (a) and corresponding signal to background ratio in (b).

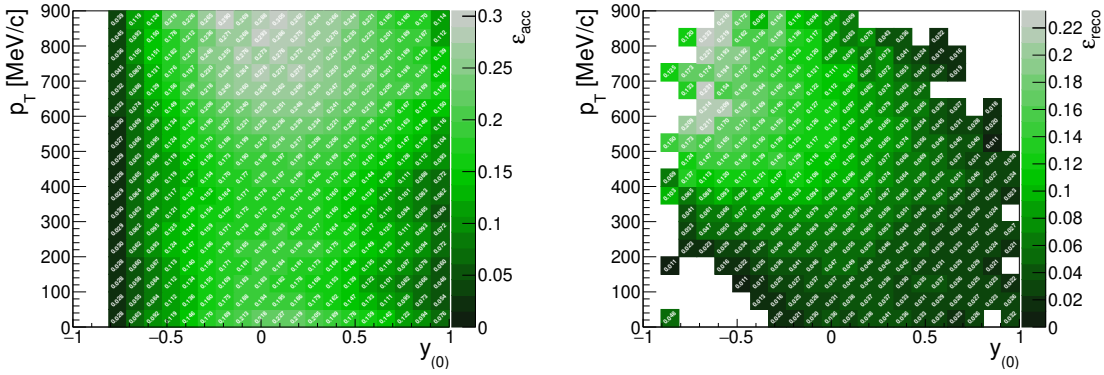

(a) (b)

Figure A.21: K^0_S acceptance in (a) and reconstruction efficiency in (b) for $0-10\,\%$ centrality class.

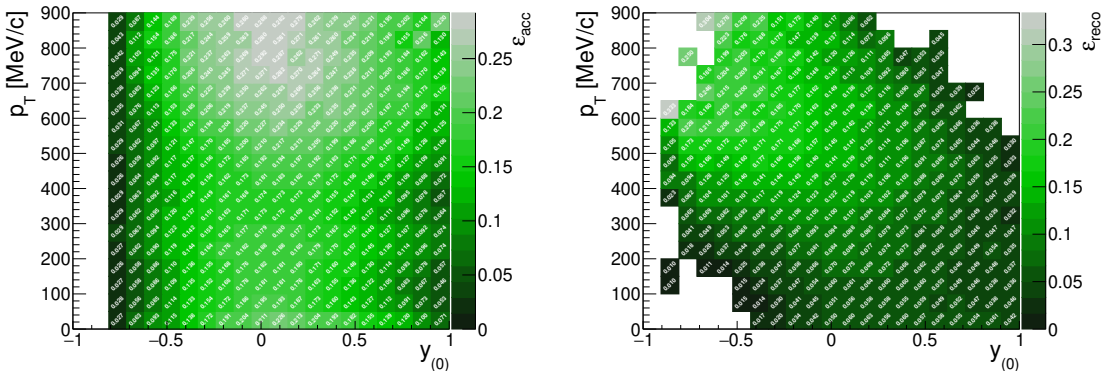

(a) (b)

Figure A.22: K^0_S acceptance in (a) and reconstruction efficiency in (b) for 10−20 % centrality class.

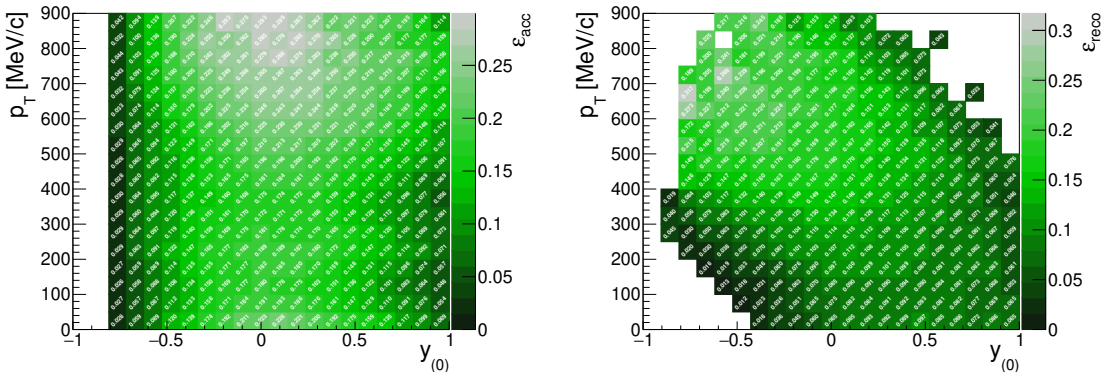

(a) (b)

Figure A.23: K^0_S acceptance in (a) and reconstruction efficiency in (b) for 20−30 % centrality class.

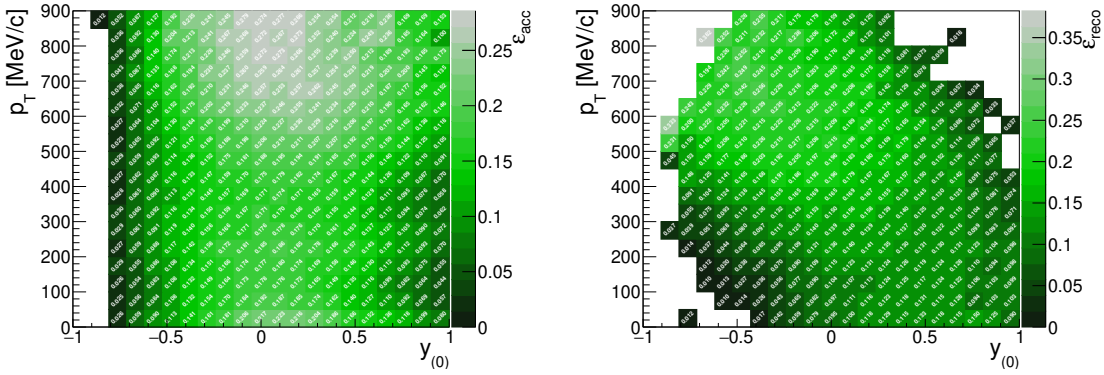

(a) (b)

Figure A.24: K^0_S acceptance in (a) and reconstruction efficiency in (b) for 30−40 % centrality class.

Appendix B

Supplementary figures for the results of kaon flow analysis

B.1 K^+ and K^0_S directed and elliptic flow comparison

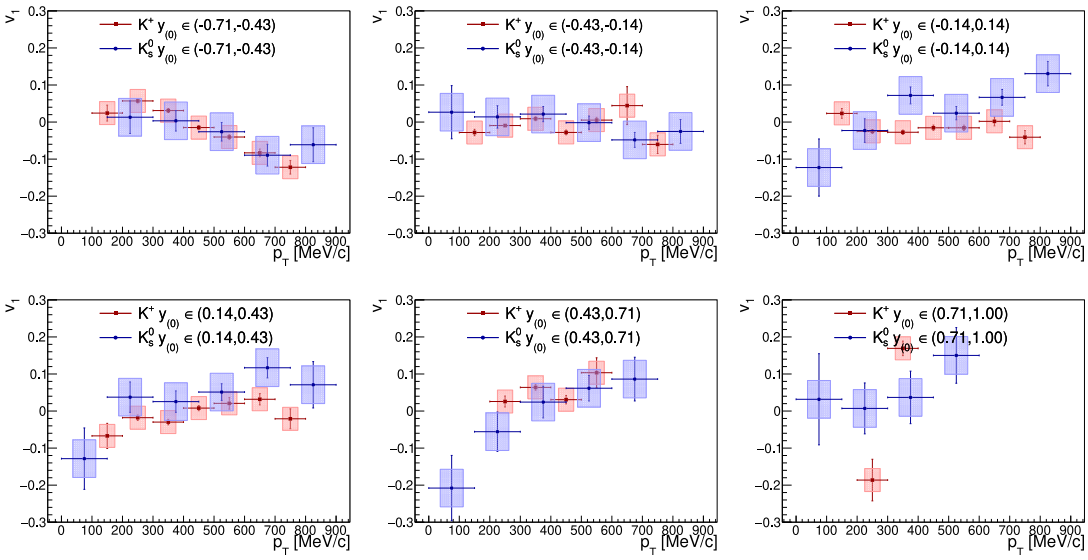

Figure B.1: Comparison of differential directed flow of K^+ and K^0_S in collisions with $0-10\%$ centrality. Error bars displayed with lines indicates statistical uncertainties, boxes are for systematic uncertainties.

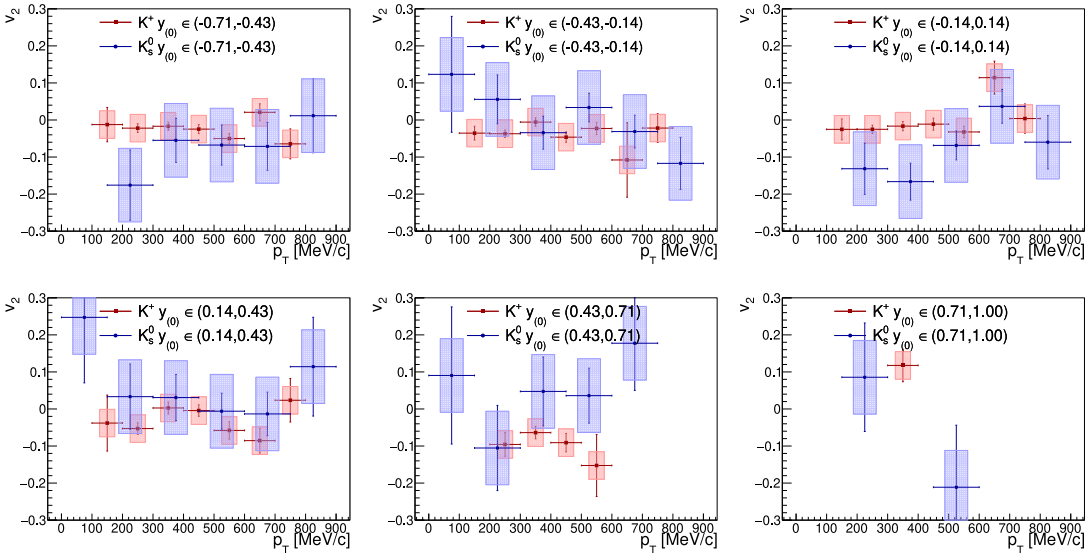

Figure B.2: Comparison of differential elliptic flow of K^+ and K^0_S in collisions with $0-10\%$ centrality. Error bars displayed with lines indicates statistical uncertainties, boxes are for systematic uncertainties.

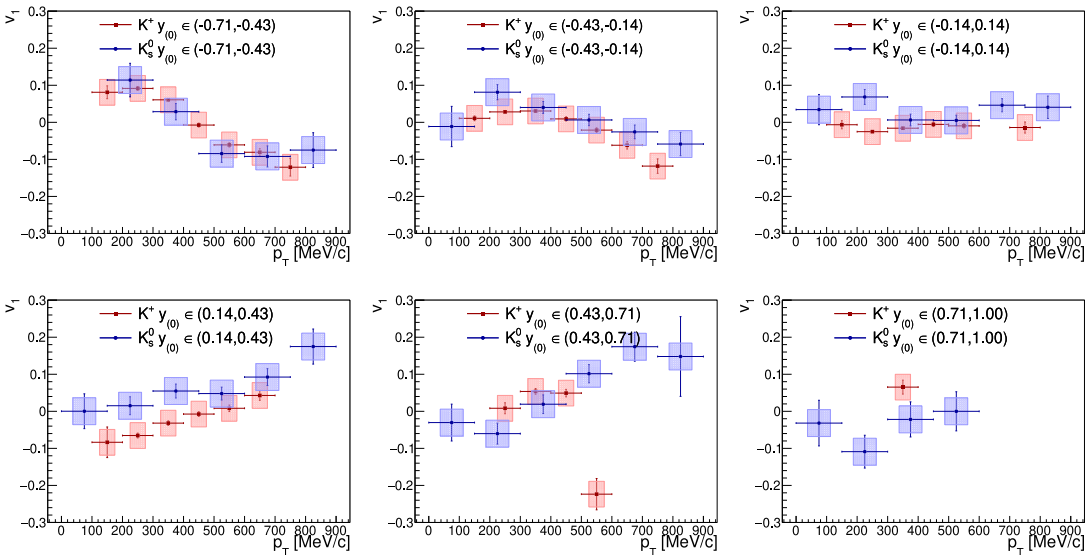

Figure B.3: Comparison of differential directed flow of K^+ and K^0_S in collisions with $10-20\%$ centrality. Error bars displayed with lines indicates statistical uncertainties, boxes are for systematic uncertainties.

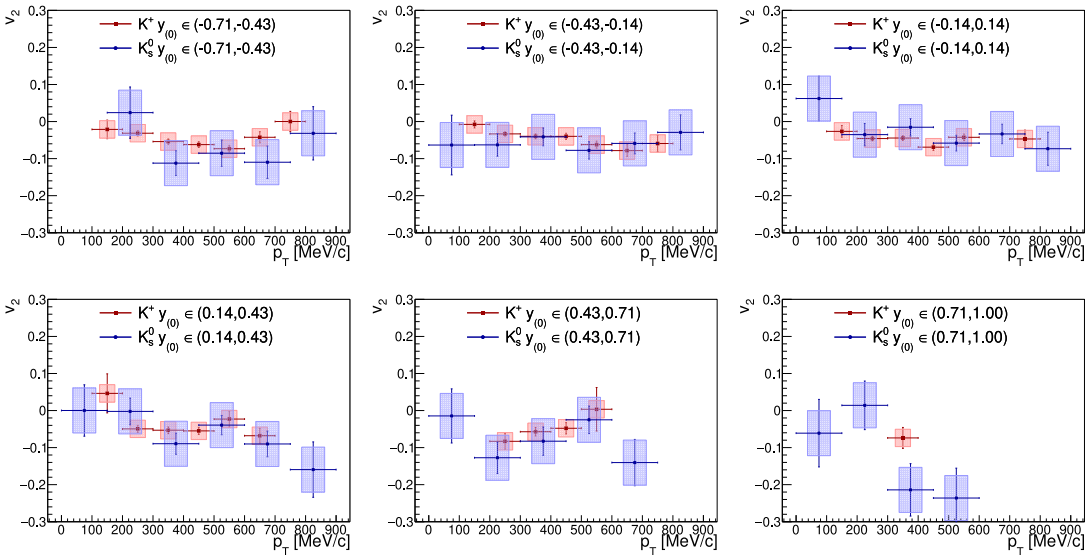

Figure B.4: Comparison of differential elliptic flow of K^+ and K^0_S in collisions with $10-20\%$ centrality. Error bars displayed with lines indicates statistical uncertainties, boxes are for systematic uncertainties.

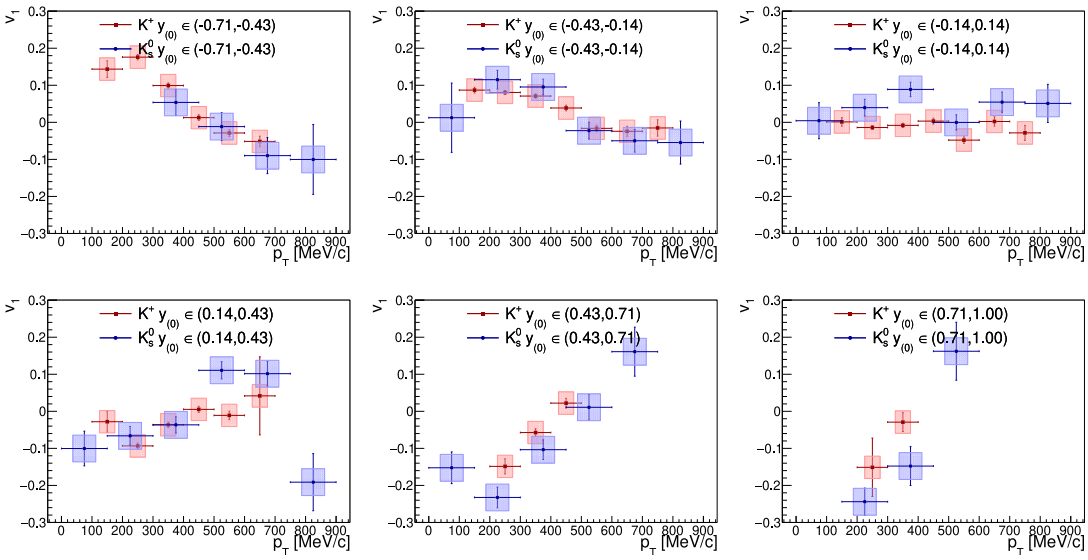

Figure B.5: Comparison of differential directed flow of K^+ and K^0_S in collisions with $30-40\%$ centrality. Error bars displayed with lines indicates statistical uncertainties, boxes are for systematic uncertainties.

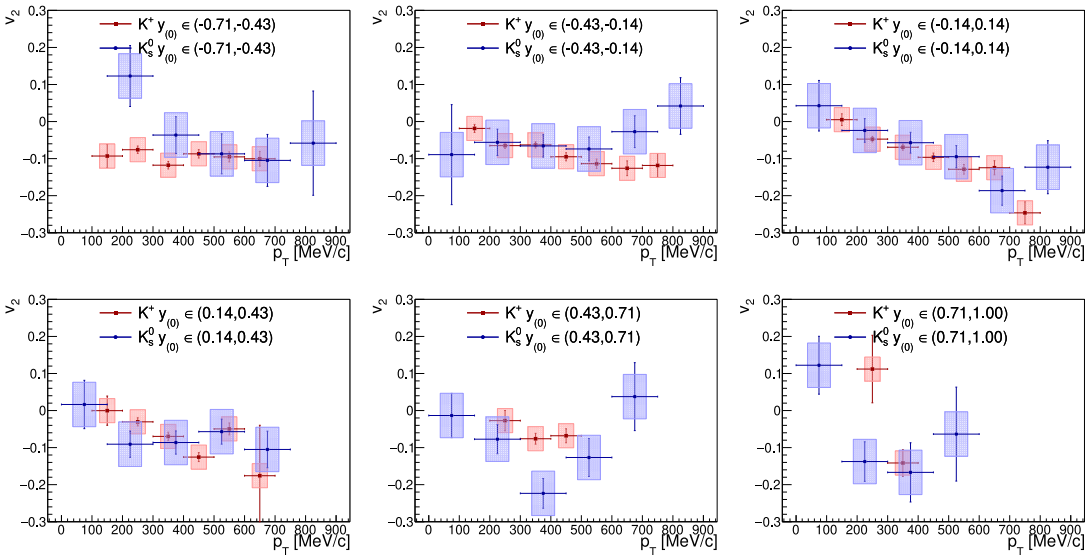

Figure B.6: Comparison of differential elliptic flow of K^+ and K^0_S in collisions with $30-40\%$ centrality. Error bars displayed with lines indicates statistical uncertainties, boxes are for systematic uncertainties.

B.2 K^+ and K^0_S flow overview plots

Left column: $v_{1,2}(y_{(0)})$ for different p_T intervals, right column: $v_{1,2}(p_T)$ for different $y_{(0)}$ intervals. Each row represents one centrality class, the label is on the right edge of figure. The error bars represent only statistical uncertainties, the systematic uncertainties are displayed with pink boxes. The interpolating lines are only meant to guide the eye.

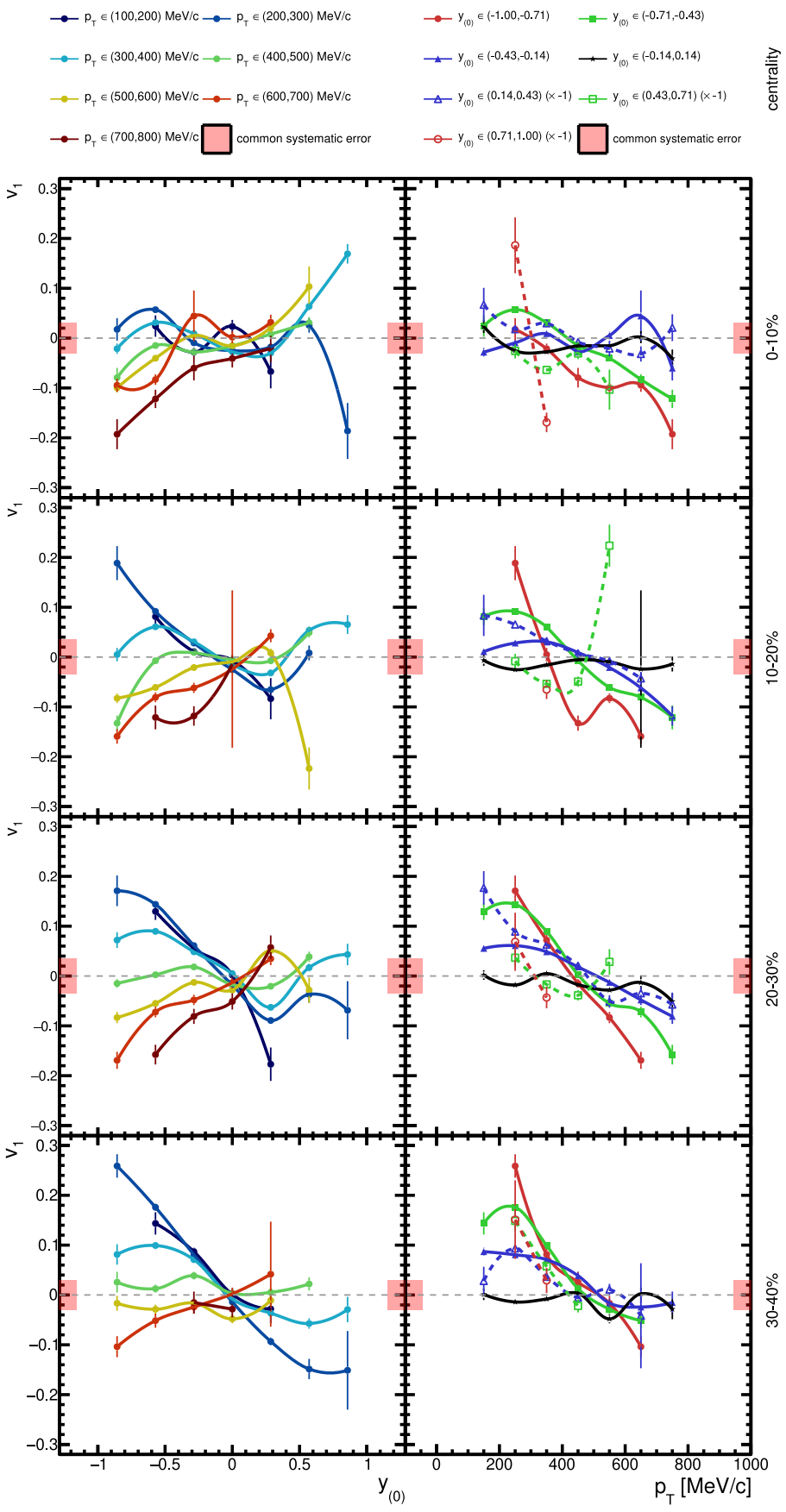

Figure B.7: Differential directed flow of K^+ measured in Au + Au collisions at beam kinetic energy $E_{\mathrm{kin,beam}} = 1.23A\,\mathrm{GeV}$ in 40% most central collisions.

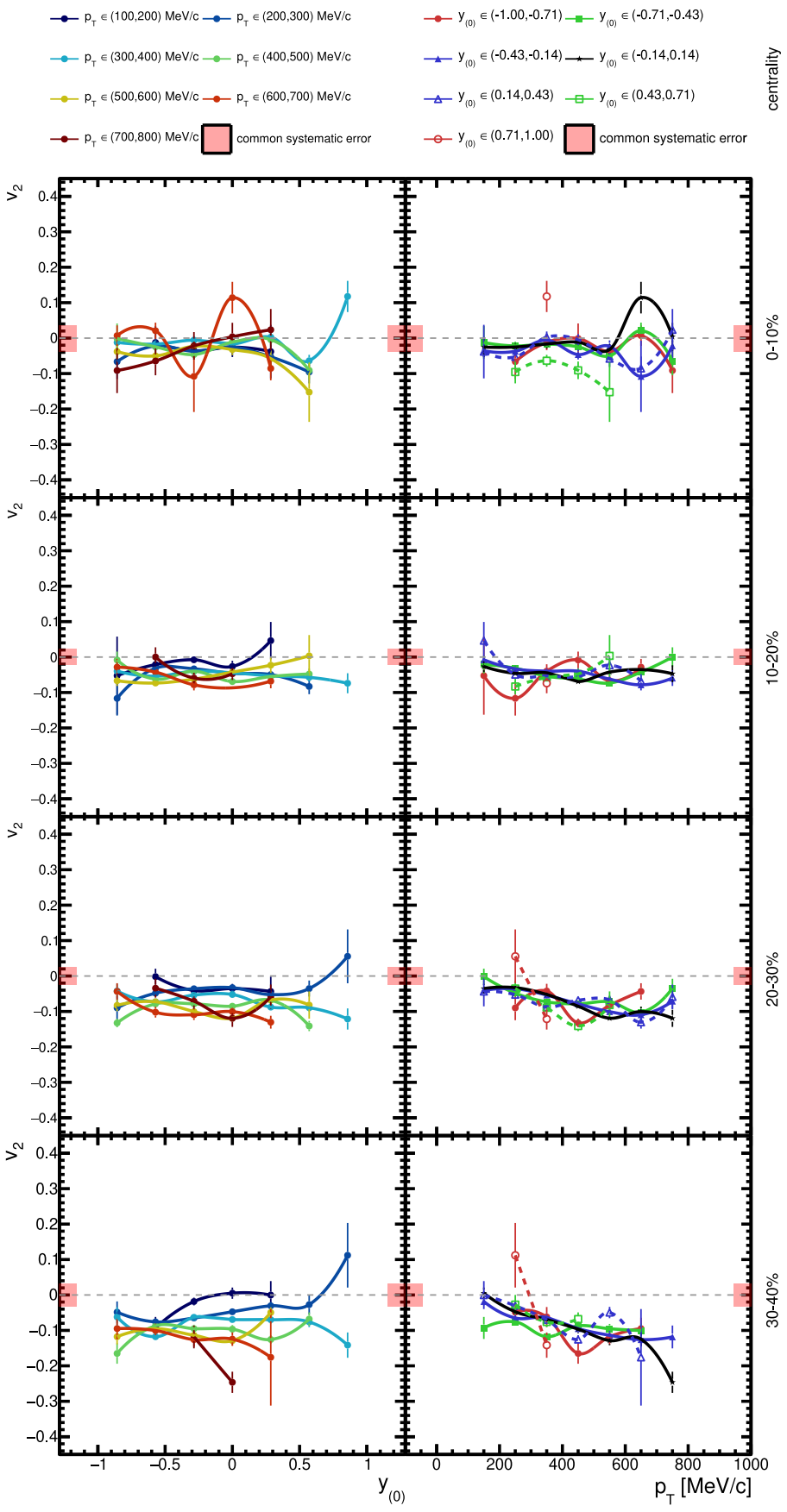

Figure B.8: Differential elliptic flow of K^+ measured in Au + Au collisions at beam kinetic energy $E_{\mathrm{kin,beam}} = 1.23A\,\mathrm{GeV}$ in 40% most central collisions.

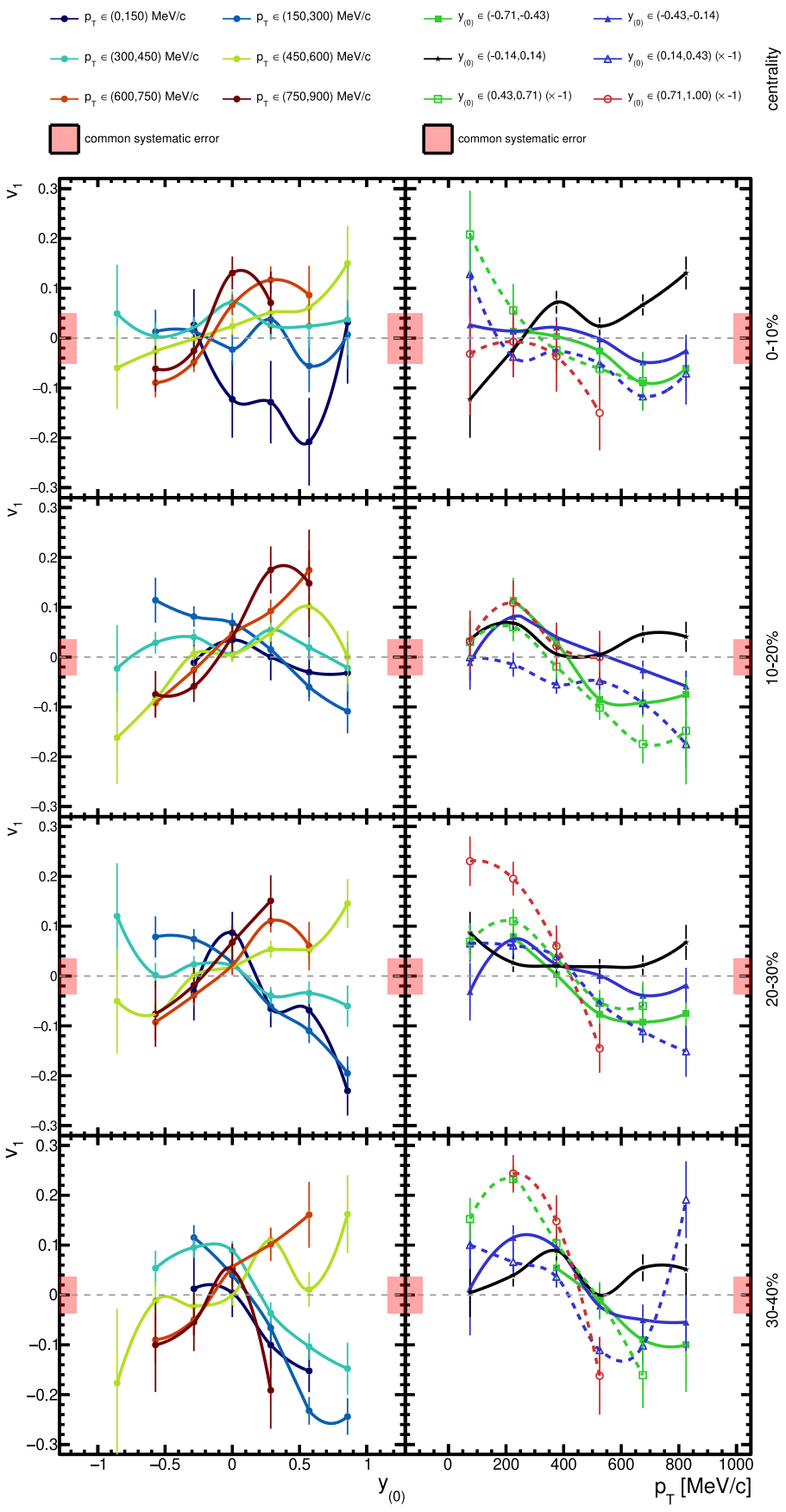

Figure B.9: Differential directed flow of K^0_S measured in Au + Au collisions at beam kinetic energy $E_{\mathrm{kin,beam}} = 1.23A\,\mathrm{GeV}$ in 40% most central collisions.

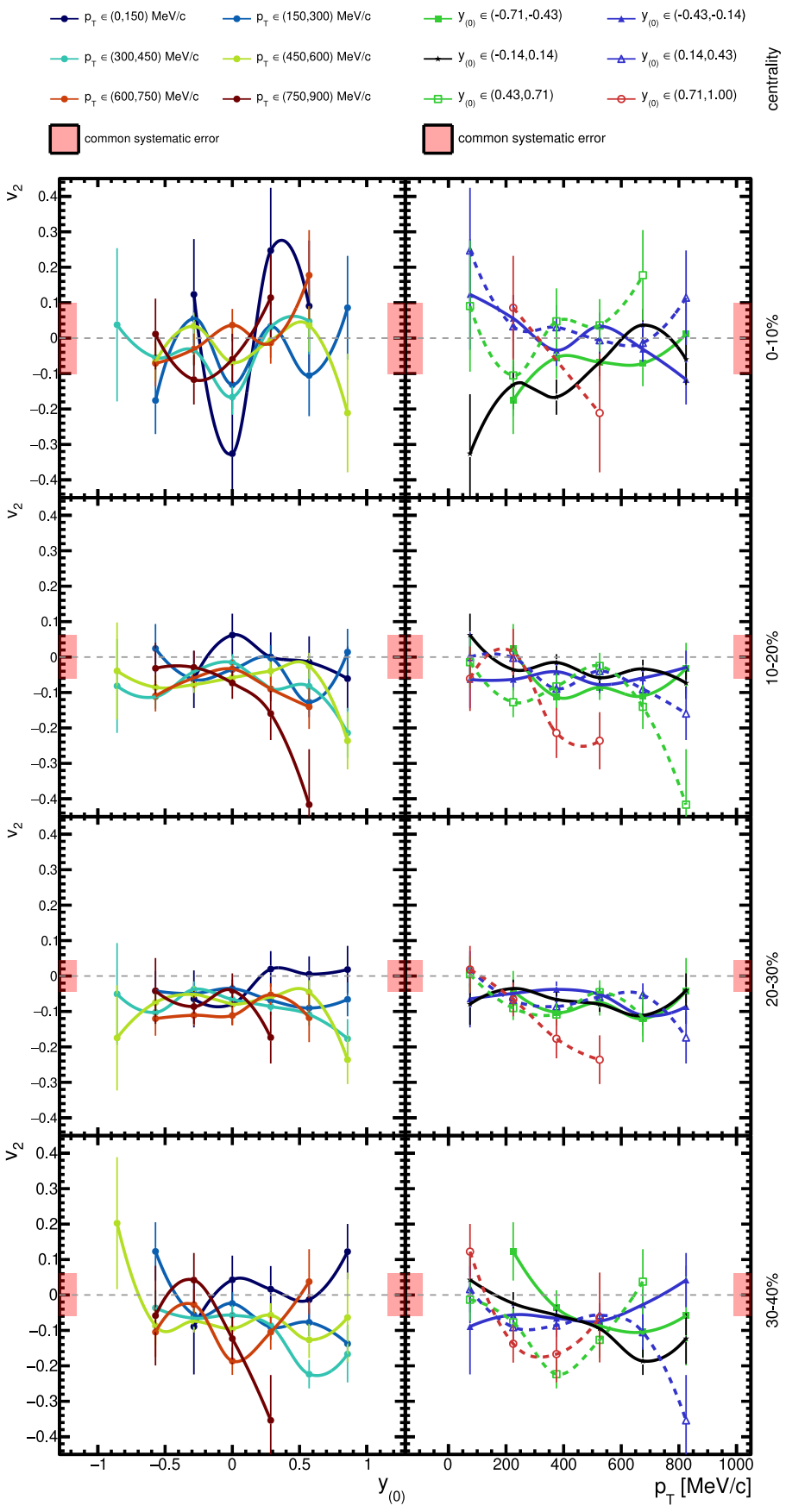

Figure B.10: Differential elliptic flow of K^0_S measured in Au + Au collisions at beam kinetic energy $E_{\mathrm{kin,beam}} = 1.23A\,\mathrm{GeV}$ in 40% most central collisions.

Appendix C

Supplementary figures for the comparison of data analysis with model predictions

C.1 K^+ flow in different centrality classes

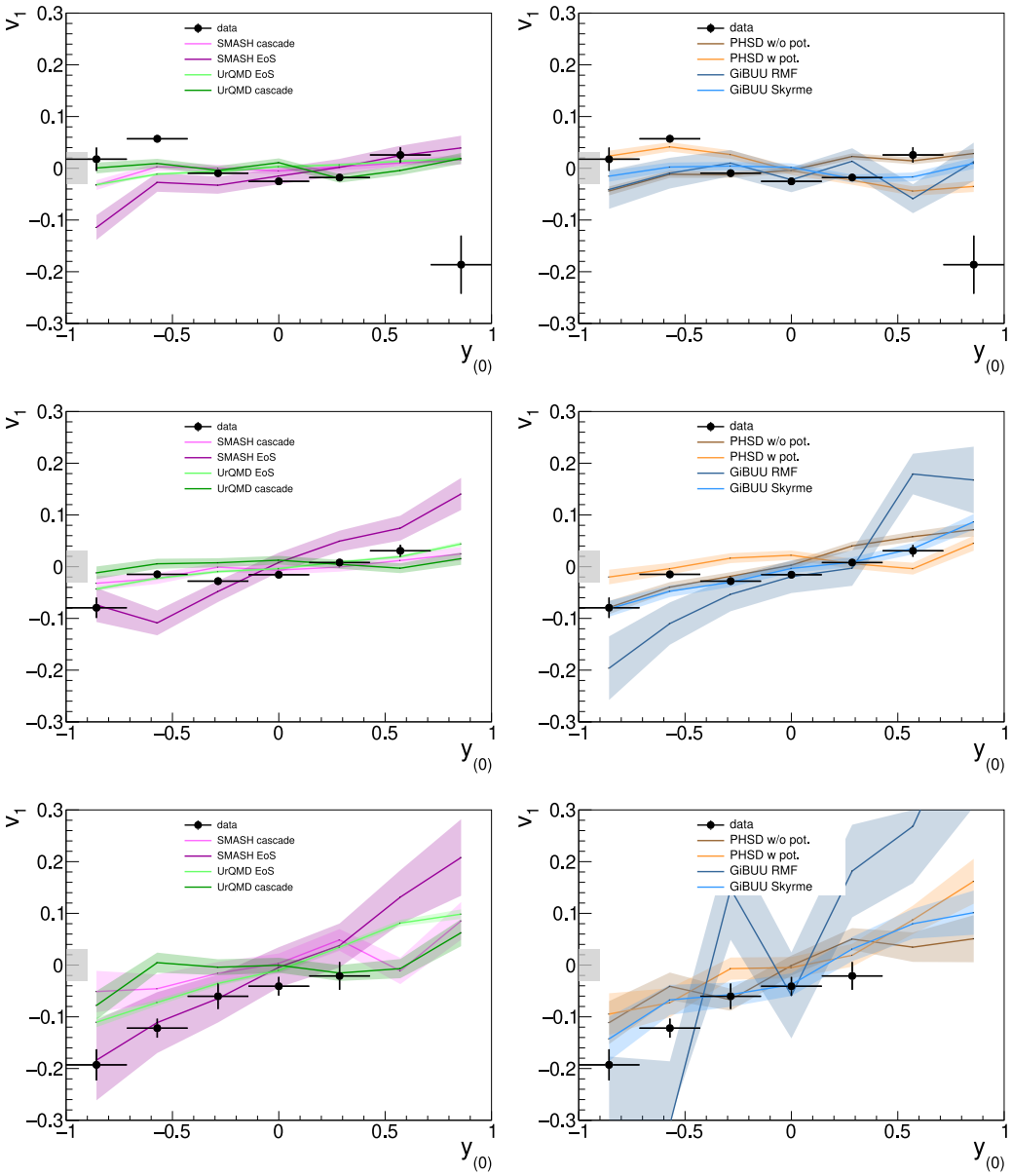

Figure C.1: K^+ directed flow in $0-10\%$ centrality class. Upper row is for $p_T \in (200, 300)\,\mathrm{MeV}/c$, middle row $p_T \in (400, 500)\,\mathrm{MeV}/c$ and lower row $p_T \in (700, 800)\,\mathrm{MeV}/c$. Gray box indicates the size of systematic uncertainty of the data points.

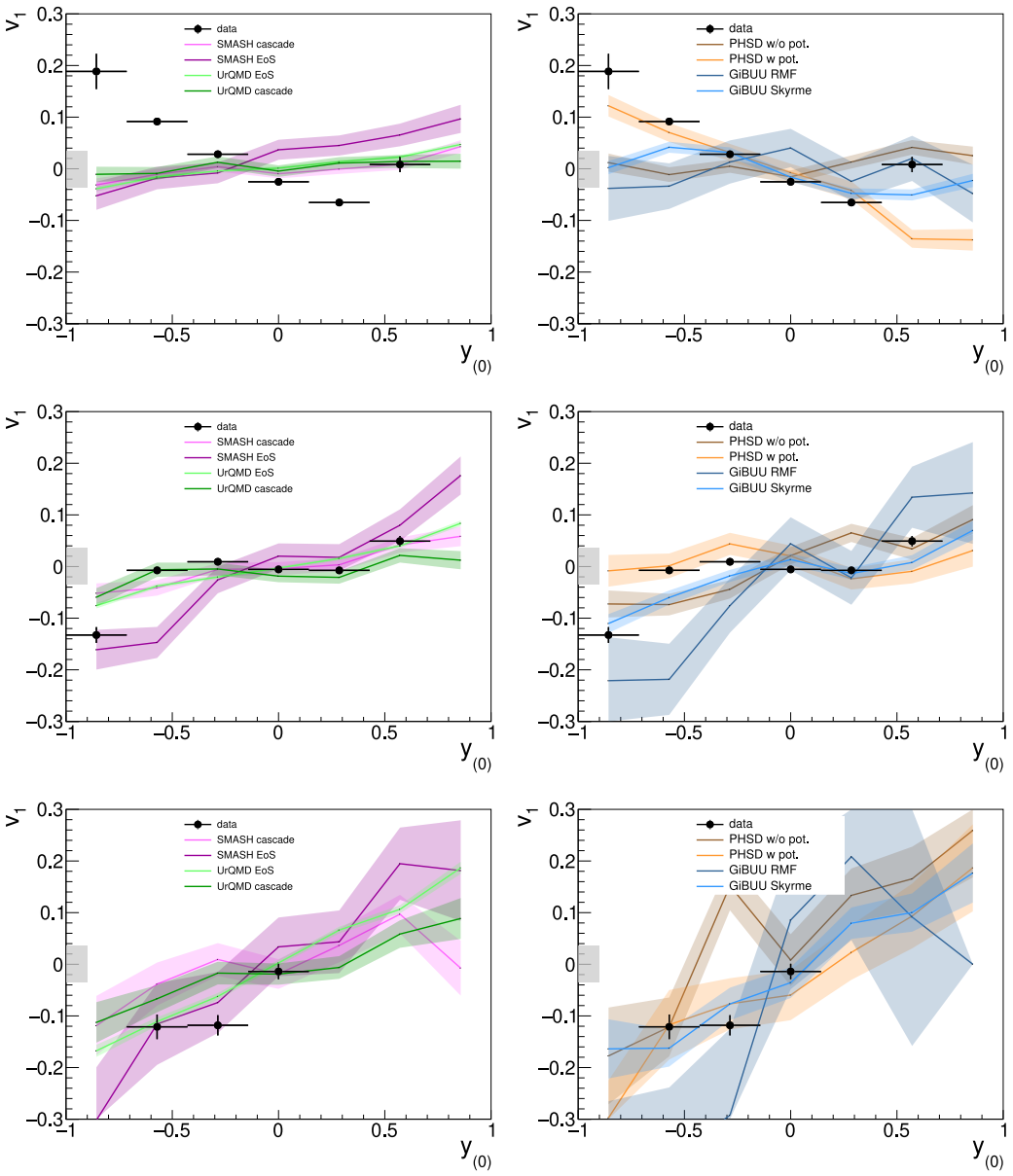

Figure C.2: K^+ directed flow in $10-20\%$ centrality class. Upper row is for $p_T \in (200, 300)\,\mathrm{MeV}/c$, middle row $p_T \in (400, 500)\,\mathrm{MeV}/c$ and lower row $p_T \in (700, 800)\,\mathrm{MeV}/c$. Gray box indicates the size of systematic uncertainty of the data points.

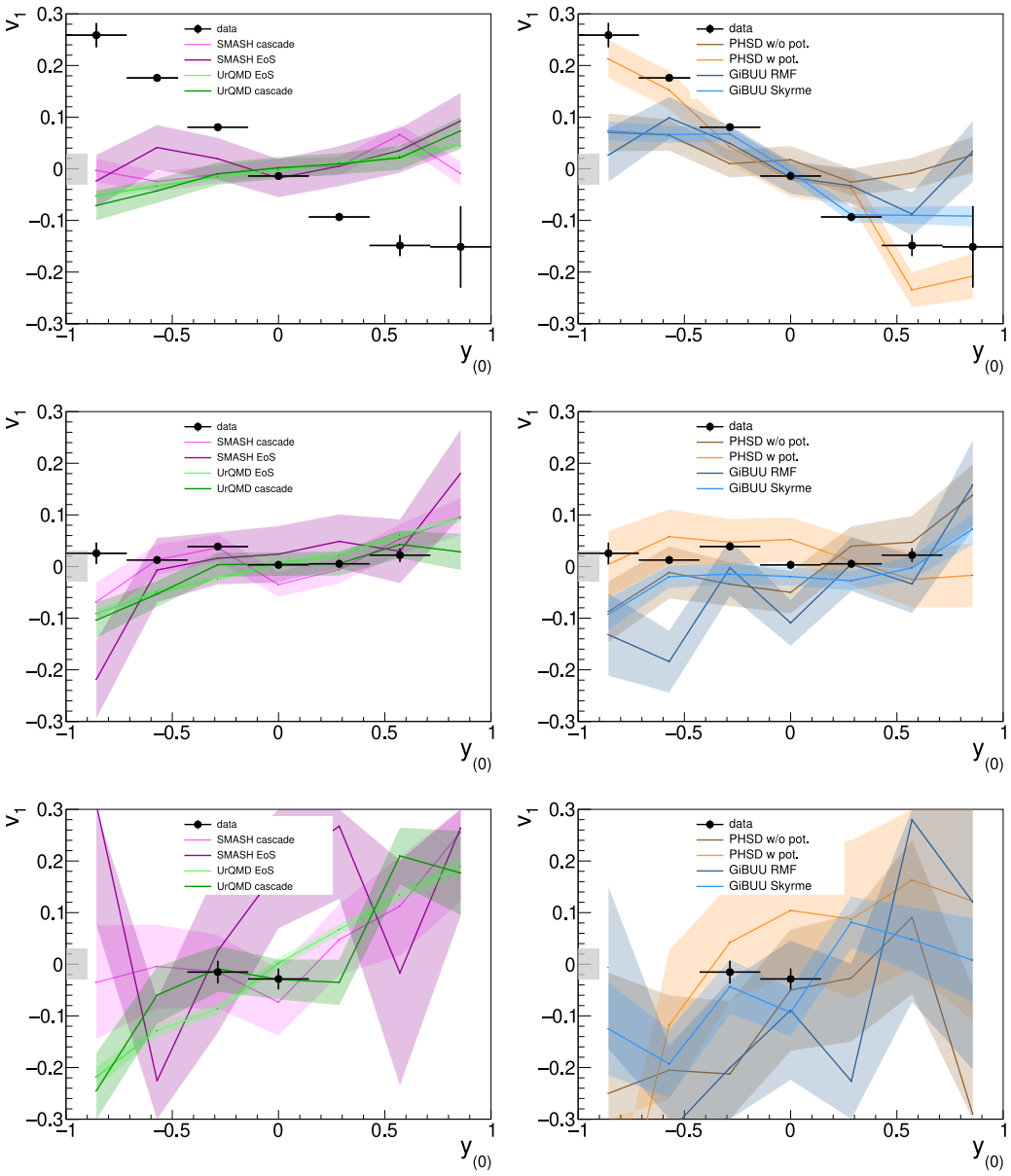

Figure C.3: K^+ directed flow in $30-40\%$ centrality class. Upper row is for $p_T \in (200, 300)\,\mathrm{MeV}/c$, middle row $p_T \in (400, 500)\,\mathrm{MeV}/c$ and lower row $p_T \in (700, 800)\,\mathrm{MeV}/c$. Gray box indicates the size of systematic uncertainty of the data points.

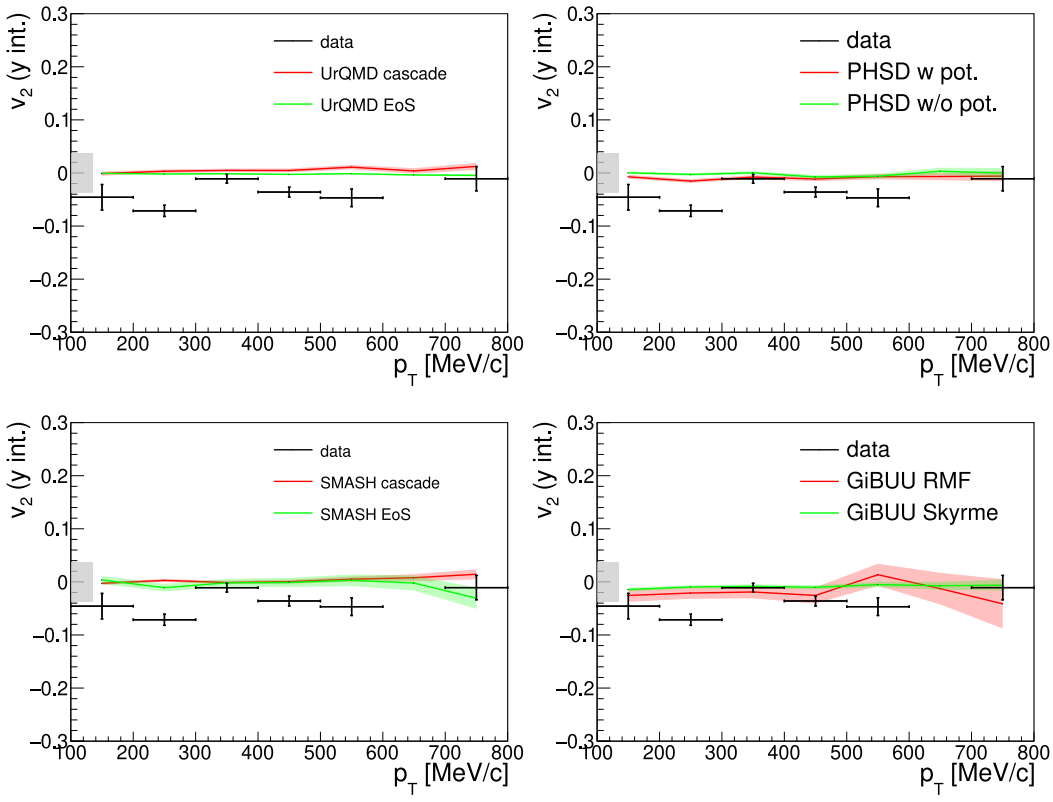

Figure C.4: Elliptic flow of positively charged kaons measured in $0-10\%$ most central Au + Au collisions at beam energy $1.23A\,\mathrm{GeV}$ confronted with selected transport model simulations. Gray box indicates the size of systematic uncertainty of the data points.

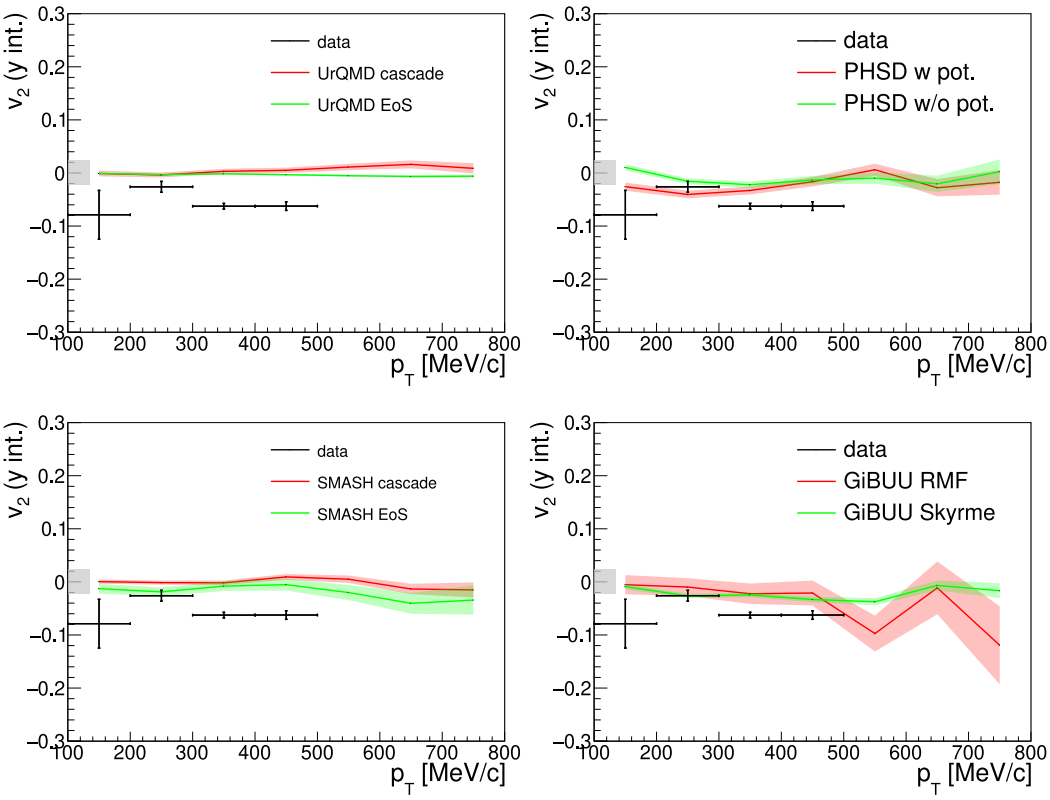

Figure C.5: Elliptic flow of positively charged kaons measured in $10-20\%$ most central Au + Au collisions at beam energy $1.23A\,\mathrm{GeV}$ confronted with selected transport model simulations. Gray box indicates the size of systematic uncertainty of the data points.

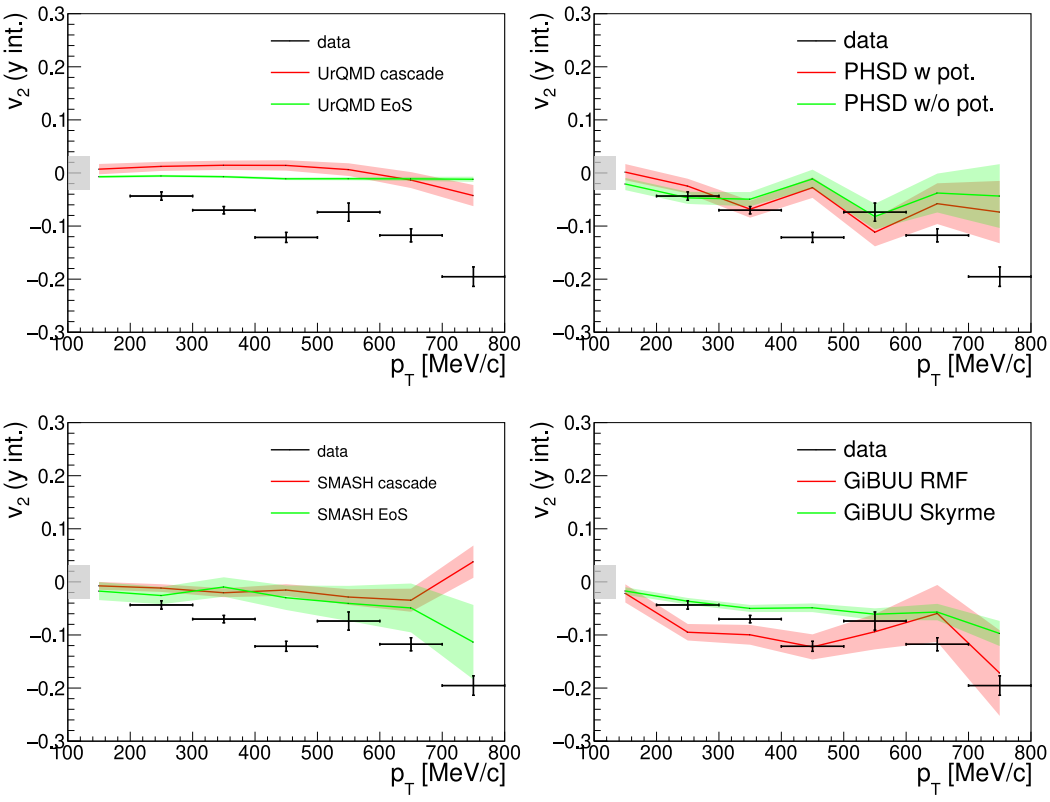

Figure C.6: Elliptic flow of positively charged kaons measured in $30-40\%$ most central Au + Au collisions at beam energy $1.23A\,\mathrm{GeV}$ confronted with selected transport model simulations. Gray box indicates the size of systematic uncertainty of the data points.

C.2 K^+ phase space distribution in models

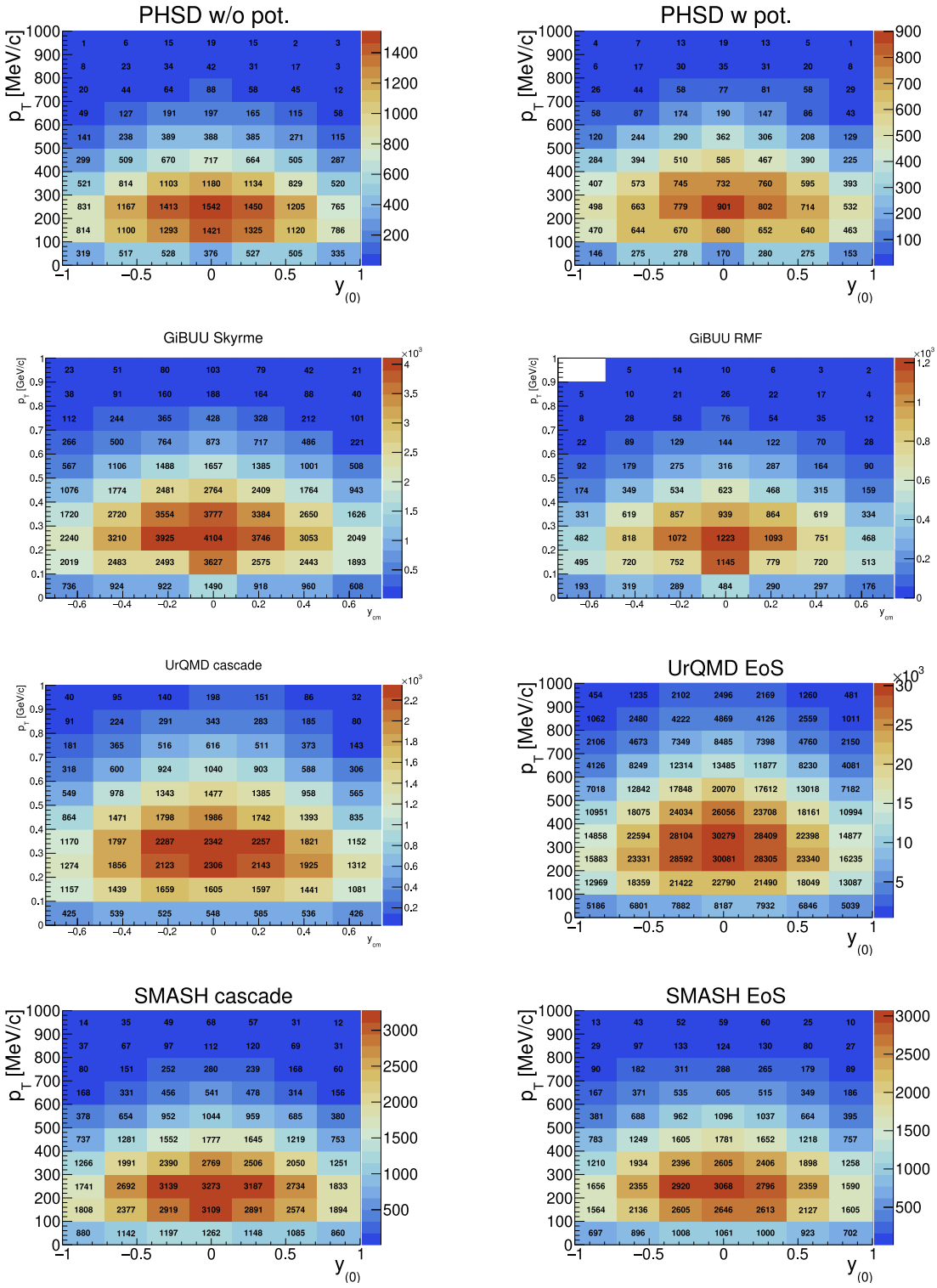

Figure C.7: K^+ phase space distribution obtained from transport calculations in $20-30\%$ centrality class. There were different number of events simulated in different models.